Aix*Marseille université

cea IRFM

DOCTORAL THESIS

Aix-Marseille University

Doctoral School: *Physique et Sciences de la Matière*

Speciality : **Énergie, Rayonnement, Plasma**

Numerical evaluations of mechanisms governing the heat transport in the edge plasma of tokamaks

Presented by:

Camille Baudoin

Board of examiners for public Ph.D. defense on February, 8th 2018

Pr. Martine BAELMANS	Referee – Professor at Leuven University
Pr. Etienne GRAVIER	Referee – Professor at University of Lorraine
Dr. Jan HORACEK	Examiner – Researcher at IPP Institute
Pr. Luc VERVISCH	Examiner – Professor at University of Normandie
Dr. Yannick MARANDET	Examiner – Researcher at CNRS, PIIM
Dr. Patrick TAMAIN	CEA supervisor – Research engineer at IRFM, CEA
Pr. Philippe GHENDRIH	PhD director – Professor at IRFM, CEA

Laboratory :

Institut de **R**echerche sur la **F**usion par confinement **M**agnétique

CEA – Cadarache

13108 Saint-Paul-lez-Durance, France

Nov 2014 – Fev 2018

Thèse de doctorat

Université d'Aix-Marseille

École doctorale: *Physique et Sciences de la Matière*

Spécialité : **Énergie, Rayonnement, Plasma**

Études numériques des mécanismes gouvernant le transport de la chaleur dans le plasma de bord des Tokamaks

Presentée par:

Camille Baudoin

Thèse soutenue publiquement le 8 Février 2018 devant le jury composé de :

Pr. Martine Baelmans	Rapporteur – Professeur à l'Université de Louvain
Pr. Etienne Gravier	Rapporteur – Professeur à l'Université de Lorraine
Dr. Jan Horacek	Examinateur – Ingénieur de recherche à l'institut IPP
Pr. Luc Vervisch	Examinateur – Professeur à l'Université de Normandie
Dr. Yannick Marandet	Examinateur – Chercheur au CNRS, PIIM
Dr. Patrick Tamain	Responsable CEA – Ingénieur de recherche à l'IRFM, CEA
Pr. Philippe Ghendrih	Directeur de thèse – Professeur à l'IRFM, CEA

Laboratoire :

Institut de **R**echerche sur la **F**usion par confinement **M**agnétique

CEA – Cadarache

13108 Saint-Paul-lez-Durance, France

Nov 2014 – Fev 2018

Résumé

La fusion nucléaire est une solution technologique prometteuse pour une nouvelle source d'énergie. Cependant, utiliser la fusion nucléaire par confinement magnétique comme source d'énergie représente un défi scientifique et technologique car cela requiert un bon confinement du plasma de cœur en même temps qu'un contrôle des flux de chaleur arrivant aux parois. Ce travail est motivé par la problématique centrale de la gestion des flux de chaleur dans les réacteurs de fusion. Cela est nécessaire pour éviter d'endommager des coûteux composants faisant face au plasma.

Dans ce contexte, il est nécessaire de faire des prédictions fiables de l'étalement de la chaleur dans le but de dimensionner correctement ces futures machines. Cela appelle à un fondement théorique décrivant la manière dont l'énergie s'échappe du plasma de cœur à travers la séparatrice, et se répartit sur les composants faisant face au plasma. Pour atteindre cet objectif, la modélisation numérique est un complément nécessaire aux expériences, car ces dernières ne donnent qu'une information partielle sur l'état du plasma due à la difficulté de mesure dans un plasma à si haute température.

Ce travail de thèse est dédié à l'étude numérique des différents aspects du transport de la chaleur dans le plasma de bord en utilisant les approches fluides. Le problème a été traité avec une approche graduelle en utilisant différent outils numériques. Une attention particulière est portée à deux mécanismes suspectés de jouer un grand rôle dans le transport de la chaleur : le transport intermittent due à la turbulence, établie comme un acteur majeur du transport des particules dans le plasma de bord en mode-L; et le transport convectif à large échelle par les vitesses de dérives, en particulier par les dérives de courbure. Les modèles dérivant de ce type de mécanisme ont récemment soulevé un intérêt particulier dû à leur bon accord avec les lois d'échelle expérimentales actuelles. Les premiers résultats des simulations anisothermes montrent que les caractéristiques générales de la turbulence ne sont pas drastiquement modifiées par la prise en compte de la dynamique de la température. Néanmoins ces simulations permettent de mettre en évidence l'existence d'un mécanisme d'instabilité additionnel en présence de fluctuations de température électronique et pointent l'importance des gradients de températures à l'origine de l'augmentation du cisaillement à la séparatrice, modifiant ainsi la pénétration de la turbulence dans la SOL. Finalement, les études à faible transport anormal ont montré l'existence d'un régime où la largeur de la Scrape-Off-Layer est régit par la dérive de courbure. Ce régime présente cependant des caractéristiques intrinsèques très complexes qui soulèvent la question de sa pertinence physique.

Abstract

Fusion devices are a promising solution for a new source of energy. However, using fusion reaction to produce power within a magnetic confinement is a scientific and technological challenge as it requires a high confinement in the core plasma at the same time as a good control of plasma exhaust on the material walls. This work is motivated by the key problematic of power handling in fusion power plants necessary to avoid damaging or even melting the expensive plasma facing components.

In this context, it is mandatory to make reliable predictions of the power spreading in order to correctly size the future Tokamaks. This calls for a theoretical ground describing the way energy escapes the core plasma through the separatrix and deposits on the PFCs. Some theoretical and experimental studies attempt to achieve such a task, however no definitive conclusion has been drawn yet, and it is still not clear what are the main mechanisms at play. To achieve this goal, numerical modelling is a necessary complement to experimental results as the latter give only an incomplete picture of the plasma state due to the difficulties inherent to measurements in the hot plasma.

This PhD work has been dedicated to the study of the different aspects of the heat transport in the edge plasma using a numerical fluid approach. The problem of interest has been approached gradually using different numerical tools. Special focus was devoted to two types of mechanisms suspected to play an important role in the heat transport: turbulence established to be a major particle transport player in L-mode plasma; and the large-scale convective transport, and in particular the role of the magnetic drifts convection. The latter has drawn much attention recently as models based on such mechanisms of transport present a good agreement with the actual SOL width scaling law in the H-mode.

First results of anisothermal simulations show that general characteristics of turbulence are not drastically modified by the inclusion of temperature dynamics. Nevertheless, these simulations allow us to highlight the existence of an additional mechanism of instability in presence of electronic temperature fluctuations and to point out the importance of the temperature gradient in the increase of the electric shear at the separatrix, modifying the penetration length of turbulence in the SOL. Finally, the study at low level of anomalous transport show the existence of regime where the Scrape-Off-Layer width is ruled by the curvature drift. This regime presents however very complex characteristics rising the question of its relevance.

Contents

Introduction

Fusion devices are a promising solution for a new source of energy. Fusion power plants would present a lot of advantages, among others: large amount of released energy, accessible feedstock supply, and little nuclear waste. However, using fusion reaction to produce power using a magnetic confinement is a scientific and technological challenge as it requires a high confinement in the core plasma at the same time as a good control of plasma exhaust on the material walls.

This work is motivated by the key problematic of power handling in fusion power plants necessary to avoid damaging or even melting the expensive plasma facing components. The understanding of the physics underlying heat transport, and more specifically the establishment of the power Scrape-Off Layer (SOL) width λ_q, is a critical task for the engineering design of future Tokamak devices such as ITER ([Loarte 07, Wischmeier 15]) and DEMO ([Wenninger 14]).

In this context, it is mandatory to make reliable predictions for power exhaust in order to correctly size the future Tokamaks, and, if possible, to take advantage of the physics knowledge to improve the design of the machine. This calls for a theoretical ground describing the way energy escapes the core plasma through the separatrix and deposits on the PFCs. Some theoretical and experimental studies attempt to achieve such a task, however no definitive conclusion have been drawn yet, and it is still not clear what are the main mechanisms at play.

To achieve this goal, numerical modelling is a necessary complement to experimental results as the latter give only an incomplete picture of the plasma state due to the difficulties inherent to measurements in the hot plasma.

The 3D turbulent fluid approach for the edge plasma is an interesting tool to study this problematic leading to international efforts on the development of edge plasma models. The code TOKAM3X developed at IRFM is a part of this ongoing effort of plasma turbulence modelling. Among others, the most advanced 3D turbulent codes are BOUT++ [Naulin 08], GBS [Ricci 12], and TOKAM3X [Tamain 16], and each of these codes have its specificity. The code BOUT++, extension of the gradient driven code BOUT precursor of 3D fluid modelling, includes several additional physics in the fluid equations, in particular energy conservation, electro-magnetic and kinetic effects. This code has recently investigated the problematic of the power SOL width with good comparison with experimental results [Chen 17]. The code GBS includes also important physical features as neutrals description, electro-magnetic physics, and self-consistent fluctuations of temperature. Recent works focus on turbulence in non-isothermal limited simulations, in particular describing the effect of the limiter position on the pressure SOL width [Loizu 14] and discussing a possible explanation for the narrow feature observed experimentally in L-mode [Halpern 17]. Earlier linear work, has been carried out on the prediction for the pressure SOL width [Mosetto 13, Mosetto 15] based on non-local linear

theory [Ricci 10, Ricci 13]. The code TOKAM3X, despite using a simpler physical model, offers the possibility to use a flexible and complex geometry, including realistic X-points [Galassi 17]. Moreover, the code has been recently extended to an anisothermal version, the study of this extended model is one of the focus of this thesis. Note that these 3D codes follow the 2D codes also used to study transport in the edge plasma, in particular the code HESEL [Rasmussen 16] and TOKAM2D [Sarazin 98]. In particular, the code HESEL has produced interesting results on L-H transition, blobs dynamics in presence of temperature dynamics [Rasmussen 15, Olsen 16].

The study of the physics of power SOL width is one of the long-term objectives of TOKAM3X and TOKAM2D. However, both codes have been used only in their isothermal version until recently. One of the aims of this work is to review the general characteristics of energy turbulent structures and heat transport in the anisothermal versions, and to draw a comparison between turbulence features in isothermal and anisothermal models.

This PhD work has been dedicated to the study of the different aspects of heat transport in the edge plasma using a numerical fluid approach. Special focus was devoted to two types of mechanisms suspected to play an important role in heat transport:

- turbulence established to be a major particle transport player in L-mode plasma. In H-mode, turbulence strongly reduced in the pedestal and near-SOL. It is thus not clear which is the main mechanism driving the transport through the separatrix.
- large-scale convective transport, and in particular the role of the magnetic drifts convection. This mechanism has drawn much attention recently as models based on such mechanisms of transport present a good agreement with the actual scaling law in the H-mode.

The problem of interest has been approached gradually using different numerical tools. In a first stage, we have studied separately the two mechanisms:

- the basic properties of turbulence and heat transport in the presence of self-consistent temperature evolution have been studied with the code TOKAM2D (Chapter 3);
- the large scale transport by the magnetic drift in realistic geometry but with a low level of anomalous transport are studied with the code SolEdge2D (Chapter 4).

Finally, the study of simulations including both mechanisms, is made in the last chapter (Chapter 5). This work has been done using the code TOKAM3X in its anisothermal version, which solves both energy turbulence and 3D geometry self-consistently in the same simulation.

Outline of the thesis

In the second chapter of this manuscript, we introduce the fluid model, and detail the assumptions followed with this approach (high collisionality, drift approximations). We then present the physics of the open-field lines due to the plasma-wall interaction, which determines the boundary conditions used in the fluid models. Finally, we detail the derivation of the equations of one of the three code used

in this thesis: TOKAM3X, as the two others studied codes (TOKAM2D, SolEdge2D) are somehow included in the TOKAM3X model.

The third chapter addresses the basic properties of turbulence in a simplified 2D geometry, and the impact of the addition of self-consistent temperature variation. First, it is found that the inclusion of temperature does not modify drastically the general features of turbulence, presenting similar intermittent structures and highly intermittent transport. Nevertheless, the presence of electron temperature fluctuations in the current parallel losses triggers an additional instability, the sheath negative resistance instability, which acts in conjunction with the interchange drive. The characterisation of the turbulence, using the input of linear analysis, has revealed that the additional instability has an impact on turbulence, and also on the perpendicular equilibrium in particular on the power decay length. The impact of ion temperature fluctuations is studied separately. Its inclusion, even though it does not trigger a new instability, impacts the turbulence characteristic and the decay length through the perpendicular balance equation, namely its impact on the vorticity expression.

The fourth chapter is dedicated to the study of large-scale transport due to magnetic drifts in simulations where the turbulence is arbitrarily set via a diffusion coefficient. In this framework, we observe the existence at low diffusion of a $\boldsymbol{\nabla} B$-drift dominated regime in which both transport and SOL widths are determined entirely by the $\boldsymbol{\nabla} B$ drift convection. Such a regime exists independently of parameters and the geometry chosen. However, the latter is also characterized by a complex plasma equilibrium presenting supersonic transition and steady-state shock. Moreover, this regime is reached only at extremely low level of transverse transport, way below the neoclassical level. Finally, we discuss the impact of some additional physics in the drift dominated regime as the addition of the centrifugal drift, the temperature evolution and the neutral inclusion.

For the fifth and last chapter, we have run TOKAM3X fluid simulations in limiter realistic geometry, one isothermal and one anisothermal, with the aim to characterize particle and energy turbulence and transport and to compare the two models. The regime found for this geometry and this set of parameters is a L-mode like regime, where turbulence is largely dominant both in particle and energy transport. Here, the contribution of $\boldsymbol{\nabla} B$-drift convection to the global transport is negligible, which is in agreement with the result of the previous chapter, as the drift dominated regime exists only at very low anomalous transport level. Moreover, we find, as in 2D simulations, that there is no significant modification of the turbulence features (intermittent structures and statistical properties) due to the addition of temperature fluctuation. However, the temperature gradients induce a key difference between isothermal and anisothermal simulations: it triggers the presence of a high amplitude electrostatic shear layer. This shear layer comes along with a reduction of the turbulent flux penetration into the SOL. However, the exact impact of the shear layer on the turbulence remains unclear as they do not appear at the same radial location.

Chapter 1

Issues of the power exhaust in Tokamak devices

1.1 Fusion basics

Nuclear fusion, reaction occurring in stars, is a reaction of two light atomic nuclei which join to form a heavier atomic nucleus. This reaction is associated with a reduction of the total mass of the system, which leads to the release of a large amount of kinetic energy of reaction products, quantified by the well-known Einstein relation $\Delta E = \Delta mc^2$. One would like to use this process as a means to have a new source of energy in the future.

However, such a reaction does not easily happen as it requires high-energy particles to permit the atomic nucleus to overcome the long-range Coulomb repulsion force and get close enough so that the short-range strong nuclear force can lead to fusion. In theory, fusion reaction would produce energy for all element lighter than iron, but in practice, on earth, only the reactions involving hydrogen isotopes are conceivable. Among those, the deuterium-tritium (D–T) reaction is the one chosen for future fusion devices. Even then, the reaction of fusion requires very high temperature of the order of 10^9 K. Given extreme temperatures involved, one can readily expect to have great challenges concerning power exhaust.

A simplified power balance of the fusion plasma gives conditions for fusion to be energetically profitable [Lawson 57]. The Lawson criteria gives the amplification factor, Q ratio between the energy produced by fusion reaction P_{fus} and the external energy input P_{ext}: $Q = P_{\text{fus}}/P_{\text{ext}}$ as a function of plasma parameters Eq.1.1:

$$f(Q) = nT\tau_E \tag{1.1}$$

where n is the plasma density, T is the plasma temperature and τ_E the energy confinement times. For economic reliability, one estimates that the amplification factor has to be above 40, or that $nT\tau_E > 3.10^{21}\text{m}^{-3}\text{keV.s}^{-1}$ [1]. The temperature being imposed by the D-T reactivity, two main ways can be followed to reach this criterion:

- Inertial Confinement Fusion with extremely dense plasma ($n \approx 10^{31}\text{m}^{-3}$) but with short con-

[1] In the world of nuclear fusion, the energy unit of electron-Volt (eV) is used as a temperature unit instead of the Kelvin. One writes equally T and $k_{\text{B}}T$ where k_{B} is the Boltzmann's constant and one has $1\,\text{eV} = 1.602 \times 10^{-19}$ J $\sim 10^4$ K

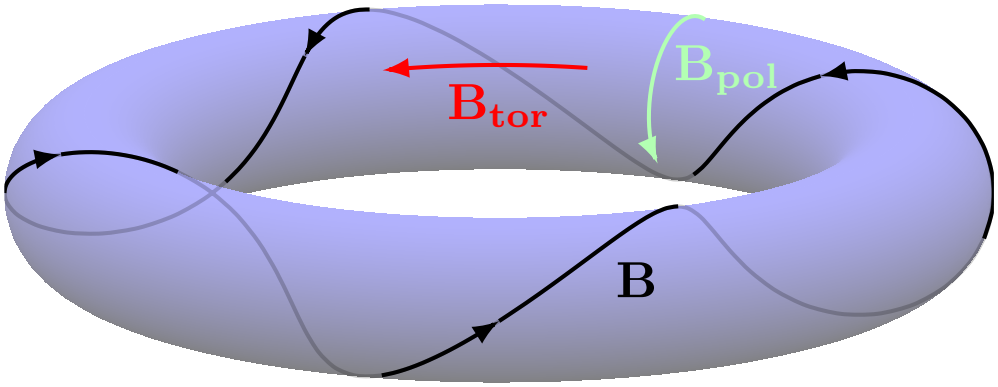

Figure 1.1: Tokamak magnetic configuration

finement times ($\tau_E \approx 10^{-11}$s), such conditions are obtained by compression of D-T pellet with laser beam.

- Magnetic Confinement Fusion with relatively low-density ($n \approx 10^{19} - 10^{20}$m^{-3}) but long confinement times (τ_E few s). This second fusion branch is the focus of this present work.

1.2 Magnetic confinement in the Tokamak configuration

1.2.1 Magnetic confinement in a Tokamak

No solid wall can withstand the extreme temperature required for fusion reactions. Thus, fusion reactions have to take place away from the wall. At this temperature, reactants are stripped from their electrons, and matter is in the plasma state. Devices for fusion by magnetic confinement take advantages of the property that charged particles in a magnetic field, $\mathbf{B}$, have a helical trajectory around field lines. The radius of this trajectory is the Larmor radius (ρ_L):

$$\rho_L = \frac{m_s v_\perp}{q_s B} \tag{1.2}$$

Where m_s, $v_\perp$, and q_s are respectively the mass, the cross-field velocity and the charge of the particle. The Larmor radius of a deuterium ion D^+ at 10 keV in a magnetic field of 3 Tesla is about 5.10^{-3} m. This way the plasma is confined in the direction transversal to the magnetic field, but is still free in the parallel direction.

In order to confine the particles in the parallel directions, the configuration of fusion devices uses closed magnetic field lines, i.e which do not intercept any solid wall, this way the hot plasma of fusion is also confined in the parallel direction. A straightforward idea is to produce a magnetic field, called toroidal field and denoted $\mathbf{B_{tor}}$ (reported in red on Fig.1.1), with circular field lines in a form of a torus using circular coils which are toroidally distributed all around the plasma.

The produced magnetic field presents inhomogeneities. Considering the Ampere's law one can readily observe that $\mathbf{B_{tor}}$ is proportional to the inverse of the distance to the center of the torus $\mathbf{B_{tor}} \propto 1/R$. The magnetic field amplitude is lower in the outer region of the torus, called Low Field Side (LFS) than the inner region the high field side (HFS). This inhomogeneity creates particles vertical drift dependent of the charge sign, thus is in the opposite direction for electrons and ions

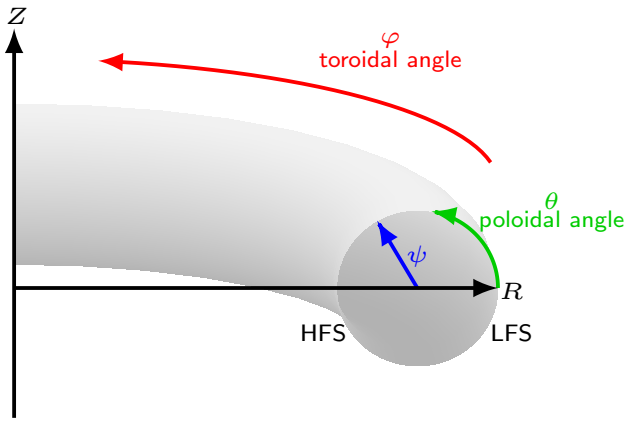

Figure 1.2: System of coordinates used in Tokamak configuration

(see section 2.2). The induced vertical charge separation leads to a fast deterioration of the plasma confinement. Therefore, a more complex magnetic configuration is required. An additional field, called poloidal field and denoted $\mathbf{B_{pol}}$ (reported in light green on Fig.1.1) is added. This field is achieved by driving a current in the plasma (current in the toroidal direction), this current is induced by induction using primary coils in the center of the plasma.

Each field line of the total magnetic field, $\mathbf{B} = \mathbf{B_{tor}} + \mathbf{B_{pol}}$, is contained in a surface, called the flux surface and labelled ψ. Except for rational values of the safety factor, denoted q Eq. (1.3), defining the winding of the magnetic field lines, a field line never closes on itself and covers the entire magnetic flux surface.

$$q(r) = \frac{\boldsymbol{B} \cdot \boldsymbol{\nabla}\varphi}{\boldsymbol{B} \cdot \boldsymbol{\nabla}\theta} \tag{1.3}$$

The plasma equilibrium on the flux surfaces ψ is described by the force balance, that writes in the ideal Magnetohydrodynamics (MHD) approximation:

$$\mathbf{B} \times \mathbf{J} = -\boldsymbol{\nabla} p \tag{1.4}$$

where $\mathbf{J}$ is the current density in the plasma and p the plasma pressure. This equation implies that the pressure is uniform on the flux surface ($\mathbf{B} \cdot \boldsymbol{\nabla} p = 0$), which can be expected from the free motion of particles on magnetic field lines. This pressure gradient is directed toward the center of the plasma, so that the pressure is higher in the center region of the plasma, where fusion reaction take place, and lower in the exterior region where the plasma is close to the material walls.

1.2.2 Limiter and divertor configurations

The plasma cannot be in an infinite volume chamber, and, inevitably above a certain radial extension, all magnetic field lines are intercepting a solid wall. The corresponding flux surfaces are called open flux surfaces, to distinguish them from the core flux surfaces, i.e. the closed flux surfaces Fig. 1.3. The first surface intercepting a solid surface is the Last Closed Flux Surface (LCFS), also called separatrix. The plasma region which intercepts the material wall, the Scrape-Off-Layer (SOL), is a region where the plasma–wall interaction takes place.

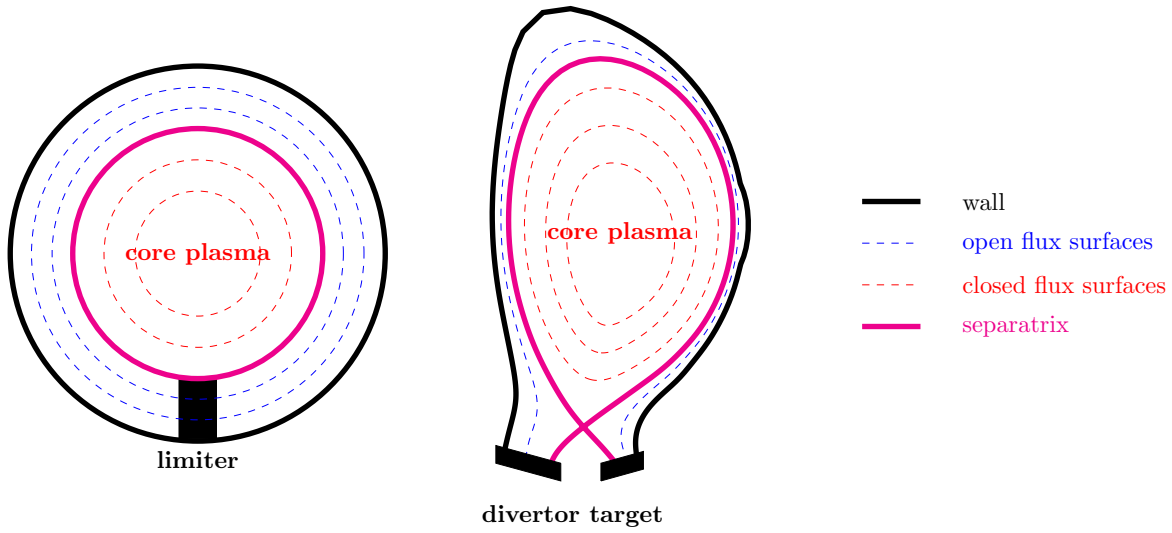

Figure 1.3: Sketch of the two geometry configuration limiter (left), divertor (right)

The SOL region is the transition between the core region, where extreme condition are required for fusion to take place, and the solid wall, where rather low temperature are needed to avoid the materials melting. It is thus a region presenting a complex physic, with important radial gradients. The Plasma-Facing Component (PFC), limiter or divertor targets, are the first components intercepting the field lines, and are designed to extract the high heat flux escaping from the core region via the plasma. It is worth to note that the PFCs act not only as a sink, but also release neutral particles, by recycling process, which are later ionized with energy provided by the plasma.

Two classes of magnetic configurations exist: limiter and the divertor configuration.

1.2.2.1 limiter configuration

The limiter configuration (represented on the left panel of Fig.1.3) is the straightforward, and historically magnetic configuration. It is not the chosen solution retained for steady-state plasma in future devices (see divertor configuration for reason). However, it remains of importance as it would be the configuration for the start-up plasma of ITER, and presents some challenge for the power exhaust problematics.

1.2.2.2 Divertor configuration

In divertor configuration, also called X-point configuration (represented on the right panel of Fig. 1.3) the plasma–wall interactions take place somehow remotely from the core plasma. This permits to avoid that plasma heavy impurity, created close to the strike point, penetrates in the core plasma and radiates energy which would deteriorate the confinement properties. Moreover, it has been shown that this configuration offers an easier access to the high confinement regime [Lipschultz 07, Pitcher 97] (see section 1.3.2.1).

1.3 Transport in Tokamak

The primary purpose of the Tokamak design is to ensure confinement (τ_E) of the fusion plasma. Such confinement requires transport in the parallel direction much faster than in the cross-field direction. However, a perfect confinement does not exist and the significant differences of temperatures between the edge and the core of the plasma impose a cross-field transport triggered by thermodynamic forces and directed to the outward region of the plasma. A good understanding of this transport is mandatory for the design of future machines for both estimation of confinement time and wall interaction problematics.

1.3.1 Classical and neoclassical transport

In the plasma, particles interact together via collisions, which leads to particles displacement from their trajectory. This process can be described by a random walk and modelled as a diffusion Eq. (1.5). This description of the transport is referred to as classical. Due to the important density and pressure gradient in the cross-field direction, the collisional mechanism results in a cross-field flux directed against the gradient, that is to say toward the exterior of the plasma.

$$\Gamma_{\perp,D} = -D_{\perp} \boldsymbol{\nabla}_{\perp} N \tag{1.5}$$

In this collisional approach, the diffusion coefficient is estimated as a function of the collision frequency, ν and the Larmor radius ρ_L, representing respectively characteristic time, spatial scales of the random walk. Thus, it can be assumed that $D_{\perp,\mathrm{c}} \sim \nu \rho_L^2$. In the edge plasma, the classical diffusion coefficient takes typical values in the range of 10^{-4} to 10^{-2} $m^2 s^{-1}$ for Deuterium ions. However, the classical description of the transport does not explain the level of cross-field transport observed in the experiments which is several orders of magnitude higher than the classical predictions.

In a torus geometry, the magnetic field presents inhomogeneity and the particles experience the variation of B along the field lines in the parallel direction, which modifies the collisional transport. The physics describing this effect is called the neoclassical description of the transport. The neoclassical estimation of the diffusion coefficient is higher than one of the classical one of a factor $\propto q^2$ (from 10 to 100) [Hinton 74]. However, the experience proved that this still is not sufficient to explain cross-field transport observed in Tokamaks.

1.3.2 Turbulent or anomalous transport

As presented previously, the collision theory is not sufficient to explain the cross-field transport, historically referred as *anomalous* transport as it was explained neither by classical nor by neoclassical theory. In the low confinement regime of the plasma (L-mode, see section 1.3.2.1), experimental evidence revealed that a large fraction of particles transport is driven by turbulence in the outer mid-plane, with high amplitude fluctuations of density, temperature and electrostatic potential in the edge plasma [Zweben 07, D'Ippolito 11]. This intermittent transport takes the form of long range filamentary structures aligned along field lines, usually called blobs or filaments. Blobs are then radially transported by the local electric drift, denoted $\mathbf{u_E}$ (see chapter 2), and the anomalous or

turbulent transport writes:

$$\Gamma_{\text{turb}} = \left\langle \widetilde{n}\widetilde{u}^{\psi}_{\mathbf{E}} \right\rangle_t \tag{1.6}$$

where $\widetilde{n}$ and $\widetilde{u}^{\psi}_{\mathbf{E}}$ represent respectively the fluctuating part of the density and of the $\mathbf{u_E}$ radial component, and $\langle\rangle_t$ represents the temporal averaging.

The turbulent transport is sometimes modelled by a diffusion term, with anomalous value for diffusion. However, if this method is practical for the global modeling of the machine, a precise comprehension of the turbulence is mandatory, especially to understand the transition towards the high confinement regime (H-mode, see section 1.3.2.1), or the asymmetry in the cross-field transport and to make reliable prediction for future devices.

1.3.2.1 H-mode and transport barriers

Turbulence is a key player in the particle cross-field transport, responsible, when fully developed, for L-mode. Tokamak reliability requires achieving high performance discharges, with the objective to reduce the turbulence in order to reach higher pressure in the confined plasma. In 1982, an unpredicted regime, the H-mode, presenting higher confinement time, has been observed for the first time in ASDEX [Wagner 82]. The transition between L-mode and H-mode is due to a reduction of turbulence in the vicinity of the separatrix. The transition comes along with steeper pressure profiles in the region of reduced turbulence, forming a pedestal, and higher plasma pressure in the core plasma, as schematically shown in Fig. 1.4. The region of reduced turbulence is called a transport barrier.

A strong poloidal velocity shear layer, observed experimentally, is believed to be a key player of turbulence reduction [Burrell 97, Terry 00]. The turbulent structures are decorrelated by this shear layer and do not propagate through the barriers transport leading to the formation of the pedestal. The mechanisms triggering the formation of this shear layer, and thus responsible for the H-mode, are not resolved yet.

One of the downside of the H-mode, is the apparition of an MHD instability which triggers high frequency relaxations of energy, in the range of 10 to 1000 Hz: the edge localized modes (ELMs). Even though this question is not treated in this work focusing on steady-state energy deposition, the ELMs are also a critical issue for the lifetime of PFCs as they deposit extremely high amounts of energy.

1.3.3 Laminar large scale transport

In H-mode, the turbulence being strongly reduced in the pedestal and near-SOL, it is not clear which is the main mechanism driving the transport through the separatrix. Some models proposed that the direct advection of the steady-state mean fields by drift velocities (see section 2.2) could explain a part of the cross-field transport:

- An Heuristic Drift-based (HD) model [Goldston 12] proposed that, in H-mode, the direct advection by magnetic drifts $\mathbf{u}_{\nabla B}$ and $\mathbf{u}_{\text{cent}}$ (see chapter 2) is the main mechanism driving the cross-field transport across the separatrix.
- It has also been shown that the electric drift also drives large scale transport, and can present a steady-state contribution to the global transport, especially in the X-point region [Galassi 17].

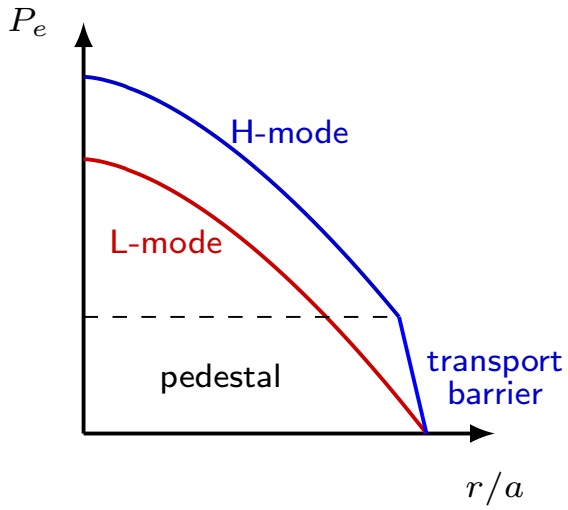

Figure 1.4: Pressure profiles in different confinement regimes: L-mode regime in red and H-mode regime in blue with the presence of a transport barrier

1.4 Power exhaust in steady-state at high performance: a critical issue for future devices

Economical viability of future fusion devices requires a sufficient power spreading onto PFC, potentially damaged by high energy deposition. For ITER, the design limit of divertor materials in steady-state is estimated at $10\,\mathrm{MW\,m^{-2}}$ [Loarte 07]. However, due to the anisotropic transport, faster along the field lines than in the transverse direction, energy escaping the core plasma reaches PFC through a narrow channel of plasma Fig.1.5. Thus, the exhaust energy is deposited on a small surface, receiving important heat flux. Nowadays, one has no certainty that ITER would stay within this constraint [Eich 13b], and power spreading is a key problematic for operation of future machine. In order to optimize the design of future machines, one needs to improve the predictive capability of the power spreading, and to have a better understanding of the physics underlying the establishment of the peak heat load is mandatory.

1.4.1 Power balance

$$P_{\mathrm{ITER}} = \underbrace{500\ \mathrm{MW}}_{\text{fusion}} + \underbrace{50\ \mathrm{MW}}_{\text{heating}} \tag{1.7}$$

In operational steady state of Tokamak, input and reaction power has to be evacuated one way or another, for ITER $P_{\mathrm{tot}} = 550\,\mathrm{MW}$, 50 MW with external heating and 500 MW with fusion. During a fusion reaction, 4/5 of energy, that is to say 400 MW, is transferred to neutrons, and the rest to the plasma. Neutrons are not confined by the magnetic field and are dispersed on the entire wall surface. In the power transferred to the plasma, about 50 MW is radiated by bremmstralung, and impurity radiation. Once again, this energy is dispersed on the entire wall surface. The 100 MW left, denoted P_{SOL}, is evacuated by plasma convection. For the need of confinement time of Tokamak, the cross-field transport of particles gyrocenter has to be small compared to the transport in the parallel

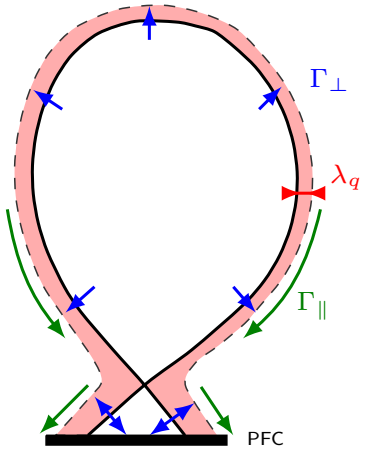

Figure 1.5: Sketch of the SOL width, s represents the radial target coordinate and s_0 the strike point position

direction. The downside is that the plasma crossing the separatrix flows towards the target without important spreading, so the power evacuated by convection will be deposited only on a small surface, which means important heat flux, and potential damage for the plasma facing component at the strike point.

1.4.2 SOL width definition

For a given power evacuated through the plasma P_{SOL}, the maximal heat flux, q_{peak} is inversely proportional to the wetted surface, S_{wet}, that is to say the surface of spreading of the heat flux. Considering the axisymmetry of the problem, the value of this surface is constrained by the width of the heat channel, denoted λ_q, and a geometric parameter defined by divertor properties (discussed in the next section).

$$q_{\mathrm{peak}} \propto \frac{P_{\mathrm{SOL}}}{S_{\mathrm{wet}}} \sim \alpha_{\mathrm{geo}} \frac{P_{\mathrm{SOL}}}{2\pi R \lambda_q} \tag{1.8}$$

The heat channel width is thus a key problematic in the heat exhaust, and λ_q results from a competition between the parallel and cross-field transport in the main SOL. From a general perspective this thin narrow layer derived from the equality:

$$\tau_\parallel \sim \tau_\perp \tag{1.9}$$

where $\tau_\parallel$ and $\tau_\perp$ are respectively the characteristic time in the parallel and in the cross-field direction.

The penetration length in the SOL λ_q is related to the physics of the SOL and its model of transport.

- For a diffusive transport model, used in transport codes (see chapter 4), λ_q is defined by the relation Eq. (1.10), where $D_\perp$ can represent classical, neoclassical or anomalous transport.

$$\frac{\lambda_q^2}{D_\perp} \sim \frac{L_\parallel}{c_s} \tag{1.10}$$

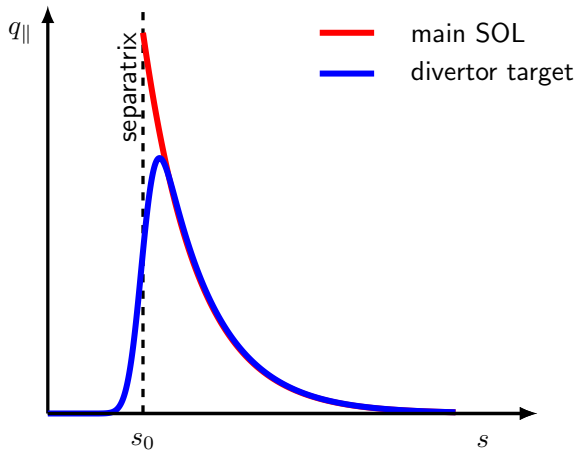

Figure 1.6: Schematic shape of the heat flux profile in the main SOL (red) and at the target (blue)

where $L_\parallel$ is the characteristic length in the parallel direction and c_s is the acoustic speed taken as the characteristic parallel velocity.

- For a convective transport model λ_q is defined by the relation Eq. (1.11). For turbulence modelling, the intermittent character of the transport has to be taken into account. An expression of a time-averaged perpendicular velocity has been proposed by Ref. [Fedorczak 17]: $v_\perp^{\text{turb}} = \frac{n_b}{n}\tau_b f_b v_b$, where n_b is the density of the blob, n the averaged local density, f_b frequency of apparition of a blob, τ_b its lifetime, and v_b its velocity.

$$\frac{\lambda_q}{v_\perp} \sim \frac{L_\parallel}{c_s} \tag{1.11}$$

It is worth to underline that the λ_q notion is somehow a theoretical view of a concept that one tends to resume to a single valued comprehension whereas it is multi-faceted. Indeed, this narrow channel has no reason to be uniform neither in time, in particular for turbulent regime, nor in space. In fact temporal disparity, poloidal and radial asymmetry has been reported from experimental results [Carralero 14, Kočan 15, Dejarnac 15, Horacek 15, Gunn 13].

1.4.3 Footprint: geometry impact

Even though the power SOL width is generally defined as the property of the main SOL, in experience, λ_q is mostly measured from the heat flux radial profile at the limiter or divertor targets, by IR measurement or/and Langmuir probe methods.

Historically, the radial profiles were supposed to follow a decaying exponential. λ_q is then defined as the e-folding decaying length: $q = q_0 \exp(-r/\lambda_q)$. The estimation of λ_q was directly extracted from the profiles at the target with two methods: by an exponential regression of the profile $\lambda_{q,\text{exp}}$, or by an integral definition $\lambda_{q,\text{int}} = \frac{\int_{\text{target}} q(s-s_0)ds}{q_{\text{peak}}}$ [Loarte 99, Fundamenski 11].

In order to get rid of obvious geometrical effects and compare different machines, λ_q is remapped at the outer mid-plane $\lambda_q \rightarrow \lambda_q/f_x$, where f_x is the flux expansion between the outer mid plane and divertor targets, $f_x = \frac{R_{\text{omp}} B_{\text{pol,omp}}}{R_{\text{tar}} B_{\text{pol,tar}}}$. Note that the flux expansion is also a parameter allowing

to decrease the peak heat load. Another geometrical effect impacting the peak heat flux is the angle between divertor tiles and the magnetic field lines ($q_{\text{wall}} = q_{\parallel} \sin(\alpha)$). Both of these geometric parameters have an impact on the peak heat load apart from the transport in the main SOL, they would be accounted in α_{geo} in Eq. 1.8. Advanced divertor concepts take advantage of these geometrical effects for the design of the divertor geometry: Snow-Flake divertor [Soukhanovskii 11, Soukhanovskii 13], SuperX-divertor [Valanju 10].

More recently, the description of heat load at the target proposed by Ref. [Eich 11] parametrizes the profile by a convolution of a decaying exponential, representing the transport in the main SOL, with a Gaussian, representing a diffusive spreading in the divertor region Eq. 1.12. This method permits getting rid of divertor effects and to extract a coherent multi-machine (JET, DIII-D, ASDEX-Upgrade, C-Mod, NSTX, MAST) empirical scaling law for λ_q in H-mode [Eich 13a, Eich 13b].

$$q_{\parallel}(\bar{s}) = \frac{q_0}{2} \exp\left(\left(\frac{S}{2\lambda_q}\right)^2 - \frac{\bar{s}}{\lambda_q f_x}\right) \operatorname{erfc}\left(\frac{S}{2\lambda_q} - \frac{\bar{s}}{S f_x}\right) + q_{\text{bg}} \quad \text{with} \quad \bar{s} = s - s_0 \tag{1.12}$$

This description separates two different physic contribution of the transport:

- The transport in the main SOL represented by λ_q. Note that here λ_q would be e-folding length of the decaying exponential profile at the divertor entrance (represented in blue on Fig. 1.6), there is no evident reason that it would be the same width at other poloidal locations of the SOL
- Divertor physics, leading to a leakage into the private-flux-region (PFR), represented by the factor S, usually called spreading factor.

Both λ_q and S have an impact on the peak heat flux. The spreading leaves some possibility to reduce q_{peak}, without playing on the main SOL transport. S can be easily linked to the integral SOL width λ_{int}, directly linked to q_{peak} and it has been shown that $\lambda_{int} = \lambda_q + 1.64S$ [Makowski 12]. A scaling low for S has been proposed, showing a main dependency in B_{pol}^{-1} both in both L-mode and H-mode [Scarabosio 15]

The separated physics motivates a distinct extrapolation of λ_q and S. However, there is no clear evidence yet that there is no interplay mechanism, justifying that both of these effects can be easily decoupled. In fact studies on TCV Tokamak have found an unexpected result: the variation of the length of the divertor impacts essentially the estimated λ_q and not the spreading factor S [Gallo 16].

1.4.4 λ_q scaling laws

The current scaling law for the H-mode, derived from the multi-machine regression of Ref. [Eich 13a], found that the strongest dependencies of λ_q is the one with B_{pol} Fig 1.7, Eq. 1.13 with a second striking and unexpected result that no dependencies on R is found.

$$\lambda_{q,\text{Eich}} \propto 0.64 B_{\text{pol}}^{-1.16} \tag{1.13}$$

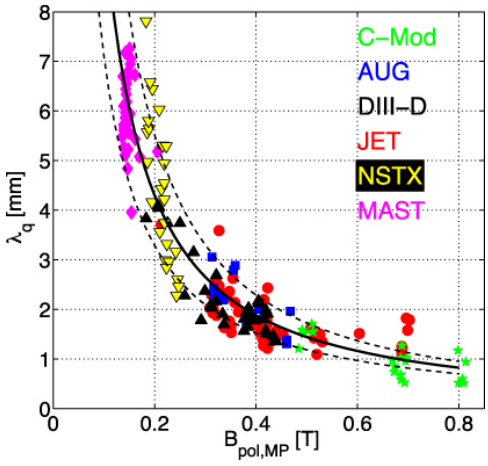

Figure 1.7: B_{pol} scaling of power SOL width

This functional dependency seems to be somehow universal and has been retrieved in other experiments [Thornton 14, Sun 15, Wang 14]. Moreover, it is worth underlining that this feature is not specific to H-mode, an empirical scaling law in L-mode show similar dependency with B_{pol}:

- In divertor configuration on JET and ASDEX-Upgrade [Scarabosio 13]

$$\lambda_q^{\mathrm{L,lim}} \approx 1.44 B_{\mathrm{pol}}^{-1.14} \tag{1.14}$$

- In limiter configuration on Tore-Supra [Gunn 13]

$$\lambda_q^{\mathrm{L,lim}} \approx 9.4 B_{\mathrm{pol}}^{-0.73} \tag{1.15}$$

The extrapolation of this H-mode scaling law gives for ITER $\lambda_q =$ 1 mm to 3 mm rising concern, as it might lead to heat flux above the constraint limit of $10\,\mathrm{MW\,m^{-2}}$ even taking into account the detachment effect (see section 1.4.5).

So far, empirical scaling laws miss a theoretical ground to back-up their prediction, and the mechanisms driving the heat transverse transport in the edge plasma are not yet fully understood. This is a central issue for the design and the sizing of future devices. Some theoretical studies attempt to describe the way energy escapes the core plasma through the separatrix and deposits on the PFC have been done, but no definitive conclusion has been drawn yet. In L-mode, it is accepted that turbulence dominates the cross-field transport, theoretical model have been proposed based on linear analysis using the gradient removal theory [Ricci 09], and based on a blob approach [Fedorczak 17] to predict the value of the SOL width in L-mode.

In H-mode turbulence is strongly reduced in the vicinity of the separatrix, and it is thus not certain whether turbulence plays the predominant role in the cross-field transport. The HD-model [Goldston 12] (described in detail in chapter 4) has attracted much interest for its good agreement with experience [Eich 13a, Faitsch 15, Sieglin 16], in particular its prediction of the dependency on B_{pol}.

1.4.5 Necessity of detachment regime

It is important to recall that the spreading of energy described above is in fact not sufficient to stay below the operational constraint of $10\,\mathrm{MW\,m^{-2}}$ for future devices like ITER, even more so for DEMO. Moreover, for the long-term erosion due to sputtering of electrons, it is further mandatory to keep the electron temperature below 5 eV [Zohm 13]. For both these issues, a so-called detached regime is foreseen. The physics of the detachment is linked to a high recycling condition. In the detached regime one observes a simultaneous decrease of density and temperature at the strike point which leads to a roll over of the plasma flux to the target. In such regime, the largest part of the incoming heat flux will be dissipated by radiation in the divertor region, and the radiated power expected is of 60% for ITER [Wischmeier 15], and 95% for DEMO [Wenninger 14]. Moreover, it permits to keep a low electron temperature at the target. However, detachment can affect the confinement properties if the heavy impurity does not stay in the divertor region.

1.4.6 Narrow feature in L-mode start-up plasma

The start-up phase of ITER discharge will be in limiter configuration, with the limiter positioned on the inner wall, i.e on the HFS wall. In this configuration, experimental $q_{\parallel}$ profiles at the limiter target exhibit double exponential features: with steeper gradient in the vicinity of the strike point ($\lambda_{q,\mathrm{narrow}} \sim$ few mm) [Kočan 15, Dejarnac 15, Horacek 15], followed by flatter profile in the far SOL. This characteristic leads to a higher peak heat load onto the inner wall: the estimated q_{peak} presents up to a factor 4 compared with the value expected from single exponential approach [Kočan 15, Arnoux 13]. Note that the work of Ref. [Kočan 15], takes into account such a narrow feature for the design of the inner-wall tiles of ITER, so that, if the current predictions are correct, the first wall material limit will not be exceeded in ITER.

A theoretical model, using 3D fluid simulation, proposed that this feature could be explained by the reduction of radial correlation due to a sheared poloidal flow $\mathbf{E} \times \mathbf{B}$ [Halpern 17]. However one needs to have a better understanding of this feature in order to avoid possible damage to the wall.

Chapter 2

Fluid modelling of the edge plasma

The study of the mechanisms underlying heat transport via experimental results is a difficult task due to the complexity of measurement in the hot plasma, in particular for ion temperature. Thus, a complementary approach of the heat transport study using numerical tools is mandatory in order to have a better understanding of the underlying physics.

In the edge plasma, the 3D turbulent fluid model is an interesting tool as it includes all the physics expected to play a role in the establishment of SOL width: self-consistent turbulence, drift, temperature dynamics etc, with a reasonable computational cost.

In this chapter, the fluid model is derived, and we present the main approximations of this approach: fluid closure, drift ordering. Moreover, some insights on the physics of the open field lines, specific to the edge plasma, are provided. In the last section, we detail one of the three numerical fluid tools used in this thesis: the code TOKAM3X in its anisothermal version. This code has been chosen as the two other models studied in this work TOKAM2D, and SolEdge2D are somehow reduced models of TOKAM3X.

2.1 Fluid approximation

Despite the great progress of supercomputers, the computational limits are still a key problem of the numerical approach, leading to modelling efforts to reduce the cost of the physical model. The most straightforward approach is the particle description, where the trajectory of each particle is computed from the equation of motion (2.1) of a particle of mass m_α and of charge q_α.

$$m_\alpha \frac{d\mathbf{v}_\alpha}{dt} = q_\alpha \left(\mathbf{E} + \mathbf{v}_\alpha \times \mathbf{B}\right) \tag{2.1}$$

Where $\mathbf{v}_\alpha$, $\mathbf{E}$ and $\mathbf{B}$ stand respectively for the particle velocity, the electric and magnetic fields. The electric and magnetic fields are generated both by external fields and by the impact of all the other plasma particles according to Maxwell's equations.

For N_p particles the computational cost is $6N_\mathrm{p}$ (6 degrees of freedom 3 for position and 3 for velocity). In spite of the low plasma density $\sim 10^{20}\mathrm{m}^{-3}$ this approach is numerically inaccessible. That leads the physicist to use more complex but less costly descriptions. Two approaches are mainly used: the kinetic approach and the fluid approach.

Kinetic approach:

The kinetic approach is a statistical approach solving the distribution function, f_s, in spatial and velocity space, its temporal evolution is described by the Boltzmann's equation (2.2). This allows to reduce the numerical cost to $N_{\text{pts}}^6 \ll 6N_{\text{p}}$ where N_{pts} is the spatial grid resolution. The gyro-kinetic approach further reduces the cost to 5 dimensions by taking the average along the cyclotron motion.

$$\partial_t f_s + \mathbf{v_s} \cdot \boldsymbol{\nabla}_r f_s + \mathbf{a}_s \cdot \boldsymbol{\nabla}_{\mathbf{v_s}} f_s = C_s \tag{2.2}$$

where C_s is the collisional operator.

Fluid approach:

The fluid approach is another step to reduce the numerical cost. It only considers averaged quantities of the distribution function, such as density, velocity and temperature, obtained by the moments of the distribution function (2.3), that is to say integrals of the distribution function along the velocity space.

$$\mathcal{M}_s^{(n)} = \int_{\Omega} \mathbf{v_s}^{\otimes n} f_s\left(\mathbf{r}, \mathbf{v_s}, t\right) d\mathbf{v_s} \text{ with } \mathbf{v_s}^{\otimes n} \equiv \underbrace{\mathbf{v_s} \otimes \cdots \otimes \mathbf{v_s}}_{\text{n times}} \tag{2.3}$$

This approach allows to further reduce the numerical cost to 3 dimensions plus time. Edge plasmas are highly collisional, in this framework, the distribution function tends to be quasi-Maxwellian (2.4).

$$f_s \approx n_s \left(\frac{m_s}{2\pi k_B T_s}\right) \exp\left(\frac{-|\mathbf{v_s} - \mathbf{u_s}|^2}{v_T^2}\right) \tag{2.4}$$

with $\mathbf{u_s}$ the fluid velocity defined later (2.4), and v_T the thermal velocity. The numerical cost of such approach will then depend on the complexity of the model (number of moment solved, additional mechanisms) and also of the spatial resolution of the grids.

2.1.1 Derivation of fluid equations

Fluid equations are obtained by taking the different moments of the kinetic equation (2.2) and then by integrating over all the 3D velocity space:

$$\int_{\mathbf{v_s}} \mathbf{v_s}^{\otimes n} \partial_t f_s d^3\mathbf{v_s} + \int_{\mathbf{v_s}} \mathbf{v_s}^{\otimes n} \boldsymbol{\nabla}_{\mathbf{x}} \cdot (\mathbf{v_s} f_s)\, d^3\mathbf{v_s} + \int_{\mathbf{v_s}} \mathbf{v_s}^{\otimes n} \boldsymbol{\nabla}_{\mathbf{v_s}} \cdot \Big(\frac{q_s}{m_s}\left(\mathbf{E} + \mathbf{v_s} \times \mathbf{B}\right) f_s\Big)\, d^3\mathbf{v_s} = \int_{\mathbf{v_s}} \mathbf{v_s}^{\otimes n} C_s d^3\mathbf{v_s} \tag{2.5}$$

One can rewrite the Equation (2.5) by considering commutative properties as:

$$\partial_t \left(\int_{\mathbf{v_s}} \mathbf{v_s}^{\otimes n} f_s d^3\mathbf{v_s}\right) + \boldsymbol{\nabla}_{\mathbf{x}} \cdot \left(\int_{\mathbf{v_s}} \mathbf{v_s}^{\otimes (n+1)} f_s d^3\mathbf{v_s}\right) + \int_{\mathbf{v_s}} \mathbf{v_s}^{\otimes n} \boldsymbol{\nabla}_{\mathbf{v_s}} \cdot \Big(\frac{q_s}{m_s}\left(\mathbf{E} + \mathbf{v_s} \times \mathbf{B}\right) f_s\Big)\, d^3\mathbf{v_s} = \int_{\mathbf{v_s}} \mathbf{v_s}^{\otimes n} C_s d^3\mathbf{v_s} \tag{2.6}$$

The exact resolution of the n^{th} momentum equations requires to know the $n + 1^{th}$ momentum, i.e solving the $n + 1^{th}$ momentum equation. Thus, only the infinite set of fluid momentum equations is equivalent to solve the kinetic model. In the fluid description, one truncates the momentum hierarchy at a certain order, and solves only few momentum equations (2 or 3). In this thesis, we discuss two

type of models:

- Isothermal models: i.e assumptions of a constant temperature, for which 2 moments equations are solved.
- Anisothermal models for which 3 moments equations are solved.

Both models rely on the classical closure used in fluid modelling, the so-called Braginskii closure, which leans on the assumptions of high collisionality (presented in section 2.1.3).

2.1.1.1 Continuity equation

For $n = 0$, the equation 2.6 writes:

$$\partial_t \left(\int_{\mathbf{v_s}} f_s d^3\mathbf{v_s} \right) + \boldsymbol{\nabla}_{\mathbf{x}} \cdot \left(\int_{\mathbf{v_s}} \mathbf{v_s} f_s d^3\mathbf{v_s} \right) + \int_{\mathbf{v_s}} \boldsymbol{\nabla}_{\mathbf{v_s}} \cdot \left(\frac{\mathbf{F}_s}{m_s} f_s \right) d^3\mathbf{v_s} = \int_{\mathbf{v_s}} C_s d^3\mathbf{v_s} \tag{2.7}$$

with $F_s = q_s \left(E + v_s \times \mathbf{B} \right)$.

Using the quasi-Maxwellian hypothesis (2.4), i.e the distribution function f_s decreases exponentially at infinity in the velocity space, one has:

$$\forall n \in \mathbb{N}, \lim_{|\mathbf{v_s}| \to +\infty} {\mathbf{v_s}}^{\otimes n} f_s = 0 \tag{2.8}$$

The third term of (2.7) can be then recomputed:

$$\int_{\mathbf{v_s}} \boldsymbol{\nabla}_{\mathbf{v_s}} \cdot \left(\frac{\mathbf{F}_s}{m_s} f_s \right) d^3\mathbf{v_s} = \lim_{\mathbf{v_s} \to +\infty} \left[\frac{\mathbf{F}_s}{m_s} f_s \right]_{-\mathbf{v_s}}^{+\mathbf{v_s}} = 0 \tag{2.9}$$

Finally, we suppose here that the collisions do not create or destroy any particles, i.e. there is no atomic reactions ($\int_{\Omega} C_s d\mathbf{v_s} = 0$). The particle balance equation then writes:

$$\partial_t n_s + \boldsymbol{\nabla} \cdot \left(n_s \mathbf{u_s} \right) = 0 \tag{2.10}$$

Using the following definition for the moments of the distribution function:

- the momentum of order 0 is by definition the mean particle density n_s

$$n_s \left(\mathbf{r}, t \right) = \mathcal{M}_s^{(0)} \left(\mathbf{r}, t \right) = \int_{\Omega} f_s \left(\mathbf{r}, \mathbf{v_s}, t \right) d\mathbf{v_s} \tag{2.11}$$

- the fluid velocity $\mathbf{u_s}$ is defined by the moment of order 1:

$$\left(n_s \mathbf{u_s} \right) \left(\mathbf{r}, t \right) = \mathcal{M}_s^{(1)} \left(\mathbf{r}, t \right) = \int_{\Omega} \mathbf{v_s} f_s \left(\mathbf{r}, \mathbf{v_s}, t \right) d\mathbf{v_s} \tag{2.12}$$

2.1.1.2 Momentum balance equation

For $n = 1$, the equation (2.6) writes:

$$\partial_t \left(\int_{\mathbf{v_s}} \mathbf{v_s} f_s d^3\mathbf{v_s} \right) + \boldsymbol{\nabla}_\mathbf{x} \cdot \left(\int_{\mathbf{v_s}} \mathbf{v_s} \otimes \mathbf{v_s} f_s d^3\mathbf{v_s} \right) + \int_{\mathbf{v_s}} \mathbf{v_s} \boldsymbol{\nabla}_{\mathbf{v_s}} \cdot \left(\frac{\mathbf{F}_s}{m_s} f_s \right) d^3\mathbf{v_s} = \int_{\mathbf{v_s}} \mathbf{v_s} C_s d^3\mathbf{v_s} \quad (2.13)$$

The particle velocity is split into its averaged part, the fluid velocity defined in (2.12) and its fluctuating part denoted $\mathbf{w_s}$ in the following $\mathbf{w_s} = \mathbf{v_s} - \mathbf{u_s}$. By definition, one has $\int_{\mathbf{v_s}} \mathbf{w}_s f_s d^3\mathbf{v_s} = 0$. Using this notation, the equation (2.13) becomes:

$$\partial_t \left(n_s \mathbf{u_s} \right) + \underbrace{\boldsymbol{\nabla}_\mathbf{x} \cdot \left(\int_{\mathbf{v_s}} \left(\mathbf{u_s} + \mathbf{w}_s \right) \otimes \left(\mathbf{u_s} + \mathbf{w}_s \right) f_s d^3\mathbf{v_s} \right)}_{=A} + \underbrace{\int_{\mathbf{v_s}} \mathbf{v_s} \boldsymbol{\nabla}_{\mathbf{v_s}} \cdot \left(\frac{\mathbf{F}_s}{m_s} f_s \right) d^3\mathbf{v_s}}_{=B} = \frac{1}{m_s} \mathbf{R}_s \quad (2.14)$$

We now develop separately A and B:

$$\begin{aligned} A &= \boldsymbol{\nabla}_\mathbf{x} \cdot \left(\mathbf{u_s} \otimes \mathbf{u_s} \int_{\mathbf{v_s}} f_s d^3\mathbf{v_s} + \mathbf{u_s} \otimes \cancel{\int_{\mathbf{v_s}} \mathbf{w_s} f_s d^3\mathbf{v_s}} + \cancel{\int_{\mathbf{v_s}} \mathbf{w_s} f_s d^3\mathbf{v_s}} \otimes \mathbf{u_s} + \int_{\mathbf{v_s}} \mathbf{w_s} \otimes \mathbf{w_s} f_s d^3\mathbf{v_s} \right) \\ &= \boldsymbol{\nabla}_\mathbf{x} \cdot \left(n_s \mathbf{u_s} \otimes \mathbf{u_s} + \int_{\mathbf{v_s}} \mathbf{w_s} \otimes \mathbf{w_s} f_s d^3\mathbf{v_s} \right) \end{aligned}$$

$$\begin{aligned} B &= \cancel{\left[\mathbf{v_s} \cdot \frac{\mathbf{F}_s}{m_s} f_s \right]_{-\infty}^{+\infty}} - \int_{\mathbf{v_s}} \frac{\mathbf{F}_s}{m_s} f_s d^3\mathbf{v_s} \\ &= -\frac{q_s}{m_s} \left(\mathbf{E} \int_{\mathbf{v_s}} f_s d^3\mathbf{v_s} + \int_{\mathbf{v_s}} \mathbf{v_s} f_s d^3\mathbf{v_s} \times \mathbf{B} \right) \\ &= -\frac{q_s}{m_s} n_s \left(\mathbf{E} + \mathbf{u_s} \times \mathbf{B} \right) \end{aligned}$$

We further introduce two fluid definitions:

- The total pressure tensor $\bar{\bar{\Pi}}_s^{\mathrm{tot}}$. One can notice that $\bar{\bar{\Pi}}_s^{\mathrm{tot}}$ is a symmetric tensor

$$\bar{\bar{\Pi}}_s^{\mathrm{tot}} = m_s \int_{\mathbf{v_s}} \mathbf{w}_s \otimes \mathbf{w}_s f_s d^3\mathbf{v_s} \quad (2.15)$$

- The collisional momentum source $\mathbf{R}_s$

$$\mathbf{R}_s = m_s \int_{\mathbf{v_s}} \mathbf{w}_s C_s d^3\mathbf{v_s} \quad (2.16)$$

Finally, the momentum balance equation writes:

$$\partial_t \left(m_s n_s \mathbf{u_s} \right) + \boldsymbol{\nabla} \cdot \left(m_s n_s \mathbf{u_s} \otimes \mathbf{u_s} + \bar{\bar{\Pi}}_s^{\mathrm{tot}} \right) = q_s n_s \left(\mathbf{E} + \mathbf{u_s} \times \mathbf{B} \right) + \mathbf{R}_s \quad (2.17)$$

2.1.2 Second moment: energy equation

The derivation of the second momentum of equation (2.2) is detailed in Annex A and leads to:

$$\partial_t \left(n_s \bar{\bar{\varepsilon}}_s\right) + \boldsymbol{\nabla} \cdot \left(\frac{1}{2} n_s \left(\bar{\bar{\varepsilon}}_s \otimes \mathbf{u_s} + \mathbf{u_s} \otimes \bar{\bar{\varepsilon}}_s\right) + \frac{1}{2} \int_{\mathbf{v_s}} m_s \mathbf{w_s} \otimes \mathbf{u_s} \otimes \mathbf{w_s} f_s d^3\mathbf{v_s} + \bar{\bar{\bar{\mathbb{Q}}}}_s\right) \tag{2.18}$$
$$= \frac{1}{2} q_s n_s \left(\mathbf{E} \otimes \mathbf{u_s} + \mathbf{u_s} \otimes \mathbf{E}\right) + \bar{\bar{W}}_s^{\mathbf{v_s} \times \mathbf{B}} + \bar{\bar{H}}_s + \frac{1}{2} \left(\mathbf{R}_s \otimes \mathbf{u_s} + \mathbf{u_s} \otimes \mathbf{R}_s\right)$$

Using the definition of fluid quantities for the momentum of second order:

- the energy tensor $\bar{\bar{\varepsilon}}_s$:

$$n_s \bar{\bar{\varepsilon}}_s \equiv \frac{1}{2} m_s n_s \mathbf{u_s} \otimes \mathbf{u_s} + \frac{1}{2} \bar{\bar{\Pi}}_s^{tot} \tag{2.19}$$

- the pressure flux tensor $\bar{\bar{\bar{\mathbb{Q}}}}_s$:

$$\bar{\bar{\bar{\mathbb{Q}}}}_s = \frac{1}{2} m_s \int_{\mathbf{v_s}} \mathbf{w_s} \otimes \mathbf{w_s} \otimes \mathbf{w_s} f_s d^3\mathbf{v_s} \tag{2.20}$$

- the collisional pressure source tensor $\bar{\bar{H}}_s$:

$$\bar{\bar{H}}_s = \frac{1}{2} m_s \int_{\mathbf{v_s}} C_s \mathbf{w_s} \otimes \mathbf{w_s} d^3\mathbf{v_s} \tag{2.21}$$

- the work tensor of the Lorentz force $\bar{\bar{W}}_s^{\mathbf{v_s} \times \mathbf{B}}$:

$$\bar{\bar{W}}_s^{\mathbf{v_s} \times \mathbf{B}} = \frac{1}{2} q_s \int_{\mathbf{v_s}} \left(\left(\mathbf{v_s} \times \mathbf{B}\right) \otimes \mathbf{v_s} + \mathbf{v_s} \otimes \left(\mathbf{v_s} \times \mathbf{B}\right)\right) f_s d^3\mathbf{v_s} \tag{2.22}$$

Equation (2.18) is a tensor equation providing the transfer of energy in the three space directions. Such precision is usually considered superfluous in standard plasma fluid codes as the pressure is assumed quasi isotropic due to collisions. In this framework, the resolution of the tensor equation would be an unnecessary numerical cost. The resolution of the total energy E^{tot} is considered sufficient to describe the transport in the edge plasmas. The equation of the energy evolution is obtained by taking the trace of the equation (2.18) and leads to the following scalar equation:

$$\partial_t E_s^{\text{tot}} + \boldsymbol{\nabla} \cdot \left(E_s^{\text{tot}} \mathbf{u_s} + \mathbf{u_s} \cdot \bar{\bar{\Pi}}_s^{\text{tot}} + \mathbf{q}_s\right) = n_s q_s \mathbf{E} \cdot \mathbf{u_s} + Q_{\parallel,s} + \mathbf{R}_s \cdot \mathbf{u_s} \tag{2.23}$$

where:

- $p_s = \frac{1}{3} \operatorname{Tr}\left(\bar{\bar{\Pi}}_s^{\text{tot}}\right)$ is the scalar pressure
- $E_s^{\text{tot}} = \frac{1}{2} m_s n_s |\mathbf{u_s}|^2 + \frac{3}{2} p_s$ is the total energy carried by the species s
- $Q_{\parallel,s} = \frac{1}{2} m_s \int_{\mathbf{v_s}} |\mathbf{w_s}|^2 C_s d^3\mathbf{v_s}$ is the collisional energy source
- $\mathbf{q}_s = \frac{1}{2} m_s \int_{\mathbf{v_s}} |\mathbf{w_s}|^2 \mathbf{w_s} f_s d^3\mathbf{v_s}$ is the heat flux

2.1.3 Braginskii closure

The Braginskii closure on plasma fluid equation [Braginskii 65] is a closure for fluid equations of 2nd or 3rd order. This closure was developed in the frame of a strongly magnetized and highly collisional plasma, i.e $\omega_{c_e}\tau_e \gg 1$ and $\omega_{c_i}\tau_i \gg 1$ where $\omega_{c_{e/i}}$ and $\tau_{e/i}$ are respectively the cyclotron frequencies and the collisional times for electrons and ions. In this limit, the plasma is close to the thermodynamic equilibrium and the distribution function exhibits a quasi-Maxwellian shape. It gives a closure for the following undetermined quantities: the friction terms R_s, the collisional energy source $Q_{\parallel,s}$, the total pressure tensor $\bar{\bar{\Pi}}_s^{\text{tot}}$, the heat flux $\mathbf{q}_s$. The principal results for single ion species plasma are recalled below.

The collisional momentum source $\mathbf{R}_s$ is made of two contributions: a friction force $\mathbf{R}^u$ due to the relative velocity between ions and electrons, and a thermal force due to the temperature gradient. For electrons, one has:

$$\mathbf{R}_e = \mathbf{R}_e^u + \mathbf{R}_e^T = en_e\left(\eta_\parallel j_\parallel \mathbf{b} + \eta_\perp \mathbf{j}_\perp\right) - 0.71 n_e \boldsymbol{\nabla}_\parallel T_e - \frac{3}{2}\frac{n_e}{\omega_{c_e}\tau_e}\mathbf{b}\times\boldsymbol{\nabla}_\perp T_e \tag{2.24}$$

where $\eta_\parallel$ and $\eta_\perp$ are respectively the parallel and perpendicular Spitzer resistivities. Moreover, one has $\mathbf{R}_e = -\mathbf{R}_i$.

The collisional energy source $Q_{\parallel,s}$ writes:

$$Q_{\parallel,i} = 3\frac{m_e}{m_i}\frac{p_e - p_i}{\tau_e} \text{ for electrons} \tag{2.25}$$

$$Q_{\parallel,e} = \eta_\parallel j_\parallel^2 + \eta_\perp j_\perp^2 + \frac{1}{en_e}\mathbf{j}\cdot\mathbf{R}_e^T - 3\frac{m_e}{m_i}\frac{p_e - p_i}{\tau_e} \text{ for ions} \tag{2.26}$$

The total pressure tensor can be decomposed in a scalar pressure part and a tensor (2.27). This decomposition is motivated by the fact that the pressure is assumed to be quasi isotropic in a high collisional plasma.

$$\bar{\bar{\Pi}}_s^{\text{tot}} = p_s\bar{\bar{I}} + \bar{\bar{\Pi}}_s^{\text{Brag}} \tag{2.27}$$

The Braginskii's tensor can be itself decomposed in 3 components: a viscous tensor, a Finite Larmor Radius tensor, and a residual tensor (2.28). Their expressions are detailed in Annex A but one will retain that $\bar{\bar{\Pi}}_s^{\text{vis}}$ is the term of higher magnitude. Moreover, the diamagnetic cancellation shows that the difference between the divergence of the diamagnetic advection and the one of the $\boldsymbol{\nabla}B$-drift advection is compensated by the highest term of the $\bar{\bar{\Pi}}_{\text{FLR}}$ divergence. This simplification will be used to replace $\mathbf{u}_*$ by $\mathbf{u}_{\nabla B}$ in the fluid equations and allows to suppress the contribution of $\bar{\bar{\Pi}}_{\text{FLR}}$.

$$\bar{\bar{\Pi}}_s^{\text{Brag}} = \bar{\bar{\Pi}}_s^{\text{vis}} + \bar{\bar{\Pi}}_s^{\text{FLR}} + \bar{\bar{\Pi}}_s^{\text{res}} \tag{2.28}$$

The heat flux q_s is made of two contributions: a friction force, and a thermal force due to the existence

of the temperature gradient.

$$\mathbf{q}_e = \mathbf{q}_e^u + \mathbf{q}_e^T = 0.71 p_e \left(u_{e_\parallel} - u_{i_\parallel}\right) \mathbf{b} + \frac{3}{2}\frac{p_e}{\omega_{c_e}\tau_e}\mathbf{b}\times\left(\mathbf{u}_{e_\perp} - \mathbf{u}_{i_\perp}\right) - \chi_{e_\parallel}\boldsymbol{\nabla}_\parallel T_e - \chi_{e_\perp}\boldsymbol{\nabla}_\perp T_e - \frac{5}{2}\frac{p_e}{m_e\omega_{c_e}}\mathbf{b}\times\boldsymbol{\nabla}_\perp T_e \tag{2.29}$$

$$\mathbf{q}_i = -\chi_{i_\parallel}\boldsymbol{\nabla}_\parallel T_i - \chi_{i_\perp}\boldsymbol{\nabla}_\perp T_i + \frac{5}{2}\frac{p_i}{m_e\omega_{c_e}}\mathbf{b}\times\boldsymbol{\nabla}_\perp T_i \tag{2.30}$$

where $\chi_{i/e}$ are respectively electron and ion thermal conductivities.

2.2 Drift ordering

The motion of a particle in magnetic field presents two main components, a free parallel motion at a velocity of the order of the thermal velocity $c_s \approx \sqrt{T_s/m_s}$, and a cross-field circular motion around the field line (the cyclotron gyro-motion). Moreover, the presence of non-uniformity of the magnetic field or of an electric field induces a transversal motion of the guiding center which moves away from the magnetic field line. Such motions are called the drift velocities. The contribution of the gyro-motion in the fluid velocity is null apart from the drift effects. Thus, the fluid velocity of species s is decomposed as follows:

$$\mathbf{u_s} = \mathbf{u}_{\parallel,\mathbf{s}} + \mathbf{u}_{\perp,\mathbf{s}} = u_\parallel \mathbf{b} + \mathbf{u}_{\perp,\mathbf{s}}$$

where $u_\parallel \mathbf{b}$ is the parallel motion and $\mathbf{u}_{\perp,\mathbf{s}}$ is the contribution of the drift velocities.

In order to find the expression of the drift velocities, one applies the so-called drift ordering used in the frame of the fluid modeling. This drift ordering relies on the assumption of two small parameters:

- The frequency ω of the studied phenomena is assumed to be smaller than the cyclotron frequency and gives us the first small parameter ε_ω (2.31).

$$\varepsilon_\omega = \frac{\omega}{\omega_c} \ll 1 \tag{2.31}$$

- The characteristic plasma perpendicular length is supposed to be higher than the Larmor radius and gives us the second small parameter ε_l (2.32).

$$\varepsilon_l = \frac{\rho_L}{l_\perp} \ll 1 \tag{2.32}$$

The motion in the perpendicular direction can be ordered as:

$$\mathbf{u}_{\perp,\mathbf{s}} = \underbrace{\varepsilon \mathbf{u}_{\perp,\mathbf{s}}{}^1}_{\text{drift of 1st order}} + \underbrace{\varepsilon^2 \mathbf{u}_{\perp,\mathbf{s}}{}^2}_{\text{drift of 2nd order}} + o\left(\varepsilon^2\right)$$

Note that the parallel velocity is at least of the same order as the zero order of the cross field motion, i.e the cyclotron motion: $|\mathbf{u}_{\parallel,\mathbf{s}}| \sim v_T \sim \rho_L/\omega_c$, where v_T is the thermal velocity.

2.2.1 Drifts of order 1

In order to isolate $\mathbf{u}_{\perp,\mathbf{s}}$, we estimate the transversal projection of the first moment equation by taking:

$$\mathbf{B}\times\left[\partial_t\left(m_s n_s \mathbf{u_s}\right)+\boldsymbol{\nabla}\cdot\left(m_s n_s \mathbf{u_s}\otimes\mathbf{u_s}+\bar{\bar{\Pi}}_s^{tot}\right)=q_s n_s\left(\mathbf{E}+\mathbf{u_s}\times\mathbf{B}\right)+\mathbf{R}_s\right] \tag{2.33}$$

Using the splitting of the velocity into parallel and perpendicular contributions, and assuming a magnetic field constant in time, the equation can be rewritten as:

$$\partial_t\left(m_s n_s \mathbf{B}\times\mathbf{u}_{\perp,\mathbf{s}}\right)+\mathbf{B}\times\boldsymbol{\nabla}\cdot\left(m_s n_s \mathbf{u_s}\otimes\mathbf{u_s}\right)+\mathbf{B}\times\boldsymbol{\nabla}\cdot\left(\bar{\bar{\Pi}}_s^{tot}\right)=q_s n_s\left(\mathbf{B}\times\mathbf{E}+B^2\mathbf{u}_{\perp,\mathbf{s}}\right)+\mathbf{B}\times\mathbf{R}_s$$

First, we can start by neglecting the following terms of an order higher than one with respect to ε_ω or ε_l:

$$\frac{\mid m_s\partial_t\left(n_s\mathbf{B}\times\mathbf{u}_{\perp,\mathbf{s}}\right)\mid}{\left|q_s n_s \mathbf{u}_{\perp,\mathbf{s}}B^2\right|}\sim\frac{m_s\omega u_\perp}{q_s u_\perp B}\sim\frac{\omega}{\omega_c}\sim\varepsilon_\omega\sim o(1)$$

In the second term of the left side of the equation one can distinguish several contributions: $\boldsymbol{\nabla}\cdot\left(m_s n_s \mathbf{u_s}\otimes\mathbf{u_s}\right)=\boldsymbol{\nabla}\cdot\left(m_s n_s {\mathbf{u}_{\parallel,\mathbf{s}}}^2\mathbf{b}\otimes\mathbf{b}\right)+\boldsymbol{\nabla}\cdot\left(m_s n_s \mathbf{u}_{\parallel,\mathbf{s}}\mathbf{b}\otimes\mathbf{u}_{\perp,\mathbf{s}}\right)+\boldsymbol{\nabla}\cdot\left(m_s n_s \mathbf{u}_{\perp,\mathbf{s}}\otimes\mathbf{u}_{\perp,\mathbf{s}}\right)$. The two last terms are of higher order and can be neglected in the drift ordering, indeed:

$$\frac{\left|\mathbf{B}\times\boldsymbol{\nabla}\cdot\left(m_s n_s \mathbf{u}_{\parallel,\mathbf{s}}\mathbf{b}\otimes\mathbf{u}_{\perp,\mathbf{s}}\right)\right|}{\left|q_s n_s \mathbf{u}_{\mathbf{s}\perp,s}\mathbf{B}^2\right|}\sim\frac{m_s n_s c_s u_\perp k_\perp}{q_s n_s u_\perp B}\sim\frac{\rho_L}{l_\perp}\sim\varepsilon_l\sim o(1)$$
$$\frac{\left|\mathbf{B}\times\boldsymbol{\nabla}\cdot\left(m_s n_s \mathbf{u}_{\perp,\mathbf{s}}\otimes\mathbf{u}_{\perp,\mathbf{s}}\right)\right|}{\left|q_s n_s \mathbf{u}_{\mathbf{s}\perp,s}\mathbf{B}^2\right|}\sim\frac{m_s n_s u_\perp^2 k_\perp}{q_s n_s u_\perp B}<\frac{\rho_L}{l_\perp}\sim\varepsilon_l\sim o(1)$$

For the first order, one retains only the viscous part of the Braginskii stress tensor (see Annex A):

$$\bar{\bar{\Pi}}_s^{\mathrm{Brag}}\approx\bar{\bar{\Pi}}_s^{\mathrm{vis}}\quad\text{as}\quad\bar{\bar{\Pi}}_s^{\mathrm{FLR}}\,,\;\bar{\bar{\Pi}}_s^{\mathrm{res}}<<\bar{\bar{\Pi}}_s^{\mathrm{vis}} \tag{2.34}$$

Moreover, apart from the curvature terms, which are neglected here, the divergence of the viscous stress tensor can be rewritten as [Bufferand 17]:

$$\boldsymbol{\nabla}\cdot\left(\bar{\bar{\Pi}}_s^{\parallel}\right)=-\frac{1}{3}\boldsymbol{\nabla}\left(p_\parallel-p_\perp\right)+\boldsymbol{\nabla}\cdot\left(\left(p_\parallel-p_\perp\right)\mathbf{b}\right)\mathbf{b}+\left(p_\parallel-p_\perp\right)\boldsymbol{\kappa} \tag{2.35}$$

With $\boldsymbol{\kappa}=\mathbf{b}\cdot\boldsymbol{\nabla}\mathbf{b}$

Finally, retaining only the term of first order, the projection of the momentum equation can be rewritten as:

$$\mathbf{B}\times\boldsymbol{\nabla}\cdot\left(m_s n_s u_\parallel^2\mathbf{b}\otimes\mathbf{b}+\bar{\bar{\Pi}}_s^{\parallel}\right)+\mathbf{B}\times\boldsymbol{\nabla}_\perp p=q_s n_s\left(\mathbf{B}\times\mathbf{E}+B^2\mathbf{u}_{\perp,\mathbf{s}}\right)+\mathbf{B}\times\mathbf{R}_s$$

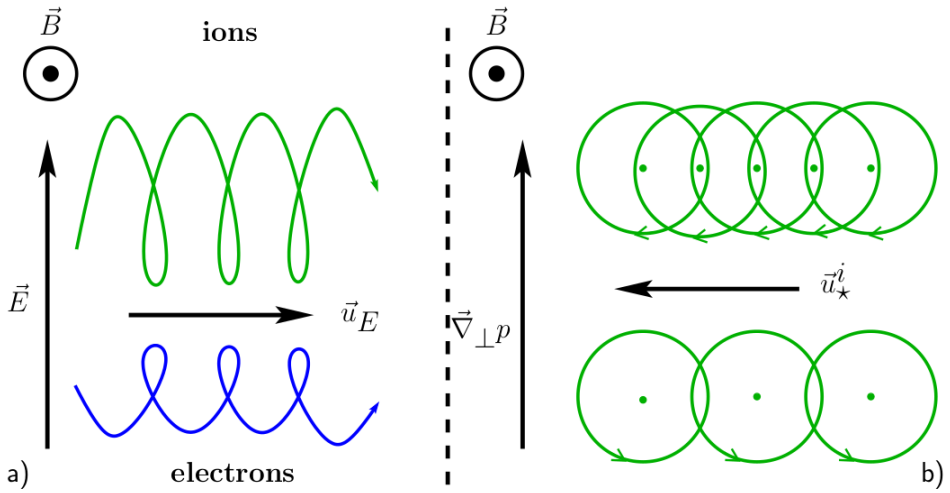

Figure 2.1: (a): Ion and electron drift in magnetic field due to electric drift (particular representation). (b): Ion drift due to diamagnetic drift (fluid representation)

Thus we get:

$$\begin{aligned}\mathbf{u}_{\perp,\mathbf{s}} &= \frac{\mathbf{E}\times\mathbf{B}}{B^2} + \frac{\mathbf{B}\times\boldsymbol{\nabla}_\perp p_s}{n_s q_s B^2} + \frac{\mathbf{B}\times\boldsymbol{\nabla}\cdot\left(m_s n_s u_\parallel^2 \mathbf{b}\otimes\mathbf{b}\right)}{n_s q_s B^2} + \frac{\mathbf{B}\times\boldsymbol{\nabla}_\perp\cdot\bar{\bar{\Pi}}_s^\parallel}{n_s q_s B^2} + \frac{\mathbf{B}\times\mathbf{R}_s}{n_s q_s B^2} \\ &= \frac{\mathbf{E}\times\mathbf{B}}{B^2} + \frac{\mathbf{B}\times\boldsymbol{\nabla}_\perp\left(p_\perp\right)}{n_s q_s B^2} + \frac{\mathbf{B}\times\boldsymbol{\nabla}\cdot\left(m_s n_s u_\parallel^2 + \left(p_\parallel - p_\perp\right)\right)}{n_s q_s B^2}\mathbf{B}\times\boldsymbol{\kappa} + \frac{\mathbf{B}\times\mathbf{R}_s}{n_s q_s B^2}\end{aligned}$$

In the hypothesis of low β (ratio of kinetic and magnetic pressure), assumed in the edge plasma modelling, the scalar pressure becomes isotropic, i.e $p_\perp - p_\parallel \approx 0$. In the following, we will consider an isotropic pressure, and we neglected the terms of collision in $\mathbf{R_s}$ even though it can be a disputable simplification at very high collisionality. The 1st-order perpendicular velocity is finally given by the sum of the $\mathbf{E}\times\mathbf{B}$ drift $\mathbf{u_E}$, the diamagnetic drift $\mathbf{u}_*$, and the centrifugal drift $\mathbf{u}_{\text{cent}}$:

$$\mathbf{u}_{\mathbf{s}\perp}^1 = \underbrace{\frac{\mathbf{E}\times\mathbf{B}}{B^2}}_{\mathbf{u_E}} + \underbrace{\frac{\mathbf{B}\times\boldsymbol{\nabla}p_s}{n_s q_s B^2}}_{\mathbf{u}_*} + \underbrace{\frac{\mathbf{B}\times\boldsymbol{\nabla}\cdot\left(m_s n_s u_\parallel^2\right)}{n_s q_s B^2}\mathbf{B}\times\boldsymbol{\kappa}}_{\mathbf{u}_{\text{cent}}} \tag{2.36}$$

We now discuss the physical meaning of these three drifts.

Electrical drift $\mathbf{u_E}$:
In the presence of an electric field $\mathbf{E}$, the cyclotron motion of a charged particle is distorted. For example, if one considers an electron, the electron is accelerated by $\mathbf{E}$ (i.e presents a larger Larmor radius), in the part of the gyro-motion where the electron velocity is in the same direction as the electric field $\mathbf{E}$. Conversely, in the part of the gyro-motion where the velocity is in the opposite orientation than $\mathbf{E}$, the electron is slowing down (i.e presents a smaller Larmor radius). This modification of the gyro-motion implies an averaged perpendicular motion of the gyro-center as schemed on Fig. 2.1 a).

For ions, the **E** force applies on the particle is reversed, however as the particle turns in the opposite direction, the final drift is consequently in the same direction as for electron. This drift depends neither on the particle charge nor on the particle mass. Thus, it does not create any current for a quasi-neutral plasma.

Diamagnetic drift $\mathbf{u}_*$:
The diamagnetic drift velocity is a fluid drift as it does not come from the drift of a single particle motion but results from the collective motion of a high number of particles (statistical effect). As illustrated on Fig. 2.1 b), the presence of a pressure gradient induces a spatial inhomogeneity of cyclotron velocity distribution. This spacial inhomogeneity results in global motion of the fluid. However, the gyro-center of each single particle does not move. And one can show that the particle flux associated with this drift is divergence-free except for the effect of the magnetic field curvature:

$$\boldsymbol{\nabla} \cdot (n_s \mathbf{u}_*) = \frac{1}{q_s} \left(\boldsymbol{\nabla} p_s \times \boldsymbol{\nabla} \frac{1}{B^2} \right) .\mathbf{B} \tag{2.37}$$

In fact, in the fluid codes used in this work, the diamagnetic drift is replaced by the so called $\boldsymbol{\nabla} B$ drift $\mathbf{u}_{\nabla B} = \pm 2 T_s \frac{\mathbf{B} \times \boldsymbol{\nabla} B}{B^3}$, as it can be shown that the divergences $\boldsymbol{\nabla} \cdot (n_s \mathbf{u}_*)$ and $\boldsymbol{\nabla} \cdot (n_s \mathbf{u}_{\nabla B})$ coincide (see Annex A).

Conversely, to the diamagnetic drift, the $\boldsymbol{\nabla} B$ drift can be understood from a particle point of view. The difference of B implies that the Larmor radius of the particle is smaller on the size of the gyro-motion where **B** is the strongest ($\rho_L \propto 1/B$). Following the same lines of thought as for $\mathbf{u_E}$ drift, one understands how the $\boldsymbol{\nabla} B$ drift induces a drift of the particle with a direction depending on $\mathbf{B} \times \boldsymbol{\nabla} B$.

Note that the diamagnetic (or $\boldsymbol{\nabla} B$) drift is charge dependent and thus drives current for a quasi-neutral plasma.

Centrifugal drift $\mathbf{u}_{\text{cent}}$:
The centrifugal drift is also a drift due to the inhomogeneity of **B** along the particle motion. This drift comes from the difference of **B** that the particle experiences along its parallel motion, when in the case of $\boldsymbol{\nabla} B$ drift it comes from the inhomogeneity encountered along the transversal gyro-motion.

The centrifugal drift is a curvature term, but can make a significant contribution to the radial flux when $u_{\parallel} \sim v_{\text{th}}$. This contribution is of the same order as the one of the diamagnetic or $\boldsymbol{\nabla} B$ drift. In the fluid modelling, this term is sometimes neglected under the hypothesis of a small Mach number. However, this drift should be considered as 1st-order term in the drift ordering, especially in the case of large amplitude flows.

The role of the drifts in the transport is twofold:

- First the drifts play a role in the dynamics of the turbulence. Indeed, the diamagnetic drift is a mechanism of destabilisation of the turbulence and the electrical drift is the mechanism of advection of the intermittent structures.
- They also play a role in transport from their averaged contribution. Indeed, the $\mathbf{E} \times \mathbf{B}$ and $\boldsymbol{\nabla} B$ drifts bring forth large scale flows, which play a role in the steady-state equilibrium of the plasma.

2.2.2 Drift of order 2: the polarisation drift

The same methodology, as the one used for the drift of order 1, leads to the expression of the drift of order 2, called the polarisation drift (2.38).

$$\mathbf{u}_{\mathrm{pol}} = \frac{m_s \mathbf{B}}{n_s q_s B^2} \times \left(\partial_t \left(n_s \mathbf{u}_{\perp,\mathbf{s}}{}^1\right) + \boldsymbol{\nabla} \cdot \left(n_s \mathbf{u}_{\perp,\mathbf{s}}{}^1 \otimes \mathbf{u}_{\mathbf{s}}\right)\right) + \frac{\mathbf{B} \times \boldsymbol{\nabla}\left(\bar{\bar{\Pi}}_s^1 + R_s\right)}{n_s q_s B^2} \tag{2.38}$$

The polarisation drift is an inertial term proportional to the mass of the particle. Thus, as $m_i/m_e \approx 1000 \gg 1$, only the contribution of the ion polarisation drift is taken into account in the fluid model. Moreover, $\mathbf{u}_{\mathbf{s}\mathrm{pol}}$ depends on the particle charge, thus as the diamagnetic drift, it generates currents.

This drift is of the second order, that is to say of an order of magnitude lower than $\mathbf{u}_{\mathbf{E}}$ and $\mathbf{u}_*$. Nevertheless, this drift plays a significant role in the equation of current conservation, as the divergence of the current associated with $\mathbf{u}_{\mathrm{pol}}$ is of the same order as the one associated with $\mathbf{u}_*$. Moreover, the electric drift does not induce any current. Consequently, one needs to keep the contribution of the polarisation drift in the divergence operator of current advection to have a coherent ordering, but it will be neglected in other advection terms. This last simplification, made for computational reasons, is disputable, as $\boldsymbol{\nabla}(n\mathbf{u}_*)$ and $\boldsymbol{\nabla}(n\mathbf{u}_{\mathrm{pol}})$ are of the same order. However, the fact that $\boldsymbol{\nabla}(n\mathbf{u}_{\mathbf{E}})$ is still of an order of magnitude higher makes it reasonable.

2.3 Physic of open field lines

The SOL is a specific region as it is comprised in-between the hot core plasma, and material PFCs. In this region, the plasma following the magnetic field lines, intercepts the material walls, leading to a plasma–wall interaction. At the solid surface, the ions and electrons recombine and neutrals are transported back in the plasma. Thus, the wall acts as a sink, but also as an indirect source for the plasma. These phenomena are not studied in details in this thesis but are of a key player for the peak heat flux management at the target. For example, these mechanisms are involved in the physics of the detachment regime, crucial for the operation of future devices (section 1.4.5).

Moreover, the charged particles arriving at the wall interact with it, which leads to a modification of the electric fields in this region. This phenomenon induces specific boundary conditions for the SOL plasma at the PFC, which needs to be correctly modelled for a coherent fluid code.

2.3.1 Boundary conditions at the wall in fluid models

Ions and electrons present different thermal velocities at the same temperature, i.e $T_e = T_i$, $v_{T_e}/v_{T_i} = \sqrt{m_i/m_e} \gg 1$. Due to this difference of velocity, the wall intercepts initially a higher flux of electrons than of ions, and thus charges negatively. Consequently, an electric field arises in the vicinity of the wall. This electric field accelerates ions, and slows down electrons until an equilibrium state is reached where ion and electron fluxes are equal.

Due to this mechanism a thin zone of charged plasma is observed in the proximity of the wall. This region is called the electrostatic sheath region. The characteristic width of the sheath corresponds to

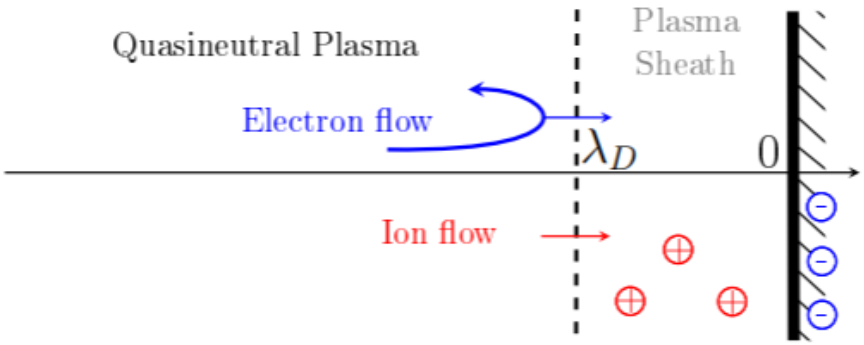

Figure 2.2: Scheme of the sheath region and the quasi-neutral plasma

the Debye length (2.39), that is to say the scale length of screening of an electric charge:

$$\lambda_D = \sqrt{\frac{\varepsilon_0 T}{e^2 n}} \tag{2.39}$$

where ε_0 is the vacuum permittivity. For a typical SOL plasma density of 10^{19} m^{-3}, an electron temperature of 50 eV, λ_D is about 10^{-5} m. Hence, the typical width of the sheath is of several orders of magnitude lower than the parallel length $L_\parallel = 2\pi qR \approx 100$ m.

Two regions of the SOL can be distinguished: the sheath region, and the remaining plasma satisfying the quasi-neutrality assumption. The Poisson equation writes differently in the two regions:

$$\frac{d^2\phi}{dz^2} = \frac{e}{\varepsilon_0}(n_e - n_i) \text{ for the sheath} \tag{2.40}$$

$$n_e \approx n_i \text{ for the quasi-neutral SOL} \tag{2.41}$$

where z is the coordinate in the parallel direction.

Considering the negligible thickness of the sheath, this region is not explicitly modelled in fluid codes. However, they are taken into account via the boundary condition at the target, so-called the Bohm conditions. These boundary conditions are derived below, and determine the equilibrium of the main quasi-neutral plasma.

2.3.2 The Bohm condition

In the following, the sheath is assumed to be collisionless due to its width, that is smaller than the mean free path. Moreover, the inertial terms of electron will be neglected and the plasma in the sheath region is assumed to be isothermal. In a first part, we derive the Bohm condition under the cold ion hypothesis ($T_i = 0$). The momentum balance equation (2.35) for electron in the parallel direction can be then rewritten as:

$$\nabla_\parallel p_e = -n_e e E_\parallel \tag{2.42}$$

$$k_B T_e \nabla_\parallel n_e = n_e e \nabla_\parallel \phi \tag{2.43}$$

giving the Boltzmann's relation:

$$n_e = n_{e,\mathrm{se}} \exp\left(\frac{e\left(\phi - \phi_{\mathrm{se}}\right)}{k_B T_e}\right) \tag{2.44}$$

where 'se' stands for the sheath entrance.

We now estimate the acceleration of the ion due to the difference of potential between an upstream point and the sheath entrance. Under the cold ion and collisionless assumption, the energy conservation energy for ions gives:

$$1/2 m_i v_\parallel^2 = -e\phi \tag{2.45}$$

Moreover, assuming that the only source of ion is upstream, the parallel momentum is constant ($n_i v_\parallel =$ constant), and one can combine particle and energy balance to get:

$$n_i = n_{\mathrm{se}} \sqrt{\phi_{\mathrm{se}}/\phi} \tag{2.46}$$

Using (2.44) and (2.46) the Poisson equation (2.40) then writes:

$$\frac{d^2\phi}{dz^2} = -\frac{e}{\varepsilon_0}\left(\sqrt{\frac{\phi_{\mathrm{se}}}{\phi}} - \exp\left(\frac{e\left(\phi - \phi_{\mathrm{se}}\right)}{k_B T_e}\right)\right) \tag{2.47}$$

The Taylor expansion of the previous equation as a function of the small parameters $\Delta\phi \approx \phi_{\mathrm{se}} - \phi > 0$ gives:

$$\frac{d^2\Delta\phi}{dx^2} = -\frac{e n_{\mathrm{se}} \Delta\phi}{\varepsilon_0}\left(\frac{e}{k_B T_e} - \frac{1}{2|\phi_{\mathrm{se}}|}\right) \tag{2.48}$$

which admits a non oscillatory solution only if:

$$\left(\frac{e}{k_B T_e} - \frac{1}{2|\phi_{\mathrm{se}}|}\right) \geq 0 \tag{2.49}$$

This expression is equivalent to the following expression (2.50), usually called the Bohm criteria.

$$v_{\mathrm{se}} \geq c_s \text{ with } c_s = \sqrt{\frac{k_B T_e}{m_i}} \tag{2.50}$$

This result can be generalized for hot ion plasma [Stangeby 00] by modifying the expression of the sound speed as following:

$$c_s = \sqrt{\frac{k_B\left(T_e + \gamma T_i\right)}{m_i}} \tag{2.51}$$

where γ is the polytropic index, in particular $\gamma = 1$ for an isothermal plasma.

2.3.3 Solid surface with an oblique angle with B: Bohm–Chodura condition

So far, the magnetic field lines have been assumed to be normal to the solid surface. However, in realistic Tokamaks, this is not the case. In fact, a large angle between the target normal and $\mathbf{B}$ is desirable in order to decrease the peak heat flux at the target $q_{\text{peak}} = q_{\parallel} \cos(\alpha)$, where α is the angle between the solid normal and B.

In this configuration, one needs to take into account the transversal drift into the previous derivation of the boundary condition, which leads to the so called Bohm-Chodura boundary condition [Chodura 86]:

$$| \left(u_{\parallel} \mathbf{b} + \mathbf{u}_{\perp} \right) \cdot \mathbf{n}_{\text{wall}} | \geq c_s | \mathbf{b} \cdot \mathbf{n}_{\text{wall}} | \tag{2.52}$$

where $\mathbf{n}_{\text{wall}}$ is the normal to the solid wall, and with the flux directed towards the wall.

2.3.4 Bohm conditions for energy balance

The sheath derivation permits to deduce the plasma outflux at the sheath entrance Γ_{se}. However, the energy outflux has still to be determined. Considering a collisionless sheath, the heat flux has to be convective and expresses as:

$$q_e = \gamma_e k_B n_e T_e \Gamma_{\text{se}} \quad \text{and} \quad q_i = \gamma_i k_B n T_i \Gamma_{\text{se}} \tag{2.53}$$

where γ_e and γ_i are the sheath transmission coefficients. Their expression can be found in Ref. [Stangeby 00], and we have $\gamma_e \approx 5$, $\gamma_i \approx 2.5$.

2.4 3D fluid model: TOKAM3X

In this section, we detail the derivation of the equation of the TOKAM3X code. It is based on an anisothermal assumption, and is one of the three codes used in this work. This code has been chosen as the two other models studied TOKAM2D and SolEdge2D are somehow reduced models of TOKAM3X.

TOKAM3X is a first principle 3D turbulence fluid code for edge plasma, which has the specificity to run in flexible and realistic geometry. The code solves fluid equations for a quasi-neutral plasma based on Braginskii's closure and the drift approximation presented previously. Recently, the code has been extended to an anisothermal version with self-consistent resolution of the temperature dynamic and gradient. Before, the code solved an isothermal set of equations with temperature constant in space and time.

TOKAM3X is a flux-driven code, hence, the quasi steady-state equilibrium profiles are self-consistent. The system is driven by volumetric sources of density (S_N), parallel momentum (S_Γ) and energy (S_E), which models the plasma influx from the central plasma. The volumetric sources are located at the inner boundary of the domain, are given a Gaussian shape in the radial direction and are homogeneous in the poloidal and toroidal directions.

Moreover, diffusive terms are added to the balance equations. Such terms represent the dissipation mechanism at scales smaller than the mesh grid, thus not modelled self-consistently. They are

mandatory for the numerical stability of the code.

On top of Braginskii's closure and the drift approximation, TOKAM3X makes further hypothesis in order to obtain the final set of equations:

- TOKAM3X is an electrostatic code: the effects of magnetic fluctuations on the transport are neglected under the low β hypothesis. Here, only the electric potential fluctuations are taken into account. With this hypothesis, $\mathbf{B}$ is considered constant in time and the electric field is equal to the gradient of the electric potential ϕ.

$$\mathbf{E} = -\boldsymbol{\nabla}\phi \tag{2.54}$$

- $m_e/m_i \approx 10^{-3}$, therefore, inertial terms of electrons are neglected with respect to the ones of ions.
- The parallel resistivity, $\eta_\parallel$ and the parallel thermal conductivities $\chi_{\parallel,e/i}$ are also simplified in the version of the code presented in this work. The parallel Spitzer resistivity $\eta_\parallel$, which normally depends on the temperature, is taken constant in time and space. In the case of the parallel thermal conductivity only the temperature dependency is conserved, and we take $\chi_{\parallel,e/i} = K_{0,e/i}T^{5/2}$ where $K_{0,e/i}$ are constant parameters.
- A Boussinesq-like approximation [Hinton 71] is realized on the current balance equation (see section 2.4.4.4).
- The centrifugal drift, only recently implemented in TOKAM3X, has not been taken into account, and the diamagnetic drift is replaced by the $\boldsymbol{\nabla}B$-drift under the diamagnetic cancellation (see section 2.1.3).

Note, that the drift of order 2, i.e the polarisation drift, is kept only in the charge balance as the current divergence of this drift is of the same order as the one of the drift of order 1. In the other equations, only the drifts of order 1 are kept even though, as mentioned in section 2.2.2, this is a disputable simplification.

2.4.1 Magnetic configuration

The magnetic field, constant in time in TOKAM3X, is fixed as an input parameter of the code. The magnetic equilibrium is assumed to be axisymmetric (i.e toroidally symmetric) and is thus described using a 2D map of the poloidal plane. The code allows using complex realistic geometries including X-point configurations. However, in this work, the studied simulations are restricted to limiter configuration. For such magnetic configurations, the magnetic equilibrium is determined by two parameters: a toroidal flux number $F = B_0R_0$ and a 2D poloidal flux function ψ. The magnetic field is computed accordingly, using the formula:

$$\mathbf{B} = \mathbf{B}_{\text{tor}} + \mathbf{B}_{\text{pol}} = F\boldsymbol{\nabla}\varphi + \boldsymbol{\nabla}\psi \times \boldsymbol{\nabla}\varphi \tag{2.55}$$

where B_{tor} and B_{pol} are respectively the toroidal and poloidal magnetic field, and φ is the toroidal angle. The iso-ψ surface are tangent to $\mathbf{B}$ and label the flux-surfaces.

The meshes used in TOKAM3X are aligned on the flux-surface. They use the covariant and contravariant basis associated with the curvilinear coordinate system (ψ, θ, φ), where θ is the coordinate along the poloidal direction.

2.4.2 Boundary condition

In the parallel direction Bohm-Chodura boundary condition are imposed at the magnetic pre-sheath entrance: $|\left(u_{\parallel}\mathbf{b} + \mathbf{u}_{\perp}\right) \cdot \mathbf{n}_{\text{wall}}| \geq c_s |\mathbf{b} \cdot \mathbf{n}_{\text{wall}}|$, $q_e = \gamma_e k_B n_e T_e \Gamma_{\text{se}}$ and $q_i = \gamma_i k_B n T_i \Gamma_{\text{se}}$

In the perpendicular direction, Neumann conditions are imposed at the inner and the outer boundary.

2.4.3 Normalisation

In the code, all quantities, F, are normalized with respect to a reference quantity. The dimensionless variables are denoted $\widehat{F}$, and defined by $\widehat{F} = F/F_0$ where F_0 is the reference quantity.

The reference density n_0, and temperature T_0 are chosen as typical values at the separatrix in Tokamaks. The reference magnetic field B_0 is defined as B on the machine magnetic axis. Spatial quantities are normalized to the Larmor radius $\rho_L = \frac{\sqrt{m_i T_0}}{eB_0}$, and time to the inverse of ion cyclotron frequency $\Omega_s = \frac{eB_0}{m_i} e$. Accordingly, electric potential ϕ, and the parallel velocity are respectively normalized to $\frac{T_0}{e}$ and $c_{s,0} = \sqrt{\frac{T_0}{m_i}}$. The reference quantities are reported on Tab. 2.1, as well as the typical value of these quantities observed in Tore Supra at the separatrix.

Quantity	$n_s(\text{m}^{-3})$	T_s (eV)	ϕ (V)	B (T)	time (s)	distance (m)	$\mathbf{u_s}$ (m.s^{-1})
Normalisation	n_0	T_0	$\phi_0 = T_0/e$	B_0	ω_c^{-1}	ρ_L	$c_{s,0} = \sqrt{T_0/m_i}$
Tore Supra	$5 \times 10^{18} - 10^{19}$	30	30	3.1	3×10^8	2×10^{-4}	5×10^4

Table 2.1: Normalisations in TOKAM3X

In the following, the normalized quantities will be denoted with upper-cases and the over parenthesis will be omitted to simplify notations (N for density , P_α for the pressure, Φ for the potential, etc...)

2.4.4 Braginskii equations in Tokam3X

2.4.4.1 Continuity equation

Considering the quasi-neutrality assumption ($n_e = n_i$), it is equivalent to solve the electron or the ion continuity equation. In Tokam3X, we choose to solve the continuity equation for electrons (2.57) because the drifts are simpler to solve for electron as the polarisation drift ($\propto m_e$) can be readily neglected. In the case of density, the divergence of $n\mathbf{u}_*$ and $n\mathbf{u}_{\nabla B}$ are rigorously the same (see Annex A), and we define the electron perpendicular velocity as:

$$\mathbf{u}_{\perp,e} = \mathbf{u}_{\mathbf{E}} + \mathbf{u}_{\nabla B,e} \tag{2.56}$$

The dimensionless continuity equation then writes:

$$\partial_t N + \boldsymbol{\nabla} \cdot \left(N \left(u_\parallel \mathbf{b} + \mathbf{u}_{\perp,e} \right) \right) = \boldsymbol{\nabla} \cdot (D_{\perp N} \boldsymbol{\nabla}_\perp N) + S_N \tag{2.57}$$

where $\boldsymbol{\nabla} \cdot (D_{\perp N} \boldsymbol{\nabla}_\perp N)$ is the diffusive term modelling small scales and S_N the source of particles in the core region. Note that in TOKAM3X the electron parallel velocity is in fact replaced by the ion parallel velocity in the all domain ($u_\parallel \sim u_{\parallel,e} \sim u_{\parallel,i}$ i.e $j_\parallel$ is neglected). This assumption is not consistent with the drift ordering at the first order and is due to the difficulty of numerical implementation of the $j_\parallel$ term in this equation. The impact of this term should be investigated in future development of TOKAM3X.

2.4.4.2 Parallel momentum balance equation

This equation is obtained from the parallel projection of the momentum balance equation (2.35) of both electrons (2.58) and ions (2.59), where the electron inertial terms and the divergence of Braginskii tensor are neglected.

$$0 = -n_e e E_\parallel - \nabla_\parallel p_e + \mathbf{R}_\parallel \tag{2.58}$$

$$m_i \left(\partial_t \Gamma_{\parallel,i} + \boldsymbol{\nabla} \cdot \left(\Gamma_{\parallel,i} (u_{\parallel,i} \mathbf{b} + \mathbf{u}_{\perp,i}) \right) \right) = n_i e E_\parallel - \nabla_\parallel p_i - \mathbf{R}_\parallel + S_{\Gamma_i} \tag{2.59}$$

where S_{Γ_i} is a source of parallel momentum on ions.

The sum of the two equations, combined to the quasi-neutrality assumption and the diamagnetic cancellation, becomes after normalisation:

$$\partial_t \Gamma_i + \boldsymbol{\nabla} \cdot \left(\Gamma_i \left(u_{\parallel,i} + \mathbf{u}_{\perp,i} \right) \right) = -\boldsymbol{\nabla}_\parallel \left(P_i + P_e \right) + \boldsymbol{\nabla} \cdot \left(D_{\perp\Gamma} N \boldsymbol{\nabla}_\perp \frac{\Gamma_i}{N} + D_{\perp N} \frac{\Gamma_i}{N} \boldsymbol{\nabla}_\perp N \right) + S_\Gamma \tag{2.60}$$

where $\Gamma_i = N_i u_{\parallel,i} \mathbf{b}$ is the ion parallel momentum, and $\boldsymbol{\nabla} \cdot \left(D_{\perp\Gamma} N \boldsymbol{\nabla}_\perp \frac{\Gamma_i}{N} + D_{\perp N} \frac{\Gamma_i}{N} \boldsymbol{\nabla}_\perp N \right)$ is the diffusive term modelling small scales.

2.4.4.3 Parallel Ohm's law

The parallel current conservation also comes from the ion and electron momentum equations. However, the inertial terms of electrons are not neglected in a first stage, and the equation on ions is multiplied by m_e/m_i which leads to:

$$m_e \left(\partial_t \Gamma_{\parallel,e} + \boldsymbol{\nabla} \cdot \left(\Gamma_{\parallel,e} (u_{\parallel,e} \mathbf{b} + \mathbf{u}_{\perp,e}) \right) \right) = -n_e e E_\parallel - \nabla_\parallel p_e - \boldsymbol{\nabla} \cdot \left(\bar{\bar{\Pi}}^{\mathrm{Brag}} \right) \cdot \mathbf{b} + R_\parallel + S_{\Gamma_e} \tag{2.61}$$

$$m_e \left(\partial_t \Gamma_{\parallel,i} + \boldsymbol{\nabla} \cdot \left(\Gamma_{\parallel,i} (u_{\parallel,i} \mathbf{b} + \mathbf{u}_{\perp,i}) \right) \right) = \frac{m_e}{m_i} \left(n_i e E_\parallel - \nabla_\parallel p_i - \boldsymbol{\nabla} \cdot \left(\bar{\bar{\Pi}}^{\mathrm{Brag}} \right) \cdot \mathbf{b} - R_\parallel + S_{\Gamma_i} \right) \tag{2.62}$$

Here $\Gamma_{\parallel,e/i}$ are non-normalized quantities

The difference of equation (2.61) and (2.62), neglecting now all the terms in m_e/m_i, and using the electrostatic assumption $E_\parallel = -\nabla_\parallel \phi$, writes:

$$m_e \left(\partial_t \Gamma_{\parallel,e} + \boldsymbol{\nabla} \cdot \left(\Gamma_{\parallel,e} u_{\parallel,e} \mathbf{b} \right) \right) - m_e \left(\partial_t \Gamma_{\parallel,i} + \boldsymbol{\nabla} \cdot \left(\Gamma_{\parallel,i} u_{\parallel,i} \mathbf{b} \right) \right) = -n_e e E_\parallel - \nabla_\parallel p_e + R_\parallel \tag{2.63}$$

Electronic inertial terms and the divergence of the Braginskii's tensor are neglected with respect to the electrostatic force. Moreover, the parallel projection of the friction term $R_\parallel$ given by Braginskii's closure 2.1.3 leads to $R_\parallel = en_e\eta_\parallel j_\parallel - 0.71n_e\nabla_\parallel T_e$ for a hydrogenic plasma. The parallel current conservation, also called the generalized Ohm's law, becomes after normalisation:

$$\eta_\parallel N J_\parallel = \boldsymbol{\nabla}_\parallel P_e - N\boldsymbol{\nabla}_\parallel \Phi + 0.71N\boldsymbol{\nabla}_\parallel T_e \tag{2.64}$$

2.4.4.4 Charge conservation

At first order, the charge conservation writes:

$$\boldsymbol{\nabla}\cdot\mathbf{j} = \boldsymbol{\nabla}\cdot\left(j_\parallel\mathbf{b}\right) + \boldsymbol{\nabla}\cdot(\mathbf{j}^*) + \boldsymbol{\nabla}\cdot(\mathbf{j}_{\text{pol}}) = 0 \tag{2.65}$$

where $\mathbf{j}_*$ and $\mathbf{j}_{\text{pol}}$ are respectively the diamagnetic and polarisation current.

The charge balance equation is expressed as a function of the vorticity (2.66), denoted W. Under the Boussinesq approximation, the vorticity writes:

$$W = \boldsymbol{\nabla}\cdot\left(\frac{1}{B^2}\boldsymbol{\nabla}_\perp\Phi + \frac{1}{NB^2}\boldsymbol{\nabla}_\perp P_i\right) \tag{2.66}$$

The development of the charge conservation (not detailed) leads to the following normalized equation:

$$\partial_t W + \boldsymbol{\nabla}\cdot\left(W\left(u_\parallel + \mathbf{u}_{\perp,i}\right)\right) = \boldsymbol{\nabla}\cdot(N(\mathbf{u}_{\nabla B,i} - \mathbf{u}_{\nabla B,e})) + \boldsymbol{\nabla}\cdot\left(J_\parallel\mathbf{b}\right) + \boldsymbol{\nabla}\cdot(D_{\perp W}\boldsymbol{\nabla}_\perp W) + S_W \tag{2.67}$$

where $\boldsymbol{\nabla}\cdot(D_{\perp W}\boldsymbol{\nabla}_\perp W)$ is the diffusive term modelling small scales, and S_W a source of vorticity.

2.4.4.5 Electron and ion energy balance equations

In both electron and ion energy balance equations (2.23), we keep only the parallel contributions, the ones of the highest magnitude ($u_\parallel \gg |\mathbf{u}_\perp|$), from the terms $n_e\mathbf{E}\cdot\mathbf{u_s}$ and $\mathrm{R_s}\cdot\mathbf{u_s}$ in coherence with the drift ordering. We thus keep $\pm u_{\parallel,i}R_\parallel$, $\pm nu_{\parallel,i}E_\parallel$. Note that as for the equation on density the electron parallel velocity is replaced by the ion parallel velocity in the energy balance equation.

Moreover, as done for the parallel momentum equation, the anisotropic part of the pressure tensor $\boldsymbol{\nabla}\cdot\left(\bar{\bar{\Pi}}^{\text{Brag}}\right)$ is not kept in the equation: $\boldsymbol{\nabla}\cdot\left(\bar{\bar{\Pi}}^{\text{vis}}\right) \propto p_\parallel - p_\perp \approx 0$ under the low β assumption and $\boldsymbol{\nabla}\cdot\left(\bar{\bar{\Pi}}^{\text{FLR}}\right)$ disappears in the frame of the diamagnetic cancellation.

The heat fluxes (2.68) and the friction sources (2.69), from the Braginskii closure, are further simplified keeping the terms of the highest magnitude because the other perpendicular terms are negligible compared with turbulent or drift transport.

$$\mathbf{q}_{e/i} = K_{0,e/i}T_{e/i}^{5/2}\nabla_\parallel T_{e/i}\mathbf{b} \tag{2.68}$$

where $K_{0,e/i}$ are constant parameters defined as an input of the code.

$$Q_{\parallel,i} = -Q_{\parallel,e} = 3\frac{m_e}{m_i}\nu_* \frac{N_e}{\tau_e}\left(T_e - T_i\right) \tag{2.69}$$

Finally, the energy conservation equations, in the normalized form, write:

$$\partial_t E_e + \boldsymbol{\nabla}\cdot\left(\left(E_e + P_e\right)u_{\parallel,i} + E_e \mathbf{u}^e_\perp\right) = \boldsymbol{\nabla}\cdot\left(K_0^e T_e^{5/2}\boldsymbol{\nabla}_\parallel T_e \mathbf{b}\right) - P_e\boldsymbol{\nabla}\cdot\left(\mathbf{u}^e_\perp\right) - \Gamma_i E_\parallel + \frac{\Gamma_i}{N}R_\parallel \tag{2.70}$$
$$+Q_{\parallel,e} + \boldsymbol{\nabla}\cdot\left(D_{\perp T_e} N\boldsymbol{\nabla}_\perp T_e + D_{\perp N}\frac{E_e}{N}\boldsymbol{\nabla}_\perp N\right) + S_{E_e}$$

$$\partial_t E_i + \boldsymbol{\nabla}\cdot\left(\left(E_i + P_i\right)u_{\parallel,i} + E_i \mathbf{u}^i_\perp\right) = \boldsymbol{\nabla}\cdot\left(K_0^i T_i^{5/2}\boldsymbol{\nabla}_\parallel T_i \mathbf{b}\right) - P_i\boldsymbol{\nabla}\cdot\left(\mathbf{u}^i_\perp\right) + \Gamma_i E_\parallel - \frac{\Gamma_i}{N}R_\parallel \tag{2.71}$$
$$+Q_{\parallel,i} + \boldsymbol{\nabla}\cdot\left(D_{\perp T_i} N\boldsymbol{\nabla}_\perp T_i + D_{\perp N}\frac{E_i}{N}\boldsymbol{\nabla}_\perp N + D_{\perp\Gamma}\Gamma_i\boldsymbol{\nabla}_\perp\frac{\Gamma_i}{N}\right) + S_{E_i}$$

where $E_e = \frac{3}{2}N_e T_e$, $E_i = \frac{3}{2}N_i T_i + \frac{1}{2}\frac{\Gamma_i^2}{N}$, and $\boldsymbol{\nabla}\cdot\left(D_{\perp T_e} N\boldsymbol{\nabla}_\perp T_e + D_{\perp N}\frac{E_e}{N}\boldsymbol{\nabla}_\perp N\right)$, and $\boldsymbol{\nabla}\cdot\left(D_{\perp T_i} N\boldsymbol{\nabla}_\perp T_i + D_{\perp N}\frac{E_i}{N}\boldsymbol{\nabla}_\perp N + D_{\perp\Gamma}\Gamma_i\boldsymbol{\nabla}_\perp\frac{\Gamma_i}{N}\right)$ are the diffusive terms modelling net small scale energy sources, and S_{E_e} and S_{E_i} are sources of electron and ion energy.

2.5 2D fluid models

In the family of fluid models, one finds also further simplified model with 2 main types of 2D codes, later studied in this work:

- 2D slab geometry model: turbulence code where the parallel dynamics is simplified with the assumption that $k_\parallel = 0$ and with a simplified geometry. This is the case of TOKAM2D, used in Chapter 3, to study the basic properties of heat turbulent transport.
- 2D mean-transport code: laminar code in realistic geometry, in which no self-consistent turbulence is solved, and turbulence is arbitrarily set via a diffusion coefficient. This is the case of SolEdge2D, used in Chapter 4, to study the drift transport in the limit of low anomalous transport. Note that in this largest version, SolEdge2D contains physics not included in TOKAM3X: neutrals, and realistic wall geometry. However, the model used in the most part of the chapter 4, can be considered as a reduced model of the TOKAM3X equations.

code	TOKAM3X	SolEdge2D	TOKAM2D
type	3D turbulent fluid	2D mean fields fluid code	2D turbulent
geometry	realistic	realistic including the walls	2D slab
cpu time for a simulation	10^8–2×10^9s	$\sim$ 4–8×10^5s	$\sim$ 2–4×10^5s

Table 2.2: Comparison of the different models: geometry, and computational cost

Chapter 3

Mechanisms of heat turbulent transport in 2D slab geometry

Turbulent transport of plasma particles has been widely discussed and described both experimentally and theoretically. However, this is not the case of heat turbulent transport, especially for ion energy transport, since in experiments electron temperature fluctuations are hard to measure and the ion temperature is practically unknown in the edge plasma.

In order to have an insight into the basic properties of heat turbulent transport, we first investigate the turbulence characteristics, and the resulting heat transport, in a simple slab geometry which does not include complex geometrical effects, and only reflects basic properties of turbulence. Moreover, the fast resolution of Tokam2D allows to scan the main parameters of the model in a short amount of time which would be too costly in a 3D model such as Tokam3X.

The impact of the inclusion of both electron and ion temperatures dynamics on turbulence and resulting heat transport are discussed in this section. Special focus is devoted to the contribution of an additional mechanism due to the interaction of sheath boundary conditions with T_e fluctuations, called the Sheath-driven Conducting-Wall (SCW) instability, in simulations including electron temperature dynamic, and to finite ion temperature effects in simulations including ion temperature dynamics.

3.1 Tokam2D: reduction of fluid modeling to a 2D model

3.1.1 Model

Tokam2D is a flux driven 2D fluid model, as TOKAM3X detailed in the previous chapter, derived from the two first moments of the distribution function for the isothermal version [Sarazin 98, Sarazin 03], and from the three first moments for the anisothermal version [Marandet 16]. The 2D treatment of the turbulence comes from the so-called *flute hypothesis* which assumes constant perturbations along the field lines, that is to say $k_{\|} = 0$, based on the fact that, in tokamaks, transport along the field lines is much faster than in the cross-field direction. The parallel losses are then modeled by taking the averaged loss along the field line between the two targets, and are represented by the sheath conductivity coefficient σ.

Tokam2D uses also a simplified geometry, the so-called *slab geometry* in which only a thin poloidal extent is treated in the limit of large aspect ratio, so that the magnetic field is considered locally as

straight lines and the effect of magnetic curvature is set by a free parameter denoted g. In the slab geometry x and y represent respectively the radial and poloidal directions.

The model solves the Braginskii's fluid equations for particle conservation (3.1), charge conservation (3.2) and electron and ion energy conservations (3.3)–(3.4). They correspond respectively to the equations (2.57), (2.67), (2.70), (2.71) of TOKAM3X model described in the previous chapter.

$$\partial_t N + [\phi, N] = -\sigma N c_s \exp\left(\Lambda - \frac{\phi}{T_e}\right) + D\nabla_\perp^2 N + S_N \tag{3.1}$$

$$\partial_t W + [\phi, W] = -\frac{g}{N}\partial_y (P_e + P_i) + \sigma c_s \left(1 - \exp\left(\Lambda - \frac{\phi}{T_e}\right)\right) + \nu\nabla_\perp^2 W \tag{3.2}$$

$$\partial_t \left(\frac{3}{2}P_e\right) + \left[\phi, \frac{3}{2}P_e\right] = -\gamma_e \sigma P_e c_s \exp\left(\Lambda - \frac{\phi}{T_e}\right) + \chi_e \nabla_\perp^2 \left(\frac{3}{2}P_e\right) + S_{E_e} - \frac{3m_e}{m_i}\tau_e^{-1}(P_e - P_i) \tag{3.3}$$

$$\partial_t \left(\frac{3}{2}P_i\right) + \left[\phi, \frac{3}{2}P_i\right] = -\gamma_i \sigma P_i c_s + \chi_i \nabla_\perp^2 \left(\frac{3}{2}P_i\right) + S_{E_i} + \frac{3m_e}{m_i}\tau_e^{-1}(P_e - P_i) \tag{3.4}$$

$$W = \nabla_\perp^2 \phi + \nabla \cdot \left(\frac{1}{N}\nabla P_i\right) \tag{3.5}$$

where $c_s = \sqrt{T_e + T_i}$ is the normalized parallel acoustic speed, $P_e = NT_e$ and $P_i = NT_i$ are respectively the electron and ion pressure, W is the generalised vorticity expression under Boussinesq's approximation, and $[a, b] = \partial_x a \partial_y b - \partial_y a \partial_x b$ is the Poisson bracket, representing the $\mathbf{E} \times \mathbf{B}$ advection. Like in Tokam3X all quantities are normalized: spatial quantities to the Larmor radius ρ_L, time to the inverse of ion cyclotron frequency Ω_s, computed with respect to a reference temperature T_0 and magnetic field B_0.

3.1.2 Parameters

In this chapter, the turbulence characteristics and the resulting cross-field transport are discussed when removing step by step the assumptions of the cold ion isothermal model, referred simply as the isothermal model in the following:

1. addition of the self-consistent variations of electron temperature governed by the equation (3.3), this reduced model is referred as anisothermal-T_e model;

2. inclusion of finite ion temperature term in the expression of the vorticity, and addition of the self-consistent variation of ion temperature governed by the equation (3.4). The model is referred as full anisothermal models.

In this chapter, the cold ion assumption in isothermal and anisothermal-T_e simulations is replaced by the simplification of the vorticity expression to $W = \nabla_\perp^2 \phi$, i.e. suppression of the finite ion temperature term in the vorticity expression. In fact, this is equivalent to a cold ion hypothesis, while keeping the terms proportional to $(T_e + T_i)$ at the same amplitude. Thus, for isothermal and anisothermal-T_e simulation, ion temperature is taken constant equal to 1 in the curvature term, ($\propto g(T_e + T_i)$), the sheath loss term ($\propto \sigma\sqrt{T_e + T_i}$), and $T_i = 0$ in the vorticity expression.

All simulations are run for a grid of 256×256 ρ_L and with an integration time of $0.2\Omega_s^{-1}$. D, ν, χ are respectively the cross-field diffusion, viscosity, and thermal conduction coefficients. These coefficients

are kept spatially constant and taken equal to $5 \times 10^{-3}\rho_L^2\Omega_s^{-1}$, of the order of neoclassical diffusion coefficients. The influx from the core plasma crossing the separatrix is mimicked by a Gaussian volumetric density source at the inner boundary, $S_N \propto \exp\{(x-x_0)^2/\Delta_x^2\}$, with $x_0 = 16$ and $\Delta_x = 8$ and homogeneous in the poloidal direction. The corresponding electron and ion energy influx $S_{E_{e/i}}$ are equal to $\zeta_{e/i} * S_N$ where $\zeta_{e/i}$ is the normalized thermal energy carried by one electron/ion. The terms $\pm\frac{3m_e}{m_i}\tau_e^{-1}(P_e - P_i)$ are collisional terms where m_e, m_i and τ_e are respectively the electron mass, the ion mass and the characteristic time of electron-ion collision. The normalised floating potential, Λ, is equal to 3.88, and the electron and ion sheath heat transmission coefficients $\gamma_{e/i}$ are respectively set to 5 and 2.5. Here, the free parameters are g, and $\zeta_{e/i}$ scanned to study their impact on turbulence and transport. In a diverted configuration the sheath conductivity would be significantly higher in the Private Flux Region (PFR) than in the main SOL. The magnetic configuration data from a typical ASDEX equilibrium [Bufferand 15, Chankin 06] was used to estimate the ratio between the main SOL and the Private Flux Region (PFR) of the sheath conductivity σ, which is found to be between almost three times higher in the PFR compared to SOL, and we obtain $\sigma \approx 1 \times 10^{-4}$ for the SOL region, $\sigma \approx 3 \times 10^{-4}$ for the PFR. In this study two sets of simulations are run, one with $\sigma = \sigma_{\mathrm{PFR}} = 2 \times 10^{-4}$, this other with $\sigma = \sigma_{\mathrm{SOL}} = 1 \times 10^{-4}$. The value for σ_{PFR} is chosen lower than the one found in the ASDEX equilibrium as turbulence barely develops in simulations with $\sigma = 3 \times 10^{-4}$. Nevertheless, the chosen value $\sigma_{\mathrm{PFR}} = 2 \times 10^{-4}$ stays a good approximation for the PFR and the σ values are somehow representative of the variation between the two regions, enough for a qualitative comparison.

3.2 Main characteristics of turbulence in TOKAM2D

3.2.1 Linear analysis methodology

Even though turbulence in Tokam2D is a highly non-linear phenomenon, it is worth studying the linear stability of the model as it offers an insight into the mechanisms driving the heat transport. In particular, turbulent structures are partly shaped by the linear instability mechanisms, and its characteristics, for instance structure size, or phase shift between density and potential fluctuations, can be seen as markers of different instabilities. This tool will be used all along this chapter, its assumption and calculation details are recalled below.

The linear analysis studies the stability of a small perturbation to the equilibrium. The method is based on the assumption that the amplitudes of fluctuations are small in regard to the mean fields. Each field f is split in a mean and a fluctuating part, respectively $\overline{f}$ and $\widetilde{f}$, $f = \overline{f} + \widetilde{f}$ with $\overline{f} = \langle f \rangle_{t,y}$. The ordering assumption of small fluctuations gives $\varepsilon = \widetilde{f}/\overline{f} \ll 1$, so that all the non-linear terms in ε^2 are neglected. The balance equations (3.1)–(3.4) and vorticity definition are developed to the first order with respect to ε, the calculus being detailed in Annex B.

We also assume to have reached a steady-state equilibrium in which equilibrium fields are of the form (3.6). It is worth mentioning here that equilibria found in turbulent simulations, presenting typical SOL width of the order of $\lambda_{N,\mathrm{turb}}$, are far from the one estimated by the linear analysis: $\lambda_{N,\mathrm{turb}} \gg \lambda_{N,\mathrm{lin}}$, evidence of strong non-linear transport. However, the choice of assuming nonetheless a quasi steady-state equilibrium is justified by the fact that the characteristic times of quasi steady-state equilibrium evolution, i.e. $1/\sigma$, λ_N^2/D are of an order of magnitude higher compared to the characteristic time of fluctuation evolution (inverse of the maximal growth rate, see in the next section).

Thus, in regard to a fluctuation the quasi steady-state is constant in time.

$$\begin{cases} \overline{N} = N_0 \exp\left(-x/\lambda_N\right) \\ \overline{T_e} = T_{e,0} \exp\left(-x/\lambda_{T_e}\right) \\ \overline{T_i} = T_{i,0} \exp\left(-x/\lambda_{T_i}\right) \\ \overline{\phi} = \Lambda \overline{T_e} \\ \text{with } \lambda_{T_e} = \frac{\lambda_N}{\sqrt{\gamma_e}-1} \text{ and } \lambda_{T_i} = \frac{\lambda_N}{\sqrt{\gamma_i}-1} \end{cases} \tag{3.6}$$

The relations between λ_N, λ_{T_e} and λ_{T_i} derive from the steady-state equations under the assumptions of exponential profiles for all fields as detailed in Annex B. Note that this analytical result is in agreement with the typical ratios λ_{T_e}/λ_N, λ_{T_i}/λ_N found in non-linear turbulent simulations.

Using the Fourier representation of the fluctuations of each field f (3.7) in the linear relationship, one obtains an equation of the form (3.8) where $M\left(\omega, k_x, k_y\right)$ is a matrix depending on ω, k_x, k_y and other parameters of the system. The system ($\widehat{N}$, $\widehat{W}$, $\widehat{\phi}$, $\widehat{T_e}$, $\widehat{T_i}$) admits a non-trivial solution if and only if the determinant of the matrix $M\left(\omega, k_x, k_y\right)$ is zero. This condition yields a 4th order polynomial relationship in ω.

$$\widetilde{f} = \sum_{k_x,k_y} \widehat{f}_{k_x,k_y} \exp(ik_x x + ik_y y) \exp(\omega_k t) \tag{3.7}$$

$$M\left(w, k_x, k_y\right) \cdot \begin{bmatrix} \widehat{N} \\ \widehat{\phi} \\ \widehat{T_e} \\ \widehat{T_i} \\ \widehat{W} \end{bmatrix} = 0 \tag{3.8}$$

This offers some information on the temporal evolution of a mode: a mode is unstable, i.e its amplitude grows in time, if it exists ω solutions of $\det\left(M\left(\omega, k_x, k_y\right)\right) = 0$ such as $\mathrm{Re}\left(\omega\right) > 0$ and is stable otherwise. The growth rate of a (k_x k_y)-mode, denoted γ, is defined as $\max\left\{\mathrm{Re}\left(\omega\right) : \det\left(M\left(\omega, k_x, k_y\right)\right) = 0\right\}$, that is to say the growth rate of the most unstable mode.

For each linear mode (ω, k_x, k_y) an associated phase shift between density and potential fluctuations, denoted $\delta_{N,\phi}$ and defined by $\delta_{N,\phi} = \arg \frac{\widehat{N}}{\widehat{\phi}}$, can also be extracted by substitution and simplification of the other fields in the linear spectral equations.

3.2.2 Characteristics of interchange turbulence in isothermal simulations

In the isothermal model with no finite ion temperature effect, the linear analysis (presented in Annex B) is considerably simplified. The remaining part of the dispersion relation ($\det\left(M\left(\omega, k_x, k_y\right)\right)$=0) yields a second order equation in ω:

$$\omega^2 + b\omega + c = 0 \tag{3.9}$$

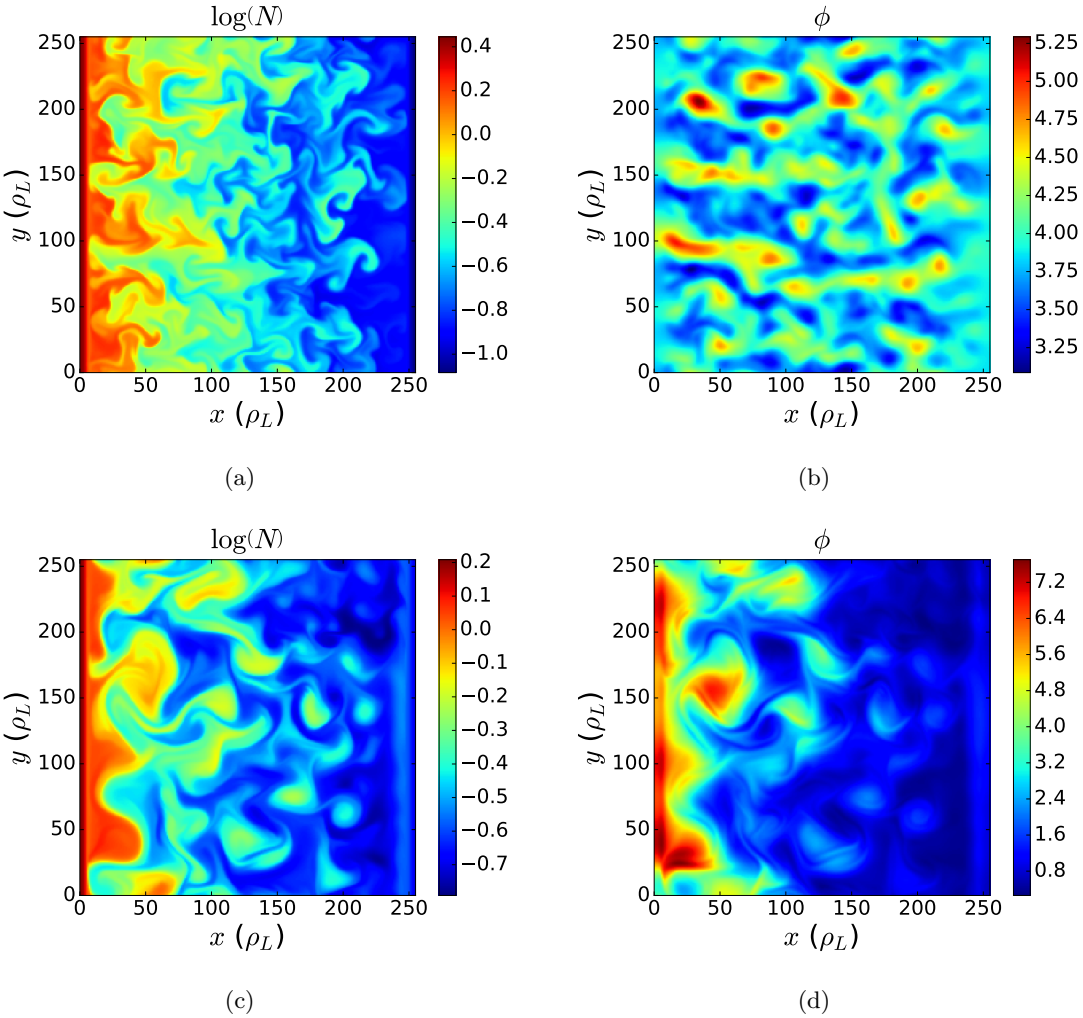

Figure 3.1: 2D snapshots of density in log-scale (left) and potential (right) for isothermal cold ions simulations (top) and full simulations (bottom) with the parameters $\sigma = 1 \times 10^{-4}$, $g = 8 \times 10^{-4}$, $\zeta_e = 5$ and $\zeta_i = 3$ for the anisothermal simulation

where $b = \frac{\sigma}{k_\perp} + \sigma + (D + \nu k_\perp)$ and $c = (\sigma + Dk_\perp)\left(\frac{\sigma}{k_\perp} + \nu k_\perp\right) - \frac{gk_y}{\lambda_N k_\perp} - ig\sigma\frac{k_y}{k_\perp}$ with $k_\perp = k_x^2 + k_y^2$. We can observe that b is a strictly positive real, thus the growth rate is equal to:

$$\gamma_k = \mathrm{Re}\left\{\frac{-b + \sqrt{b^2 - 4c}}{2}\right\} \tag{3.10}$$

One can readily deduce that the term b has a stabilizing effect, as γ_k is a decreasing function of b. Small spatial scales (high $k_\perp$) are damped by the diffusive terms with a stabilizing effect proportional to $k_\perp^2$, while large scales are damped by the current parallel loss σ. The most unstable mode $k_{\max}$ will result from the competition between this two stabilizing effects. In isothermal simulations, the only instability at play is the interchange instability, and the destabilization comes from the interplay between the density gradient and the curvature (i.e. the term $\propto g/\lambda_N$)

In turbulent simulations, the particle source induces the creation of a density gradient which builds up until the interchange modes become unstable. As one can observe on Fig. 3.1a) b), these

unstable modes form finite poloidal structures, usually referred as filaments or blobs, characterized by long radial elongations ($k_x < k_y$). Due to the quasi phase quadrature between density and potential fluctuations, expected from linear analysis, the structures propagate radially advected by the $\mathbf{E} \times \mathbf{B}$ radial velocity. In the far SOL, blobs lose their coherence and split into smaller structures damped by the diffusive effect.

In steady-state, the simulations present an important intermittent feature, characterized by a high fluctuation level defined as the standard deviation normalized by the mean field, i.e. for density $\sigma\left(N\right)_{t,y} / \left\langle N\right\rangle_{t,y}$. Note that in 2D simulations the averaging is made both in the temporal and poloidal direction assumed to play the same role on the statistics (ergodic hypothesis). In the TOKAM2D simulations, the fluctuation level of density is of the order 10% to 50% in relatively good agreement with experimental results [Horacek 10, Hornung 13]. This turbulent flux starts from the source and propagates radially outward in a quasi-ballistic motion, with a characteristic velocity of the order of $0.05c_s$ of the same order of magnitude as found in Ref. [Myra 06]. The probability density function (PDF) of the $\mathbf{E} \times \mathbf{B}$ flux is far from a Gaussian and presents a large positive tail representative of rare but strong flux event in the outward direction responsible for the largest part of the transport [Sarazin 98, Sarazin 03].

3.2.3 Impact of electron and ion temperature dynamics

Properties of turbulent transport in Tokam2D have been largely studied with the isothermal closure, and using the cold ion approximation, i.e $T_e = \text{constant}$, $T_i = 0$ [Sarazin 98, Sarazin 03], highlighting the properties of strongly intermittent turbulence. Although the electron and ion temperature equation structures are rather similar to the density equation, turbulence in the full anisothermal model presents, for the same set of parameters, significant differences compared to the isothermal model as illustrated on Fig. 3.1 c) and d).

The most striking effect is the modification of the shape of the intermittent structures. They present a larger poloidal extends (i.e small k_y) and appears to be less radially elongated than in the isothermal case. Moreover, they do not exhibit the typical mushroom shape observed in isothermal simulations and the structures appear to stay somehow more coherent, i.e. to split up less into smaller streamers.

In the light of the linear analysis of the anisothermal model, and of the literature, we can already underline two impacts of the inclusion of temperature dynamics that could be a potential explanation for these differences. Each of this effect will be further studied in details in the following of the chapter.

Effect of the inclusion of electron temperature dynamics:
The T_e-fluctuations have an impact on the current parallel losses via Bohm boundary conditions. The inclusion of the T_e fluctuations in the current sheath losses term modifies the mode number of the most unstable mode. Indeed, the stabilizing term $\sigma c_s \exp\left(\Lambda - \frac{\phi}{T_e}\right)$ includes now T_e fluctuations, and the linear stabilizing term $\sigma c_s \frac{\widehat{\phi}}{T_e}$ becomes $\sigma c_s \left(\frac{\widehat{\phi}}{T_e} - \Lambda \frac{\widehat{T_e}}{T_e}\right)$. It is equivalent to a reduction of the effective parallel resistivity, i.e. a reduction of linear stabilizing term of the large scales. Consequently, one expects that the most unstable mode will be at a lower k_y, i.e. larger poloidal structures.

This is the focus of the section 3.3 of this chapter. In particular, we will show that the presence of T_e fluctuations in the sheath loss is responsible for another instability explaining the modification

of turbulence characteristics.

Effect of the inclusion of finite ion temperature effect:
The inclusion of finite ion temperature effect, that is to say the inclusion of the diamagnetic contribution to the polarization drift in the vorticity expression (the second term in $W = \boldsymbol{\nabla}\cdot\left(\frac{1}{B^2}\boldsymbol{\nabla}\phi + \frac{1}{NB^2}\boldsymbol{\nabla}P_i\right)$) has been pointed out in the literature to impact turbulence properties [Bisai 13, Olsen 16, Jovanović 08, Madsen 11]. In particular, the study of the seeded blob dynamics shows that it is responsible for more coherent structures. This particular effect will be discussed in the section 3.3 of this Chapter.

Finally, it is worth underlying that electron temperature radial gradient forces the apparition of potential radial gradient (Fig. 3.1 d) via the sheath loss condition. The induced poloidal flow creates an additive channel for energy transfer between turbulence and mean flow.

3.3 Turbulent heat transport in the presence of electron temperature fluctuations

3.3.1 Superposition of two instabilities in the presence of self-consistent electron temperature fluctuations

In this section, only the impact of electron temperature fluctuations is studied, i.e $\widetilde{T_i} = 0$, $\lambda_{T_i} = \infty$ and $W = \nabla_\perp^2\phi$. The main difference in the linear stability of the model between the isothermal model and the T_e model is the apparition of an additional linear instability [Berk 91, Berk 93, Cohen 94], the electron temperature gradient instability induced by sheath conductivity, also known as Sheath-driven Conducting-Wall (SCW) instability, which acts on top of the well-known interchange instability. Let us first recall briefly the mechanisms triggering each instability and their principal characteristics:

- interchange instability is driven by the curvature of the magnetic field, and is unstable when both pressure and magnetic field gradient are directed in the same direction, equivalent to $g \geq 0$ in the model. Thus, this mechanism is unstable only in the Low Field Side (LFS) of tokamaks.
- Sheath Conductive Wall instability is driven by the impact of the T_e fluctuations on sheath losses.

As the latter instability is less known we start by briefly explaining its mechanism in the simplest form. The mechanism can be summarized in 4 simplified steps schemed in Fig.3.2. The most reduced model to explain the mechanisms takes the following assumptions: no density or ion temperature fluctuations $\widetilde{N} = \widetilde{T_i} = 0$, and no dissipative processes $D = \nu = \chi = 0$, so the system of equation becomes:

$$\begin{cases} \partial_t W + [\phi, W] = \sigma\sqrt{T_e}\left(1 - \mathrm{e}^{\Lambda - \frac{\phi}{T_e}}\right) \\ \partial_t T_e + [\phi, T_e] = -\gamma_e \sigma P_e c_s \mathrm{e}^{\Lambda - \frac{\phi}{T_e}} \end{cases} \tag{3.11}$$

1. First let us consider a small sinusoidal perturbation of T_e (represented by a full blue line) to the equilibrium (represented by a dashed blue line) in the presence of a T_e gradient.

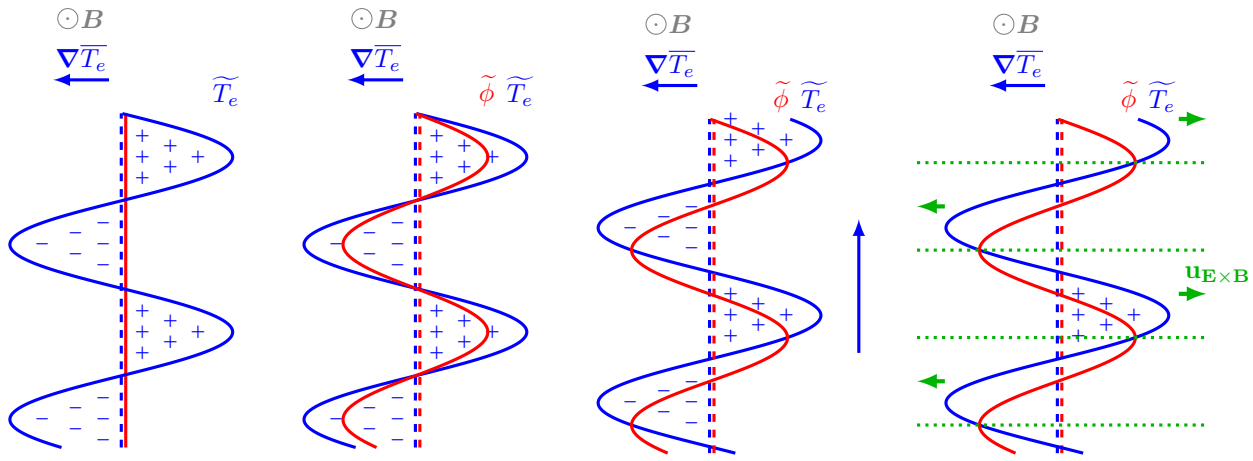

Figure 3.2: Scheme of the processes of the Sheath Conductive Wall instability. Time increases from left to right

2. The sheath condition in the current balance equation will enforce a potential fluctuation $\widetilde{\phi}$ in phase with $\widetilde{T_e}$.

3. The $\mathbf{E}\times\mathbf{B}$ advection creates a positive phase shift between $\widetilde{T_e}$ and $\widetilde{\phi}$ due to the mean T_e gradient.

4. For such mode, if one considers a positive structure of T_e fluctuation, and the direction of the electric drift $\mathbf{u}_{\mathbf{E}\times\mathbf{B}}$, reported in green, one can notice that the part of the positive structure transported in the counter $\boldsymbol{\nabla} T_e$ direction is larger than the one transported in the $\boldsymbol{\nabla} T_e$ direction, hence the initial fluctuation is amplified, i.e. the mode is unstable.

We now, study the linear stability of the model, in order to disentangle the roles of these instabilities, we have set-up reduced models which separate their contribution in the global linear analysis:

- reduced model of SCW instability: the interchange instability is simply cancelled by setting the curvature term to zeros, i.e. $g = 0$;

- reduced model of interchange instability: the most reduced way to cancel the SCW instability is to take away the contribution of the fluctuation of temperature in the exponential part of the parallel loss term in the equation of current conservation, i.e. replacing the sheath loss term $\exp\left(\Lambda - \frac{\phi}{T_e}\right)$ by $\exp\left(\Lambda - \frac{\phi}{\langle T_e\rangle_{t,y}}\right)$ in (3.2).

The linear growth rate as a function of poloidal mode number and for $k_x = 0$ of the isothermal model and its decomposition in the contribution of each instability, Fig. 3.3a, reveals that the SCW instability destabilizes larger spatial scales, i.e. is unstable at lower k_y than the interchange one. Thus, the SCW instability is the one responsible for the fact that the most unstable mode in the anisothermal model, indicated by a marker, occurs at lower poloidal mode number than in the isothermal model. In fact the scales are destabilized by the interchange instability in the anisothermal case are even smaller than in the isothermal case due to the additional contribution of the temperature gradient in the curvature term g.

Another noticeable difference in the linear instability is the typical phase shift between fluctuation of density and potential, i.e. $\arg\left(\widehat{N}/\widehat{\phi}\right)$. The analytical linear results Fig. 3.3b. predict a phase

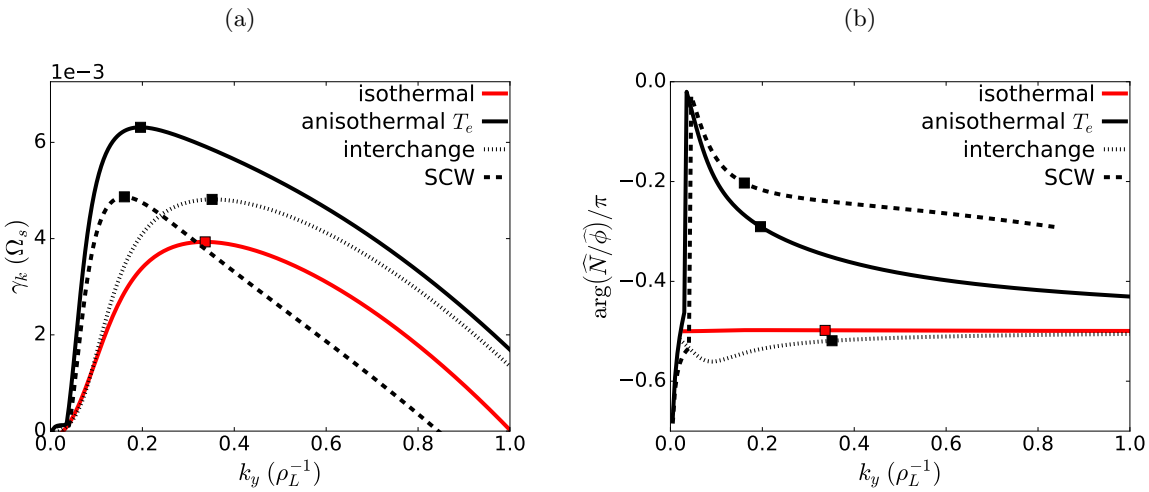

Figure 3.3: Linear growth rate (**a**) and linear phase shift between density and potential fluctuations (**b**) for T_e model, anisothermal SCW, interchange reduced models and isothermal model for $\sigma = 1 \times 10^{-4}$, $g = 4 \times 10^{-4}$, $\lambda_N = \left(\sqrt{\gamma_e} - 1\right) \lambda_{T_e} = 30\rho_L$ as a function of the poloidal mode number k_y and for $k_x = 0$. The linear phase shift is reported only for mode presenting a positive growth rate

quadrature between $\widetilde{N}$ and $\widetilde{\phi}$ for the interchange instability in the isothermal model ($\arg\left(\widehat{N}/\widehat{\phi}\right) \approx \pi/2$ at all k_y), when for the full T_e model or the SCW reduced model the shift phase between $\arg\left(\widehat{N}/\widehat{\phi}\right)$ is close to zero at very low k_y unstable modes ($k_y < 0.15\rho_L^{-1}$), and decreases down to 0.25π at high k_y in SCW reduced model and down to 0.4π in the anisothermal model. At the maximal value of the growth rate, $\arg\left(\widehat{N}/\widehat{\phi}\right)$ are respectively equal to 0.2π (SCW) and 0.3π (anisothermal-T_e).

Fig. 3.4a. depicts a 2D map of the maximal linear growth rate as a function of the local gradient lengths and T_e, for $\sigma = \sigma_{\text{PFR}}$, $\sigma = \sigma_{\text{SOL}}$. The black line is the delimitation between the predominance domain of the two instabilities ($\gamma_{\text{max,int}} = \gamma_{\text{max,SCW}}$). For the main SOL parameters (left), the interchange instability has a broader domain of predominance ($\gamma_{\text{max,int}} > \gamma_{\text{max,SCW}}$). Yet if we look at the ratio between the SCW and interchange instability ($\gamma_{\text{max,SCW}}/\gamma_{\text{max,int}}$), Fig. 3.4b. we observe that the ratio is around 1 for the most part of the domain of local parameter, so the SCW instability is not negligible with respect to the interchange one. On the contrary, for PFR parameters (right), the SCW instability has a broader domain of predominance. Moreover, for low T_e, expected in the PFR, the SCW instability is largely predominant $\gamma_{\text{max,SCW}}/\gamma_{\text{max,int}} > 2$. On Fig. 3.4b, we also observe that the ratio $\gamma_{\text{max,SCW}}/\gamma_{\text{max,int}}$ decreases with T_e for a given value of local gradients and for the two values of σ, so the relative predominance of the interchange instability is favored by an increase of T_e. To conclude, we keep in mind that both effects of σ and T_e on the linear stability favor the SCW instability in the PFR, which might play an important role in this region.

3.3.2 Modification of turbulence characteristics in non-linear simulations with the additional SCW instability

We now turn to non-linear simulations to understand how the turbulence is influenced by the additional SCW instability in light of the linear analysis. The reduced models for each instability applied in the linear analysis can also be used in non-linear simulations to study separately the characteristics of the

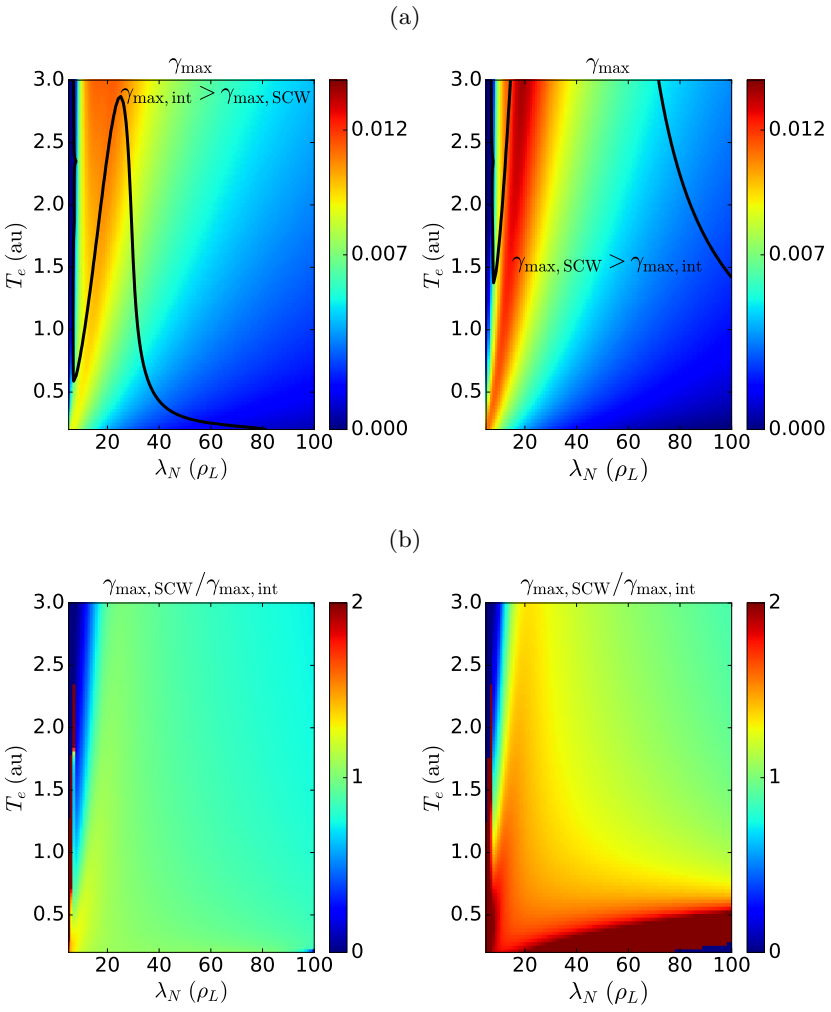

Figure 3.4: (**a**) Maximal growth rate ($\gamma_{\max}$) for anisothermal-T_e model for σ_{SOL} (left) and σ_{PFR} (right), and (**b**) ratio of maximal growth rate between SCW and interchange instability, for $g = 4 \times 10^{-4}$ and $\sigma = 1 \times 10^{-4}$ (left) and for $\sigma = 2 \times 10^{-4}$ (right) as a function of T_e and λ_N with $\lambda_{T_e} = \frac{\lambda_N}{\sqrt{\gamma_e - 1}}$

turbulence driven by each instability. Note that in numerical simulations, the averaging of fluctuation of T_e in sheath loss term for the pure interchange model can only be done in the poloidal direction, i.e $\exp\left(\Lambda - \frac{\phi}{\langle T_e \rangle_y}\right)$.

Let us start by mentioning that all types of simulations, regardless of the driving instability, exhibit high amplitude structures of density, potential and temperature (in anisothermal cases) reminiscent of the so-called blobs observed in experiments. Nevertheless, the characteristics of these structures change with the model and as a function of the main parameters (g, σ and ζ).

In order to discriminate the intermittent structures we proceed to a conditional averaging for all fields f (density, temperatures and electric potential), where we consider only the fluctuating part of the events of high amplitude compared to the mean field, defined in (3.12) where i_{cond} is a conditional value, and where $\sigma_N(x)$ is the standard deviation of density in time and space for a given radial position x. In the following we take $i_{\mathrm{cond}} = 2$.

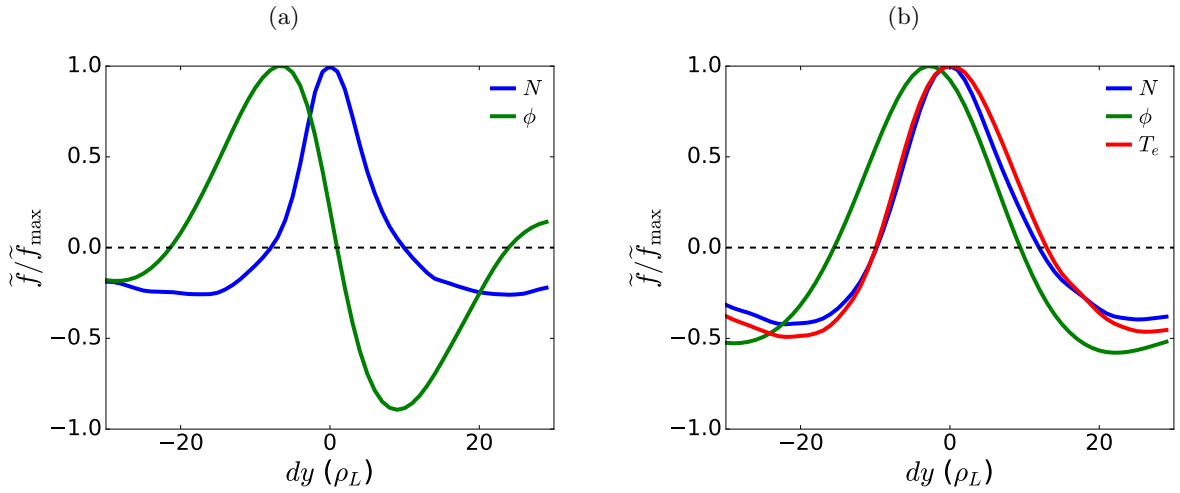

Figure 3.5: Conditional averaging of the intermittent structures of density, potential and electron temperature normalized by their maxima for isothermal (**a**) and T_e (**b**) simulations

$$\begin{cases} \widetilde{f}_{i_{\text{cond}}}(t,x,y) = f(t,x,y) - \langle f(t,x,y)\rangle_{t,y} \text{ for } (x,y,t) : N(t,x,y) \geq \langle N(t,x,y)\rangle_{t,y} + i_{\text{cond}}\sigma_N(x) \\ \widetilde{f}_{i_{\text{cond}}}(t,x,y) = 0 \text{ elsewhere} \end{cases} \tag{3.12}$$

For a given radial position, each event, or blob, can be defined by its temporal and poloidal position $(t_b,\, y_b)$ corresponding to the local center of mass of $\widetilde{N}_{i_{\text{cond}}}$. On Fig. 3.5 the averaged fields on all blobs at the radial position $x = 70\rho_L$ on poloidal extend of $30\rho_L$ on both sides of the maxima are reported for isothermal and T_e model. The shape of such averaged structure shows two main differences between the two models: larger structures in the anisothermal-T_e, and a clear re-correlation of the density and potential fluctuations. We can also note that the structures of density and temperature coincide almost perfectly.

Now in order to characterize the poloidal spatial scale of each intermittent structure, we first operate the conditional averaging defined previously, and restrict our interest to the radial position where the turbulent structures are fully developed (here $x = 70\rho_L$). Then the blob poloidal size is estimated by the autocorrelation length, denoted L_{ac} and defined as the width at half maximum amplitude of the autocorrelation function (3.13) on a poloidal extend of $30\rho_L$ on both size of blob position:

$$\forall\,(t_{\text{b}}, y_{\text{b}})\,,\, f_{\text{auto}}(\tau) = \int_y \widetilde{N}_{i_{\text{cond}}}(t_{\text{b}}, y)\,\widetilde{N}_{i_{\text{cond}}}(t_{\text{b}}, y+\tau)\,y \tag{3.13}$$

On Fig 3.6 the probability density function (PDF) of the autocorrelation length, L_{ac}, is reported for the 4 types of simulation: isothermal, T_e, and both SCW and interchange reduced model. We observe that the most represented spatial scale in anisothermal simulation is larger ($\approx 10\rho_L$) than in the isothermal simulation ($\approx 8\rho_L$). In light of the linear analysis, this difference is likely to be due to the SCW instability, as it is the one destabilizing large scales, when the interchange instability

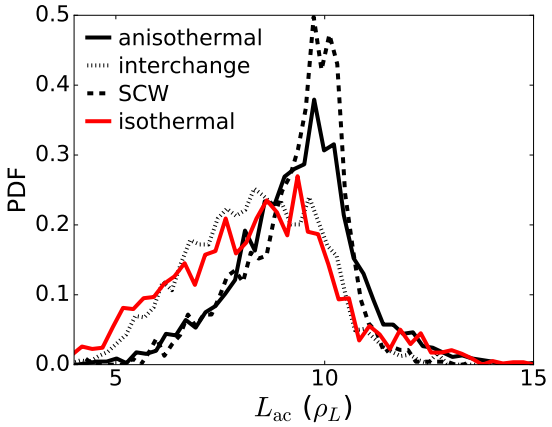

Figure 3.6: PDF of poloidal autocorrelation length of density fluctuations at the radial position $x = 70\rho_L$ for -T_e, pure interchange, pure SCW and isothermal simulations for $g = 8 \times 10{-}4$, and $\sigma = 1 \times 10^{-4}$

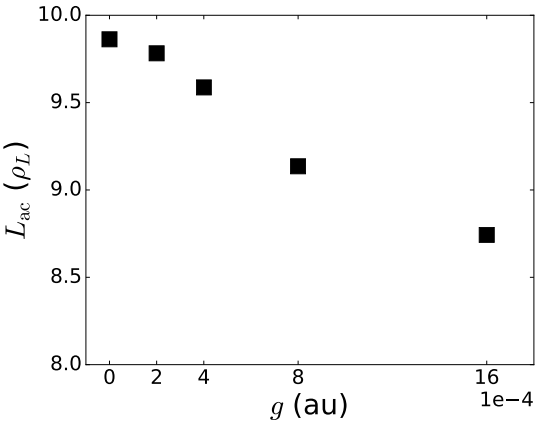

Figure 3.7: Averaged autocorrelation length in anisothermal simulation as a function of g for $\sigma = 1 \times 10^{-4}$

destabilizes even smaller scales in the anisothermal system than in the isothermal one. Indeed, the spatial scales distribution of the anisothermal-T_e system presents a similar shape as the one of the pure SCW simulation, even though the peak around $10\rho_L$ has a lower amplitude. On the contrary, the distribution for the pure interchange simulations coincides almost exactly with the one of the isothermal simulation. We conclude that the SCW has a stronger impact on spatial scales distribution, even though for this value of parameters $g = 8 \times 10^{-1}$, $\sigma = 1 \times 10^{-1}$ and $\overline{T_e} \approx 1$, $\gamma_{\rm max,int}$ is 1.5 times higher than $\gamma_{\rm max,SCW}$. This is in agreement with the results found in the reference [Sarazin 98], which proposes that the inverse cascade of energy excites large scales of turbulence. As a consequence, the size of turbulent structures is mostly determined by the value of the smallest unstable poloidal mode, and thus determined by the SCW instability.

Besides, if we look at the variation of the mean value of $L_{\rm ac}$ Fig 3.7, somehow representative of the relative weight of the two types of distribution, we see that the mean $L_{\rm ac}$ decreases with the increase of g, namely with increasing $\gamma_{\rm max,int}/\gamma_{\rm max,SCW}$, confirming that the SCW instability is the one which triggers the destabilisation of the larger scales. The $L_{\rm ac}$ variation with ζ is in agreement with this conclusion, but is not reported as less significant due to the fact that in this range of T_e the ratio $\gamma_{\rm max,int}/\gamma_{\rm max,SCW}$ does not exhibit important variations.

Another noticeable difference in non-linear simulation is that the addition of T_e fluctuations triggers a re-correlation between density and potential fluctuations. This characteristic is estimated by the relative phase shift between potential and density turbulent structures denoted $\delta_{N/\phi}$, here no conditional averaging is operated, however the results are in agreement with the conditional averaging results. The phase shift is defined as the arc-cosine of the correlation coefficient of $\widetilde{N}$ and $\widetilde{\phi}$:

$$\delta_{N/\phi} = \arccos\left(\frac{\left\langle \widetilde{N}\widetilde{\phi}\right\rangle_{y,t}}{\left\langle \widetilde{N}^2\right\rangle_{y,t}^{1/2}\left\langle \widetilde{\phi}^2\right\rangle_{y,t}^{1/2}}\right) \tag{3.14}$$

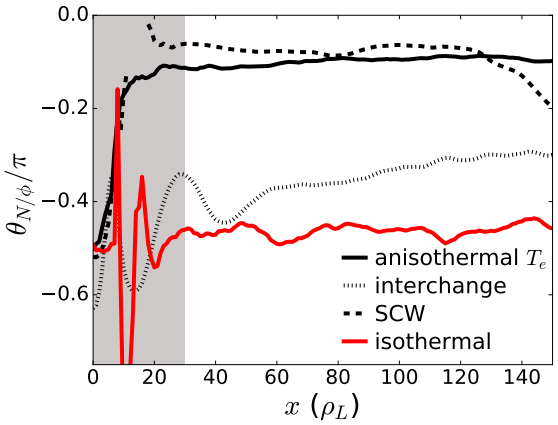

Figure 3.8: Radial profile of $\delta_{N/\phi}$ for isothermal, T_e , pure interchange , and pure SCW simulations, for $\sigma = 1 \times 10^{-4}$, $g = 8 \times 10^{-4}$, $\zeta = 5$. The radial extent where the turbulence is fully developed in all type of simulations is depicted by the white area, whereas the grey zones correspond to the zone of influence of the source

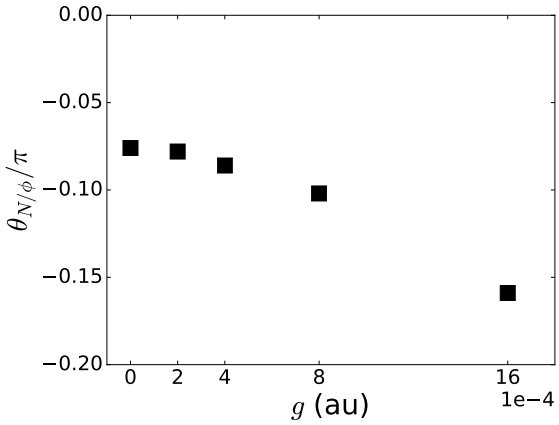

Figure 3.9: Averaged phase shift in anisothermal simulation the radial extent [40,125] as a function of g for $\sigma = 1 \times 10^{-4}$

Isothermal simulations present the typical phase shift of the interchange instability $\delta_{N/\phi} = \frac{\pi}{2}$, when in simulations we find $\delta_{N/\phi} \approx 0.1 - 0.15\pi$, Fig. 3.8. If we look at simulations driven by only one instability, we note that the phase shift for the full system is almost equal to the one of the SCW instability $\delta_{N/\phi} \approx 0.1\pi$ and the one of the pure interchange simulation is closer to the one of the isothermal system $\delta_{N/\phi} \approx 0.35 - 0.4\pi$. Once again the re-correlation of density and potential fluctuations can be attributed to the addition of the SCW instability, this result is the one expected in regard with the result of the linear analysis. Besides by varying g, i.e the relative importance of the two instabilities, we find that $\delta_{N/\phi}$ increases as $\gamma_{\max,\text{int}}/\gamma_{\max,\text{SCW}}$, i.e. increases with g, and thus the phase shift is an instability-weight marker. As for L_{ac} variation with ζ are not significant due to a weak variation of $\gamma_{\max,\text{int}}/\gamma_{\max,\text{SCW}}$ in the range of parameters considered and are not reported on the plot.

Another important result from the conditional averaging Fig. 3.5, is that electron temperature structures, and even more so electron energy structures, coincide with the ones of the density. This result is confirmed by the low phase shift between density estimated with this method: $\delta_{N/T_e} \leq 0.05\pi$ for all the studied parameters. Thus, in this regime, the energy is transported by the fluctuation of density.

The non-local intermittent transport translates into a broadened PDF[1] of the particle turbulent flux which is positively skewed. The turbulent flux of particle, defined as $\Gamma_{N,\text{turb}} = -\widetilde{N}\partial_y\widetilde{\phi}$, is characterized by the superimposition of a Gaussian centered on zero corresponding to a diffusive-like transport and a log-normal distribution for the tails corresponding to the intermittent bursts, responsible for the largest part of the particle transport [Sarazin 03]. On Fig. 3.10 a., we observe a significant reduction of the PDF tail between isothermal and T_e simulation. The positive skewness (i.e. the third standardized statistical moment) is reduced within a ratio comprised between 1.5 and 2.5 depending

[1]Note that the x-axis is normalized by the standard deviation, the PDF integral is thus not equal to one

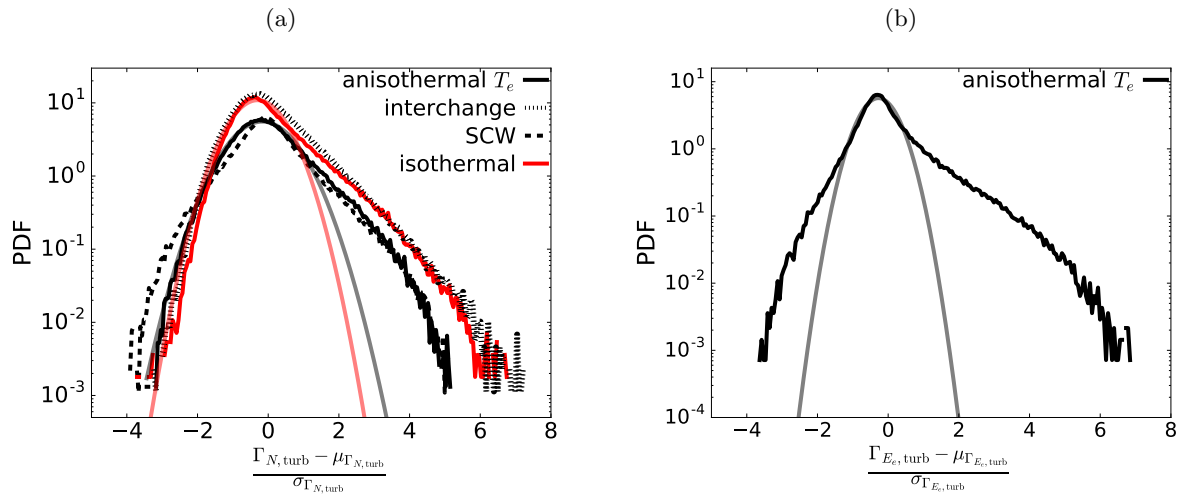

Figure 3.10: PDF of particle turbulent flux (**a**) and of energy turbulent flux (**b**) for T_e, pure interchange, pure SCW and isothermal simulations, a Gaussian fit of the PDF is reported in transparent for anisothermal-T_e and isothermal simulations. PDF are reported in log scale, centered on zeros, normed by standard deviation

on the radial position (Fig 3.11) b. The decrease of the skewness for $\Gamma_{N,\text{turb}}$ could be linked to the reduction of $\delta_{N/\phi}$, that was proved as one of the reasons for this asymmetry [Carreras 96]. This seems to be confirmed by the shape of the PDF of the reduced models, indeed the PDF of the interchange reduced simulations, presenting a quasi phase quadrature between density and potential fluctuating parts, is close to the one of isothermal simulations, with similar skewness $\gamma_{\Gamma_{N,\text{turb}}} \in [1, 1.5]$. On the contrary, shape of the PDF in the reduced SCW simulations is close to the one of the anisothermal, with lower skewness $\gamma_{\Gamma_{N,\text{turb}}} \in [0.3, 0.7]$, in agreement with the lower phase shift between density and potential fluctuations.

The fluctuation level of $\Gamma_{N,\text{turb}}$ is higher in the T_e simulation Fig. 3.11 a. compared to isothermal simulation, and the fluctuation level of the full model is comprised between the one of the two models. Note that once again the fluctuation level of the pure interchange simulation is close to the one of the isothermal simulation.

Now, the PDF of radial turbulent flux of the electron energy $\gamma_{Ee,\text{turb}} = -\frac{3}{2}\widetilde{P_e}\partial_y\widetilde{\phi}$ for the T_e simulation exhibits a longer tail of the distribution than the ones of $\Gamma_{N,\text{turb}}$. This can be explained by the fact that the fluctuations of N and T_e coincide almost, so that the co-occurrence of two rare events of N and T_e will be even further in the tail considering the transport of energy. This feature of the transverse transport is really important to keep in mind when talking about the problematics of plasma facing components. In the case of an intermittent non-local transport, the time averaged heat foot-print is not representative of the extreme and rare events that the PFC has to face up, and which can drastically reduce the time life of the components.

To summarize this section two main conclusions can be drawn:

- The SCW instability plays a predominant role in the turbulence features and seems to be the one setting the turbulence scales, and the re-correlation between density and potential fluctuations.

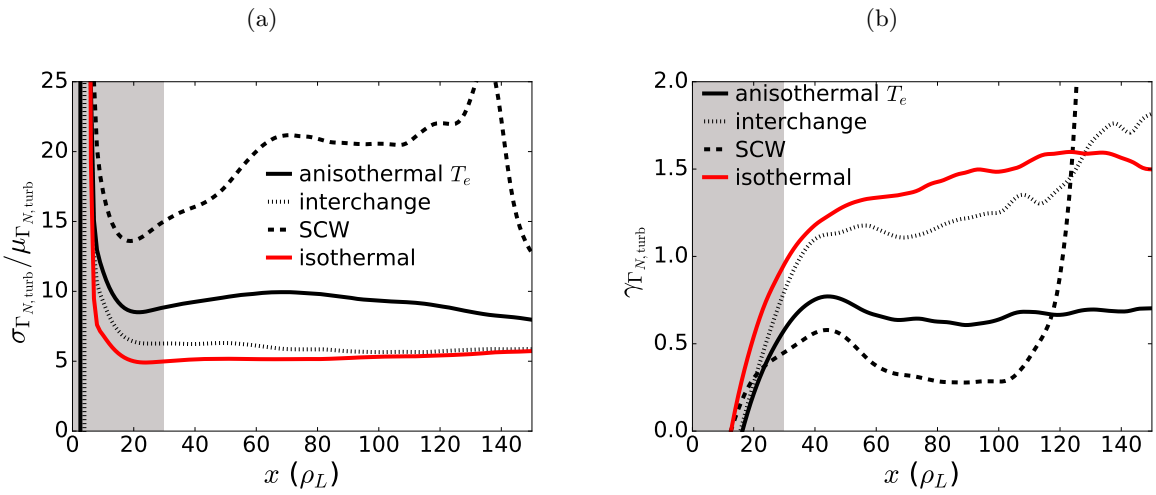

Figure 3.11: Radial profile of the fluctuation level (**a**) and skewness (**b**) of particle turbulent flux for T_e, pure interchange, pure SCW and isothermal simulations, the source area is colored in grey

- The intermittent structures of density and temperature coincide, and so T_e or P_e fluctuations present the same features as the ones of density leading larger intermittency for the energy flux than for the particle flux.

3.3.3 Heat turbulent transport: a non-linear superimposition of the two instabilities

In the previous section we have shown that the addition of electron temperature fluctuations have a significant impact on the turbulence features. As in Tokam2D, the turbulence is responsible for more than 90% of the transport, one can expect an impact on the time-averaged radial transport.

In order to compare the transport in isothermal and T_e model, we first look at the density radial profiles. The most striking impact of T_e fluctuations can be observed on the shape of the density profile represented in log scale Fig. 3.12a. For isothermal simulations we obtain a purely exponential profile, whereas for anisothermal-T_e simulations exhibits slope variations. This is also found on other field profiles: P_e, T_e, ϕ. This feature can be explained by the existence of a poloidal shear flows $\partial_x^2 \langle\phi\rangle_{y,t}$ in anisothermal-T_e simulations, created by the presence of non constant T_e gradient, and as the sheath condition imposes $\langle\phi\rangle_y \approx \langle\Lambda T_e\rangle_y$, the averaged shear is likewise non-zero Fig. 3.12b. As mentioned earlier, this shear flow creates a channel for energy transfer between turbulence and mean flow, the shear flow impacts turbulence and consequently the profile, which explains the presence of slope variations. The correlation between the averaged shear and the flux profile is clear, indeed slope variations of density profile appears at the same radius as the shear extrema indicated by a black marker on the anisothermal-T_e radial density profile.

Even though we have underlined the intermittent feature of the turbulent transport, the radial transport is summed up, here, to the single value of SOL width, representative somehow of an averaged transport. The SOL width of a field f is defined as the e-folding length of the time and poloidal

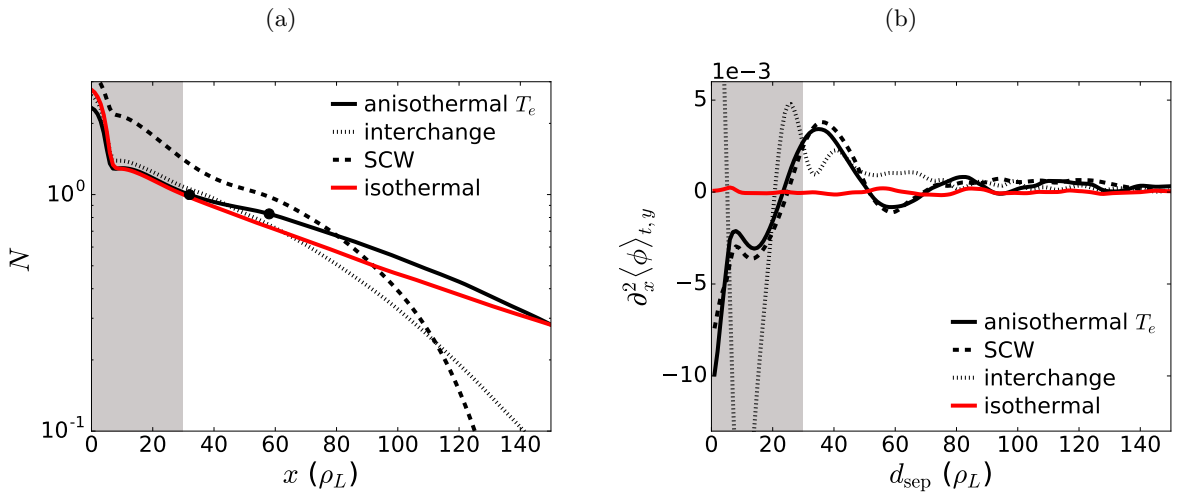

Figure 3.12: Radial profiles of density (in log-scale) (**a**) and $\partial_x^2 \langle\phi\rangle_{y,t}$ (**b**) for T_e, pure interchange, pure SCW and isothermal simulations. The source area is colored in grey

averaged radial profile $\langle f \rangle_{t,y}$, denoted λ_f, and estimated by the least squares regression on the radial extent $x \in [30, 150]$ where turbulence is fully developed.

As for turbulence characteristics, the linear analysis permits to have an insight in the mechanisms likely to dominate the non-linear dynamics according to the gradient removal theory (GR) [Ricci 09, Ricci 13]. This theory permits to link the growth rate of a linear mode to the SOL width. The fundamental assumption is that the saturation of the turbulence occurs when the local flattening due to the perturbation counterbalances the background density gradient, that is to say $k_x \widetilde{N} \sim \widetilde{N}/\lambda_N$. The following steps and hypothesis permits to obtain the relationship (3.15) linking the growth rate of the dominating mode and the particle SOL width.

- the balance between the parallel losses and the radial transport gives $\partial_x \Gamma_x \sim \Gamma_x/\lambda_N \sim \frac{\overline{N}}{c_s \sigma}$, with Γ_x the turbulent flux $\Gamma_x = N \partial_y \phi \sim k_y \widetilde{\phi} \widetilde{N}$;
- the leading order of the density equation, i.e $\partial_t N = [N, \phi]$, gives an additional relationship between $\widetilde{\phi}$ and gives $\gamma \widetilde{N} \sim \overline{N}/\lambda_N k_y \widetilde{\phi}$ which permits suppressing $\widetilde{\phi}$ in the radial turbulent flux;
- Finally it is assumed that $k_x \sim \sqrt{k_y/\lambda_N}$, as proposed by the Refs. [Mosetto 13, Mosetto 15, Ricci 13] in non-local linear-theory for interchange instability. Note that, here, we take the same assumption for the SCW instability. This is justified by the fact such instability can be seen as a drift-wave like mechanism following $k_x \sim \sqrt{k_y/\lambda_N}$ in non-local linear-theory.

$$\lambda_N \sim \frac{1}{c_s \sigma} \left(\frac{\gamma}{k_y} \right)_{\max} \tag{3.15}$$

On Fig. 3.13a. we report the SOL width estimate based on the gradient removal theory for the different reduced models, and the SOL width found in numerical simulations for different values of g. The scaling on SOL width as a function of g shows that the gradient removal theory estimates correctly the increasing trend of λ_N with g for both isothermal and the T_e models. However, the λ_N value is not exactly predicted: for the isothermal model the ratio between the linear theory and the non-linear

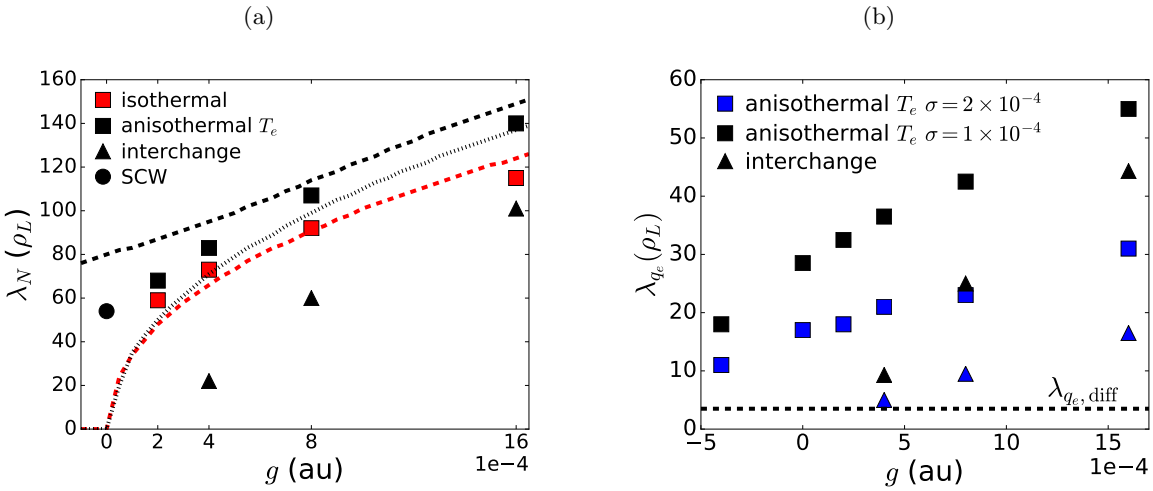

Figure 3.13: (**a**): Density SOL width λ_N as a function of g for $\sigma = 1 \times 10^{-4}$ estimated by the gradient removal theory for the isothermal (red dashed line), interchange (dot black line), and anisothermal-T_e (black dashed line) models, and estimated from non-linear simulations (marker). (**b**): Power SOL width λ_{q_e} as a function of g for $\sigma = 1 \times 10^{-4}$ and $\sigma = 2 \times 10^{-4}$ in non-linear simulations for the interchange, SCW and anisothermal-T_e models, the estimated value for pure diffusive transport is reported by a black dashed line

simulation results stays relatively low with a relative error below 17%. For the anisothermal-T_e model, λ_N from the non-linear simulations shows a negative offset in comparison with the linear prediction, the absolute value of the relative errors decreases with g from more than 20% for $g = 2 \times 10^{-4}$ down to less than 10% for $g = 16 \times 10^{-4}$. Now if we look at the reduced models, in both type of non-linear simulations the SOL width is significantly smaller than the one predicted by the GR theory, with a relative error of more than 30% in both case. For both reduced model, SOL widths from numerical simulations exhibit greater discrepancy with the GR prediction than in the T_e model, which seems to point out that the global transport results from a non-linear interaction between the two instabilities. Thus, the rather correct estimate from the gradient removal theory in anisothermal-T_e simulations could be fortuitous as it seems that non-linear interactions plays a role in the radial transport.

In conclusion even though the gradient removal theory predicts correctly the trends of the SOL widths, non-linear effects seem to have an important role so that this theory will not be sufficient in itself to give a robust prediction of the SOL width. Moreover, we have shown that both instabilities contribute to the radial transport.

The heat radial transport is characterised in the non-linear simulations by the power e-folding length λ_q, with $q_{\parallel,e} = \gamma_e \sigma c_s P_e \exp(\Lambda - \phi/T_e)$. On Fig 3.13b. λ_q is reported as a function of g and for $\sigma = \sigma_{\mathrm{SOL}}$ and $\sigma = \sigma_{\mathrm{PFR}}$ for the 3 models. We first note that, as for λ_N, power e-folding lengths of the pure interchange and pure SCW simulations, respectively $\lambda_{q,\mathrm{int}}$, and $\lambda_{q,\mathrm{SCW}}$ ($g = 0$), are both smaller than the one of the anisothermal-T_e simulation, so the two instabilities are contributing to the global heat transport. Besides $\lambda_{q,\mathrm{int}}$ and $\lambda_{q,\mathrm{SCW}}$ are also significantly larger than the power e-folding length estimated for a pure diffusive simulation $\lambda_{q,\mathrm{diff}} \approx 5\rho_L$, so their turbulent transport is

efficient. For $\sigma = 1 \times 10^{-4}$, one or the other instability is dominating depending on g, for $g = 4 \times 10^{-4}$ $\lambda_{q_e,\mathrm{SCW}} > 2 * \lambda_{q_e,\mathrm{int}}$, for $g = 8 \times 10^{-4}$ $\lambda_{q_e,\mathrm{SCW}} \approx \lambda_{q_e,\mathrm{int}}$ and for $g = 16 \times 10^{-4}$ $\lambda_{q,\mathrm{SCW}} < \lambda_{q,\mathrm{int}}$, however for $\sigma = 2 \times 10^{-4}$ the SCW instability dominates ($\lambda_{q_e,\mathrm{SCW}} > \lambda_{q_e,\mathrm{int}}$) the heat transport for any value of g, thus as predicted by the linear analysis, the SCW instability is expected to have a greater relative weight in the divertor region. Furthermore, the ratio $\lambda_{q_e,\mathrm{int}}/\lambda_{q_e}$ is smaller in simulation with $\sigma = 2 \times 10^{-4}$ than in the one $\sigma = 1 \times 10^{-4}$, reinforcing the previous conclusion.

Actually for both σ_{SOL}, and σ_{PFR}, even with a negative curvature ($g = -4 \times 10^{-4}$) the SCW instability drives turbulence with a λ_q well above $2\lambda_{q,\mathrm{diff}}$. With our simplified model, the ratio of transport between the internal and the external legs of the divertor $\lambda_{q,g=4\times10^{-4}}/\lambda_{q,g=-4\times10^{-4}}$ (for both value of σ) would be smaller than 2.

In conclusion, if the turbulence features are strongly influenced by the characteristics of the SCW instability, probably due to an important inverse cascade toward the low k_y mode, the turbulent transport seems to by driven from an interplay between the two instabilities, and both contribute to the transport.

Let us also mention, here, that we could have chosen for the reduced interchange model to take the averaged of electron temperature in all sheath loss terms, that is to say also for the equation on density and electron energy Eq (3.1) and (3.3). The reduced model has been run, the turbulence features of such reduced interchange model are qualitatively the same as the model presented in this section. However, the SOL widths were significantly impacted. This can be explained by the impact of the average on the amplitude of the sheath loss terms. Indeed, if we compare the amplitude of the particle parallel losses in anisothermal-T_e simulations: 1) without averaging on T_e, $\Gamma_{N,\parallel} = \sigma c_s N \exp(\Lambda - \phi/T_e)$, and 2) with averaging, $\Gamma_{N,\parallel,*} = \sigma c_s N \exp(\Lambda - \phi/\langle T_e \rangle)$, we find $\Gamma_{N,\parallel}/\Gamma_{N,\parallel,*}$ varies between 2 and 6 depending on the radius due to the phasing between ϕ and T_e. Hence, the inclusion of T_e fluctuations in the sheath loss term has not only an impact on the cross-field dynamic but also on the amplitude of the parallel losses.

SCW instability: a potential player in the divertor region or in start-up L-mode plasma

In this section we have shown that the SCW instability contributes substantially to the heat turbulent transport. However, the reduced 2D-fluid model does not take into account the effect of the strong magnetic shear in the X-point region that would prevent the sheath instability to propagate into the main SOL [Ryutov 04]. Hence, it is unlikely that such instability could play a role in the main SOL of a diverted plasma.

Nonetheless, it could play a role in start-up L-mode limited plasma and also on the turbulence in the divertor region. In particular, it could be of interest in the study of the spreading factor S [Eich 11], as suggested in Refs. [Ryutov 04, Myra 97]. Indeed, it provides an additional mechanism to spread the heat flux in the divertor region and thus reducing the heat loads which is also a key factor for the heat flux exhaust problematics. Moreover, contrary to the interchange instability, the SCW instability would be unstable on both divertor legs and our simulations predict a ratio of only 2 between the SOL widths of inner and outer legs.

3.4 Turbulent heat transport in the presence of ion temperature dynamics

Fluid codes historically used the cold ions hypothesis based on the idea that the ions were motionless in comparison to electrons due to their higher inertia. Furthermore, in the SOL, the potential follows the electron temperature, thus it was expected to have a greater impact on turbulence features. However experimental measurements show that the ion temperature is systematically higher than the electron temperature in the edge plasma [Kočan 11], and T_i/T_e even reached 10 for some tokamaks. Thus, the inclusion of finite ion temperature is required to describe properly the turbulence in the edge plasma. Moreover, the ion temperature dynamics has been recently a field of interest in the edge plasma turbulence and it has pointed out that the inclusion of finite ion temperature in the model impacts the seeded blob dynamics [Bisai 13, Olsen 16, Jovanović 08, Madsen 11]. In this section, we study the impact of the addition of self-consistent T_i fluctuations first on the linear stability of the model, then on the turbulence characteristics and heat transport. A special focus is devoted to the contribution of the inclusion of T_i in the vorticity term, which is shown to play a critical role in the model.

3.4.1 Linear damping of small spatial scales in the presence of finite ion temperature effect

The linear analysis shows that the inclusion of self-consistent fluctuations of ion temperature does not trigger any supplementary instability in our 2D-model. Indeed, the growth rate falls to negative value when the destabilizing terms of interchange and SCW instabilities are set to zero.

The principal linear impact of the addition of T_i fluctuations is to damp more efficiently the small scales (large k_y) Fig. 3.14a. Indeed, the growth rates of both full anisothermal and anisothermal-T_e models are quasi-equal for $k_y < 0.15\rho_L^{-1}$, but for $k_y > 0.2\rho_L^{-1}$, $\gamma_{\max}$ decreases drastically faster in the full anisothermal model. The unstable mode of largest k_y is about $0.5\rho_L^{-1}$ for the full anisothermal model compared with more than 1 for the anisothermal-T_e model. In consequence, the impact on the growth rate of interchange instability (destabilizing large k_y) is more important than for SCW instability (destabilizing small k_y) (results not reported here). Concerning the linear phase shift between density and potential fluctuations, Fig. 3.14b, the impact of T_i fluctuations is to increase its amplitude for $k_y > 0.1\rho_L^{-1}$, and the absolute value of the phase shift of the most unstable mode is about to 0.45π in the full anisothermal model compared to 0.3π in anisothermal-T_e model.

The linear analysis also points out that the inclusion of finite ion temperature in the vorticity expression is the dominant contribution when considering the role of the ion temperature inclusion as it will be re-discussed later in the section. Indeed, if one considers the two following intermediate models:

- anisothermal-T_e GV (for Generalized Vorticity): model taking into account the finite ion temperature in the vorticity expression but no T_i fluctuations, i.e. T_i = constant and $W = \nabla_\perp^2\phi + \nabla\cdot(T_i\nabla\ln N)$;
- full anisothermal SV (for Simplified Vorticity): model taking into account T_i fluctuations but not the finite ion temperature in the vorticity expression but no T_i fluctuations, i.e. T_i = fluctuating and $W = \nabla_\perp^2\phi$;

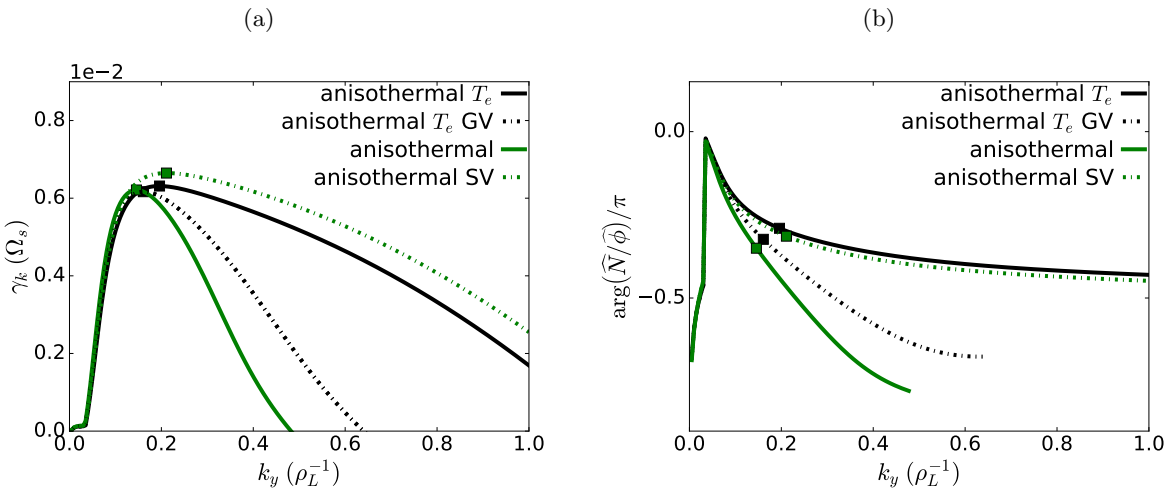

Figure 3.14: (**a**) Linear growth rate and (**b**) linear phase shift between density and potential fluctuations for the full anisothermal, full anisothermal SV, anisothermal-T_e model, and anisothermal-T_e GV model for $\sigma = 1 \times 10^{-4}$, $g = 4 \times 10^{-4}$, and $\lambda_N = \left(\sqrt{\gamma_e} - 1\right)\lambda_{T_e} = \left(\sqrt{\gamma_i} - 1\right)\lambda_{T_i} = 30\rho_L$ s a function of the mode number k_y and for $k_x = 0$. Linear phase shift is reported only for mode presenting a positive growth rate

one finds that the anisothermal-T_e GV model presents the same impact as the full anisothermal model on both the linear growth rate and the phase shift, even though the effects are less marked. On the contrary, the full anisothermal SV presents similar growth rate and the phase shift as the anisothermal-T_e model. Thus, the inclusion of finite ion temperature in the vorticity expression is the dominant additional contribution between in the linear stability of the full anisothermal and anisothermal T_e model.

The scan of T_i, presented on Fig 3.15, shows that the increase of T_i damps more efficiently small scales, thus favors large scales, and yields to a larger of linear phase shift between N and ϕ.

3.4.2 Highly intermittent turbulence in the presence of finite ion temperature

On Fig. 3.16a) the typical blob shape for full non-linear simulation with $\zeta_i = 3$ (where ζ_i is the normalized thermal energy carried by one ion) at $x = 70\rho_L$ is reported. The anisothermal simulation with $\zeta_i = 3$ are the one comparable to the anisothermal-T_e with $T_{i,0} = 1$ as $T_i \approx 1$. The typical size of the structure is the same for both models, result also confirmed by the PDF of the blob size (not reported here). This reinforces the assumption that the inverse cascade favors the modes of lowest k_y, as the linear stability of both models coincides only for low k_y, that is to say the ones setting the poloidal spatial scales under the assumption of an inverse cascade. Nonetheless, a strong damping of small spatial scales, predicted by the linear analysis, is observable indeed in the far SOL in the full anisothermal model.

The absolute phase shift $|\delta_{N/\phi}|$ is also slightly larger in the full model in agreement with the linear analysis $\delta_{N/\phi} \approx 0.15\pi$, however such low phase shift is still a marker of the SCW instability, which seems to be also at play in the full anisothermal model.

Finally, it is worth noting that the structures of density and both temperature, $\widetilde{N}$, $\widetilde{T_e}$, $\widetilde{T_i}$ coincide

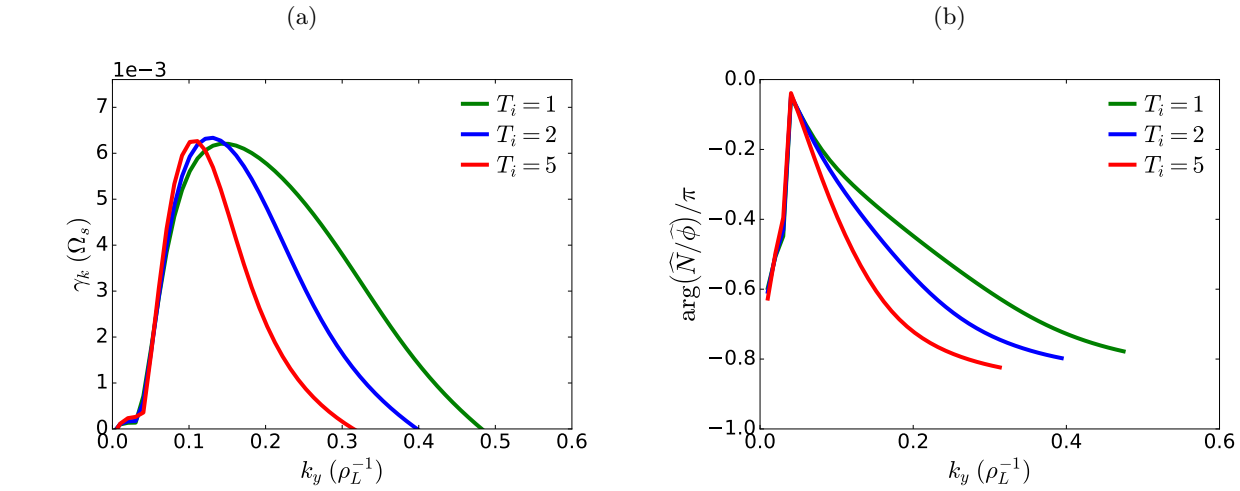

Figure 3.15: (**a**) Linear growth rate and (**b**) linear phase shift between density and potential fluctuations for the full model, for $\sigma = 1 \times 10^{-4}$, $T_e = 1$, $g = 4 \times 10^{-4}$, $\lambda_N = \left(\sqrt{\gamma_e} - 1\right) \lambda_{T_e} = \left(\sqrt{\gamma_i} - 1\right) \lambda_{T_i} = 30\rho_L$ and $T_i = 1, 2, 5$ as a function of the poloidal mode number k_y and for $k_x = 0$. The linear phase shift is reported only for mode presenting a positive growth rate

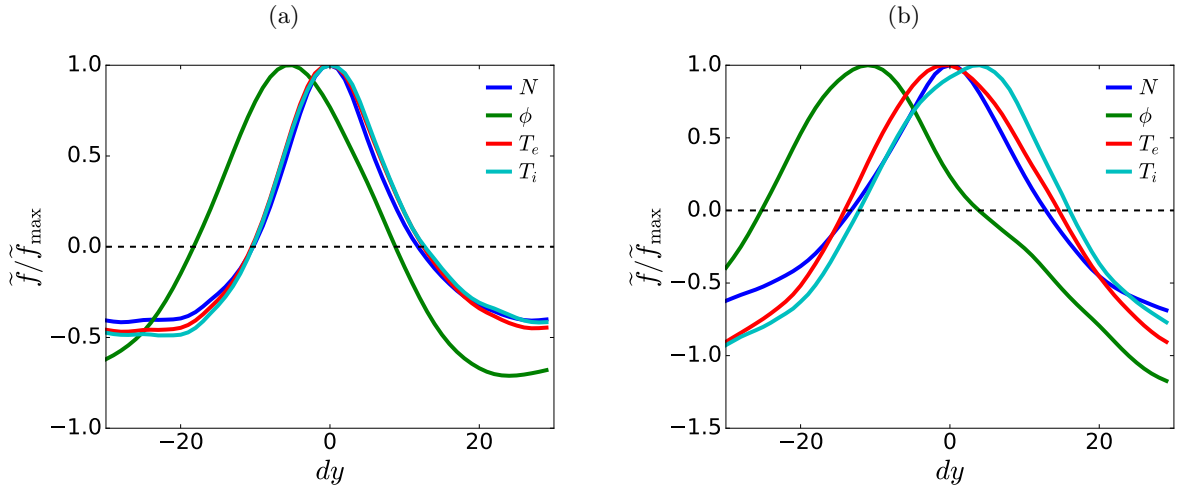

Figure 3.16: Conditional averaging of the intermittent structures of density, potential, electron and ion temperatures normalized by their maxima for simulations with $g = 8 \times 10^{-4}$, $\sigma = 1 \times 10^{-4}$, $\zeta_e = 5$, $\zeta_i = 3$ (a) and $\zeta_i = 10$ (b)

perfectly as for anisothermal T_e simulations.

The increase of T_i has a significant impact on the blob shape, as it can be observed when we compared the conditional averaging Fig 3.16 for $\zeta_i = 3$ (left) and $\zeta_i = 10$ (right). The scale of blobs increases with an elevation of T_i: the mean size of blobs is $11\rho_L$ for $\zeta_i = 10$ in comparison with $9.5\rho_L$ for $\zeta_i = 3$. The absolute phase shift increases also with the elevation of T_i, not only between $\widetilde{N}$ and $\widetilde{\phi}$. Note that, both features are in agreement with the prediction of the linear analysis Fig. 3.15.

Statistical properties:

The inclusion of the ion temperature dynamic impacts also the statistical distribution of the turbulent transport, as one can observe on the PDF[2] of the radial turbulent flux of the electron energy. For equivalent parameters, the full simulation presents a longer tail corresponding to the intermittent transport in comparison with the anisothermal-T_e one Fig 3.17. This corresponds to an elevation of the positive skewness by a ratio around 1.5 Fig 3.18b. It is important to underline that corresponding anisothermal T_e GV simulation presents the same shape as the full anisothermal simulation, even though the skewness is 20% smaller, while in the case of the full anisothermal SV model, the tail of the PDF (i.e the skewness) is significantly reduced (the PDF is not reported for readability purpose but this can be observed on the skewness Fig 3.18b). This result is coherent with the linear study which underlines that the inclusion of finite ion temperature in the vorticity expression is the dominant contribution when considering the ion temperature inclusion. In fact this is in agreement with the study one seeded blob [Olsen 16] which has shown that the inclusion of ion temperature dynamics does not affect the properties of the blob beyond this finite ion temperature effects.

Unlike the skewness, the level of fluctuation of Γ_{turb,E_e} is not significantly impacted by ion temperature dynamics, and is about 5 regardless of the anisothermal model considered Fig 3.18. This suggests that the addition of T_i favors extreme but rare events of outward energy transport as the mean fluctuation level is the same but nonetheless the extreme intermittent events are more represented. Moreover, this high intermittent feature is favored by the elevation of T_i, which impacts significantly the PDF of the fluxes. Indeed, for high ζ_i, i.e high T_i, the PDFs of Γ_{turb,E_i} exhibit a peaked shaped around the maximum of the PDF Fig. 3.16b. The higher the ion temperature, the steeper the peak. This peaked shape is characterised by a drastic increase of the kurtosis, representative of weight of the PDFs long tails. Hence, the increase of T_i further favors of the number of extreme outward burst transporting high amount of energy.

3.4.3 Enhancement of interchange driven mechanism in heat transport with finite ion temperature

3.4.3.1 Enhancement of the transport due to a non-linear mechanism

Considering the prediction of the SOL width from the gradient removal theory with the same assumptions as presented before, we would expect a rather weak impact of the ion dynamics on the SOL density width. However, this is not the case in non-linear simulation due to a greater discrepancy between linear prediction and non-linear simulation Fig 3.19. If the gradient removal theory predicts rather correctly the λ_N dependency on g in the anisothermal-T_e model, this is not the case for the

[2]Note that the x-axis is normalized by the standard deviation, the PDF integral is thus not equal to one

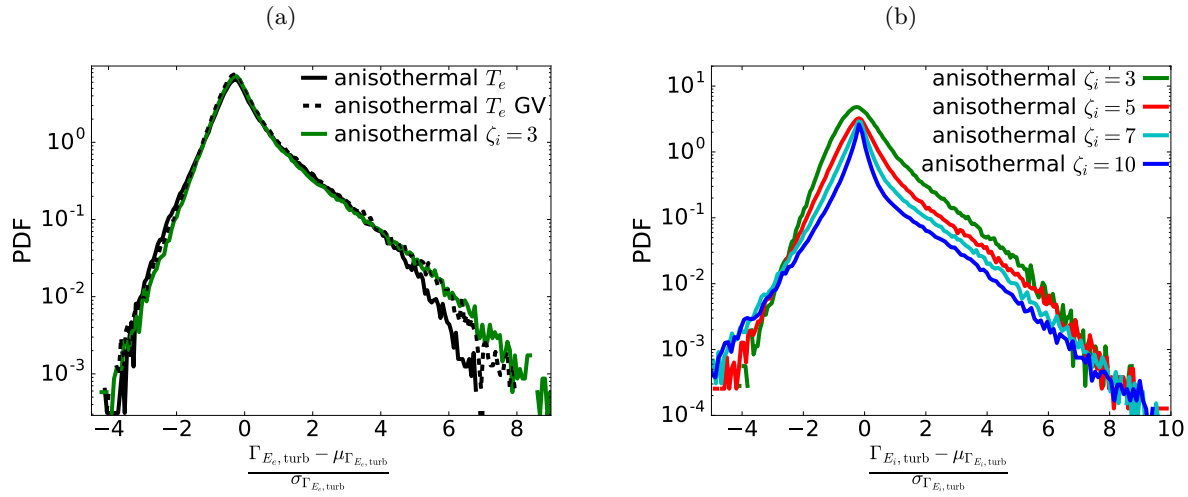

Figure 3.17: (**a**): PDF of ion energy turbulent flux for T_e, anisothermal-T_e GV and full anisothermal simulations. (**b**): PDF of ion energy turbulent flux for the full anisothermal simulations for $\zeta_i \in [3, 5, 7, 10]$. PDF are reported in log scale, centered on zeros, normalized by standard deviation

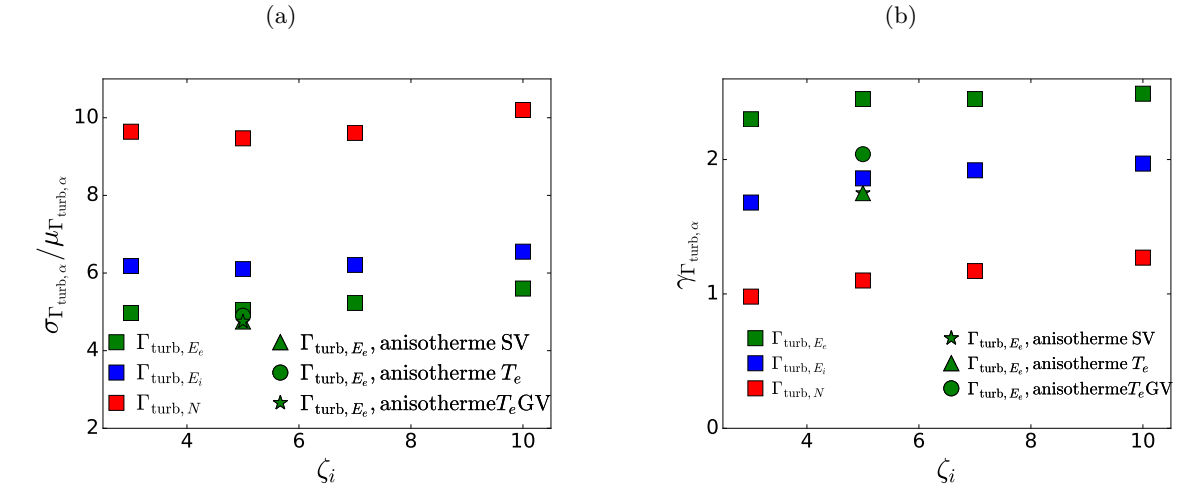

Figure 3.18: Averaged fluctuation level (**a**) and skewness (**b**)on the radial extent [30,150] in simulation as a function of $\zeta_i = 3$ for $\sigma = 1 \times 10^{-4}$ a,d $g = 8 \times 10^{-4}$ and for other reduced anisothermal models

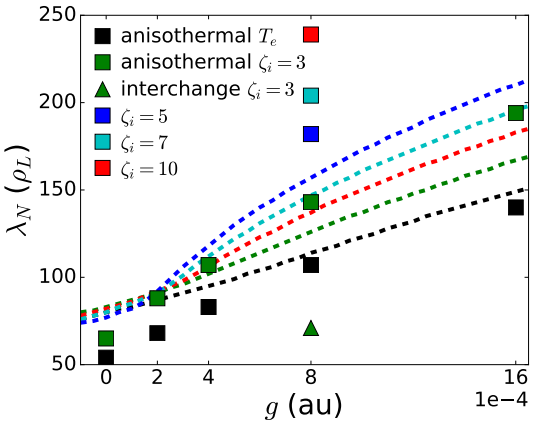

Figure 3.19: Density SOL width λ_N as a function of g for $\sigma = 1 \times 10^{-4}$ estimated by the gradient removal theory for T_e, anisothermal full model with T_i values corresponding to the simulation $\zeta_i = 3, 7, 5$ and 10 and estimated from non-linear simulations

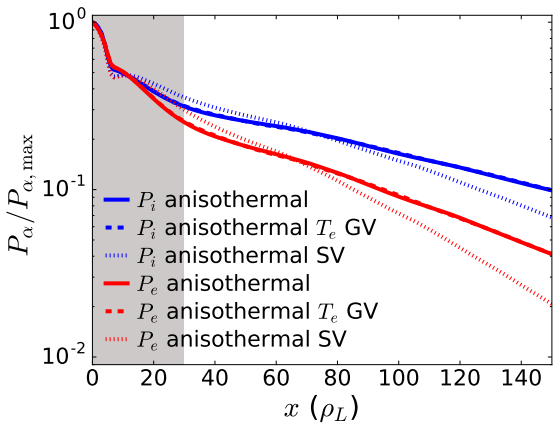

Figure 3.20: Ion and electron pressure radial profile for full anisothermal, anisothermal-T_e GV and anisothermal SV non-linear simulations with $g = 8 \times 10^{-4}$ and $\sigma = 1 \times 10^{-4}$

full model. Indeed, the gradient removal theory significantly underestimates the λ_N dependency on g: $\lambda_N \approx \lambda_{N,\mathrm{SCW}} + 10g$ in the linear theory against $\lambda_N \approx \lambda_{N,\mathrm{SCW}} + 20g$ in non-linear simulations.

This discrepancy can be explained by the addition of complexity in the model, we have already found that the predictions were more satisfying in the isothermal model, with both qualitatively and quantitatively agreements, than in the anisothermal-T_e model, where only qualitative trends were retrieved. Here, the non-linear results digress even more from linear theory.

Hence, if the shape of turbulent structures is, at least partly, shaped by the linear stability of the system, the prediction of the SOL width based on the linear stability seems to be too imprecise for experimental predictions as the transport results from non-linear interactions. Note that this is coherent with the fact that the simulations including T_i present statistical properties corresponding to highly intermittent transport (high skewness, and kurtosis).

In particular, here, the increase of the positive dependence between λ_N and g suggests that the finite ion temperature effect favors the transport driven by the interchange instability via a non-linear phenomenon. Another argument for this is that in non-linear simulation, λ_N is larger in the full anisothermal model for $g = 8 \times 10^{-4}$ ($\lambda_{N,\mathrm{int}} = 71\rho_L$) than the in anisothermal-T_e one ($\lambda_{N,\mathrm{int}} = 55\rho_L$), even though the linear prediction is the same for the two models ($\lambda_N \approx 100\rho_L$).

3.4.3.2 Predominant effect of the finite ion temperature inclusion

As shown in the results on linear analysis and statistical properties, the impact of ion dynamics are mainly attributed to the finite ion temperature inclusion in the vorticity expression. This result is also true for the turbulent transport. Let us consider two simulations: 1) a simulation with the full ion dynamic, 2) a simulation without ion temperature fluctuations but with the term of generalized vorticity and the same ion temperature profile of the first simulation. One can notice, on Fig 3.20, that both ion and electron pressure profiles match exactly for the two simulations. On the contrary, the

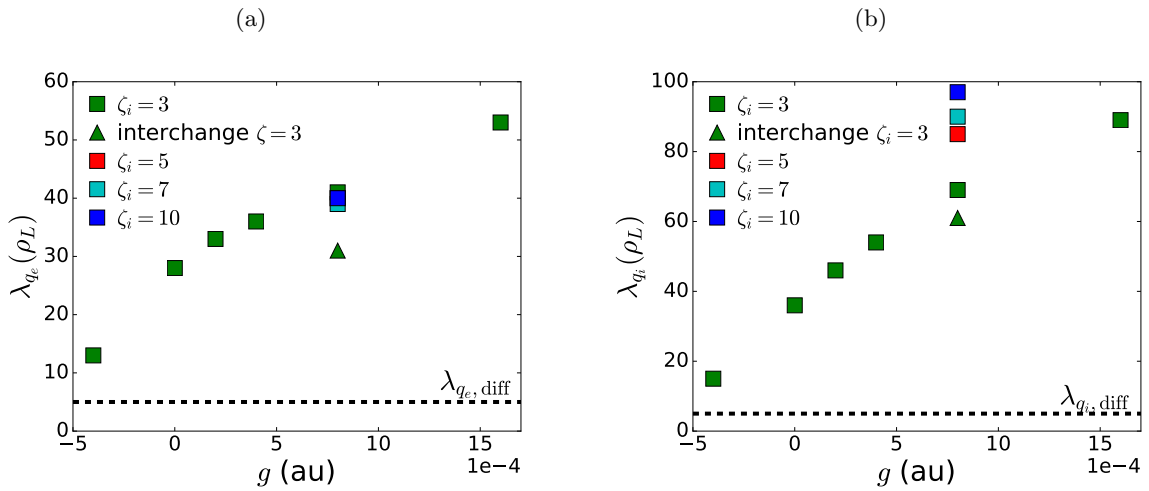

Figure 3.21: Power SOL width λ_{q_e} (**a**) and λ_{q_i} (**a**) as function of g for $\sigma = 1 \times 10^{-4}$ for interchange , SCW (i.e. $g = 0$) and full anisothermal simulation

profile of the corresponding simulation with T_i fluctuations but with simplified vorticity term presents a weaker transport (steeper gradient) than the two others.

Hence, one can conclude that the finite ion temperature in the generalized vorticity is the one triggering an increase of radial transport.

3.4.3.3 Heat transport

Now we can look at the transport of ion and electron energy characterised respectively by λ_{q_e} and λ_{q_i}, e-folding length of $q_{\parallel,e}$ and $q_{\parallel,i}$ with $q_{\parallel,i} = \gamma_i \sigma c_s P_i$. On Fig 3.21, λ_{q_i} and λ_{q_e} are reported as a function of g and for $\sigma = 1 \times 10^{-4}$ for the 3 models. As observed in anisothermal-T_e simulations power SOL width λ_{q_e} and λ_{q_i} of both reduced interchange and SCW simulations, respectively $\lambda_{q_\alpha,\mathrm{int}}$, and $\lambda_{q,\alpha\mathrm{SCW}}$ ($g = 0$), are both smaller than the one of the anisothermal simulation, so the two instabilities are contributing to the global heat transport. However, the ratio $\lambda_{q_e,\mathrm{int}}/\lambda_{q_e}$ for $g = 8 \times 10^{-4}$ is higher when ion dynamics is taken into account: $\lambda_{q_e,\mathrm{int}}/\lambda_{q_e} \approx 0.75$ against 0.6 in the anisothermal-T_e model. Moreover, $\lambda_{q_i,\mathrm{int}}/\lambda_{q_i} = 0.9$ is higher than the one for q_e thus interchange instability is even more important for the ion energy transport. This reinforces the conclusion on λ_N, that ion temperature dynamics triggers an increased transport driven by the interchange instability.

Nonetheless, $\lambda_{q_e,\mathrm{SCW}}$ and $\lambda_{q_i,\mathrm{SCW}}$ are also both well above the value of the pure diffusive e-folding length $\lambda_{q,\mathrm{diff}}$. The turbulence triggered by the SCW instability does not seem to be damped by the inclusion of ion dynamics, in fact $\lambda_{q_e,\mathrm{SCW,aniso}} > \lambda_{q_e,\mathrm{SCW,aniso}\,T_e}$. Hence, the inclusion of ion temperature dynamics does not refute the conclusion of the previous section that the SCW instability should be considered as a potential player in the divertor region or in start-up L-mode plasma.

Finally, one can notice that the elevation of T_i does not affect λ_{q_e}, λ_{q_i} the same way. Indeed, unlike λ_{q_i} which presents a positive dependency on ζ_i, λ_{q_e} is roughly constant with ζ_i. This difference does not come from the cross-field transport of ion and electron energy, as $\lambda_{\Gamma_{E_e,\mathrm{turb}}}$,$\lambda_{\Gamma_{E_i,\mathrm{turb}}}$ are both increasing functions of T_i, but is a result of an increase of the parallel losses of electron energy with T_i. This effect is due to the fact that the SOL width is not only set by the efficiency of the perpendicular

transport but results from a competition between parallel and perpendicular transport.

To summarize this section two main conclusions can be drawn:

- The predominant effect of the inclusion of ion temperature is attributed to the impact of the finite ion temperature in the vorticity: explaining both the modification of turbulence characteristics and cross-field transport.
- The ion temperature inclusion triggers an enhancement of the cross-field transport presenting highly intermittent characteristics and is attributed to the interchange instability.

3.5 Conclusions

Even though the inclusion of temperature does not appear to drastically modify the general features of turbulence, one observes a modification of the shape of the turbulent structures in anisothermal models, and consequently a modification of the cross-field transport. In this chapter we underline the principal effect of the inclusion of the electron temperature and of ion temperature explaining this difference.

The principal effect of the electron temperature inclusion is identified to be the presence of a new instability mechanism. The characterisation of turbulence, using the input of linear analysis, has revealed that the additional instability has a great impact on turbulence characteristics. This instability appears also to play a significant role in the heat transport in conjunction with the interchange drive, impacting thus the power decay length.

The impact of ion temperature fluctuations is studied separately. The finite ion temperature is identified as the key player of the modification of the turbulence and heat transport. Its inclusion, even though it does not bring a new instability, seems to trigger an enhancement of the perpendicular transport, presenting highly intermittent features at high T_i. This increase of the perpendicular transport is attributed to the interchange instability acting via a non-linear effect.

Chapter 4

Large scale convective transport via magnetic drifts

The current multi-machine scaling of λ_q in H-mode found that the strongest dependency is the one with the poloidal field, B_{pol}, giving $\lambda_{q,\text{target}} \propto B_{\text{pol}}^{-1}$ [Eich 13a, Eich 13b]. Even beyond these studies, the B_{pol} dependency seems to be a robust result and has been retrieved in several works [Thornton 14, Sun 15] and even for L-mode scaling laws [Scarabosio 13, Gunn 13]. Theoretical models based on turbulent transport have been proposed to predict λ_q in L-mode [Fedorczak 17, Ricci 09]. However, in H-mode turbulence is strongly reduced in the pedestal and near-SOL. It is thus not clear which is the main mechanism driving the transport through the separatrix. Indeed, turbulent process, like studied in the previous section with Tokam2D, might not be the predominant mechanism of transport anymore and other mechanisms like large scale convection by plasma drift are pointed out to play a significant role in this regime. Especially the Heuristic Drift-based (HD) model [Goldston 12] proposed that the curvature drift is the main mechanism driving the cross-field transport across the separatrix in H-mode, determining entirely the SOL power width. Similar description of the edge transport were earlier proposed by Ref. [Hinton 74] with a neoclassical approach. Such neoclassical drift-orbit effect has attracted much interest for its good agreement with experience [Eich 13a, Faitsch 15, Sieglin 16], in particular its prediction of the dependency on B_{pol}.

The work presented in this chapter aims at understanding the impact of the convective transport via the curvature drifts in the limit of weak collisional and anomalous transport. Similar work has been published [Reiser 17, Meier 16] assessing the existence of a regime where the SOL width is related to the $\boldsymbol{\nabla} B$-drift. In this study we further investigate the implication of such a $\boldsymbol{\nabla} B$-drift dominated regime: its characteristics, its parametric dependencies and its limits with a mean-field transport code, SolEdge2D. In a first step, this approach allows us to study the impact of drifts separated from the complexity of the turbulence phenomenology in realistic geometry and in different regimes of transport. However, it is worth keeping in mind that one should go towards more complete models, which would take into account mechanisms of interplay between turbulence and large scale convection (topic of the last chapter). Especially since the drift governed by $\boldsymbol{\nabla} B$ is charge dependent. It thus has the ability to govern charge separation or at least polarisation, therefore generates electric fields and consequent $\mathbf{E} \times \mathbf{B}$ drift.

4.1 Study of drifts convective transport with arbitrarily level of anomalous transport in SolEdge2D code

SolEdge2D is a mean-field transport code: turbulence is not solved self-consistently but is arbitrarily set via a diffusion coefficient, and thus permits to run simulation in a chosen regime of transport: L-mode (high anomalous transport, i.e high diffusion) but also H-mode (low anomalous transport). In this discussion, one assumes that the anomalous transport in the SOL is arbitrarily low, this statement has a large impact on the physics and the way it is addressed. In this context, the transport code with reduced numerical cost allows studying many cases, for example performing scans of parameters, but also adding some complementary physics like the implementation of the wall-plasma interaction, physics of neutral species etc... In this section, the model used for this study is briefly described, see [Bufferand 15] for more details. We also underline the strong simplifying assumptions made.

SolEdge2D is a mean-field transport fluid code that assumes toroidal axisymmetry of all fields and solves Braginskii equations for electrons and an arbitrary number of ions species. In the single ion case, of interest in this chapter, the equation of the ion density n, parallel ion velocity $u_\parallel$, and temperature of electrons and ions T_e and T_i (4.1)-(4.5) are solved using a finite volume numerical scheme. At the scale of the mesh grid, larger than the Debye length, the quasi-neutrality is justified, and one has $n = n_e = n_i$. Moreover, in this work, we do not consider the physics of charge balance following the framework of the HD-model, which was the starting point of our study. However, as already mentioned, this is a restrictive assumption since the $\boldsymbol{\nabla} B$-drift is charge dependent and induces a charge separation.

$$\partial_t n + \boldsymbol{\nabla}\cdot\left(nu_\parallel \mathbf{b} + n\mathbf{u}_\perp\right) = S^n \tag{4.1}$$

$$\partial_t\left(nu_\parallel\right) + \boldsymbol{\nabla}\cdot\left(nu_\parallel\left(u_\parallel\mathbf{b}+\mathbf{u}_\perp\right)\right) = -\boldsymbol{\nabla}_\parallel\frac{p_i}{m_i} + \frac{q_i n E_\parallel}{m_i} + \frac{R_{ei}}{m_i} + \boldsymbol{\nabla}\cdot\left(\nu_\perp n\boldsymbol{\nabla}_\perp u_\parallel\right) + S^{nu} \tag{4.2}$$

$$\begin{aligned}&\partial_t\left(\frac{3}{2}nT_i + \frac{1}{2}m_i n u_\parallel^2\right) + \boldsymbol{\nabla}\cdot\left(\left(\frac{5}{2}nT_i + \frac{1}{2}m_i n u_\parallel^2\right)\left(u_\parallel\mathbf{b}+\mathbf{u}_\perp\right)\right)\\ &= \boldsymbol{\nabla}\cdot\left(\kappa_i\boldsymbol{\nabla}_\parallel T_i\mathbf{b} + \chi_\perp n\boldsymbol{\nabla}_\perp T_i + \nu_\perp n\boldsymbol{\nabla}_\perp\left(\frac{1}{2}m_i u_\parallel^2\right)\right) + q_i n u_\parallel E_\parallel + u_\parallel R_{ei} + Q_{ei} + S^{E_i}\end{aligned} \tag{4.3}$$

$$\partial_t\left(\frac{3}{2}nT_e\right) + \boldsymbol{\nabla}\cdot\left(\frac{5}{2}nT_e\left(u_\parallel\mathbf{b}+\mathbf{u}_\perp\right)\right) \tag{4.4}$$

$$= \boldsymbol{\nabla}\cdot\left(\kappa_e\boldsymbol{\nabla}_\parallel T_e\mathbf{b} + \chi_\perp n\boldsymbol{\nabla}_\perp T_e\right) - enu_\parallel E_\parallel - u_\parallel R_{ei} - Q_{ei} + S^{E_e} \tag{4.5}$$

Where $\mathbf{b}$ denotes the direction of the magnetic field $\mathbf{b} = \frac{\mathbf{B}}{B}$, m_i is the ion mass and Q_{ei} is an energy transfer due to collision. The inertia and viscosity terms of electrons are neglected giving $enE_\parallel = \boldsymbol{\nabla}_\parallel(p_e) - R_{ei}$ where $E_\parallel$ is the parallel electric field and R_{ei} is the parallel friction force. Note that contrarily to TOKAM2D and TOKAM3X, the present equations are not normalized.

In standard 2D transport code, turbulence is inhibited as turbulence requires the treatment of the two transverse directions which is not compatible with the toroidal axisymmetry assumption. Cross-field anomalous and collisional transport is arbitrarily set via diffusion operator: $\boldsymbol{\nabla}\cdot(-D_\perp\boldsymbol{\nabla}_\perp n)$. The cross-field flux is then equal to $n\mathbf{u}_\perp = -D_\perp\boldsymbol{\nabla}_\perp n + n\mathbf{u}_{\text{drift}}$. The diffusion coefficient $D_\perp$ stands for the local level of anomalous and collisional transverse transport. For all the following simulations, $D_\perp$ is set to $1\,\text{m}^2\,\text{s}^{-1}$ on a zone of few millimeters at the inner and outer borders to avoid edge effect,

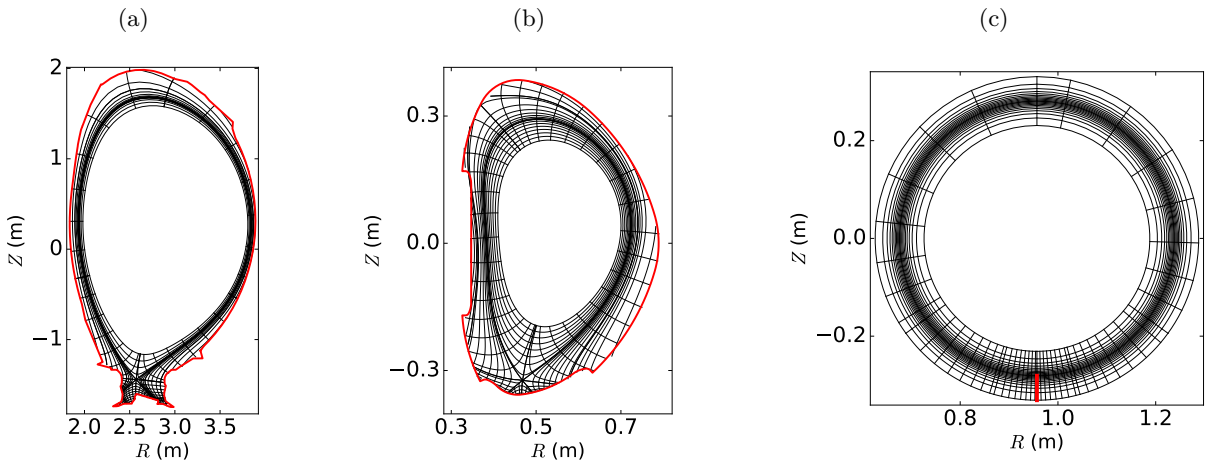

Figure 4.1: Sketch of computational grid (black lines) for the diverted JET-like **(a)** and COMPASS-like **(b)** plasma equilibria with the wall position (red lines), for the analytical circular equilibrium **(c)** with the limitor position (red lines). For the purpose of readability only one in three edges in reported for JET-like grid and one in four for circular geometry

and is a constant, labeled D, on the rest of the grid. D is the main free parameter of this work and will be scanned to study the impact of the fluid drifts on the transverse transport for different levels of anomalous and collisional transport. The viscosity ν is equal to the diffusivity D, and for anisothermal simulations ion and electron thermal diffusivities, respectively χ_e and χ_i, are equal but fixed separately from ν and D.

In this work, only the magnetic drifts are considered, $\mathbf{u}_{\text{drift}} = \mathbf{u}_{\nabla B,i} + \mathbf{u}_{\text{cent}}$, where $\mathbf{u}_{\nabla B}$ denotes the $\boldsymbol{\nabla} B$-drift (4.6) (in the fluid approach $n\mathbf{u}_{\nabla B}$ divergence coincides with the divergence of the diamagnetic drift flux), and $\mathbf{u}_{\text{cent}}$ (4.7) denotes the centrifugal drift [Chankin 97].

$$\mathbf{u}_{\nabla B,i} = \frac{\mathbf{B} \times \boldsymbol{\nabla} p_i}{qnB^2} \tag{4.6}$$

$$\mathbf{u}_{\text{cent}} = \frac{mv_{\parallel}^2}{qB^2} \mathbf{B} \times \mathbf{b} \cdot \boldsymbol{\nabla} \mathbf{b} \tag{4.7}$$

The magnetic field is in the normal direction, that is to say $\mathbf{u}_{\nabla B}$ is downwards for ions. Note that as the charge balance is not solved, a reduced model of SolEdge2D is considered where the electric drift is omitted. This restrictive assumption will be re-discussed in the section on the limits of the model (4.4.3).

In the following, three set of simulations are considered:

1. simulations including no drifts, referred as diffusive simulations,
2. simulations including only $\boldsymbol{\nabla} B$-drift,
3. simulations including both $\boldsymbol{\nabla} B$ and centrifugal drifts.

In a first stage, the plasma is supposed isothermal, and T is constant on all the domain, with $T_e = T_i = 50\,\text{eV}$, and neutrals are not taken into account to stay within the assumptions of the

HD-model. These assumptions are relaxed later to evaluate how they impact the transport and the plasma equilibrium.

The simulated domain extends from closed flux surfaces in the vicinity of the separatrix, with Dirichlet condition imposed to density ($n = 10^{19}\,\mathrm{m}^{-3}$) at the core boundary, to open flux surfaces up to the wall. In the parallel direction Bohm boundary condition are imposed at the sheath entrance. Simulations have been run for three magnetic equilibria, as illustrated on Fig 4.1, a) a realistic diverted JET-like geometry on a 80×139 (r, θ)-grid with the following parameters $R_0 = 2.895\,\mathrm{m}$, $a = 0.950\,\mathrm{m}$, q_{95} defined as the safety factor on the flux-surface ψ such as $\psi/\psi_{\mathrm{sep}} = 0.95$ is about 5 and $B_0 = 2.2\,\mathrm{T}$, b) a realistic diverted COMPASS-like geometry on a 48×139 (r, θ)-grid with the following parameters $R_0 = 0.55\,\mathrm{m}$, $a = 0.17\,\mathrm{m}$, $q_{95} \approx 4$, $B_0 = 1.15\,\mathrm{T}$, 2) an analytical circular geometry on a 240×180 (r, θ)-grid, with the following parameters $R_0 = 1.075\,\mathrm{m}$, $a = 0.287\,\mathrm{m}$, $q_{95} \approx 4$, $B_0 = 1\,\mathrm{T}$. On diverted equilibria, a penalization technique is used that enable simulation of the plasma up to the first wall reported with a red line on Fig 4.1 a and b.

4.2 Properties and implications of the magnetic drift transport in the edge plasma

Before investigating the cross-field transport by magnetic drift in numerical simulations, let us first recall some properties of the diamagnetic drift and associated model of SOL at reduced turbulent transport. First, we proceed to an estimation of the SOL width associated with such mechanism. We then study what would be the consequences, or the markers, of a large scale convective transport by $\boldsymbol{\nabla} B$-drift. Finally, we recall the assumptions and the derivation of the heuristic drift based model which has been taken as a starting point for the simplified model used in the following work.

4.2.1 Estimation of a SOL width associated with the ∇B drift convection

As described in Chapter 1, the SOL width results from a competition between the parallel and cross-field transport in the main SOL. Hence, one can define a fundamental SOL width associated with a mechanism by taking the equality between the parallel characteristic time and the characteristic time associated with this mechanism. We can thus get an estimate of the SOL width with:

$$\tau_{\parallel} \sim \tau_{\perp} \qquad \text{i.e} \qquad \frac{v_{\parallel}}{L_{\parallel}} \sim \frac{v_{\boldsymbol{\nabla} B}}{\lambda_{\boldsymbol{\nabla} B}} \tag{4.8}$$

The characteristic velocity of the vertical $\boldsymbol{\nabla} B$-drift writes:

$$v_{\boldsymbol{\nabla} B} \sim \frac{T}{BR} \tag{4.9}$$

Moreover, we take the acoustic speed $c_s \propto \sqrt{T}$ as the characteristic parallel velocity, and $L_{\parallel} \sim qR$. One thus has a fundamental definition of $\lambda_{\boldsymbol{\nabla} B}$:

$$\lambda_{\boldsymbol{\nabla} B} \sim \frac{v_{\boldsymbol{\nabla} B} L_{\parallel}}{v_{\parallel}} \sim \frac{TqR}{BRc_s} \propto \mathcal{A}\sqrt{T} B_{\mathrm{pol}}^{-1} \tag{4.10}$$

where $\mathcal{A} = a/R$ is the aspect ratio a being the small radius.

4.2.2 Contribution of the diamagnetic drift to flux-surface averaged transport

In order to consider the contribution of the diamagnetic drift to the global transport, we study here the flux surface averaging contribution, which conveniently provides a means to identify the transport from one surface to another irrespectively of the flows within the surfaces. The flux surface averaging for the source governed by the divergence of a flux, $\boldsymbol{\nabla} \cdot (f\mathbf{u})$, writes:

$$\langle \boldsymbol{\nabla} \cdot f\mathbf{u} \rangle_{\mathrm{FS}} = \int_{S(\psi)} f \frac{\mathbf{u} \cdot \boldsymbol{\nabla}\psi}{|\boldsymbol{\nabla}\psi|} \mathrm{d}S \tag{4.11}$$

where ψ is the label of the magnetic surface $S(\psi)$, by construction one has $\left\langle \boldsymbol{\nabla} \cdot \left(f_{\parallel} \mathbf{b} \right) \right\rangle_{\mathrm{FS}} = 0$.

The charge balance equation in steady-state or quasi-neutral condition is:

$$\boldsymbol{\nabla} \cdot \mathbf{J} = 0 \tag{4.12}$$

with $\mathbf{J} = J_{\parallel}\mathbf{b} + \mathbf{J}_*$. Here, we consider only the contribution of $\boldsymbol{\nabla}B$-drift, as one can show that the divergence of the diamagnetic current coincides with the one of $\mathbf{J}_{\boldsymbol{\nabla}B}$ under the assumption of low β. Note that, for two species quasi-neutral plasma, the electric drift and diffusive transport are ambipolar, i.e $\mathbf{J}_{\mathbf{E}} = e\boldsymbol{\Gamma}_{\mathbf{E},i} - e\boldsymbol{\Gamma}_{\mathbf{E},e} = 0$ and $\mathbf{J}_{\mathbf{D}} = e\boldsymbol{\Gamma}_{D,i} - e\boldsymbol{\Gamma}_{D,e} = 0$. One can then determine the flux surface average of Eq.4.12 which gives the following constraint that charge conservation on a magnetic surface requires a balance of the $\mathbf{J}_{\boldsymbol{\nabla}B}$ current (4.13).

$$\langle \boldsymbol{\nabla} \cdot \mathbf{J} \rangle_{\mathrm{FS}} = 0 \Leftrightarrow \langle \boldsymbol{\nabla} \cdot \mathbf{J}_{\boldsymbol{\nabla}\mathbf{B}} \rangle_{\mathrm{FS}} = \int_{S(\psi)} \mathbf{J}_{\boldsymbol{\nabla}B} \cdot \frac{\boldsymbol{\nabla}\psi}{|\boldsymbol{\nabla}\psi|} \mathrm{d}S = 0 \tag{4.13}$$

If one now considers the particle balance, the equation for the main ion species is given by:

$$\partial_t n_i + \boldsymbol{\nabla} \cdot \Gamma_i = \mathcal{S} \tag{4.14}$$

with $\boldsymbol{\Gamma}_i = \boldsymbol{\Gamma}_{\mathbf{E},i} + \boldsymbol{\Gamma}_{\boldsymbol{\nabla}B,i} + \boldsymbol{\Gamma}_{D,i} + \Gamma_{\parallel,i}\mathbf{b}$. Moreover, $\boldsymbol{\Gamma}_{\boldsymbol{\nabla}B,i}$ can be expressed as a function of $\mathbf{J}_{\boldsymbol{\nabla}B} = e\boldsymbol{\Gamma}_{\boldsymbol{\nabla}B,i} - e\boldsymbol{\Gamma}_{\boldsymbol{\nabla}B,e}$: $\boldsymbol{\Gamma}_{\boldsymbol{\nabla}B,i} = \frac{P_i}{e(P_i+P_e)}\mathbf{J}_{\boldsymbol{\nabla}B}$. One can then determine the flux surface average equation for the particle balance of ions with no particles source $\mathcal{S} = 0$:

$$\partial_t \langle n \rangle_{FS} + \int_{S(\psi)} \left(\frac{P_i}{e\left(P_i + P_e\right)} \mathbf{J}_{\boldsymbol{\nabla}B} + \boldsymbol{\Gamma}_{E,i} + \boldsymbol{\Gamma}_{D,i} \right) \cdot \frac{\boldsymbol{\nabla}\psi}{|\boldsymbol{\nabla}\psi|} \mathrm{d}S = 0 \tag{4.15}$$

In steady state and in the limit where no particle flux driven either by the electric drift or cross-field diffusion, $\boldsymbol{\Gamma}_{\mathbf{E},i} = \boldsymbol{\Gamma}_{D,i} = 0$, the only transport term is associated to the $\boldsymbol{\nabla}B$-drift. Furthermore, Eq. 4.13 and Eq 4.15 impose that such transport has to come with strong pressure poloidal up/down asymmetry, as already underlined in [Chankin 13], as $P_i/(P_i + P_e)$ must exhibit a dependence on θ to obtain a non-zero flux-surface averaged transport. In particular, a model with T_e and T_i constant leads to $P_i/(P_i + P_e) = T_i/(T_i + T_e) =$ constant. Hence, temperature inhomogeneity then appears

essential for a transport associated with the $\boldsymbol{\nabla}B$-drift. Indeed, without this inhomogeneity, no particle transport is possible without violating the charge balance i.e. $\langle \boldsymbol{\nabla}\cdot\mathbf{J}_{\boldsymbol{\nabla}B}\rangle_{\mathrm{FS}} \neq 0$.

In fact, the neoclassical theory would give similar insight. Indeed, in the neoclassical description, transport associated to the magnetic curvature depends on the collisions. Thus, in this framework, one needs a certain level of diffusion to have a transport associated with the magnetic drift.

4.2.3 Presentation of the HD-model

In this section, we recall the main assumptions and follow the calculation of the heuristic drift-based model presented in the paper [Goldston 12].

The main assumption of the model is that turbulence does not play a role in the transport of particles in H-mode and the only remaining source of particles for the SOL is attributed to the $\boldsymbol{\nabla}B$ and centrifugal drift direct advection. The particle SOL width at the target is interpreted as a neoclassical drift-orbit effect. Hence, λ_n is determined by the integrated radial displacement of the poloidal flux, denoted $\Delta\psi_p$, by $\boldsymbol{\nabla}B$ and centrifugal drift transverse advection between the outer mid-plane and the divertor entrance and remapped at the outer mid-plane. The radial displacement writes:

$$\Delta\psi_p = \int_{\mathrm{MP}}^{X_{\mathrm{pt}}} \left(\left(\mathbf{u}_{\boldsymbol{\nabla}B}+\mathbf{u}_{\mathrm{cent}}\right)\cdot\nabla\psi_p\right)\frac{\mathrm{d}l_{\parallel}}{v_{\parallel}} = \int_{\mathrm{MP}}^{X_{\mathrm{pt}}} \left(\left(\mathbf{u}_{\boldsymbol{\nabla}B}+\mathbf{u}_{\mathrm{cent}}\right)\cdot\nabla\psi_p\right)\frac{B}{B_p v_{\parallel}}\mathrm{d}l_p \tag{4.16}$$

The further assumption that the parallel speed is constant and equal to the half of the sound speed between the mid-plane and the entrance in the divertor region $v_{\parallel} \approx c_s/2$ is made. Moreover, the centrifugal component is implicitly neglected under the assumption that $|\mathbf{u}_{\boldsymbol{\nabla}B}/\mathbf{u}_{\mathrm{cent}}| \sim \left(v_{\parallel}/c_s\right)^2 \sim 0.25$ is small, and only the contribution of the $\boldsymbol{\nabla}B$-drift is taken into account, i.e $\mathbf{u}_{\boldsymbol{\nabla}B} = \frac{2T}{eZRB}\mathbf{z}$. With the poloidal magnetic field written as $B_p = \frac{|\boldsymbol{\nabla}\psi_p|}{R}$, the equation is simplified to:

$$\Delta\psi = \frac{2T}{Zev_{\parallel}}\int_{\mathrm{MP}}^{X_{\mathrm{pt}}}\left(\mathbf{z}\cdot\frac{\boldsymbol{\nabla}\psi_p}{|\boldsymbol{\nabla}\psi_p|}\right)\mathrm{d}l_p = \frac{4Ta}{Zec_s} \tag{4.17}$$

It is worth stressing that such a displacement considered here as a kinetic calculation does not necessary imply transport. As recalled before, in the neoclassical theory, transport associated with such effect exists only when adding collisions.

Finally the SOL width remapped at the outer mid-plane writes:

$$\lambda_n = \frac{\Delta\psi_p}{|\boldsymbol{\nabla}\psi_p|_{\mathrm{MP}}} = 2\sqrt{2}a\frac{B}{(B_pR)_{\mathrm{MP}}}\rho_L \propto \sqrt{T_{\mathrm{sep}}}B_p^{-1} \tag{4.18}$$

Note that the parametric dependencies of $\lambda_{\boldsymbol{\nabla}B}$ in (4.10) are the one found by the HD-model, as it follows similar lines of thought. One retrieves here the dependence of the SOL width on B_p^{-1}. Until now, only the particle SOL width were considered. The last assumption of the model is that the electron anomalous heat transport ($\chi_{\mathrm{anolamous}} = 1\,\mathrm{m}^2\,\mathrm{s}^{-1}$) is fast enough to fill the particle plasma

channel with electron heat, so that:

$$\lambda_q \approx \lambda_n \propto \sqrt{T_{\text{sep}}} B_p^{-1} \tag{4.19}$$

Note that the assertion $\lambda_n \approx \lambda_q$ is equivalent to $\lambda_T \gg \lambda_n$.

4.3 Drift dominated regime characterised by a complex plasma equilibrium

In this section one first seeks a regime where the cross-field transport through the separatrix is dominated by the $\boldsymbol{\nabla} B$-drift. Even in a low turbulence regime it is not evident that such a regime could exist. Indeed, as presented in the previous section, the current conservation implies that an outward $\boldsymbol{\nabla} B$-drift transport requires a strong up/down pressure asymmetry, this result is also underlined in Ref. [Chankin 13]. The second goal is to characterise such a regime and the associated SOL width. In the last part, we compare our results with the HD-model.

4.3.1 Existence of convective transport by magnetic drift at low anomalous transport in JET-like geometry

In order to reach a regime of $\boldsymbol{\nabla} B$-drift dominated transport the anomalous and collisional transport, set arbitrarily via the diffusion coefficient D in the model, is decreased until finding such a regime. To study the role played by the $\boldsymbol{\nabla} B$-drift in the particle transverse transport, two sets of JET-like isothermal simulations are first considered, the diffusive case, and the case including only the $\boldsymbol{\nabla} B$-drift, for various levels of D. In these sets of simulations the coefficient D is scanned between $1\,\mathrm{m^2\,s^{-1}}$ and $2.0 \times 10^{-4}\,\mathrm{m^2\,s^{-1}}$, with the aim to find out at which level of transport would appear a regime where the large-scale convection by $\mathbf{u}_{\nabla B}$ is the main mechanism of particle transverse transport and what would be the properties of such a plasma equilibrium.

On Fig. 4.2a. the total particle flux through the separatrix due to diffusion (4.20) and to the convection via $\mathbf{u}_{\nabla B}$ (4.21) are reported for both $\boldsymbol{\nabla} B$-drift and purely diffusive simulations as a function of $D_\perp$.

$$\langle \Gamma_{\perp,D} \rangle_{FS} = \int_{\text{sep}} -D_\perp \boldsymbol{\nabla}_\perp n \cdot \boldsymbol{\nabla} \psi \tag{4.20}$$

$$\langle \Gamma_{\perp,\boldsymbol{\nabla} B} \rangle_{FS} = \int_{\text{sep}} n \mathbf{u}_{\nabla B} \cdot \boldsymbol{\nabla} \psi \tag{4.21}$$

Note that all the plotted fluxes are normalized by the mean density at the separatrix. For $D \geq 1 \times 10^{-2}\,\mathrm{m^2\,s^{-1}}$, the diffusive operator is responsible for all the transport and the averaged convective $\mathbf{u}_{\nabla B}$ flux is even sightly negative. In that range of D, there is no significant difference of $\Gamma_{\perp,n}$ between simulations with or without drift, in both cases the particle flux scales as $\sqrt{D}$, expected for a standard diffusive process. At $D = 1 \times 10^{-2}\,\mathrm{m^2\,s^{-1}}$, the $\mathbf{u}_{\nabla B}$ convective contribution in the particles balance starts to rise and its relative weight continues to rise with the decreasing level of diffusive transport to end up largely dominant for $D \leq 1 \times 10^{-3}\,\mathrm{m^2\,s^{-1}}$, with a contribution of more than 90% in the total balance. Hence, a $\boldsymbol{\nabla} B$-drift dominated regime is reached at low transverse transport.

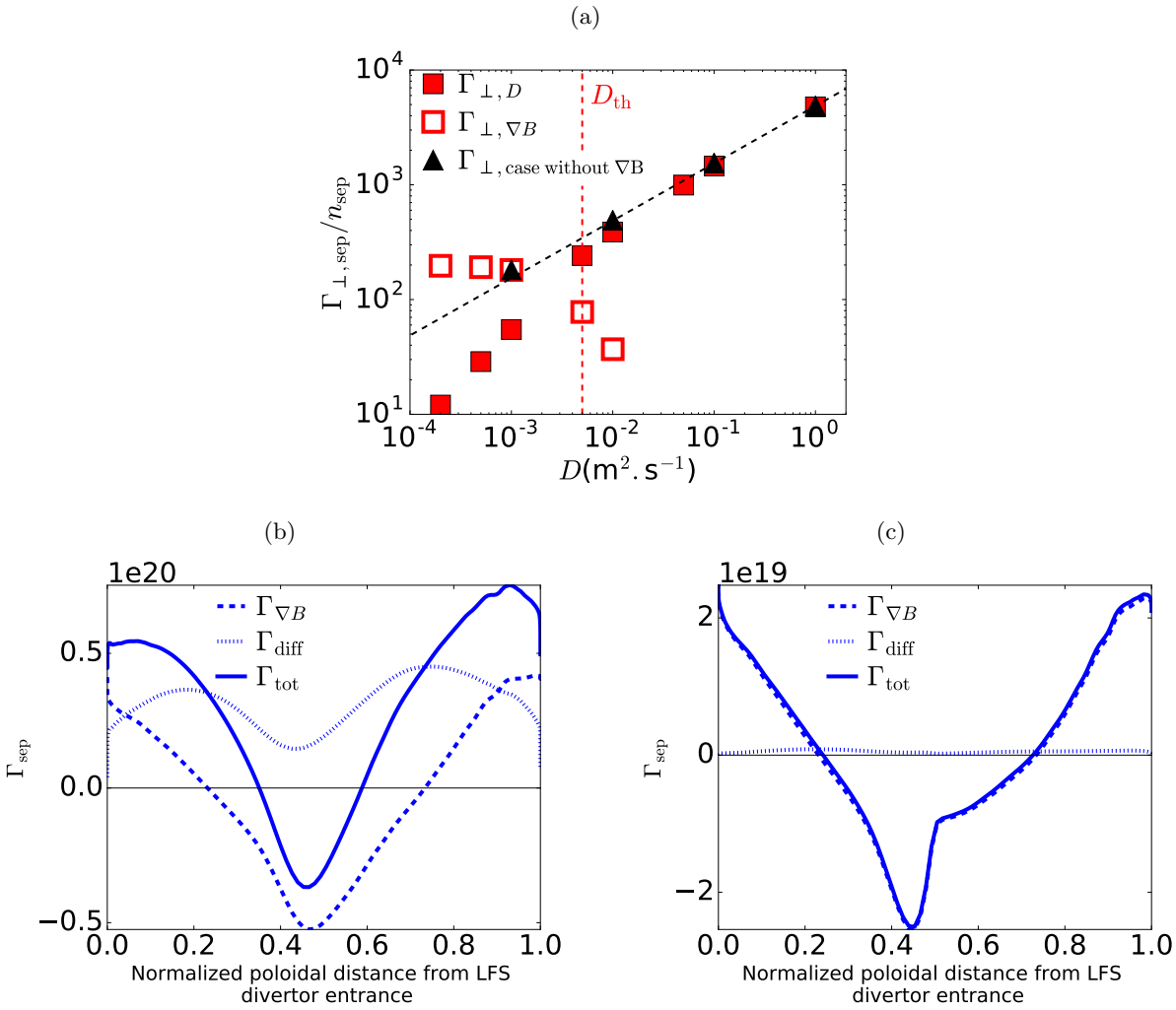

Figure 4.2: (a): Total particle fluxes through the separatrix normalized by the mean density due to diffusion (full red square), to ∇B drift (empty red square) for ∇B-drift simulations, and for diffusive simulations (black triangles) as a function of D. (b), (c): Poloidal distribution of the particle flux in ∇B drift simulations: total (full line), by diffusion (dot-dashed line), by $\mathbf{u}_{\nabla B}$ (dashed line) for $D = 1 \times 10^{-1}\,\text{m}^2\,\text{s}^{-1}$ (b) and $D = 1 \times 10^{-3}\,\text{m}^2\,\text{s}^{-1}$ (c)

In the previous section, we have shown that in the limits of very low anomalous and collisional transport, the ∇B-drift transport has to come with temperature inhomogeneity in the poloidal direction. In the studied isothermal simulations, the transport should thus tend towards zero when D tends towards zero. One has to keep in mind that it is somewhat a contradictory result probably linked to the restrictive assumptions made in the model, in particular, the lack of the charge balance and electric field. It could also be due to spurious numerical effects. However, test of convergence with the grid seems to point out that the spurious effect are not dominant as the results are stable with the grid resolution.

In the following, we denote D_{th} the threshold value of D, where we first observe a significant contribution of ∇B-drift to the total flux, we take $\Gamma_{\perp,\nabla B}/\Gamma_{\text{tot}} > 10\%$ as reference. In this set of simulations, we find $D_{\text{th}} = 5 \times 10^{-3}\,\text{m}^2\,\text{s}^{-1}$. D_{th} will also be referred as the transition towards the ∇B-drift dominated regime. At this level of D, the diffusion source in the ∇B-drift simulations

decreases faster than for the purely diffusive simulations due to a relative flattening of the radial profile around the separatrix (see section 4.3.3.2).

To evaluate where is the implication of these diffusion coefficients values, let us recall some typical values of the diffusion coefficient used when addressing anomalous transverse transport, as well as classical and neoclassical processes. The typical diffusion for anomalous transport used in the pedestal to match profiles in H-mode plasmas is of the order of $1 \times 10^{-1}\,\mathrm{m^2\,s^{-1}}$ [Chankin 06, Horton 05, Kallenbach 04, Gulejová 07]. Moreover, the estimation of diffusion representing the dissipative process as established in Ref. [Fundamenski 07] gives a typical diffusion of $D_\mathrm{C} \approx 1.5 \times 10^{-3}\,\mathrm{m^2\,s^{-1}}$ for classical process and $D_\mathrm{NC} \approx 2.5 \times 10^{-2}\,\mathrm{m^2\,s^{-1}}$ for neoclassical process. Thus, the transition towards a drift dominated regime appears to take place well below the neoclassical level and $\mathbf{u}_{\nabla B}$ is predominant only at a diffusion level lower than the classical level, which raises the question of the possibility of achieving such a regime. The onset of such a transport regime agrees with the previous works of [Reiser 17, Meier 16]. In [Meier 16] this regime appears at higher D, but this difference can be explained by the parameters of the simulations, in particular a higher temperature at the inner boundary of $T_e = T_i = 500\,\mathrm{eV}$, which seems of little relevance for a JET-like simulation, while a range of temperature of 50 eV to 100 eV used in this work.

It is important to stress that the appearance of a flux-surface averaged particle transport by $\mathbf{u}_{\nabla B}$ is inevitably associated with strong poloidal asymmetries. On Fig. 4.2b. and 4.2c. the poloidal local flux is reported, at relatively high diffusion $D = 0.1\,\mathrm{m^2\,s^{-1}}$, $\mathbf{u}_{\nabla B}$ convection is then found to contribute significantly locally, but with the symmetry the positive flux at the bottom strictly compensates the sink at the top, so the flux-surface contribution is negligible. Conversely, at low anomalous transport, Fig. 4.2c, the $\mathbf{u}_{\nabla B}$ convective flux exhibits an up-down asymmetry, and the source at the bottom of the torus becomes bigger than the sink at the top, explaining the rise of its weight in the flux-surface balance.

4.3.2 Complex equilibrium and supersonic transition in drift dominated regime

In the previous section, it has been shown that at D ($D \leq 1 \times 10^{-3}\,\mathrm{m^2\,s^{-1}}$) the convection by $\mathbf{u}_{\nabla B}$ is the predominant particle source for the SOL, at both local and global scales. Let us now characterise the plasma equilibrium in such a regime. On Fig. 4.3 a poloidal profile in the near SOL of the density (a) and parallel Mach number $M = \frac{\sqrt{m_i}\,u_\parallel}{\sqrt{T_e+T_i}}$ (b) are reported. At $D > 2 \times 10^{-2}$, the density is almost constant in the poloidal direction, and the Mach number relatively low far from the target. At low D, the most striking result is the appearance of a complex parallel equilibrium presenting a supersonic transition that comes along with the rise of sharp gradients and strong asymmetry of the density in the poloidal direction. Note that the density tends to be higher at the bottom of the torus, in agreement with the direction of the $\mathbf{u}_{\nabla B}$ convection which leads to an effective particle source in $-\sin\theta$ where θ is the poloidal angle with $\theta = 0°$ at the outboard mid-plane and $\theta = 90°$ at the top. This supersonic transition at low D comes from the strong asymmetry of the effective particle source, composed of a large source at the bottom of the torus and a large sink at the top, creating important Pfirsch–Schlüter return flows. When decreasing the diffusion coefficient, the pressure gradient increases, and it enlarges the Pfirsch–Schlüter flows amplitude ($\Gamma_{\parallel,PS} \propto \boldsymbol{\nabla} P$), reaching a supersonic transition coming along with a steady-state shock in the poloidal direction. It has been verified that the transition is in agreement with the model of supersonic transition presented in [Ghendrih 11] with the annulation of

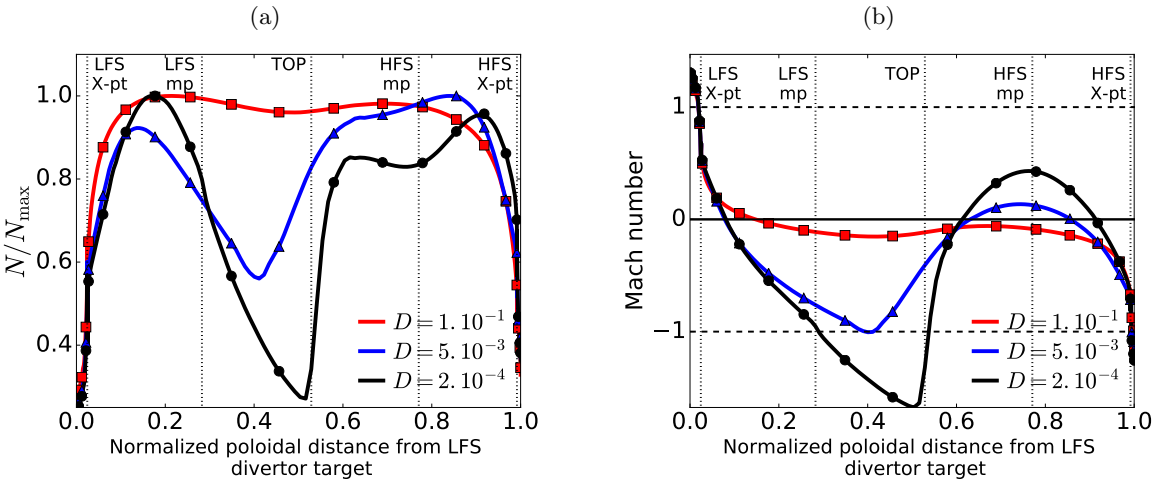

Figure 4.3: Poloidal profile in the near SOL ($\frac{r}{a} = 1.004$) of the normalized density (a), and the parallel Mach number (b) for ∇B-drift simulations for $D = 1 \times 10^{-1}\,\mathrm{m^2\,s^{-1}}$ (red line with square), $D = 5 \times 10^{-3}\,\mathrm{m^2\,s^{-1}}$ (blue line with triangles), and $D = 2 \times 10^{-4}\,\mathrm{m^2\,s^{-1}}$ (black line with circle)

derivative the control parameter $A = \frac{2M}{1+M^2}$ at each transition between subsonic and supersonic flows.

In fact this transition can be explained by a reduced model for the parallel equilibrium Eq. (4.22). In a steady-state equilibrium, the continuity equation and the momentum balance can be simplified in Eq. (4.22) by assuming that:

1. the parallel particle flux distribution is of the form $S_1 + S_2 \cos\left(\frac{2\pi z_\parallel}{L_\parallel}\right)$, where $z_\parallel$ is the parallel coordinate and $L_\parallel$ the parallel length, representing a constant diffusive flux and a sinusoidal $\mathbf{u}_{\nabla B}$ flux in a circular geometry

2. the total pressure is uniform in the parallel direction, that is to say $nT\left(1+M^2\right)$ is conserved. It can be rewritten as $\frac{\Gamma_\parallel^2}{n} + n$ is constant in the isothermal case (with $\Gamma_\parallel = nu_\parallel$).

3. the Mach number is equal to 1 at both targets

$$\begin{cases} \partial_{z_\parallel}\Gamma_\parallel = S_1 + S_2\cos\left(\frac{2\pi z_\parallel}{L_\parallel}\right) \\ \partial_{z_\parallel}\left(\frac{\Gamma_\parallel^2}{n} + n\right) = 0 \\ |M| = 1 \quad \text{for} \quad z_\parallel = 0, L_\parallel \end{cases} \tag{4.22}$$

This system has the following analytical solution:

$$\begin{cases} \Gamma_\parallel\left(z_\parallel\right) = S_1(z_\parallel - 0.5) + S_2\sin\left(\frac{2\pi z_\parallel}{L_\parallel}\right) \\ M\left(z_\parallel\right) = \frac{1}{2}\left(-1 \pm \sqrt{\Delta}\right) \\ \text{with}: \Delta = S_1^2 - 4\Gamma_\parallel^2\left(z_\parallel\right) \end{cases} \tag{4.23}$$

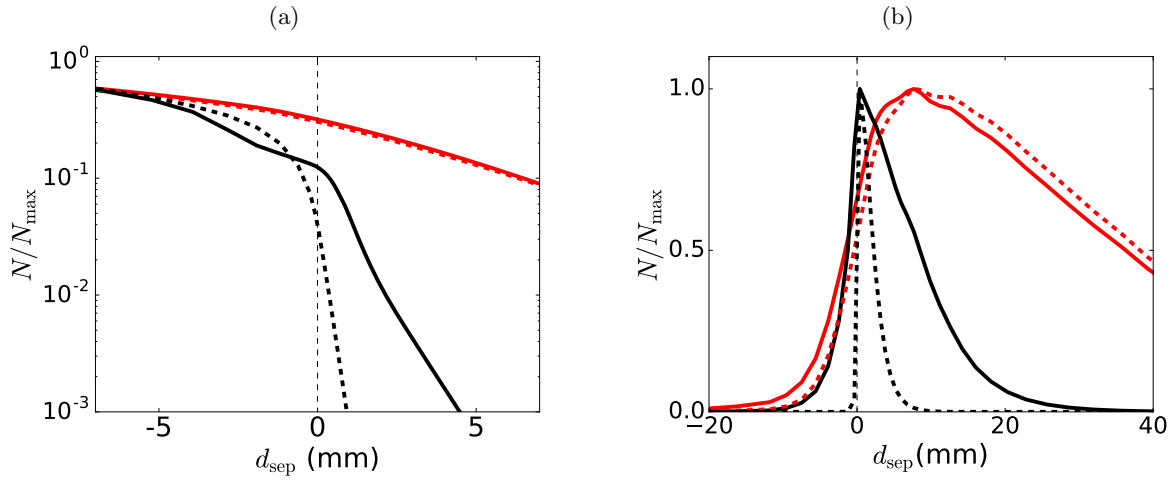

Figure 4.4: Density radial profile for diffusive (dashed lines) and $\boldsymbol{\nabla} B$-drift (full lines) simulations at the outer mid-plane (a), and at the outer target (b), for $D = 1 \times 10^{-1}\,\mathrm{m^2\,s^{-1}}$ (red), and $D = 2 \times 10^{-4}\,\mathrm{m^2\,s^{-1}}$ (black)

and it is found that for $\frac{S_2}{S_1} > 4.6$ no subsonic smooth solution exists, thus it allows us to predict the threshold in D when the supersonic bifurcation first appears. The diffusive particle flux is equal to $D\boldsymbol{\nabla} N = D\frac{n}{\lambda_n}$, with $\lambda_n = \sqrt{\frac{2\pi q R_0 D}{c_s}}$ for a standard diffusive process. For the contribution of the $\boldsymbol{\nabla} B$-drift, the coefficient S_2 corresponds to the maximum of the flux by diamagnetic drift $S_2 = n\mathbf{u}_{\nabla B,\max}$. Note that $\mathbf{u}_{\nabla B}$ in the isothermal case in only a function of the geometry as the temperature is imposed. Thus, the bifurcation towards a supersonic transition should appear at value of diffusion, labelled here D_{trans}, described by the following equation:

$$\frac{\mathbf{u}_{\nabla B,\max}}{\frac{D_{\text{trans}}}{\lambda_n}} = \frac{\sqrt{2\pi q R_0}\mathbf{u}_{\nabla B,\max}}{\sqrt{c_s D_{\text{trans}}}} = 4.6 \;\text{ i.e }\; D_{\text{trans}} = \frac{2\pi q R_0 \mathbf{u}^2_{\nabla B,\max}}{4.6^2 c_s} \tag{4.24}$$

The numerical application of Eq. 4.24 gives $D_{\text{trans}} \approx 1.5 \times 10^{-2}\,\mathrm{m^2\,s^{-1}}$ for a JET-like configuration. In simulations supersonic flows first occur at $D = 5 \times 10^{-3}\,\mathrm{m^2\,s^{-1}}$ that it to say at lower diffusion than predicted. This discrepancy can be explained by the assumption of a circular geometry in our model Eq. (4.22). Moreover, the numerical scheme order was shown to impact the value of the transition through its ability or not to capture shocks accurately. In fact for a circular geometry with a 2nd order WENO scheme, the 1D-model predicts the correct value of D_{trans}.

It is worth noting that the rise of the $\mathbf{u}_{\nabla B}$ convective transport appears in our numerical simulation at the same diffusion as supersonic transition, i.e $D_{\text{trans}} = D_{\text{th}}$, therefore it seems to be a necessary condition to be in a drift dominated regime of transport as it allows strong symmetry breaking of the density.

4.3.3 Saturation of the SOL width at low anomalous transport

4.3.3.1 On definitions of the SOL width

We now aim to define a SOL width looking at the radial profiles Fig. 4.4 at the outer mid-plane (a) and at the outer target (b). For $D < D_{\text{th}}$ radial profiles follow the classical description of a decreasing

exponential. Profiles of both set of simulations, with or without $\mathbf{u}_{\nabla B}$, coincide except for a small inward shift of the peak at the outer target due to the inward direction of $\mathbf{u}_{\nabla B}$ below the X-point Fig. 4.4 b. However, for simulations with supersonic transitions, profiles of simulations with and without drift differ significantly. Moreover, profiles at the outer mid-plane of $\boldsymbol{\nabla} B$-drift simulations are not well fitted by an exponential function, thus the definition of SOL width by a single e-folding length is no longer relevant. Hence, we use the so-called integral decay length, denoted $\lambda_{n,\mathrm{int}}$ and defined by $\lambda_{n,\mathrm{int}} = \int_{\mathrm{SOL}} N(r)dr/N_{\mathrm{sep}}$. This is a convenient definition as it permits comparing exponential profiles with more complex ones.

Another way to define the SOL's width, most commonly used in experiments [Eich 13a], is to proceed with an Eich's fit [Eich 11], convolution of a decreasing exponential and a Gaussian at the outer target profile (see Chapter 1 (1.12) for more details), the resulting estimation of the SOL width is denoted $\lambda_{n,\mathrm{Eich}}$. Since it is the most commonly used in experiments, this Eich's definition is prioritized to investigate this model. Nevertheless, if in this set of simulations profiles at the outer target are well described by an Eich's fit, it is not always the case, and in such cases we settle for the integral description. Note that all estimates of SOL width take into account the flux expansion by remapping profiles at the outer mid-plane in order to get rid of geometry effects.

It is also important to point out that gradients vary not only in the radial direction but also in the poloidal direction. On Fig 4.5 we observe that at low diffusion $\lambda_{n,\mathrm{int}}$ is uniform for purely diffusive simulations, but presents variation in the poloidal direction in the drift dominated regime. In this set of JET-simulations variations stay at a moderate levels (of a factor about 1.5) but in other set of simulations (see section 4.4.1) poloidal variation amplitude of $\lambda_{n,\mathrm{int}}$ can reach a factor 4. In conclusion one must keep in mind that an estimation of a SOL width by a single value summarises the transverse transport but is an oversimplification and hides the complexity of the plasma equilibrium.

4.3.3.2 SOL width saturation in $\boldsymbol{\nabla} B$-drift dominated regime

On Fig. 4.6, $\lambda_{n,\mathrm{Eich}}$ is reported as a function of D. The estimate of the HD-model for the simulation parameters and geometry is also reported in blue dashed line, but the comparison with the model will be discussed latter in the section 4.3.7. We observe a perfect $\sqrt{D}$ scaling for purely diffusive simulations. The code is therefore robust in this low diffusion regime and is not dominated by spurious numerical diffusion. As the use of low diffusion coefficient are numerically challenging we also proceeded to a test of convergence with the grid spatial resolution, and found that the estimate of λ_n does not change when increasing the resolution of the grid in $\boldsymbol{\nabla} B$-drift simulations.

For $\boldsymbol{\nabla} B$-drift simulations, $\lambda_{n,\mathrm{Eich}}$ scales also as diffusive simulations for $D \geq 5 \times 10^{-3}\,\mathrm{m^2\,s^{-1}}$ that is to say for $D > D_{\mathrm{th}}$, which is in agreement with the result of section 4.3.1 where we have established that the diffusive operator is largely dominant in the transport in that range of D. This transport mechanism is thus the one setting the SOL width. This is followed by a stagnation of $\lambda_{n,\mathrm{Eich}}$ corresponding to the transition towards the drift dominated regime, and $\lambda_{n,\mathrm{Eich}}$ saturates at a non-zero value when D tends towards zero. Hence, at low diffusion, one finds indeed a regime where the $\boldsymbol{\nabla} B$-drift is the mechanism determining entirely the SOL width. In such regime, $\lambda_{n,\mathrm{Eich}}$ does not depend on the diffusion level. One can then define the SOL width associated with the $\boldsymbol{\nabla} B$-drift large scale

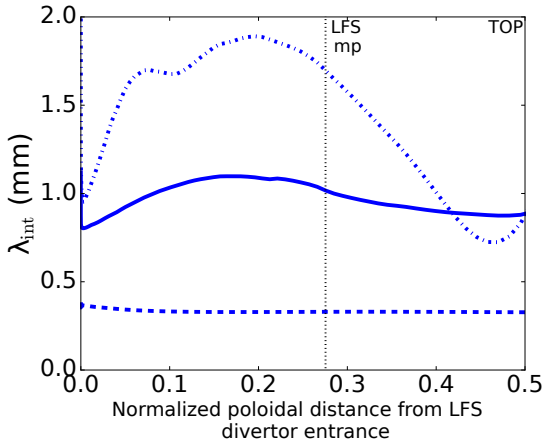

Figure 4.5: Poloidal profile of $\lambda_{n,\mathrm{int}}$ for diffusive (dashed line), ∇B-drift (full line) and both ∇B and centrifugal drift (dot-dashed line) simulations for $D = 2 \times 10^{-4}\,\mathrm{m^2\,s^{-1}}$

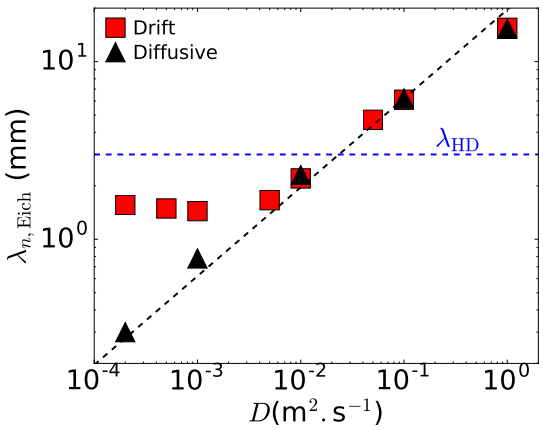

Figure 4.6: $\lambda_{n,\mathrm{Eich}}$ for purely diffusive (black triangles), and for ∇B-drift (red square) simulations as a function of the diffusion coefficient, the dashed straight lines represents the $\sqrt{D}$ scaling, and the x- and y-axis are in log-scale, for JET-like simulation

transport by $\lambda_{\nabla B} = \lim \lambda_{D\to 0}$. Here, we find $\lambda_{\nabla B} \approx 1.5\,\mathrm{mm}$.

The same scan can be made for $\lambda_{n,\mathrm{int}}$ estimated at the outer mid-plane, that gives similar trends but with a lower value of stagnation $\approx 1\,\mathrm{mm}$. Note that once again the λ saturation appears at the same time as the supersonic transition, that is to say $D_{\mathrm{th}} = D_{\mathrm{trans}}$, confirming that the ∇B-drift dominated regime is governed by a complex parallel equilibrium.

4.3.4 Parametric dependencies

In order to have further insight in this transport regime, we now look at the parametric dependencies of the SOL width in $\lambda_{\nabla B}$-drift in such regime. The scanned parameters are: the temperature $T_e = T_i = T$ for $T = 25\,\mathrm{eV}$, $50\,\mathrm{eV}$, $75\,\mathrm{eV}$ and $100\,\mathrm{eV}$, and both poloidal and toroidal magnetic fields B_{pol} and B_{tor}, which vary independently. Note that here the scaling is done for $\lambda_{n,\mathrm{int}}$ because the target profiles at high T and low B_{pol} are not well fitted with an Eich's description. However, we have already assessed that the trends of $\lambda_{n,\mathrm{Eich}}$ and $\lambda_{n,\mathrm{int}}$ are similar.

On Fig. 4.7 we report $\lambda_{n,\mathrm{int}}$ for the lowest diffusion coefficient $D = 2 \times 10^{-4}\,\mathrm{m^2\,s^{-1}}$ as an estimate for $\lambda_{\nabla B} = \lim_{D\to 0} \lambda_{\mathrm{int}}$ as a function of the main parameters. Note that for all parameters, the plasma is in a ∇B-drift dominated regime at such low value of D. We find that the SOL width depends on two principal parameters: the temperature and the poloidal magnetic field. First, $\lambda_{\nabla B}$ presents a positive correlation with T, of the form T^{α} with α strictly lower than 0.5 ($\lambda_{n,\mathrm{int}} \propto \sqrt{T}$ is indicated by dashed lines). The scaling in B_{pol} shows a decreasing dependency of $\lambda_{\nabla B}$ with B_{pol}, close from the inverse dependency $\lambda_{n,\mathrm{int}} \propto B_{\mathrm{pol}}^{-1}$ observed in experiments.

The discrepancies of the numerical results with the rough estimation $\lambda_{\nabla B} \propto \mathcal{A}\sqrt{T}{B_{\mathrm{pol}}}^{-}1$ Eq. 4.10 can be explained by the fact the parallel flows evolve with B_{pol} and T, but this evolution is not captured by the simplified estimation. In fact, the estimation of $\lambda_{\nabla B}$ as the integrated radial displacement driven by the ∇B-drift should depend on the parallel velocity and on the parallel length travelled by particles flowing toward the outer divertor target. On Fig. 4.8, we observe that the

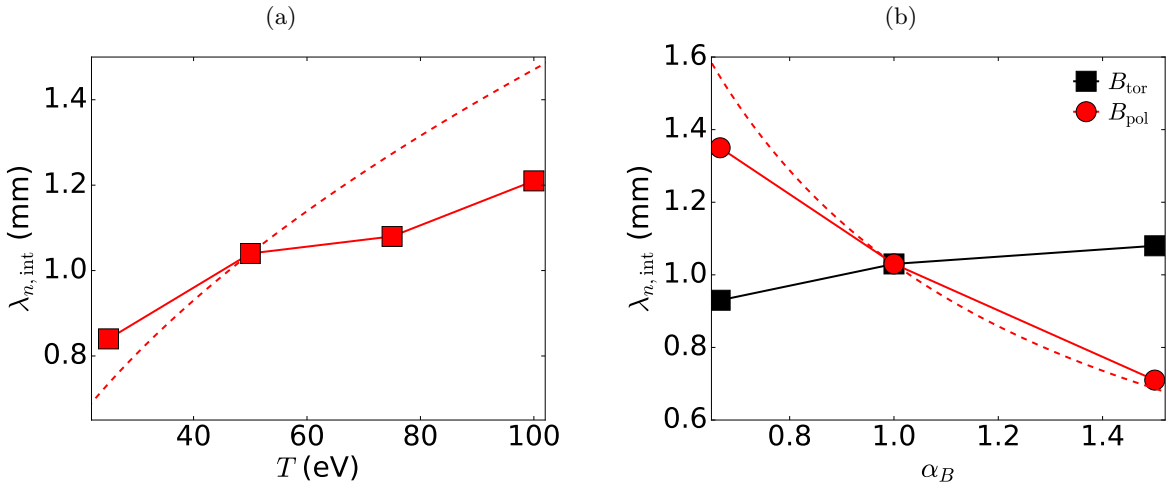

Figure 4.7: $\lambda_{n,\mathrm{int}}$ SOL for ∇B-drift simulations at $D = 2 \times 10^{-4}\,\mathrm{m^2\,s^{-1}}$ as a function of the temperature with red dashed lines representing the $\sqrt{T}$ scaling (a) and as a function of the multiplicative factor, α_B, on B_{pol} and B_{tor} with dashed lines representing the B_{pol}^{-1} scaling (b)

stagnation point, separating particles flowing to the outer target and to the top of the machine, moves downward with an increase of T or a decrease of B_{pol}. This explain the weaker correlation between $\lambda_{\nabla B}$ and T as the effective parallel length travelled by the particles decreases with T, which is not accounted in the estimation of the $\lambda_{\nabla B}$ scaling.

Finally, it is worth noting that there is an additive functional dependency with B_{tor} Fig.4.7 b), weaker than the one in B_{pol} (15% of relative variation of λ for B_{tor} against 60% for B_{pol}), but not completely negligible either. This effect is also explainable by the parallel flows evolution, following the same lines of thought as given above.

4.3.5 Drift dominated regime in other geometries

The scan of the level of anomalous transport has been made for two other geometries: a circular limited and a COMPASS divertor magnetic equilibrium (Fig 4.1), to study whether the conclusions drawn in the previous sections are robust in other equilibria and to study what is the impact of the geometry on the results. Though the HD-model has been developed for divertor configuration, it is also interesting to study its application in circular configuration since the model has been pointed out to be a potential explanation for the narrow feature in start-up plasma [Kočan 15, Goldston 15]. In this section $\lambda_{n,\mathrm{int}}$ at the outer mid-plane is used for the definition of the SOL width in order to compare the circular and the divertor geometry.

The same pattern is retrieved, with two regimes depending on the level of anomalous transport:

1. a diffusive dominated regime at high D where $\lambda_{n,\mathrm{int}}$ scales as $\sqrt{D}$
2. a drift dominated regime with a stagnation of $\lambda_{n,\mathrm{int}}$ and a non-zero limit when D tends toward zero.

Let us stress that the threshold value of D, D_{th} for the stagnation of $\lambda_{n,\mathrm{int}}$ occurs in both case at D_{trans}, that is to say the bifurcation towards supersonic flows, hence the supersonic flows are a

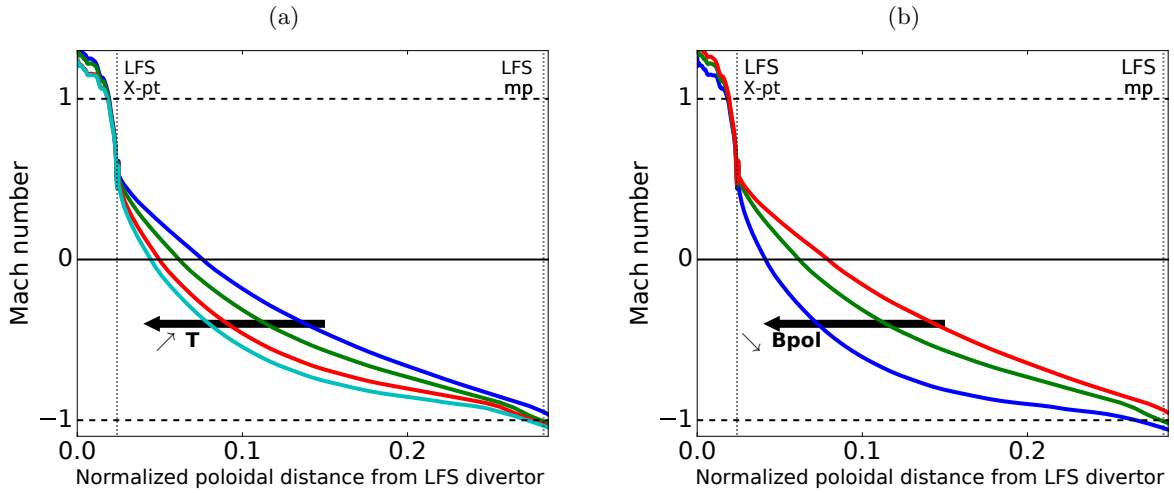

Figure 4.8: Mach number poloidal profile in the near SOL, for ∇B-drift simulations for $D = 2 \times 10^{-4}\,\mathrm{m^2\,s^{-1}}$ for several temperatures $T = 25\,\mathrm{eV}$, $50\,\mathrm{eV}$, $75\,\mathrm{eV}$ and $100\,\mathrm{eV}$ respectively blue, green, red, cyan lines (a), and different $B_{\mathrm{pol}} = 1/1.5, 1, 1.5 \times B_{\mathrm{pol},0}$ respectively blue, green, red lines (b)

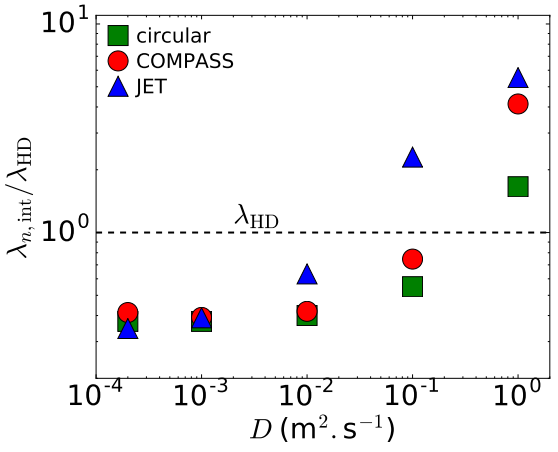

Figure 4.9: $\lambda_{n,\mathrm{int}}$ for ∇B-drift simulations normalized by the heuristic model prediction in JET-like (blue triangles), COMPASS-like (red circle) and circular geometry (green square) both x- and y-axis are in log-scale

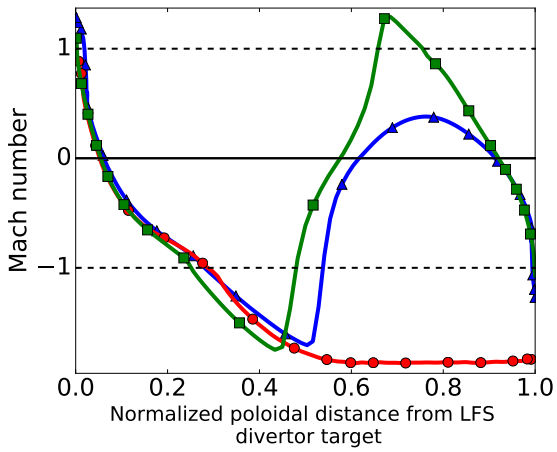

Figure 4.10: Mach number parallel profile for JET-like (blue with triangle) COMPASS-like (red line with circle) and circular (green line with square) geometry at a distance of $\lambda_{n,\mathrm{int}}$ from the separatrix and for $D = 2 \times 10^{-4}\,\mathrm{m^2\,s^{-1}}$

characteristic inherent to the $\boldsymbol{\nabla}B$-drift dominated regime which does not depend on the geometrical configuration. In both geometry D_{trans} is correctly predicted by the simplified 1D-model presented in section 4.3.2 predicting $D_{\text{trans}} = 1.8 \times 10^{-1}\,\text{m}^2\,\text{s}^{-1}$ for circular geometry with a transition for D between $1 \times 10^{-1}\,\text{m}^2\,\text{s}^{-1}$ and $5 \times 10^{-1}\,\text{m}^2\,\text{s}^{-1}$ in the simulations, and $D_{\text{trans}} = 2.8 \times 10^{-1}\,\text{m}^2\,\text{s}^{-1}$ for COMPASS geometry with a transition for D between $1 \times 10^{-1}\,\text{m}^2\,\text{s}^{-1}$ and $5 \times 10^{-1}\,\text{m}^2\,\text{s}^{-1}$ in the simulations.

We now compare the value of stagnation $\lambda_{\boldsymbol{\nabla}B}$ with the HD-model estimate, that is to say a SOL width proportional to $\frac{a}{R}\sqrt{T}B_{\text{pol}}^{-1}$ also obtained in (4.10). We observe on Fig 4.9a) that the ratio $\lambda_{\boldsymbol{\nabla}B}/\lambda_{\text{HD}}$ is approximately constant $\sim 2-3$ for the three geometries. This invariable ratio in the three geometry could be explained by the similarity of the parallel equilibrium. Indeed, on Fig 4.10 reporting the Mach number poloidal SOL profile at a distance $\lambda_{n,\text{int}}$ from the separatrix, one can observe that the profiles at the LFS coincide for the three geometries. This interpretation is consistent with the previous assertion that the parallel equilibrium has a strong impact on the establishment of λ in this regime and that the discrepancy with the rough scaling law comes from the assumption of constant parallel speed and parallel length. This also explains that we find about the same ratio for all geometries for the same LFS parallel flows. At the high field side, the parallel flows differ greatly because of the symmetry breaking of divertor configuration: for COMPASS geometry the $\mathbf{u}_{\nabla B}$ contribution is weaker at the HFS due to the triangularity implying weaker Pfirsch–Schlüter flows. On the contrary the circular geometry presents a relatively symmetric parallel profile.

4.3.6 Power SOL width

The previous model does not address explicitly the heat transport. In this section, we further look at the impact of self-consistent electron and ion temperatures variations on particles and power SOL width.

Simulations are run for two values of thermal diffusivities $\chi_i = \chi_e = 1\,\text{m}^2\,\text{s}^{-1}$,$\chi_i = \chi_e = 0.1\,\text{m}^2\,\text{s}^{-1}$, chosen as they are representative of the classical value of thermal conductivities in the pedestal used in mean field fluid simulations to fit H-mode experiment [Chankin 06, Horton 05, Kallenbach 04, Gulejová 07]. Concerning the boundary conditions, the electron and ion temperatures at the inner boundary is taken constant, are equal to 100 eV. On Fig. 4.11, we observe that, for $1\,\text{m}^2\,\text{s}^{-1}$, the value of $\lambda_{n,\text{int}}$ as a function of D follows the same trend as in the isothermal simulation, and the value of saturation of $\lambda_{n,\text{int}}$ is similar to the one found in isothermal simulation $\lambda_{n,\text{int}} = 1.1\,\text{mm}$. Moreover, we find that $\lambda_{n,\text{int}} \approx \lambda_{q,\text{int}}$, under the assumption of high thermal diffusivity. Let us also underline that the equilibrium presents the same feature as in isothermal simulations, that is to say the presence of supersonic flows and steady-state shock.

Simulations have been also run for this $\chi = 0.1\,\text{m}^2\,\text{s}^{-1}$. It is found that the value of $\lambda_{n,\text{int}}$ at low D is not impacted, but as we could expect the value of stagnation of $\lambda_{q,\text{int}}$ is smaller but only by about 15%. In this range of χ, the power SOL width are not strongly impacted due to the fact that $\lambda_T \gg \lambda_n$.

Thus, in the $\boldsymbol{\nabla}B$-drift dominated regime, and for the chosen thermal diffusivities, the assumption that $\lambda_q \approx \lambda_n$ seems reasonable, and the inclusion of temperature variations does not impact drastically the equilibrium.

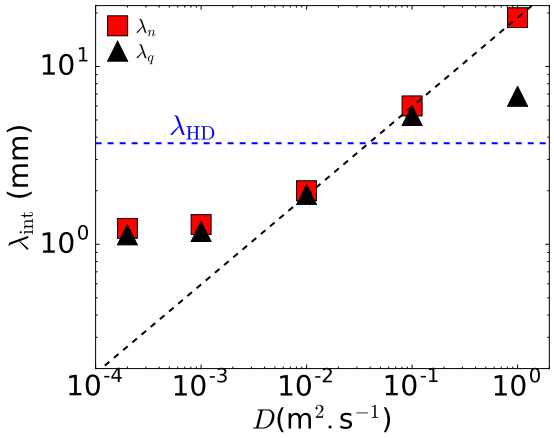

Figure 4.11: $\lambda_{n,\rm int}$ and $\lambda_{q,\rm int}$ for ∇B-drift simulations as a function of the diffusion coefficient in anisothermal JET-like simulation (a)

4.3.7 Comparison of the numerical results with HD-model

The reduced model used in this section corresponds to the main assumption made in the heuristic drift based model. Hence, it is worth comparing $\lambda_{n,\rm Eich}$ with the one predicted by the HD-model $\lambda_{\rm HD} = 2\sqrt{2}\frac{a\sqrt{T_{\rm sep}}}{(B_{\rm pol}R)_{\rm OMP}}$. The numerical application for the JET geometry gives $\lambda_{\rm HD} \approx 3\,$mm namely twice the limit found in simulations $\lim_{D\to 0}\lambda_{n,\rm Eich} \approx 1.5\,$mm. Let us recall that this discrepancy between our numerical results and the HD-model estimate is also retrieved for the other geometry (section 4.3.5). Moreover, the functional dependency on T ($\lambda_{\rm HD} \propto \sqrt{T}$) is not retrieved in our simulations. The scaling in $B_{\rm pol}$, although it shows a better agreement with the model, is not unquestionable. Indeed, the dependency seems to be weaker than predicted, as highlighted by the lower $B_{\rm pol}$ point, showing a variation 40% lower than the HD-model prediction Fig. 4.7b).

The discrepancy between numerical results and the model is readily explainable by the parallel equilibrium, important in the establishment of the SOL width in the drift dominated regime. Indeed, the reduced model predicts $\lambda_{n,\rm Eich}$ under the assumption that the parallel velocity is constant and equal to $c_s/2$ in the lower outer quadrant of the SOL, while the Mach number at low diffusion varies between -c_s and c_s in this poloidal extent (Fig 4.3). Moreover, it assumes that particles flow from the outer target to the entry of the divertor when in low diffusion simulations the stagnation point is halfway between the outer mid-plane and the X-point so particles crossing the separatrix at the outer mid-plane flow to the top of the machine and not downward to the divertor target. In conclusion, within the main hypothesis of the model, the assumption of a ∇B-drift dominated regime seems to lead to a contradiction with the first heuristic made that "the parallel flow along B to the divertor competes at order unity with the usual Pfirsch–Schlüter parallel flow to the opposite side of the plasma" [Goldston 12].

4.4 Consequence of the relaxation of the simplifying assumptions

In the previous section we have analysed outstanding features of the ∇B-drift dominated regime. However, we know that important simplifying assumptions have been made for this model. In this

section, we discuss the inclusion of missing physics: drifts not accounted for, recycling physics, charge balance, and their potential impact on the SOL plasma balance.

4.4.1 Inclusion of the centrifugal drift

In fluid models, the centrifugal drift is often neglected under the assumption of small mach number in the SOL, $\frac{|\mathbf{u}_{\text{cent}}|}{|\mathbf{u}_{\nabla B}|} = M^2 << 1$. However, we have previously assessed that in $\boldsymbol{\nabla} B$-drift driven simulations supersonic flows are at play, thus neglecting $\mathbf{u}_{\text{cent}}$ is not relevant. In this section, the impact of the centrifugal drift on the transverse transport, parallel equilibrium and resulting SOL width is investigated in a JET-like magnetic configuration. For this purpose, we compare simulations including both $\boldsymbol{\nabla} B$ and centrifugal drifts with ones including only the $\boldsymbol{\nabla} B$-drift.

On Fig 4.12 we observe that the centrifugal drift flux is the largest term in the local particle flux crossing the separatrix. However, its flux-surface averaged contribution is negligible $\langle \Gamma_{\text{cent}} \rangle_{\text{FS}} \,/\, \langle \Gamma \text{tot} \rangle_{\text{FS}} < 10\%$. Contrary to the $\boldsymbol{\nabla} B$-drift flux, the centrifugal drift flux is not only dependent on the density but also on the parallel flows amplitude. Now, the later presents opposite asymmetry to the one of density, as a result the centrifugal drift has a negligible contribution to the particle flux averaged on a flux-surface. Nevertheless, $\mathbf{u}_{\text{cent}}$ has an indirect impact on the transverse transport, through the modification of the poloidal equilibrium and $\langle \Gamma_{\nabla B, \text{with } \mathbf{u}_{\text{cent}}} \rangle_{\text{FS}} \approx 1.25 \times \langle \Gamma_{\nabla B, \text{without } \mathbf{u}_{\text{cent}}} \rangle_{\text{FS}}$. The plasma equilibrium response to the centrifugal drift is complex, and hard to capture as it results from a complex inter-play between symmetry breaking of both the parallel velocity and the density, however several effects on the plasma equilibrium and the transverse transport can be underlined.

The first impact of $\mathbf{u}_{\text{cent}}$ is to stimulate the symmetry breaking. Poloidal profiles present greater variation for the parallel Mach number but also for $\lambda_{n,\text{int}}$ (Fig 4.13 and 4.5) when it is included in the model. The amplitude of variation in the poloidal direction of $\lambda_{n,\text{int}}$ at the LFS for simulation with centrifugal is twice the one for the same simulations without $\mathbf{u}_{\text{cent}}$, and the maximum of the Mach number is 1.5 times greater in the case with $\mathbf{u}_{\text{cent}}$. Moreover, $\mathbf{u}_{\text{cent}}$ favors the transition towards supersonic flows which appears at higher D for simulations including $\mathbf{u}_{\text{cent}}$ (above $1 \times 10^{-2}\,\text{m}^2\,\text{s}^{-1}$ against $5 \times 10^{-3}\,\text{m}^2\,\text{s}^{-1}$ for simulation including only $\boldsymbol{\nabla} B$-drift).

This drift has also an impact on radial profiles. At $D < D_{\text{th}}$, radial profiles exhibit three distinct layers (Fig 4.14) in simulation including $\mathbf{u}_{\text{cent}}$. When moving from the separatrix to the far SOL, one first finds a boundary layer, of about 1.5 mm wide, characterised by flat gradient, followed by a second layer with steeper gradients and finally the last layer with intermediate gradients. The first layer can be interpreted as a thin layer due to the radial displacement via drift convection of particles from the core. Simulations with only $\boldsymbol{\nabla} B$-drift included present also the same kind of pattern although less marked. The second layer is a layer where the transport would be essentially diffusive, in fact the e-folding length in this layer is about the same as the one in simulations without diffusion. The explanation of the third layer is not straightforward, but is most probably linked to the rise of the diffusion coefficient at the outer border of the mesh, or to the boundary condition at the wall. Note that this feature is also retrieved at the outer target, with irregular radial profile presenting a flat layer in the area of the strike point. The scaling of $\lambda_{n,\text{int}}$ as a function of D gives the same trend with or without the inclusion of $\mathbf{u}_{\text{cent}}$ (Fig 4.15), $\lambda_{n,\text{int}}$ saturates at a higher value in simulation with $\mathbf{u}_{\text{cent}}$ than in the one with only $\boldsymbol{\nabla} B$ ($\lambda_{\text{lim}} \approx 1.5\,\text{mm}$), but is still 2 times smaller than the value predicted by the HD-model.

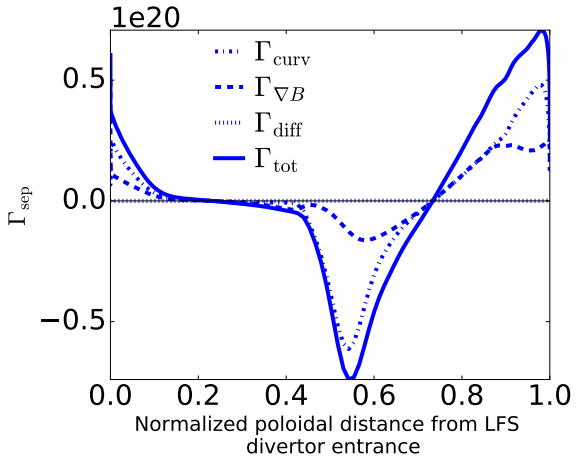

Figure 4.12: Poloidal profile of the local radial flux due to diffusion, ∇B-drift, centrifugal drift, and total contribution for $D = 2 \times 10^{-4}\,\mathrm{m^2\,s^{-1}}$ in JET-like simulations

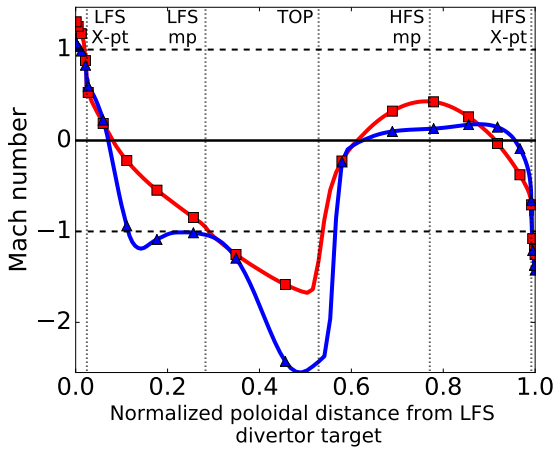

Figure 4.13: Poloidal profile of Mach number in the near SOL ($\frac{r}{a} = 1.004$) for ∇B-drift simulation (red with square markers) and for ∇B and centrifugal drift simulation (blue with triangle markers) for $D = 2 \times 10^{-4}\,\mathrm{m^2\,s^{-1}}$

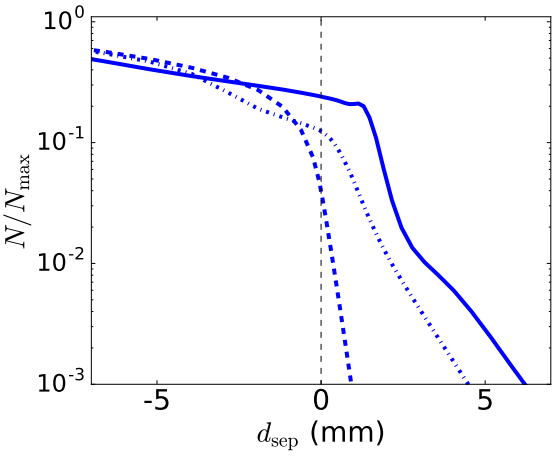

Figure 4.14: Density radial profile for diffusion (blue dashed lines), ∇B-drift (blue dot-dashed lines), and ∇B and centrifugal drift (blue full lines) simulations at the outer mid-plane and for $D = 2 \times 10^{-4}\,\mathrm{m^2\,s^{-1}}$

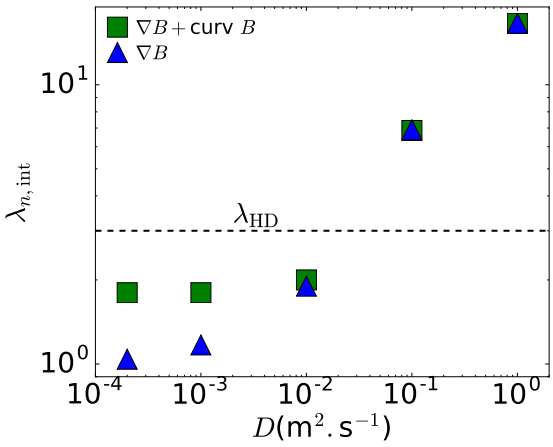

Figure 4.15: $\lambda_{n,\mathrm{int}}$ SOL for ∇B-drift simulations (blue triangles), and ∇B and centrifugal drift simulations (green squares) as a function of the diffusion coefficient for JET-like simulation

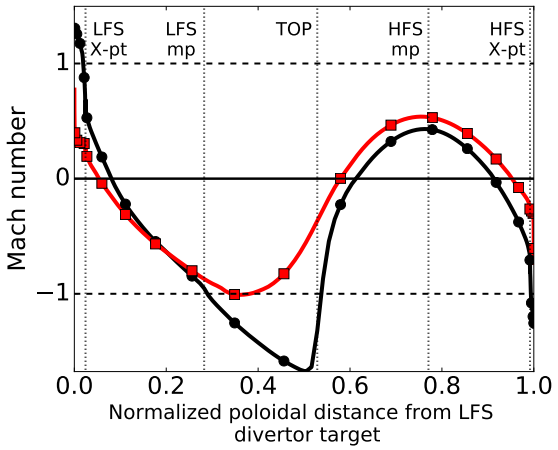

Figure 4.16: Mach number poloidal profile in the near SOL, for ∇B-drift simulations for $D = 2 \times 10^{-4}\,\mathrm{m^2\,s^{-1}}$ for simulation with neutral species (red with square markers), without neutral species (black with circle markers)

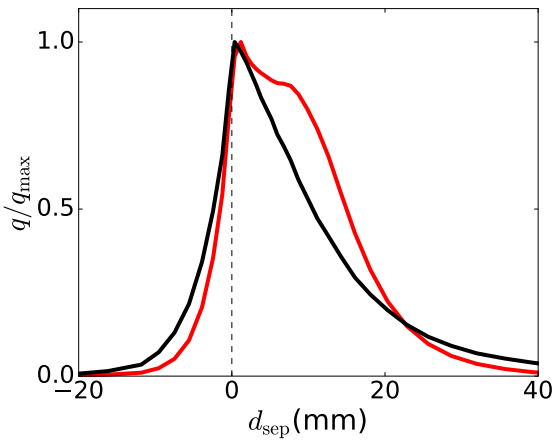

Figure 4.17: Heat flux radial profile ∇B-drift simulations at the outer target for $D = 2 \times 10^{-4}\,\mathrm{m^2\,s^{-1}}$ for simulation without (red line) and with (black line) the inclusion of neutral species

4.4.2 Impact of recycling

Finally, we study the impact of the inclusion of neutral species in a low recycling regime in the case where only the ∇B-drift is taken into account. Simulations have been run with tungsten PFC for the divertor target and beryllium PFC for outer wall, with recycling coefficients of 0.99 and 1. respectively, the density is set at $1 \times 10^{20}\,\mathrm{m^{-3}}$ at the inner boundary and the density at the separatrix is about $1 \times 10^{19}\,\mathrm{m^{-3}}$ in order to be in a low recycling regime (i.e. the framework of the HD-model) and a diffusion coefficient is taken equal to $2 \times 10^{-4}\,\mathrm{m^2\,s^{-1}}$ to study the ∇B dominated regime. The inclusion of neutrals is expected to impact the results as it modifies the value of parallel velocity in the divertor region, and we have previously showed that the parallel equilibrium plays a major role in the establishment of the SOL width. On Fig. 4.16 we observe that the inclusion of neutral species results in smaller amplitude of parallel flows, even if a supersonic transition is still reached in this case. This also impacts the parallel variations of the density which are of a smaller amplitude and less abrupt.

Looking at the profiles at the outer mid-plane, we observe that the simulation including neutral species presents radial profiles (not reported here) with flatter gradient, resulting in a larger SOL width, $\lambda_{n,\mathrm{int}} = 1.7\,\mathrm{mm}$ and $\lambda_{q,\mathrm{int}} = 1.5\,\mathrm{mm}$. This can be explained by the fact that the Mach number amplitude is lower in the lower-outer quadrant, so that particles crossing the separatrix at the bottom and flowing toward the top of the machine, are drifting during a longer time, resulting in a larger SOL width at the outer mid-plane. But the SOL width are of the same order of magnitude and still lower than the prediction of the HD-model. However, if we now look at the outer target profile, we observe the inverse effect, both density and heat flux profiles of simulation without the inclusion of neutral are more spread than in the case with inclusion of neutral Fig 4.17. The detailed study of the physics in the divertor region is out of the scope of this work, but let us mention several mechanisms that can explain this effect. First it is important to underline that the repartition of particle sources is completely modified, and the ionization of neutrals in the divertor region becomes a major player in

the source for the plasma. This tends to decouple the physics of the main SOL and divertor explaining that we observe opposite variation of the profile in the two regions. This effect can also be observed in the parallel flow amplitude, in simulations without neutral only a thin boundary layer at the vicinity of the separatrix presents a Mach number close to zeros, when in simulation with neutral the Mach number is close to zero at the divertor entrance on all the radial domain of the SOL. The fact that the radial profile at the outer target presents sharper gradients at the strike point in the case including neutrals could be partly due to ionization. Indeed, this mechanism is proportional to the local density, so will be maximum at the strike point, this way reinforcing the plasma source at the peak location.

4.4.3 Inclusion of the charge balance and electrostatic drift

In the model studied in this chapter the charge balance is not considered, and therefore $\mathbf{E}\times\mathbf{B}$ drift is not included, following the framework of the HD-model. However, we know that the $\boldsymbol{\nabla}B$ drifts are charge dependent, and in the $\boldsymbol{\nabla}B$-drift dominated regime, the principal mechanism of transport leads to a charge separation and must therefore drives significant electric fields. Moreover, it has been shown that the electric drift has not only an importance in $\mathbf{E}\times\mathbf{B}$ turbulence but also drives large scale transport that need to be taking into account even for a laminar approach [Galassi 17].

Due to numerical constraint, too demanding in the regime of low D considered here, no simulation including the drift $\mathbf{E}\times\mathbf{B}$ have been run yet. However one could expect a strong effect of the addition of the drift, especially in the low anomalous transport regime. Indeed, for a quasi-adiabatic electric field model, one has $\phi(\theta) \propto \ln N(\theta)$. Considering the large poloidal inhomogeneities of density, it would create a large $\partial_\theta\phi$, i.e. a large radial $\mathbf{E}\times\mathbf{B}$ drift velocity u^r_E. Such $\mathbf{E}\times\mathbf{B}$ flows could modify significantly the equilibrium.

Finally, in the $\boldsymbol{\nabla}B$-dominated regime, we expect high amplitude parallel Pfirsch-Schlüter return currents (if they were considered) of the order of $j_{\text{sat}} \sim 10^5$ A.m^{-2}. Even though this is still several orders of magnitude lower than the plasma current, one could question to what extent it would impact the plasma local equilibrium.

In conclusion, the question of the charge balance and consequent electric drifts is critical for the studied regime and should be a priority for further investigations.

4.5 Interpretation and conclusion on the drift dominated regime

In this chapter, we have studied the impact of the $\boldsymbol{\nabla}B$-drift on the cross-field transport and on the SOL's width for different levels of anomalous transport using the fluid code SolEdge2D.

The first conclusion of this work is that in all cases, including anisothermal simulations, simulations taking account neutral species, and all geometries, a $\boldsymbol{\nabla}B$-drift dominated regime is reached at low D. In such regime, the cross-field transport is dominated by the $\boldsymbol{\nabla}B$-drift contribution and the value of SOL particles or power width is set by the magnetic drift and does not depend anymore on D. However, the relevance of such a regime, beyond the neglected physics, is disputable as it presents some intrinsic problematics:

- Existence only at level of diffusion way below the neoclassical level. As underlined in the section 4.2, the existence of a regime where the $\boldsymbol{\nabla}B$-drift is responsible for non-zero cross-field transport

in the limit of extremely low diffusion level is problematic, as the neoclassical transport associated with curvature drift requires collisions. In particular, in the isothermal model, it raises the question of the charge conservation in the model (see section 4.2.2).

- Complex equilibrium presenting steady-state shocks associated with supersonic transitions that should have been observed in experiments. Furthermore, in this regime characterised by large Mach number amplitude, the impact of the centrifugal drift should be explicitly taking into account, as discussed in section 4.4.1.

The comparison with the HD-model shows that in all the numerical studies in section 4.2, corresponding to the framework of the model, the resulting SOL width differs from the HD-model estimate by a factor at least 2 (up to 3). This discrepancy can be explained by the hypothesis on the parallel equilibrium in contradiction with a $\boldsymbol{\nabla} B$-dominated regime as proven by the 1D-model presented in section 4.3.2. As for the turbulent 2D-models, we hence observe that one cannot abstain from a coherent resolution of the parallel transport, which impacts also the SOL width.

Finally, the problematics raised by the study of the $\boldsymbol{\nabla} B$-drift dominated regime call for further investigations of the model. In particular, it calls for a self-consistent resolution of the charge balance and of the electric field.

Chapter 5

Turbulent heat transport in 3D toroidal geometry

Study of 3D turbulent simulations is mandatory to understand the mechanism of heat turbulence, approached with a 2D model in Chapter 2, together with large-scale convective transport, approached with a transport code in Chapter 3. Moreover, the 3D geometrical effects can also impact turbulence. In particular, the third dimension allows to study a more realistic $\mathbf{E} \times \mathbf{B}$ plasma rotation known to impact turbulence particles flux at the separatrix and to play a role in the apparition of the H-mode.

The fluid code TOKAM3X, used in this chapter, includes the physics suspected to play a significant role in the heat transport: diffusion, drifts and turbulence, and solved the fluid equations in a realistic geometry. The study of the physics of SOL power width is one of the long-term objectives of the code, however, the code has been used only in its isothermal version until recently. Here, the recent version of the 3D fluid code TOKAM3X, including self-consistent variation of both electron and ion temperature, is used to investigate the impact of the addition of temperature dynamics on the properties of turbulence and heat transport. In particular, the objective of this chapter is to answer two questions:

- Does the inclusion of temperature dynamics have a significant impact on the turbulence and transport characteristic ?
- Does the heat transport present the same characteristics as the particles transport. Indeed, this is not evident since the recent experimental observation on various machines found unexplained narrow features in the radial decay of the parallel heat flux [Arnoux 13, Kočan 15].

Particle turbulence and transport have been already described using the previous version of TOKAM3X in Ref. [Tamain 14, Tamain 15, Colin 15a], but this is the first study addressing the question of heat transport in this code. A comparison between results of one isothermal and one anisothermal equivalent simulation is drawn to point out the impact of temperature dynamics. The simulations run for the study are all in a L-mode like regime, with electrostatic turbulence largely dominating the transport.

5.1 TOKAM3X anisothermal simulations: numerical and geometry set up

The equations of TOKAM3X: the density conservation (5.1), the parallel ion momentum conservation (5.2), the charge conservation (5.3), the electron and ion energy conservation (5.4)–(5.5), and the parallel Ohm's law (5.6), detailed in chapter 2 are recalled here below:

$$\partial_t N + \boldsymbol{\nabla}\cdot\left(N\left(u_\parallel + \mathbf{u}^e_\perp\right)\right) = \boldsymbol{\nabla}\cdot\left(D_{\perp N}\boldsymbol{\nabla}_\perp N\right) + S_N \tag{5.1}$$

$$\partial_t \Gamma_i + \boldsymbol{\nabla}\cdot\left(\Gamma_i\left(u_\parallel + \mathbf{u}^i_\perp\right)\right) = -\boldsymbol{\nabla}_\parallel(P_i) - N\boldsymbol{\nabla}_\parallel\phi - R_\parallel + \boldsymbol{\nabla}\cdot\left(D_{\perp\Gamma}N\boldsymbol{\nabla}_\perp\frac{\Gamma_i}{N} + D_{\perp N}\frac{\Gamma_i}{N}\boldsymbol{\nabla}_\perp N\right) + S_\Gamma \tag{5.2}$$

$$\partial_t W + \boldsymbol{\nabla}\cdot\left(W\left(u_\parallel + \mathbf{u}^i_\perp\right)\right) = \boldsymbol{\nabla}\cdot\left(N(\mathbf{u}_{\nabla B,i} - \mathbf{u}_{\nabla B,e})\right) + \boldsymbol{\nabla}\cdot\left(J_\parallel\mathbf{b}\right) + \boldsymbol{\nabla}\cdot\left(D_{\perp W}\boldsymbol{\nabla}_\perp W\right) + S_W \tag{5.3}$$

$$\begin{aligned}\partial_t E_e + \boldsymbol{\nabla}\cdot\left(\left(E_e + P_e\right)u_\parallel + E_e\mathbf{u}^e_\perp\right) &= \boldsymbol{\nabla}\cdot\left(K^e_0 T_e^{5/2}\boldsymbol{\nabla}_\parallel T_e\mathbf{b}\right) - P_e\boldsymbol{\nabla}\cdot\left(\mathbf{u}^e_\perp\right) + \Gamma_i\boldsymbol{\nabla}_\parallel\phi + u_\parallel R_\parallel \\ &+ Q_{\parallel,e} + \boldsymbol{\nabla}\cdot\left(D_{\perp T_e}N\boldsymbol{\nabla}_\perp T_e + D_{\perp N}\frac{E_e}{N}\boldsymbol{\nabla}_\perp N\right) + S_{E_e}\end{aligned} \tag{5.4}$$

$$\begin{aligned}\partial_t E_i + \boldsymbol{\nabla}\cdot\left(\left(E_i + P_i\right)u_\parallel + E_i\mathbf{u}^i_\perp\right) &= \boldsymbol{\nabla}\cdot\left(K^i_0 T_i^{5/2}\boldsymbol{\nabla}_\parallel T_i\mathbf{b}\right) - P_i\boldsymbol{\nabla}\cdot\left(\mathbf{u}^i_\perp\right) - \Gamma_i\boldsymbol{\nabla}_\parallel\phi - u_\parallel R_\parallel \\ &+ Q_{\parallel,i} + \boldsymbol{\nabla}\cdot\left(D_{\perp T_i}N\boldsymbol{\nabla}_\perp T_i + D_{\perp N}\frac{E_i}{N}\boldsymbol{\nabla}_\perp N + D_{\perp\Gamma}\Gamma_i\boldsymbol{\nabla}_\perp\frac{\Gamma_i}{N}\right) + S_{E_i}\end{aligned} \tag{5.5}$$

$$\eta_\parallel N\mathbf{J}_\parallel = \boldsymbol{\nabla}_\parallel P_e - N\boldsymbol{\nabla}_\parallel\Phi + 0.71N\boldsymbol{\nabla}_\parallel T_e \tag{5.6}$$

where $E_e = \frac{3}{2}N_eT_e$ and $E_i = \frac{3}{2}N_iT_i + \frac{1}{2}\frac{\Gamma_i^2}{N}$, $\Gamma_i = Nu_\parallel$.

Three simulations have been run:

- An isothermal simulation with $T_e = T_i = 1$
- An anisothermal simulation where the amplitudes of the energy sources (S_{E_e}, S_{E_i}) have been chosen so that the electron and ion temperature at the separatrix are of the same order as in the first isothermal simulation ($T_{e,\text{aniso}} + T_{i,\text{aniso}} \approx 2$)
- An isothermal simulation with the same temperature radial profiles as the anisothermal simulation, denoted as isothermal $\boldsymbol{\nabla}T$ simulation in the rest of this chapter.

The three simulations are in a limiter geometry with circular concentric flux surfaces, the minor radius, a, is equal to $256\rho_L$, and the aspect ratio to 3.4. This size is of the order of a small Tokamak for example COMPASS. This simple geometry allows in a first approach to understand the basic properties of turbulence and transport in the anisothermal model. The studies on divertor geometry are out of the scope of this chapter and should be discussed in future work in complement to the work with an isothermal model [Galassi 17].

The simulated physical domain extends from the closed flux surface $r_{\min}/a = 0.8$, to the open flux surfaces $r_{\max}/a = 1.2$. In the parallel direction, only half of the torus is simulated, and Bohm-Chodura boundary conditions are imposed at the sheath entrance. Simulations are run for a $64 \times 512 \times 64$ (ψ, θ, φ)-grid and with an integration time of $1\,\Omega_s^{-1}$.

Under the TOKAM3X normalization described in chapter 2, the parallel resistivity of the plasma $\eta_\parallel$ is taken constant in space and time and equal to 1×10^{-5} in this set of simulations. Note that

its dependency on T_e ($\eta_\parallel \propto T_e^{-3/2}$) is not taken into account as it is a first stage work towards a more complete model. Moreover, given the chosen normalization, the typical value of $\eta_\parallel$ in a medium-size Tokamak is about 10^{-6}, thus smaller than the parameter retained here. This choice is due to numerical cost considerations. The influence of the value and dependency of the parallel resistivity will have to be discussed in future work. The cross-field diffusion coefficients, $D_{\perp,F}$, for each field F, are fixed to $D_{\perp,F} = 5 \times 10^{-3}$ and the coefficients of parallel conduction for electrons and ions, $K_0^{e/i}$, are respectively equal to 1×10^6 and 1×10^4. Unlike the parallel resistivity value, the chosen value for these coefficients is of the same order as the typical value in a medium-size Tokamak.

In Tokam3X, the computation of the electrostatic potential requires the inversion of the vorticity operator, a highly demanding computational step. In the isothermal simulation, this operator does not depend on time and can be inverted once and for all at the beginning of the simulation within the Boussinesq approximation. However, in anisothermal simulation, the operator expression depends on electron temperature via Bohm boundary conditions. The operator is thus time dependent, and should be inverted at each time step. In order to reduce the computational cost, this operator expression is modified only every 50 time steps, and the operator is inverted accordingly. Nevertheless, the fact that the characteristic time of turbulence is about $400\,\Omega_s^{-1} >> 50\,\Omega_s^{-1}$ suggests that the dynamics are probably recaptured correctly even though the operator is not solved at each time step.

5.2 Turbulence characteristics in anisothermal 3D simulation

In this section, we characterise general features of particle and energy fluctuating structures observed in the anisothermal simulation, and we draw a comparison with the isothermal simulation with constant temperature $T_e = T_i = 1$.

5.2.1 Common features and differences between isothermal and anisothermal simulations

Both isothermal and anisothermal 3D simulations exhibit turbulent fluctuations of density, potential and also electron and ion temperatures in the anisothermal case represented on Fig. 5.1. On Fig. 5.2 representing the density on a flux surface at an arbitrary time, one can observe that the turbulent structures form quasi field-aligned filaments, usually referred to as blobs by analogy with 2D simulations. They propagate intermittently through the SOL as coherent structures on long distances reminiscent of experimental observations [Fedorczak 11, Dudson 08]. Furthermore, fluctuations of density and electron temperature present the classical ballooning feature signature of interchange-like turbulence. Indeed, fluctuations in the SOL region exhibit a poloidal asymmetry, and turbulence intensity is higher at the outer mid-plan than at other poloidal locations. Note that these characteristics were already obtained for the transport of particles in the isothermal previous version of TOKAM3X presented in Ref. [Tamain 14, Tamain 15, Colin 15a].

These blobs are advected by the $\mathbf{E} \times \mathbf{B}$ drift leading to a turbulent outward flux for each field F denoted $\Gamma_{F,\text{turb}}$ (5.7). And the flux-surface averaged of the $\mathbf{E} \times \mathbf{B}$ turbulent flux ($\langle \Gamma_{F,\text{turb}} \rangle_{\theta,\varphi}$) exhibits long radial structures penetrating into the SOL Fig. 5.13.

$$\Gamma_{F,\text{turb}} = \widetilde{F}\, \widetilde{u}_{\mathbf{E}\times\mathbf{B},\psi} \tag{5.7}$$

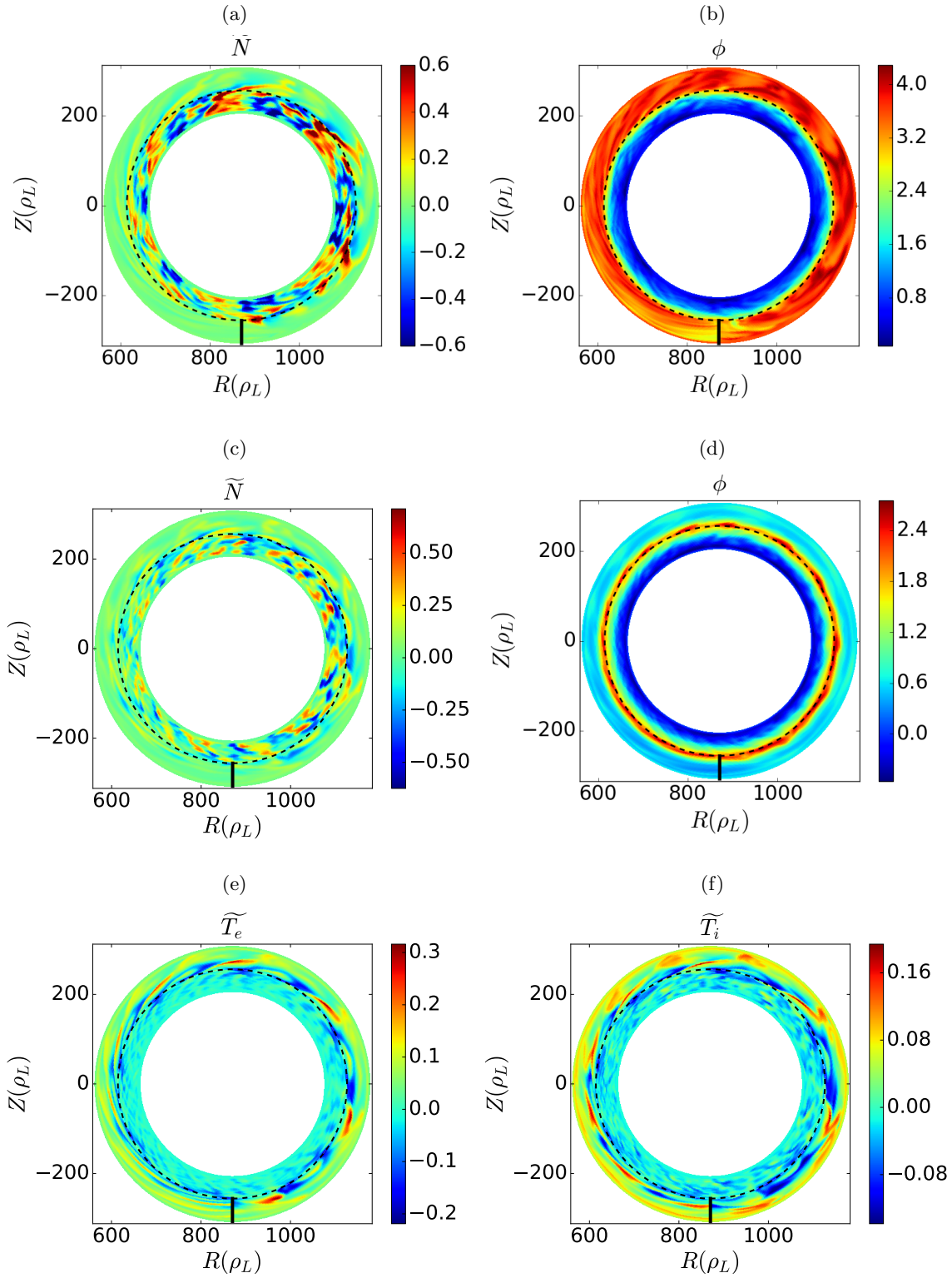

Figure 5.1: Snapshots of poloidal cross-section of density fluctuations ($\widetilde{N}$) for isothermal simulation (a) and anisothermal simulation (c), of potential ($\widetilde{\phi}$) for isothermal simulation (b) and anisothermal simulation (d), and of electron ($\widetilde{T_e}$) (e) and ion ($\widetilde{T_i}$) (f) temperature fluctuations for anisothermal simulation

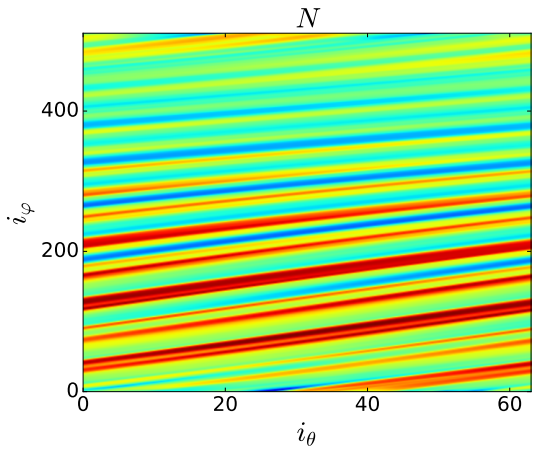

Figure 5.2: Snapshots density on a flux-surface in the near SOL

Even though the intermittent main features are observed both in isothermal and anisothermal simulations, one can already note differences on turbulent structures on Fig. 5.1:

Radial potential profiles: in the anisothermal simulation, the potential profile presents a maximum in the vicinity of the separatrix, when in isothermal simulation the radial variation of the potential is more or less monotone. This ring of high potential corresponds to a zone of high shear discussed in section 5.3.2. This difference on potential between the two simulations will be explained by two different effects in the core and in the SOL region:

- In the core region, the diamagnetic contribution to the polarization drift in the vorticity expression (the second term in $W = \boldsymbol{\nabla} \cdot \left(\frac{1}{B^2} \boldsymbol{\nabla} \phi + \frac{1}{NB^2} \boldsymbol{\nabla} P_i \right)$) pulls the potential to follow the opposite of the ion temperature gradient.
- In the SOL region, the Ohm law forces the potential to follow the electron temperature via the sheath boundary condition. Thus, the potential presents a radial gradient in the anisothermal case when it is rather flat in the isothermal case.

Penetration of density intermittent structures into the SOL: in the isothermal simulation, density intermittent structures present a larger radial extend, and some of the structures even cross all the SOL and go up to the wall. In anisothermal simulation, it is not anymore the case and it seems that density turbulent structures are decorrelated from structures in the core plasma after crossing the separatrix. In fact, this observation could be linked to the presence of a high amplitude shear layer at the separatrix. This effect will be discussed in section 5.3.2 of this chapter.

Finally, one can observe that the turbulent structures of both electron and ion temperature present different spatial repartition than the one of density, indeed they are no large amplitude fluctuations of the temperature in the core region, and there are only evident in the SOL region. This point will be further discussed on properties of turbulence in section 5.2.2.

5.2.2 Characterisation of turbulence structures in TOKAM3X

To study turbulence properties, we start by a characterisation of the shape of intermittent bursts of density, potential, and ion and electron energy in the poloidal and temporal directions. In order to

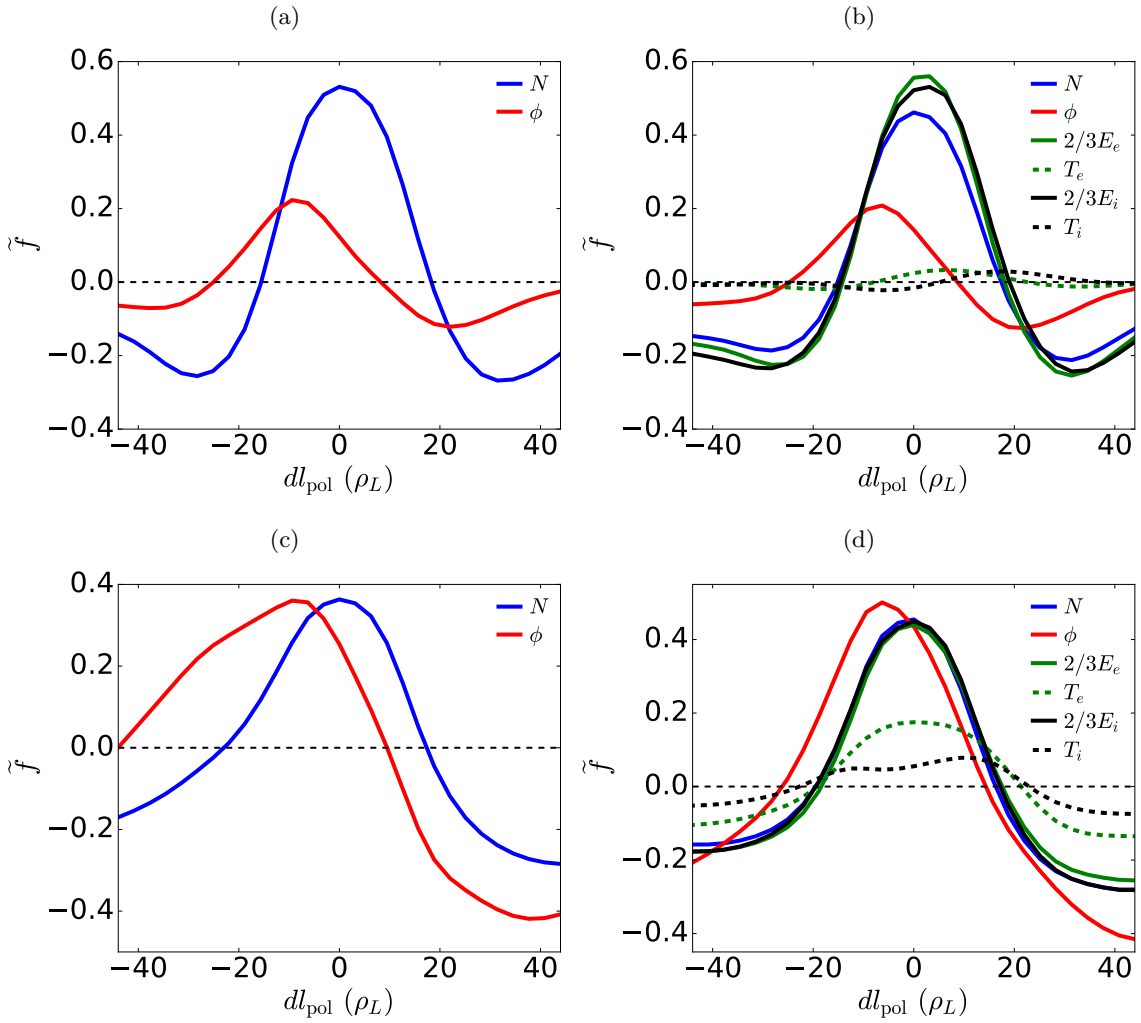

Figure 5.3: Poloidal profiles of intermittent structures using conditional averaging of density, potential, ion and electron energy and ion and electron temperature for isothermal (left) and anisothermal simulations (right) in the core region $\psi/a = 0.9$ (top), and in the SOL region $\psi/a = 1.05$ (bottom).

discriminate the high amplitude events, we proceed to a conditional averaging for density, energies and electric potential. The conditioning is made on N, and only the events with an amplitude higher than 2 local standard deviation above the local mean field in toroidal and temporal direction are considered, as done in section 3.3.2 for Tokam2D.

In 3D simulations, the intermittent structures are determined by their position in temporal, and both poloidal and toroidal directions (t_b, θ_b, φ_b). Due to the ballooning nature of turbulence, the different poloidal position are not equivalent, as turbulence characteristics exhibit large inhomogeneities in this direction [Tamain 14]. For this reason, the area of averaging is restricted to a poloidal extend of 15° on both sides of the outer mid-plane, i.e. the region where turbulence is the most developed.

One can also define an averaged phase-shift, denoted δ, in order to quantify a phase shift between two fields. δ is defined as the arc-cosine of the correlation coefficient of fluctuations between the two fields 5.8 (here no conditional averaging is applied).

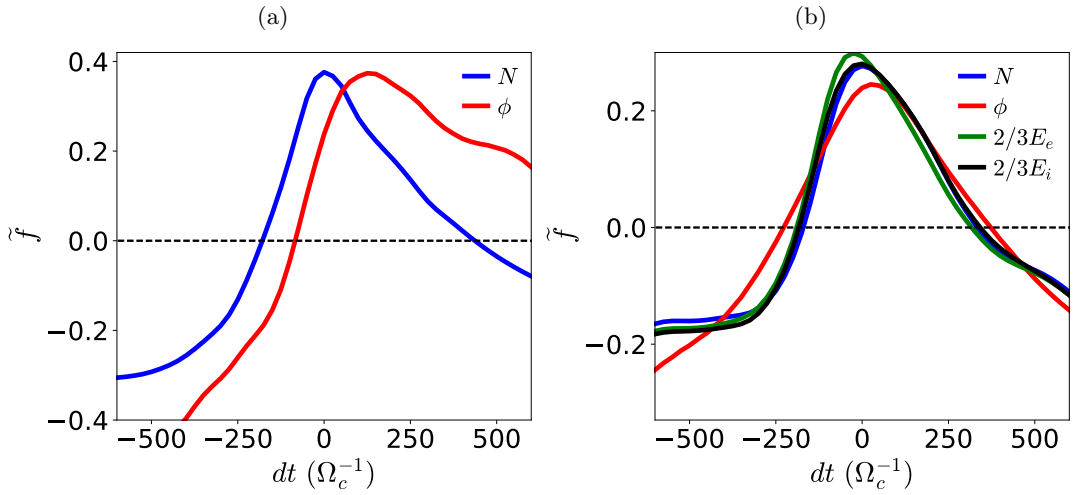

Figure 5.4: Temporal profiles of the intermittent structures using conditional averaging of density, potential, ion and electron energy for isothermal (left) and anisothermal simulations (right) in the SOL region $\psi/a = 1.05$.

$$\delta_{N/\phi}(\psi,\theta) = \arccos\left(\frac{\left\langle \widetilde{N}\widetilde{\phi}\right\rangle_{t,\varphi}}{\left\langle \widetilde{N}^2\right\rangle_{t,\varphi}^{1/2}\left\langle \widetilde{\phi}^2\right\rangle_{t,\varphi}^{1/2}}\right) \tag{5.8}$$

On Fig 5.3. the typical bursts of density, potential, energies and temperatures are reported for isothermal (T_e and T_i constant) and anisothermal simulations. The radial positions ($\psi/a = 0.9$, $\psi/a = 1.05$) have been chosen to be both far from the source area and the walls. The averaging is made on at least 300 events. We check that the sample size is statistically significant by drawing different sub-samples of 150 events with almost no variability in the conditional averaging results. First, if one compares the density and energy turbulence, one observe that the structures of N and of both $2/3 * E_e$ and $2/3 * E_i$ coincide almost perfectly in shape and in amplitude. In the core region, this can be readily explained by the fact that the amplitude of temperature fluctuations are negligible, about 10 times smaller in comparison to the ones of density. Hence, in the core region, the energy turbulence is entirely due to the fluctuation of density and can be resumed by the study of particles turbulence.

In the SOL region, the $\widetilde{T_e}$ and $\widetilde{T_i}$ amplitudes are also smaller than the one of $\widetilde{N}$, but not negligible (about 2 times smaller for $\widetilde{T_e}$ and 3 times for $\widetilde{T_i}$). However, $\widetilde{T_e}$ and $\widetilde{T_i}$ are rather well correlated with $\widetilde{N}$ with $\delta_{N,T_{e/i}}(\psi,\theta) < 20\ °$, which explains the fact that density and energy structures coincide also in this region.

We now compare the results between isothermal and anisothermal simulations. In the core region the structures of density and potential of the two types of simulations present similar characteristics. In both simulations, we find the same poloidal correlation length $\sim 10\rho_L$ (defined in section T2D), and a quasi perfect phase quadrature between density and potential fluctuations in agreement with the experimental observation that found the potential to be in phase with the electric field i.e $\delta_{N/\phi} \approx \pi/2$ [Fedorczak 11].

In the SOL region, we observe a strong re-correlation between density and potential structures in the anisothermal simulation. In fact, this correlation gets stronger when moving from the separatrix to the far SOL, and the averaged phase shift between $\widetilde{N}$ and $\widetilde{\phi}$ at the outer mid-plane, $\delta_{N/\phi,\mathrm{iso}}(\psi, 0°)$ goes from $\sim \pi/2$ in the core region down to 0.2π in the far SOL. In the isothermal simulation, $\widetilde{N}$ and $\widetilde{\phi}$ present also a re-correlation in the SOL, however this is less marked than in the anisothermal case, and $\delta_{N/\phi,\mathrm{iso}}(\psi, 0°)$ goes only down to $\approx 0.3\pi$. One can speculate that this could be attributed to the fact that electron temperature fluctuations are taken into account in the Bohm boundary condition at the target, which has been proved to trigger a re-correlation of the structures of N and ϕ in the 2D models Tokam2D due to the sheath-driven conductive wall instability. Note that the turbulent structures have been studied at other poloidal locations, and similar characteristics are retrieved both at the top and at the inner mid-plane.

Finally, if we consider the temporal profile of the intermittent structures in the SOL region Fig 5.4 we find that the shape of the turbulent structures in isothermal and anisothermal simulations presents once again similar shape, in particular they exhibit the same time scale $\sim 400\Omega_c^{-1}$.

Note that all the conclusions presented on turbulent structures on isothermal simulation with constant temperature are also valid for the isothermal simulation with temperature profiles thus the differences observe in this section can indeed be attributed to the temperature dynamics.

5.2.3 Statistical properties

One can further study the intermittent features by looking at the statistical properties of turbulence. In agreement with experimental results, turbulence in 3D simulations presents a high fluctuation level of density at the outer board SOL, with the same order of magnitude in isothermal and anisothermal simulations, comprised between 30% and 40%. The density fluctuations exhibit a poloidal asymmetry, with a smaller amplitude at the inner board, lower than 20% for both type of simulations.

The low fluctuation level of temperatures in the core region, lower than 5%, is in agreement with the previous results (section 5.2.2) showing that the temperature fluctuations are negligible in the core region. In the SOL region, the temperature fluctuation levels at the outer board are smaller than the ones of density, $\sim 20\%$ for T_e and $\sim 10\%$ for T_i. Moreover, they do not present any evident in/out board asymmetry in comparison with density. However, as the temperature fluctuations are coherent with the ones of density, it results in a high level of energy fluctuation level at the outer board, higher than for density, 40% to 70% for E_e and 30% to 50% for E_i, with important in/out board asymmetry.

In fact the statistical properties of the temperature could have two main physical explanations detailed below.

First, a significant difference between the equation of density and the ones of energy is the presence of the fast parallel diffusive terms $\boldsymbol{\nabla}\cdot\left(K_0^{e/i}T_{e/i}^{5/2}\boldsymbol{\nabla}_\parallel T_{e/i}\mathbf{b}\right)$ with $K_0^{e/i}\sim 10^4-10^6\gg 1$ in the equations of energy. The expression in the divergence is of several orders of magnitude higher than other terms of advection of the order of one or less. If one considers a flux-surface in the core region with an irrational safety-factor value, all points in this flux surface would be fast linked with each other due to the strong parallel transport. This homogenization on a flux surface could thus explain the low level

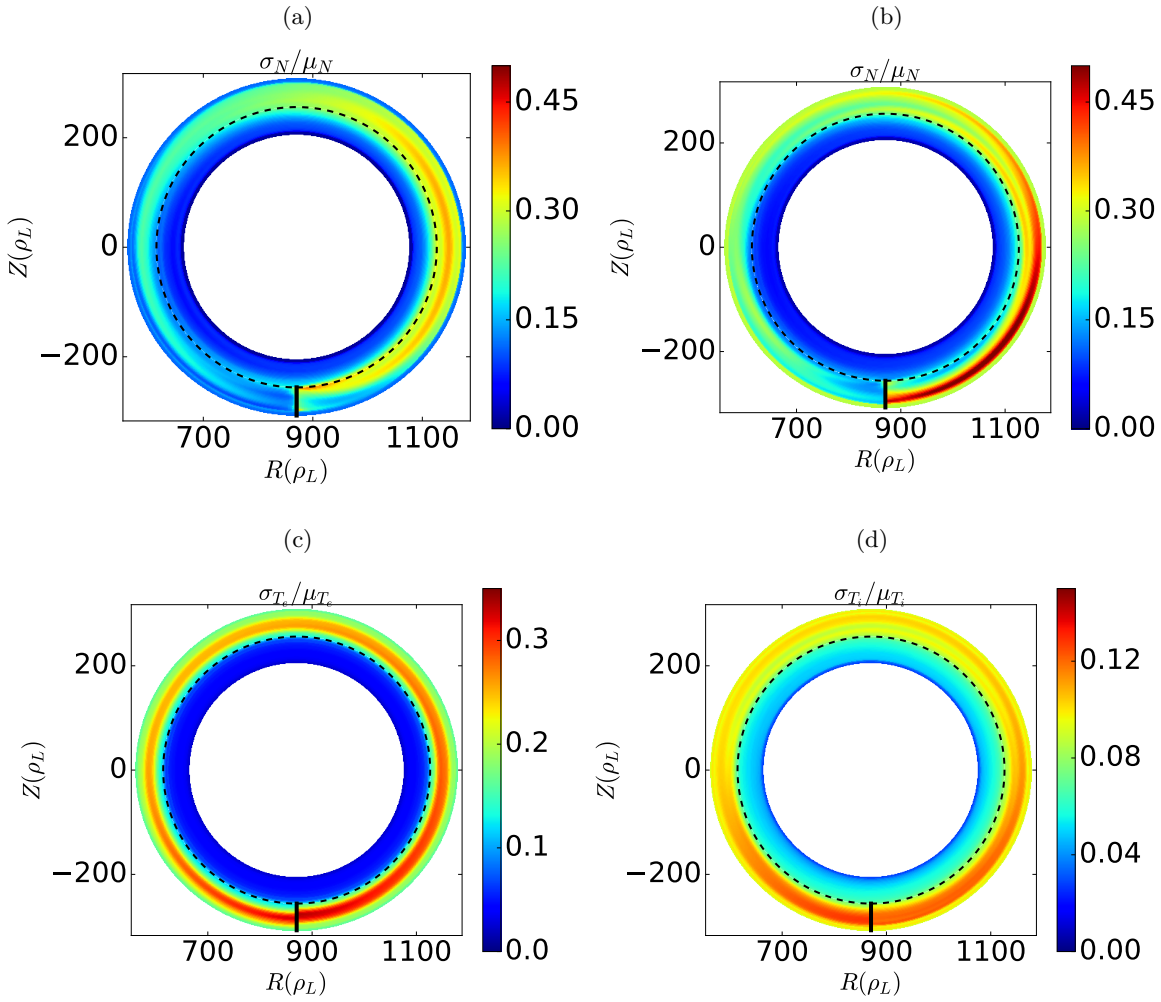

Figure 5.5: Poloidal map of level of fluctuations of density in isothermal simulation (a) and for density (b), electron (c) and ion temperature (d) in anisothermal simulations

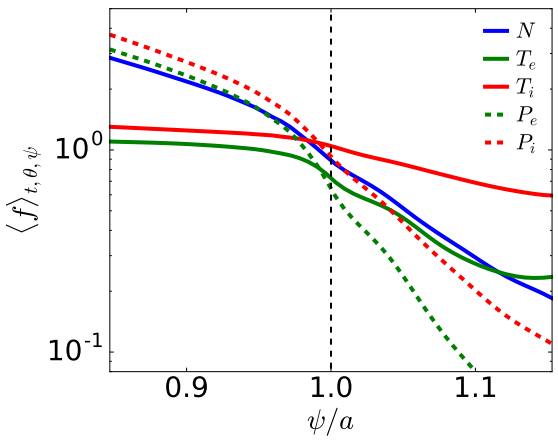

Figure 5.6: Flux-surface averaged radial profiles of the density, of the electron and ion temperature and of the electron and ion pressure for the anisothermal simulation.

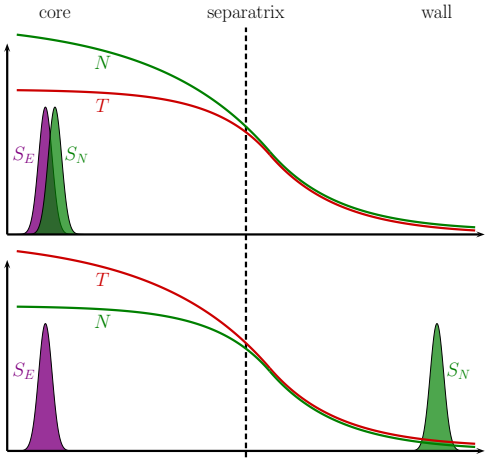

Figure 5.7: Scheme of the particle and energy sources as implemented in the code (top) and as are expected in reality (bottom) TOKAM3X and consequent density and temperature profiles

of temperature fluctuations in the core region. This argument can also explain the low fluctuation level in the SOL, however the symmetry breaking due to the presence of the wall can explain that the intermittent structures of temperatures are more developed in this region. In the same way, the smaller poloidal asymmetry of the fluctuation level of temperatures (i.e. less ballooned) can also be attributed to this fast homogenization in the parallel direction.

It is worth to note that this high parallel diffusion is difficult to handle computationally and necessitate a specific numerical scheme [Günter 05]. This term could also be a source of an artificial spurious effect damping partially temperature fluctuations. This question has not been investigating yet but would need further numerical verification such as the one presented in Ref. [Cartier-Michaud 16].

The second explanation comes from the fact that, in the code, both sources of particle and energy are located at the inner boundary, as TOKAM3X does not include self-consistent particle fuelling. On the contrary, in reality, the principal source of particles comes from the wall region, and only the source of energy is located in the core region, as illustrated on Fig. 5.7. In TOKAM3X, the source location has for consequence that the density profile presents an important gradient in a core region Fig. 5.6. This important gradient combined with the high density fluctuation level is responsible for a large intermittent particle transport, efficient enough to transport both particles and energy from the core to the SOL region, without further fluctuations or gradients of temperature. In fact, the temperature gradients in the core are negligible compared to the one of density Fig. 5.6, and ion and electron pressure profiles coincide almost with the density profile. If the fuelling in particles were self-consistent, one could expect a different pattern with a flatter density profile in the core region and sharper temperature profiles, inducing more temperature fluctuations in the core region.

On Fig. 5.8, the PDF of the particles and energy turbulent fluxes at the outer mid-plane are reported for anisothermal simulations in the SOL at $\psi/a = 1.05$. The PDFs of particles and energy turbulent fluxes are representative of a highly intermittent transport, with a shape far from a Gaussian

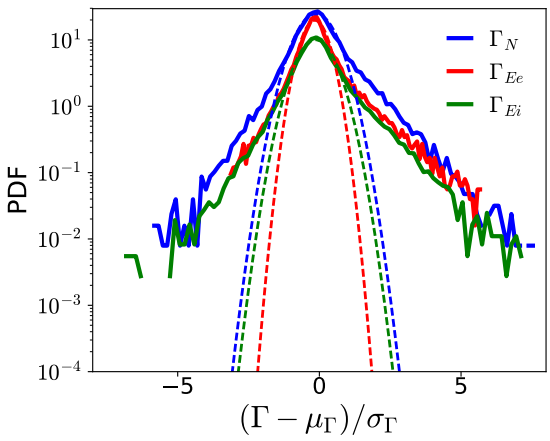

Figure 5.8: PDF of particles and energy turbulent flux in anisothermal simulations at the outer mid-plane and at the radial location $r/a = 1.1$ a Gaussian fit of the PDF is reported in dashed lines. PDF are reported in log scale, centered on zeros, normalized by standard deviation

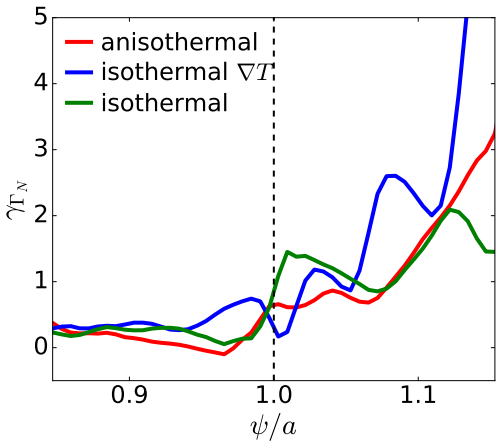

Figure 5.9: Radial profile at the outer mid-plane of the skewness

distribution representative of a diffusive-like transport. They exhibit a long tail both for large positive or negative values. The weight of the PDF wings can be quantified by the kurtosis momentum $\mathcal{K}$, the kurtosis has a strong radial dependency and goes from 1 in the core region up to more than 10 in the far SOL Fig. 5.9. In spite of the presence of a tail in the negative part, the distribution of the turbulent transport is nonetheless positively skewed, from about 1 in the near SOL up to 4 in the far SOL, explained by the fact that the tail in the positive part is longer. The amplitudes of skewness and kurtosis are about the same in isothermal and anisothermal simulation, presenting similarity with the work presented in [Tamain 15], small skewness and kurtosis in the core region and increasing in the vicinity of the separatrix and all along the SOL.

In conclusion of this section, we have shown that in the studied regime:

- Turbulence exhibits similar characteristics in isothermal and anisothermal simulations: similar intermittent structures, level of fluctuations, characteristic scales...
- In the present regime, we observe flat temperature profiles and little temperature fluctuations in the core region. This has for consequences that in the core region the energy structure coincides with the ones of density, and the $\mathbf{E}\times\mathbf{B}$ turbulent transport is transported by density fluctuations.

5.3 Transport of particles and energy in Tokam3X

5.3.1 Intermittent transport of particles and energy in Tokam3X

We now characterise the cross-field transport averaged on flux surfaces. On Fig 5.10, the different contributions to the ion energy flux on the flux-surfaces are reported as a function of the radial position for anisothermal simulation. The figure is not reported for the electron energy flux, as the

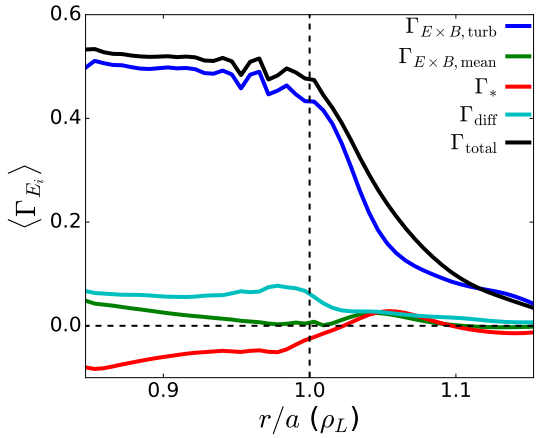

Figure 5.10: Ion energy flux averaged on a flux-surface as a function of the radius for anisothermal simulations

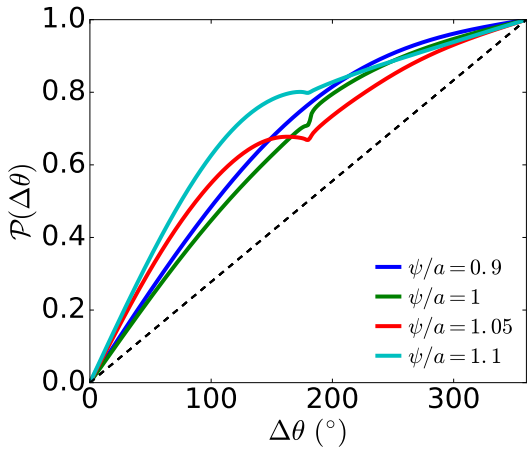

Figure 5.11: Proportion $\mathcal{P}$ of the total $\mathbf{E}\times\mathbf{B}$ ion energy flux flowing through a poloidal angular section of $\Delta\theta$ centred on the outboard mid-plane.

fluxes present exactly the same characteristics. Note that here, the fluctuating and the mean-field components of $\mathbf{E}\times\mathbf{B}$ cross-field fluxes are separated and defined as follows:

$$\langle F u^{\psi}_{\mathbf{E}\times\mathbf{B}}\rangle_{t,\theta,\varphi} = \underbrace{\langle F\rangle\langle u^{\psi}_{\mathbf{E}\times\mathbf{B}}\rangle_{t,\theta,\varphi}}_{\Gamma^{\text{mean-field}}_{\mathbf{E}\times\mathbf{B}}} + \underbrace{\langle \widetilde{F}\widetilde{u}^{\psi}_{\mathbf{E}\times\mathbf{B}}\rangle_{t,\theta,\varphi}}_{\Gamma^{\text{turb}}_{\mathbf{E}\times\mathbf{B}}} \text{ for } F \in N, E_e, E_i \tag{5.9}$$

The flux surface balance reveals that, in the studied regime, the radial transport of both particles and energy is governed by the $\mathbf{E}\times\mathbf{B}$-advection of intermittent structures $\Gamma^{\text{turb}}_{\mathbf{E}\times\mathbf{B}}$ which weights for more than 80% of the total flux at the separatrix Table 5.1. This result is also valid for the particles flux of the two isothermal simulations, thus one can conclude that the studied regime here is an L-mode like regime for the three types of simulation.

F	N_{iso}	$N_{\text{iso},\boldsymbol{\nabla}T}$	N_{aniso}	E_e	E_i
$\frac{\Gamma_{\mathbf{E}\times\mathbf{B},F}}{\Gamma_{\text{tot},F}}$	90%	70%	84%	90%	93%

Table 5.1: Contribution of the Γ_{turb} to the total flux at the separatrix for particles, electron and ion energy balance and for both isothermal and anisothermal simulations

Moreover, the $\mathbf{E}\times\mathbf{B}$ radial fluxes present the classical ballooning feature, which can be estimated by $\mathcal{P}$ the fraction of transport $\mathbf{E}\times\mathbf{B}$ advected within a poloidal extend of θ around the outer mid-plane:

$$\mathcal{P}(\psi,\Delta\theta) = \frac{\int_{-\Delta\theta/2}^{+\Delta\theta/2}\langle\Gamma_{\psi,\mathbf{E}\times\mathbf{B}}\rangle_{t,\varphi}\,\mathrm{d}\theta}{\oint\langle\Gamma_{\psi,\mathbf{E}\times\mathbf{B}}\rangle_{t,\varphi}\,\mathrm{d}\theta} \tag{5.10}$$

On Fig. 5.11 $\mathcal{P}$ is reported for the ion energy flux in the anisothermal simulations and at several radial positions. As for the radial profiles of the flux, the figure for electron energy is not reported, as the $\mathbf{E}\times\mathbf{B}$ flux presents exactly the same ballooning characteristic. One can observe that the ion energy $\mathbf{E}\times\mathbf{B}$ flux averaged in time and ϕ-direction presents a ballooned distribution, and more

than 75% of the $\mathbf{E} \times \mathbf{B}$ flux crosses the separatrix in outer half of the torus, as already reported in [Colin 15b]. This ballooning property is retrieved both in the core and in the SOL region. Thus, this is a property of edge turbulence and not only the SOL, even though the ballooning distribution is less marked in the core region. Note that for radial positions in the SOL, the curves decrease in the vicinity of $\Delta\theta = 180°$ that is to say when the poloidal extend comes close to the limiter. This effect is due to inward flux in the limiter region.

In Table 5.2, the values of $\mathcal{P}$ for $\psi/a = 1.1$ and $\Delta\theta = 120°$ are reported for the fields N, E_e and E_i for the three studied simulations. We deduce that the ballooning property is retrieved for all fields and both isothermal and anisothermal simulations. However, one can note that the simulation without temperature gradient exhibits a lower value of $\mathcal{P}$ in the SOL, which is also true for other radial location.

This ballooning transport is responsible for important poloidal asymmetries on density which presents a variation of a factor about almost 2 between inner and outer mid-plane.

F	N_{iso}	$N_{\text{iso},\boldsymbol{\nabla}T}$	N_{aniso}	E_e	E_i
$\mathcal{P}\,(\psi/a = 1.1, \Delta\theta = 120°)$	60%	77%	73%	73%	71%

Table 5.2: $\mathcal{P}$ at the radial position $\psi/a = 1.1$ for particles, electron and ion energy balance and for both isothermal and anisothermal simulations

Finally, in the three simulations, the transport driven by $\boldsymbol{\nabla}B$-drift advection does not contribute significantly to the total flux neither in particle nor in energy balance ($|\Gamma_*/\Gamma_{\text{tot}}| < 5\%$). The observed plasma regime is thus far from the $\boldsymbol{\nabla}B$-dominated regime presented in Chapter 4. Nevertheless, this is in agreement with results presented previously. Indeed, a coarse estimation of the diffusion corresponding to the anomalous transport in the simulations gives $D_{\text{anomalous}} = \frac{\sqrt{2}\lambda_N^2}{2\pi q R_0} \approx 2\,\text{m}^2\,\text{s}^{-1}$, well above the diffusion values of transition towards the $\boldsymbol{\nabla}B$-drift dominated regime. Hence, no universal conclusions on the role of this type of mechanism can be drawn without further investigations, specifically concerning H-mode like regime.

5.3.2 Impact of the shear layer on the cross-field transport

Even though the cross-field transport at the separatrix is dominated by $\mathbf{E} \times \mathbf{B}$ turbulence in the three studied simulations, there is a significant difference of the radial shear of the poloidal $\mathbf{E} \times \mathbf{B}$ velocity Eq. 5.11 in the vicinity of the separatrix.

$$\partial_\psi \left\langle \frac{1}{B} \partial_\psi \phi \right\rangle_{\theta,\varphi} \tag{5.11}$$

In anisothermal simulation, the amplitude of the shear is twice the one in isothermal simulation Fig. 5.12 a). Moreover, the isothermal simulation with temperature gradients also exhibits this shear increase with the same amplitude. Thus, the shear increase can be attributed to presence of temperature gradients and not to the addition of temperature dynamics. The addition of temperature gradient combines two different effects:

- T_i-gradient impacts the potential profile in the core region via the modification of the second

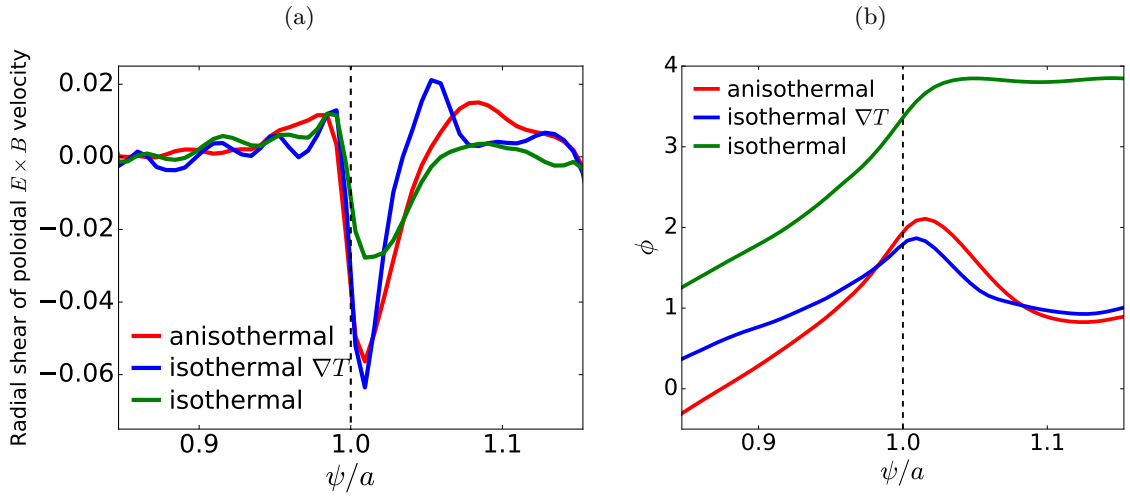

Figure 5.12: Flux-surface averaged radial profile of the radial shear of the poloidal $\mathbf{E}\times\mathbf{B}$ velocity (left) and of the electrostatic potential (right) for anisothermal, isothermal $\boldsymbol{\nabla}T$ and isothermal simulations (right)

term of the generalized vorticity. However, considering the flat ion temperature profiles in the core region Fig 5.6, one expects little impact of the T_i-gradient on the potential profile in the core region.

- T_e-gradient modifies the potential which follows $3T_e$ in the SOL due to the sheath boundary condition.

Now, on Fig. 5.12 b), one can observe that the potential radial profiles of anisothermal and isothermal simulations present a similar slope in the core region, as expected from the similar gradients of N and P_i Fig 5.6. The principal difference is observed in the SOL region where the potential decreases in the simulations including $\boldsymbol{\nabla}T_e$, when it stays rather constant in the case with constant temperature. Hence, one concludes that, in this regime, the increase of the shear amplitude can be attributed to the additional $\boldsymbol{\nabla}T_e$ modifying the potential in the SOL region.

The electrostatic shear is known to be responsible for a decorrelation of the turbulent structures [Fedorczak 13], which penetrates deeper into the SOL in the presence of a smaller shear amplitude. This mechanism has been known for a long time and early limiter experiments in TEXTOR already suggested that the radial electric field and induced poloidal rotation played a crucial role in the creation of transport barrier [Taylor 89, Weynants 92]. On Fig. 5.13, we report the flux-surface averaged of the particular $\mathbf{E}\times\mathbf{B}$ flux as a function of time and the radial position. We observe indeed that the $\mathbf{E}\times\mathbf{B}$ flux in isothermal simulation with constant temperature presents a longer penetration length than in the simulations presenting a high amplitude shear layer (i.e the anisothermal and isothermal $\boldsymbol{\nabla}T$ simulations). This would lead to think that the shear amplitude is the mechanism responsible for a reduction of the penetration of turbulent structures into the SOL.

If we now look to the ratio of $\mathbf{E}\times\mathbf{B}$ particles turbulent flux in the total flux Fig. 5.14, we observe that for the isothermal $\boldsymbol{\nabla}T$ and anisothermal simulations, the proportion of the turbulent transport in the total flux falls down to respectively 50% and 65% in the SOL. However, in the anisothermal

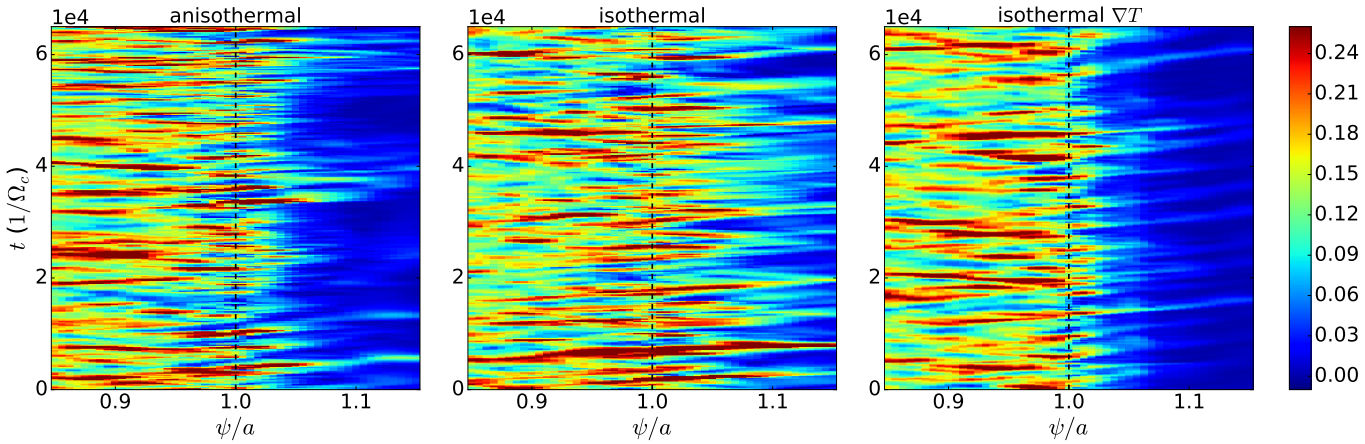

Figure 5.13: Color plot of the flux-surface averaged radial $\mathbf{E} \times \mathbf{B}$ particles flux as a function of time and radius for anisothermal simulation (left), isothermal simulation with T constant (middle), and isothermal $\boldsymbol{\nabla} T$ (right)

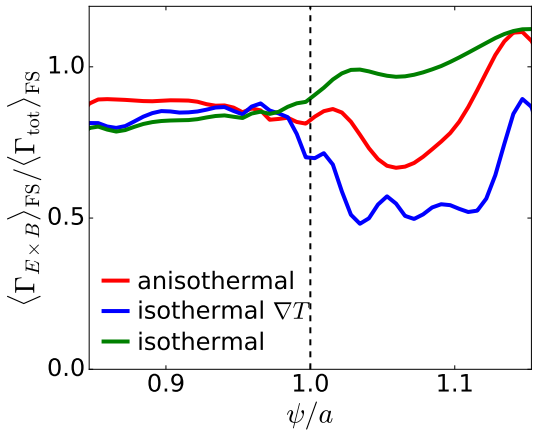

Figure 5.14: Ratio between the flux-surface averaged of radial $\mathbf{E} \times \mathbf{B}$ particles flux and total radial flux as a function of the radius for anisothermal simulation (blue), isothermal simulation with T constant (green), and isothermal $\boldsymbol{\nabla} T$ (red)

simulation, the maximal reduction of turbulence ($\psi/a \approx 1.05$) is located after the radial position of the shear layer ($\psi/a \approx 1.005$). Hence, even though we expect the high amplitude shear layer and the reduction of the turbulence in the SOL to be linked somewhat, the mechanism of interplay between the shear layer and the reduction of the turbulent flux in the SOL remains unclear, and requires further investigations. So far, one cannot talk about a transport barrier since the $\mathbf{E} \times \mathbf{B}$ transport proportion in the global balance does not decrease significantly in the vicinity of the separatrix, i.e., the region of high shear amplitude.

It is worth noting that the reduction of the turbulent transport is less pronounced in the anisothermal case, which could be attributed to a modification of the turbulence dynamics, for instance due to the existence of an additional mechanism of instability at play in the presence of temperature fluctuations.

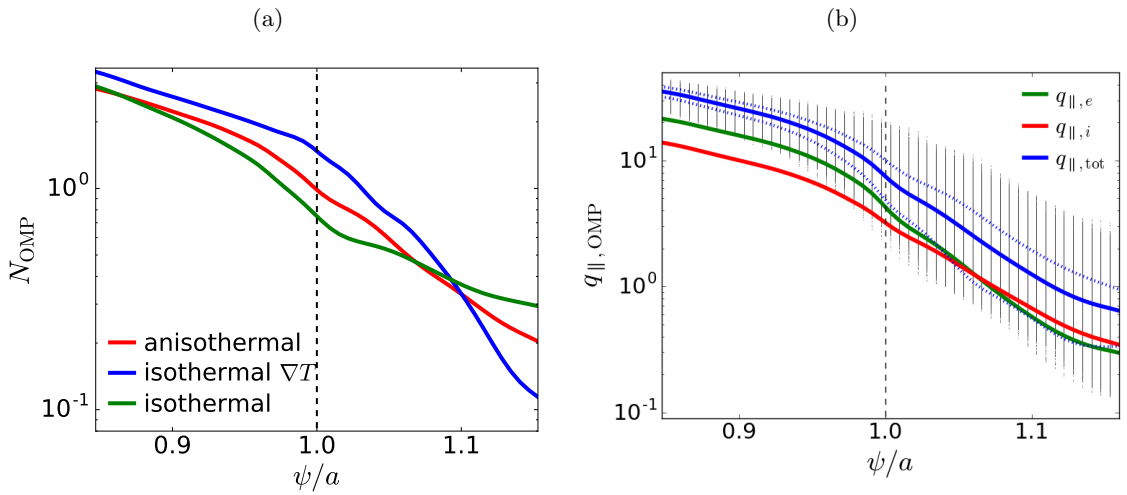

Figure 5.15: (a): Radial profile of density at the outer-mid plane for isothermal, isothermal $\boldsymbol{\nabla} T$ and anisothermal simulations. (b): Radial profile of the heat fluxes at the outer-mid plane, grey dots represent the dispersion of the value at each radial position, and the dashed lines the standard deviation for the total heat flux.

The amplitude of the shear seems also to have an impact on the SOL density profiles. In isothermal simulation with $T_e = T_i = 1$, other things being equal in particular transverse transport, the density profiles should be steeper than in anisothermal and isothermal $\boldsymbol{\nabla} T$ simulations. Indeed, in the SOL $T_{e,\mathrm{aniso}} + T_{i,\mathrm{aniso}} < 2$: $T_{e,\mathrm{aniso}} + T_{i,\mathrm{aniso}} \approx 1.3$ at $\psi/a = 1.05$ and ≈ 1 at $\psi/a = 1.1$ and ≈ 1. Thus, the parallel sheath losses ($\propto \sqrt{T_e + T_i}$) are smaller by a factor up to $\sqrt{2}$ in the anisothermal case. However, one can observe on Fig. 5.15 a), that the density gradient in the isothermal simulation is of the same order as the one in the anisothermal and isothermal $\boldsymbol{\nabla} T$ simulation, the SOL's profiles are even flatter in the isothermal case Fig. 5.17. This can be explained by the reduction of cross-field transport due to the smaller penetration length of turbulent structures into the SOL in anisothermal simulation, which compensates the reduction of the parallel losses.

5.4 SOL width in TOKAM3X

In this final section, we draw some characteristics of the power SOL width observed in the anisothermal simulation, the objective is not to give a quantitative description of λ_q for an experimental comparison but to look at the qualitative features of the heat flux profiles.

Here, we define the power SOL width (λ_q) as the e-folding length of the parallel heat flux (5.12).

$$q_\parallel = q_{\parallel,e} + q_{\parallel,i} = \gamma_e \sqrt{T_e + T_i} N T_e + \gamma_i \sqrt{T_e + T_i} N T_i \tag{5.12}$$

The e-folding length is estimated by a least squares regression.

On Fig. 5.15 b), the radial profiles averaged in the toroidal direction and time of electron, ion and total heat flux are reported at the outer mid-plane. On q_e profile, one can observe a slight stiffening of the profile at the separatrix. This feature, if not striking on radial profiles, is easily observed on the radial profile of the local gradient Fig. 5.16 b), presenting higher gradient amplitude in the vicinity

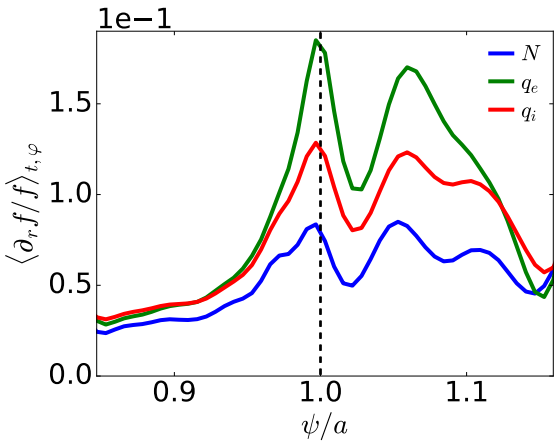

Figure 5.16: Radial profiles of local inverse decay length for density, electron and ion parallel heat fluxes

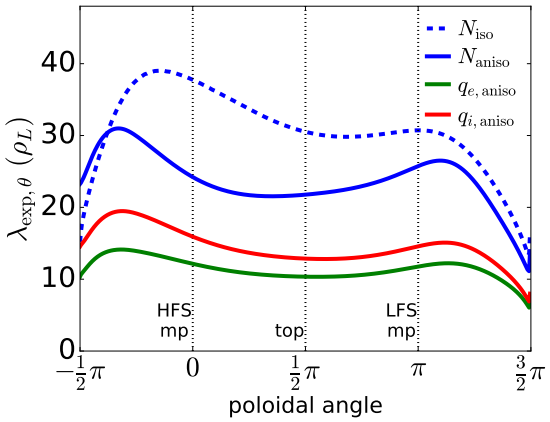

Figure 5.17: e-folding decay length $\lambda_{\exp}$ as a function of the poloidal position for density and electron and ion heat flux, $\theta = 0°$ being the outer mid-plane and $\theta = 90°$ the top of the machine

of the separatrix. This increase of the gradient is more significant for the heat flux profiles than for the density profile, which is reminiscent of the narrow feature observed in experiment. This feature is probably linked to the presence of the shear at the separatrix as suggested by Ref. [Halpern 17], however further work on this question would be required to have a better understanding of this physics. Moreover, as said in the previous section, ∇B-drift transport does not contribute significantly to the global energy transport, which seems to point out that it is not the mechanism responsible for the λ_q narrow feature as suggested by Ref. [Kočan 15, Goldston 15].

On Fig. 5.15 b), the values of each temporal and toroidal point are reported as small scatter, which also permits to remark that the heat flux profile in the SOL is highly intermittent. In particular, the maximal value of the heat flux is about 3 times the mean values at the separatrix, but this ratio goes up to more than 5 in the far SOL, thus the temporal variation of heat flux should not be overlooked.

Finally, on Fig. 5.17, the estimation of λ_q is reported as a function of the poloidal location. Observe that the SOL width presents also significant poloidal asymmetry, observed experimentally in L-mode for particle SOL width [Gunn 07], the factor between the maximal and minimal value of the λ_q as function of the poloidal location is about 2. The poloidal asymmetries are the same for all the fields N, q_e and q_i, with the highest values of λ_q around the outer board, where turbulence takes place.

5.5 Conclusion

In this chapter, we have shown that turbulence in the anisothermal simulation presents similar characteristics (fluctuating structures and statistical properties) than in the isothermal ones. Hence, the impact of the temperature fluctuations on turbulence in 3D simulations is less striking than in 2D simulations. The clear impact of the SCW instability described with TOKAM2D is not observed, even though the high correlation between density and potential fluctuation in the SOL region in the anisothermal simulation is reminiscent of this mechanism. However, only one anisothermal simulation has been run so far, and further investigations, in particular with a parametric scan, would be

necessary to study the presence of the SCW instability in 3D simulation.

In the present simulations, the plasma regime is close to an L-mode like regime where the transport is dominated by turbulence. The transport of particles and energy presents the same characteristics (highly intermittent, ballooned) and is close from the ones observed in the isothermal simulations. This is in agreement with the fact that, in the studied simulations, the density fluctuations are the ones responsible for the turbulent fluxes of energy, and that temperature fluctuations are rather low.

Nevertheless, a key difference between the isothermal and anisothermal simulations is observed with the apparition of a shear layer of larger amplitude in anisothermal simulations. The shear amplitude is due to the presence of an electron temperature gradient, which pulls the potential to follow T_e in the SOL region. However, such a shear does not seem driven by the addition of temperature dynamics as a shear layer of the same amplitude is retrieved in an isothermal simulation with corresponding temperature gradients. Moreover, this shear layer seems to be come along with a reduction of the flux penetration length observed both in isothermal $\boldsymbol{\nabla} T$ and anisothermal simulations, but the clear interplay between turbulence and this shear layer remains unclear.

Considering all the characteristics observed in this work it seems to point out that in the studied regime, the addition of temperature dynamics has not a strong impact apart from the one due to the addition of temperature gradient.

Finally, we have shown that the power heat fluxes are highly inhomogeneous (in time and space) in particular a narrow features reminiscent of experimental results is observed on the heat flux profile. However, the mechanism responsible for such feature is not clear identify, and this problematic would need further investigations.

Conclusions and perspectives

This work was motivated by the power exhaust problematics. This is a critical issue for the economical viability of future fusion devices requiring a sufficient power spreading on Plasma Facing Component potentially damaged by high energy deposition. For a given input power, the peak heat flux at the target is set by the SOL heat channel width, λ_q, and divertor spreading. Hence, the heat channel width is a key parameter for tokamak operation. This work is dedicated to the improvement of the understanding of the physics underlying the heat transport, a critical task for the engineering design of future Tokamak devices like ITER and DEMO.

The study of turbulent heat transport in anisothermal L-mode like simulations has been realised using two fluid codes: TOKAM2D, a 2D model with simplified geometry, which has permitted us to review the basic properties of energy turbulent structures and transport and TOKAM3X which has allowed us to have a more complete approach with the study of 3D properties of the turbulence.

The first conclusion drawn from the comparison between isothermal and anisothermal model is that the inclusion of self-consistent fluctuations of temperature does not change the general phenomenology of the turbulence. Indeed, in isothermal and anisothermal simulations, one observes the same kind of intermittent structures with comparable shapes and highly intermittent transport. In 3D simulation, one retrieves the same poloidal asymmetries (ballooned fluctuation levels and ballooned turbulent fluxes) which are characteristic of interchange turbulence. Furthermore, in 3D simulations, we point out that the turbulent flux of energy seems to be transported almost entirely by density fluctuations. One should be caution with this conclusion, as no parametric scans has been performed so far with TOKAM3X simulations. Thus, the result of the present studied regime might not stand in other types of regime (for example H-mode, divertor simulations, or other regime of collisionality). In particular, we point out that if the neutral description was included, the modification of the particle source localisation could lead to a completely different pattern with a flatter density profile in the core region, inducing more temperature fluctuations. Nevertheless, if this were proved to be true, at least in a certain range of parameters, this is significant information permitting to reduce the numerical cost of the simulation under certain conditions.

Although the general phenomenology of turbulence stays the same, one can also point out differences between isothermal and anisothermal models. First, the inclusion of electron temperature fluctuations drives a drift-wave-like mechanism of instability, the sheath negative resistance instability, triggered by the T_e fluctuations in the Bohm boundary conditions. In the simulations, this additional mechanism acts on top of the well-known interchange drive. The characterisation of the turbulence features in TOKAM2D simulations, using the input of linear analysis, has revealed that the addi-

tional instability has a significant impact: it increases the turbulence scales, triggers a re-correlation between density and potential fluctuation, and a reduction of the statistical skewness. This instability impacts not only the turbulence characteristics but also the steady-state equilibrium, thus the SOL width, through the modification of the level of cross-field turbulent transport and of the parallel losses. Although this mechanism has been clearly identified only in the 2D simulation, some features in 3D simulations seems to point out that such mechanism could also be at play in anisothermal simulations.

Finally, another key difference between isothermal and anisothermal simulations can be underlined. In 3D simulations, the addition of temperature gradients, whether one takes into account temperature fluctuations or not, triggers a high amplitude shear layer via the modification of the potential profile. This shear layer seems to impact somewhat the turbulence, resulting in a consequent reduction of turbulent flux penetration length. However, the mechanism of interaction between the shear layer and the turbulence remains unclear. This impact on turbulence might also have something to do with large inhomogeneity observed on the heat flux radial profiles in the SOL region. More specifically, the heat flux radial profiles present a sharp narrow feature reminiscent of experimental results. However, as for the role of the shear layer, the physics of the formation of such a narrow feature remains unclear and requires further investigation.

Going towards the understanding of transport mechanisms at play in the H-mode regime, we have studied the plasma equilibrium in the limits of low anomalous transport with the means of transport code. In this paradigm, the work on SolEdge2D was entirely dedicated to the study of the large scale transport by magnetic drifts as such drift orbits effects has been pointed out as a potential key player in the transport in H-mode plasma. The first conclusion of this work is that in all cases, including anisothermal simulations, simulations taking account neutral species, and all geometries, a $\boldsymbol{\nabla} B$ drift dominated regime is reached at low anomalous transport level. In this regime, the value of the SOL particle or power width is set by the $\boldsymbol{\nabla} B$ drift and does not depend anymore on the diffusion level. However, the relevance of such regime remains questionable as it exits only at extremely low level of transverse transport, way below the neoclassical level.

Furthermore, this regime is also characterized by a complex plasma equilibrium presenting supersonic transition and steady-state shocks. If this regime indeed exist, one should be able to retrieve its highly distinctive characteristic in experiments, namely high poloidal inhomogeneities as well as important poloidal gradients of the density and the parallel Mach number. So far, such characteristic has never been reported in experience. However, this is to balance with the fact that one has only an incomplete picture of the plasma state for each experiment. This is specially true for H-mode experience where it is challenging to dive probes into the plasma without taking risks for the integrity of the diagnostic. Hence, to draw further conclusions on the relevance of such mechanism one should design dedicated experimental sessions.

In any case, if this $\boldsymbol{\nabla} B$ drift dominated regime was proved to exist, one should take into account the complexity of the parallel equilibrium in order to make a reliable estimate. In particular, the centrifugal drift should not be neglected.

Our results cast also a new light on the heuristic-drift based model, which relies on such a type of regime, and allows us to discuss its validity and its limits. We show that the oversimplification of the parallel dynamics leads to discrepancies with the numerical estimations. The SOL widths found

in numerical simulations are significantly lower, of a factor that comprise between 2 and 3, than the estimate of HD-model. Moreover, the parametric functional dependencies of the estimate, in particular the one on T, are not perfectly retrieved.

Finally, to further investigate large scale convective transport it would be necessary to look deeper into the role of additional physics. In particular one should investigate the role of neutral in different recycling regimes and above all the impact of the inclusion of $\mathbf{E} \times \mathbf{B}$ drift. If the study of the charge balance is out of the scope of this work, due to its high numerical complexity, we expect an important response with it inclusion. Indeed, in the $\boldsymbol{\nabla} B$-drift dominated regime, the principal mechanism of transport leads to a charge separation. Hence, taking into account the charge balance would lead to an important response of the electric field, and to large parallel Pfirsch–Schlüter return currents. Further work on this question is mandatory in order to have a better understanding of this physics

Conclusions on both turbulence and large-scale transport have been drawn in this work. However, we should go further into the investigation of their interplay and predominance in different regimes with 3D turbulent simulations in realistic geometry. So far, no parametric scans have been performed for TOKAM3X anisothermal simulations due to their numerical cost. The anisothermal simulation studied in the present work exhibits a regime close to L-mode, where both particle and energy transports are largely dominated by turbulence, with $\Gamma_{\text{turb}}/\Gamma_{\text{tot}} \sim 75\%$. Thus, we cannot draw any statement on the existence of a $\boldsymbol{\nabla} B$ drift dominated regime in a turbulent simulation. In fact, the high level of anomalous transport observed in the turbulent simulation is well above level of the transition towards a $\boldsymbol{\nabla} B$-drift dominated regime found in Chapter 4. Hence, the fact that the $\boldsymbol{\nabla}$ drift does not contribute to the total flux of the turbulent simulation is in agreement with the results of the work dedicated the large-scale drift transport.

Likewise, the conclusion on the high similarity of turbulence phenomenology between anisothermal and isothermal simulations only stands for the studied regime (L-mode) at relatively high collisionality. Especially, the result that the energy transport is essentially driven by the density fluctuations is susceptible to change, in particular as mentioned earlier with a self-consistent description of the neutral species. Furthermore, in 3D simulations, we could expect a greater impact of temperature fluctuations for higher SOL temperatures (for example by an injected power scan). Indeed, it would increase the parallel thermal conductivity ($\propto T^{5/2}$) and might impact the parallel gradients coming along with new mechanisms. However, one could be confident on the fact that the general phenomenology of turbulence would stay the same as this result is true for all the parameters tested in 2D simulations.

In future work, we will aim to obtain a transport barrier, and to reach a H-mode like regime to study the mechanisms at play in such case. In particular, one should proceed to a scan of the ion power injection, pointed out to trigger the creation of transport barrier in experiment [Ryter 14] and in 2D fluid code [Rasmussen 15]. Furthermore, we should also study divertor configurations which contributes to the appearance of an edge transport barrier both in experiments but also in TOKAM3X isothermal simulations (work of Davide Galassi).

Taking a step back, we have seen all along this thesis that the SOL width is a notion of usually resumed to a single value, but hiding a more complex picture. Indeed, the heat channel has no reason to be uniform neither in time, in particular for turbulent regime, nor in space. Moreover, the SOL width

results from a complex interplay between the parallel dynamics and the perpendicular transport and none of them should be overlooked.

Appendix A

Details for derivation of fluid equation

A.1 Equality of divergence of the particle flux associated to the diamagnetic drift and to drift

$$\begin{aligned}
\boldsymbol{\nabla}\cdot(n\mathbf{u}_*) &= -\boldsymbol{\nabla}\cdot\left(n\frac{\mathbf{B}\times\boldsymbol{\nabla}p}{nqB^2}\right)\\
&= -\boldsymbol{\nabla}\left(\frac{1}{B^2}\right)\cdot(\mathbf{B}\times\boldsymbol{\nabla}p) - \frac{1}{B^2}\boldsymbol{\nabla}\cdot(\mathbf{B}\times\boldsymbol{\nabla}p)\\
&= -\boldsymbol{\nabla}\left(\frac{1}{B^2}\right)\cdot(\mathbf{B}\times\boldsymbol{\nabla}p) - \frac{1}{B^2}\left(\underbrace{(\boldsymbol{\nabla}\times\mathbf{B})}_{=0 \text{ under ...}}\cdot\boldsymbol{\nabla}p - \mathbf{B}\cdot(\boldsymbol{\nabla}\times\boldsymbol{\nabla}p)\right)\\
&= \boldsymbol{\nabla}\left(\frac{1}{B^2}\right)\cdot(\boldsymbol{\nabla}p\times\mathbf{B})
\end{aligned}$$

$$\begin{aligned}
\boldsymbol{\nabla}\cdot(n\mathbf{u}_{\nabla B}) &= -\boldsymbol{\nabla}\cdot\left(2\underbrace{nT}_{=p}\frac{\mathbf{B}\times\boldsymbol{\nabla}B}{B^3}\right)\\
&= -\boldsymbol{\nabla}\left(\frac{2p}{B^3}\right)\cdot(\mathbf{B}\times\boldsymbol{\nabla}B) - \frac{2p}{B^3}\boldsymbol{\nabla}\cdot(\mathbf{B}\times\boldsymbol{\nabla}B)\\
&= -\boldsymbol{\nabla}\left(\frac{2p}{B^3}\right)\cdot(\mathbf{B}\times\boldsymbol{\nabla}B) - \frac{2p}{B^3}\left(\underbrace{(\boldsymbol{\nabla}\times\mathbf{B})}_{=0 \text{ under ...}}\cdot\boldsymbol{\nabla}B - \mathbf{B}\cdot(\boldsymbol{\nabla}\times\boldsymbol{\nabla}B)\right)\\
&= -\frac{2}{B^3}\boldsymbol{\nabla}p\cdot(\mathbf{B}\times\boldsymbol{\nabla}B) - 2p\boldsymbol{\nabla}\left(\frac{1}{B^3}\right)\cdot(\mathbf{B}\times\boldsymbol{\nabla}B)\\
&= -\frac{2}{B^3}\boldsymbol{\nabla}B\cdot(\boldsymbol{\nabla}p\times\mathbf{B}) - \frac{6p}{B^4}\boldsymbol{\nabla}B\cdot(\mathbf{B}\times\boldsymbol{\nabla}B)\\
&= \boldsymbol{\nabla}\left(\frac{1}{B^2}\right)\cdot(\boldsymbol{\nabla}p\times\mathbf{B})
\end{aligned}$$

We thus get $\boldsymbol{\nabla}\cdot(n\mathbf{u}_{\nabla B}) = \boldsymbol{\nabla}\cdot(n\mathbf{u}_*)$

A.2 Braginskii's closure

In the following, we consider a plasma of two species: electrons and one ion species of hydrogen isotope. The limit case of strongly magnetized plasma ($\omega_{c_e}\tau_e \gg 1$ and $\omega_{c_i}\tau_i \gg 1$) is considered in Braginskii's closure.
The total pressure tensor $\bar{\bar{\Pi}}_s^{tot}$ is decomposed into a scalar pressure p_s and a residual tensor $\bar{\bar{\Pi}}_s^{\text{Brag}}$:

$$\bar{\bar{\Pi}}_s^{tot} = p_s\bar{\bar{I}} + \bar{\bar{\Pi}}_s^{\text{Brag}} \tag{A.1}$$

For a standard basis $(\mathbf{e}_x, \mathbf{e}_y, \mathbf{e}_z)$ in which $\mathbf{b} = \mathbf{e}_z$, this Braginskii's stress tensor $\bar{\bar{\Pi}}_s^{\text{Brag}}$ writes :

$$\begin{pmatrix} -\frac{\eta_0^s}{2}(W_{xx}+W_{yy}) - \frac{\eta_1^s}{2}(W_{xx}-W_{yy}) - \eta_3^s W_{xy} & -\eta_1^s W_{xy} + \frac{\eta_3^s}{2}(W_{xx}-W_{yy}) & -4\eta_1^s W_{xz} - 2\eta_3^s W_{yz} \\ -\eta_1^s W_{xy} + \frac{\eta_3^s}{2}(W_{xx}-W_{yy}) & -\frac{\eta_0^s}{2}(W_{xx}+W_{yy}) - \frac{\eta_1^s}{2}(W_{yy}-W_{xx}) + \eta_3^s W_{xy} & -4\eta_1^s W_{yz} + 2\eta_3^s W_{xz} \\ -4\eta_1^s W_{xz} - 2\eta_3^s W_{yz} & -4\eta_1^s W_{yz} + 2\eta_3^s W_{xz} & -\eta_0^s W_{zz} \end{pmatrix}$$

In this formulation, the rate-of-strain tensor $\bar{\bar{W}}$ is a measure of the deformation of plasma volume elements and is defined as:

$$W_{jk} = \frac{\partial u_j}{\partial x_k} + \frac{\partial u_k}{\partial x_j} - \frac{2}{3}\delta_{jk}\nabla\cdot\mathbf{u} \tag{A.2}$$

The Braginskii's stress tensor formulation (A.2) involves three different viscosity coefficients which differ slightly for ions and electrons:

$$\begin{aligned} \eta_0^i &= 0.96 p_i\tau_i \quad ; \quad \eta_0^e = 0.73 p_e\tau_e \\ \eta_1^i &= 0.3\frac{p_i}{\omega_{c_i}^2\tau_i} \quad ; \quad \eta_1^e = 0.51\frac{p_e}{\omega_{c_e}^2\tau_e} \\ \eta_3^i &= 0.5\frac{p_i}{\omega_{c_i}} \quad ; \quad \eta_3^e = -0.5\frac{p_e}{\omega_{c_e}} \end{aligned} \tag{A.3}$$

One can notice that the ratios between these three viscosity coefficients are proportional to powers of $\omega_{c_s}\tau_s$:

$$\frac{\eta_0^s}{\eta_3^s} \propto \omega_{c_s}\tau_s \gg 1 \quad ; \quad \frac{\eta_0^s}{\eta_1^s} \propto (\omega_{c_s}\tau_s)^2 \gg 1 \quad ; \quad \frac{\eta_3^s}{\eta_1^s} \propto \omega_{c_s}\tau_s \gg 1 \tag{A.4}$$

which leads to:

$$\eta_0^s \gg \eta_3^s \gg \eta_1^s \tag{A.5}$$

It is thus convenient to separate the Braginskii's stress tensor into three tensors according to the dependency of these different viscosity coefficients:

$$\bar{\bar{\Pi}}_s^{\text{Brag}} = \bar{\bar{\Pi}}_s^{\text{vis}} + \bar{\bar{\Pi}}_s^{\text{FLR}} + \bar{\bar{\Pi}}_s^{\text{res}} \tag{A.6}$$

Viscous tensor: Terms proportional to η_0^s correspond to the viscous part of Braginskii's stress tensor:

$$\bar{\bar{\Pi}}_s^{\text{vis}} = \begin{pmatrix} -\frac{\eta_0^s}{2}(W_{xx}+W_{yy}) & 0 & 0 \\ 0 & -\frac{\eta_0^s}{2}(W_{xx}+W_{yy}) & 0 \\ 0 & 0 & -\eta_0^s W_{zz} \end{pmatrix} \tag{A.7}$$

Gyro-viscous or Finite Larmor Radius tensor:

$$\bar{\bar{\Pi}}_s^{\text{FLR}} = \begin{pmatrix} -\eta_3^s W_{xy} & \frac{\eta_3^s}{2}(W_{xx}-W_{yy}) & -2\eta_3^s W_{yz} \\ \frac{\eta_3^s}{2}(W_{xx}-W_{yy}) & \eta_3^s W_{xy} & 2\eta_3^s W_{xz} \\ -2\eta_3^s W_{yz} & 2\eta_3^s W_{xz} & 0 \end{pmatrix} \tag{A.8}$$

Residual viscous tensor:

$$\bar{\bar{\Pi}}_s^{\text{res}} = \begin{pmatrix} -\frac{\eta_1^s}{2}(W_{xx}-W_{yy}) & -\eta_1^s W_{xy} & -4\eta_1^s W_{xz} \\ -\eta_1^s W_{xy} & -\frac{\eta_1^s}{2}(W_{yy}-W_{xx}) & -4\eta_1^s W_{yz} \\ -4\eta_1^s W_{xz} & -4\eta_1^s W_{yz} & 0 \end{pmatrix} \tag{A.9}$$

A.3 Derivation of energy equation

$$\underbrace{\partial_t \left(\int_{\mathbf{v}} \mathbf{v} \otimes \mathbf{v} f_s d^3\mathbf{v} \right)}_{A} + \underbrace{\boldsymbol{\nabla}_{\mathbf{x}} \cdot \left(\int_{\mathbf{v}} \mathbf{v} \otimes \mathbf{v} \otimes \mathbf{v} f_s d^3\mathbf{v} \right)}_{B} + \underbrace{\int_{\mathbf{v}} \mathbf{v} \otimes \mathbf{v} \boldsymbol{\nabla}_{\mathbf{v}} \cdot \left(\frac{\mathbf{F}_s}{m_s} f_s \right) d^3\mathbf{v}}_{C} = \int_{\mathbf{v}} \mathbf{v} \otimes \mathbf{v} C_s d^3\mathbf{v} \tag{A.10}$$

$$\begin{aligned}
A &= \partial_t \left(\int_{\mathbf{v}} \mathbf{v} \otimes \mathbf{v} f_s d^3\mathbf{v} \right) \\
&= \partial_t \left(\int_{\mathbf{v}} (\mathbf{u}_s + \mathbf{w}_s) \otimes (\mathbf{u}_s + \mathbf{w}_s) f_s d^3\mathbf{v} \right) \\
&= \partial_t \left(\int_{\mathbf{v}} \mathbf{u}_s \otimes \mathbf{u}_s f_s d^3\mathbf{v} + \cancel{\int_{\mathbf{v}} \mathbf{u}_s \otimes \mathbf{w}_s f_s d^3\mathbf{v}} + \cancel{\int_{\mathbf{v}} \mathbf{w}_s \otimes \mathbf{u}_s f_s d^3\mathbf{v}} + \int_{\mathbf{v}} \mathbf{w}_s \otimes \mathbf{w}_s f_s d^3\mathbf{v} \right) \\
&= \partial_t \left(n_s \mathbf{u}_s \otimes \mathbf{u}_s + \frac{1}{m_s} \bar{\bar{\Pi}}_s^{tot} \right)
\end{aligned}$$

$$\begin{aligned}
B &= \boldsymbol{\nabla}_{\mathbf{x}} \cdot \left(\int_{\mathbf{v}} \mathbf{v} \otimes \mathbf{v} \otimes \mathbf{v} f_s d^3\mathbf{v} \right) \\
&= \boldsymbol{\nabla}_{\mathbf{x}} \cdot \left(\int_{\mathbf{v}} (\mathbf{u}_s + \mathbf{w}_s) \otimes (\mathbf{u}_s + \mathbf{w}_s) \otimes (\mathbf{u}_s + \mathbf{w}_s) f_s d^3\mathbf{v} \right) \\
&= \boldsymbol{\nabla}_{\mathbf{x}} \cdot \Big(\int_{\mathbf{v}} \mathbf{u}_s \otimes \mathbf{u}_s \otimes \mathbf{u}_s f_s d^3\mathbf{v} + \int_{\mathbf{v}} \mathbf{u}_s \otimes \mathbf{u}_s \otimes \mathbf{w}_s f_s d^3\mathbf{v} + \int_{\mathbf{v}} \mathbf{w}_s \otimes \mathbf{u}_s \otimes \mathbf{u}_s f_s d^3\mathbf{v} + \int_{\mathbf{v}} \mathbf{u}_s \otimes \mathbf{w}_s \otimes \mathbf{u}_s f_s d^3\mathbf{v} \\
&\quad + \int_{\mathbf{v}} \mathbf{w}_s \otimes \mathbf{w}_s \otimes \mathbf{u}_s f_s d^3\mathbf{v} + \int_{\mathbf{v}} \mathbf{w}_s \otimes \mathbf{u}_s \otimes \mathbf{w}_s f_s d^3\mathbf{v} + \int_{\mathbf{v}} \mathbf{u}_s \otimes \mathbf{w}_s \otimes \mathbf{w}_s f_s d^3\mathbf{v} \int_{\mathbf{v}} \mathbf{w}_s \otimes \mathbf{w}_s \otimes \mathbf{w}_s f_s d^3\mathbf{v} \Big) \\
&= \boldsymbol{\nabla}_{\mathbf{x}} \cdot \Big((\mathbf{u}_s \otimes \mathbf{u}_s \otimes \mathbf{u}_s) \int_{\mathbf{v}} f_s d^3\mathbf{v} + \mathbf{u}_s \otimes \mathbf{u}_s \otimes \cancel{\int_{\mathbf{v}} \mathbf{w}_s f_s d^3\mathbf{v}} + \cancel{\int_{\mathbf{v}} \mathbf{w}_s f_s d^3\mathbf{v}} \otimes \mathbf{u}_s \otimes \mathbf{u}_s + \mathbf{u}_s \otimes \cancel{\int_{\mathbf{v}} \mathbf{w}_s f_s d^3\mathbf{v}} \otimes \mathbf{u}_s \\
&\quad + \left(\int_{\mathbf{v}} \mathbf{w}_s \otimes \mathbf{w}_s f_s d^3\mathbf{v} \right) \otimes \mathbf{u}_s + \int_{\mathbf{v}} \mathbf{w}_s \otimes \mathbf{u}_s \otimes \mathbf{w}_s f_s d^3\mathbf{v} + \mathbf{u}_s \otimes \left(\int_{\mathbf{v}} \mathbf{w}_s \otimes \mathbf{w}_s f_s d^3\mathbf{v} \right) + \frac{2}{m_s} \bar{\bar{\bar{Q}}}_s \Big) \\
&= \boldsymbol{\nabla}_{\mathbf{x}} \cdot \left(n_s \mathbf{u}_s \otimes \mathbf{u}_s \otimes \mathbf{u}_s + \frac{1}{m_s} \left(\bar{\bar{\Pi}}_s^{tot} \otimes \mathbf{u}_s + \mathbf{u}_s \otimes \bar{\bar{\Pi}}_s^{tot} \right) + \int_{\mathbf{v}} \mathbf{w}_s \otimes \mathbf{u}_s \otimes \mathbf{w}_s f_s d^3\mathbf{v} + \frac{2}{m_s} \bar{\bar{\bar{Q}}}_s \right)
\end{aligned}$$

$$\begin{aligned}
C &= \int_{\mathbf{v}} \mathbf{v} \otimes \mathbf{v} \boldsymbol{\nabla}_{\mathbf{v}} \cdot \left(\frac{\mathbf{F}_s}{m_s} f_s \right) d^3\mathbf{v} \\
&= -\left(\int_{\mathbf{v}} \frac{\mathbf{F}_s}{m_s} \otimes \mathbf{v} f_s d^3\mathbf{v} + \int_{\mathbf{v}} \mathbf{v} \otimes \frac{\mathbf{F}_s}{m_s} f_s d^3\mathbf{v} \right) \\
&= -\frac{q_s}{m_s} \left(\int_{\mathbf{v}} \mathbf{E} \otimes \mathbf{v} f_s d^3\mathbf{v} + \int_{\mathbf{v}} (\mathbf{v} \times \mathbf{B}) \otimes \mathbf{v} f_s d^3\mathbf{v} + \int_{\mathbf{v}} \mathbf{v} \otimes \mathbf{E} f_s d^3\mathbf{v} + \int_{\mathbf{v}} \mathbf{v} \otimes (\mathbf{v} \times \mathbf{B}) f_s d^3\mathbf{v} \right) \\
&= -\frac{q_s}{m_s} \left(\mathbf{E} \otimes \int_{\mathbf{v}} \mathbf{v} f_s d^3\mathbf{v} + \int_{\mathbf{v}} \mathbf{v} f_s d^3\mathbf{v} \otimes \mathbf{E} + \frac{2}{q_s} \bar{\bar{W}}_s^{\mathbf{v} \times \mathbf{B}} \right) \\
&= -\frac{q_s}{m_s} n_s \left(\mathbf{E} \otimes \mathbf{u}_s + \mathbf{u}_s \otimes \mathbf{E} \right) - \frac{2}{m_s} \bar{\bar{W}}_s^{\mathbf{v} \times \mathbf{B}}
\end{aligned}$$

Appendix B

Linear analysis of Tokam2D

B.1 Tokam2D Conservation Equations

$$\partial_t N + [\phi, N] = -\sigma N\sqrt{T_e + T_i}\mathrm{e}^{\Lambda-\phi/T_e} + D\boldsymbol{\nabla}_\perp^2 N \tag{B.1}$$

$$\partial_t W + [\phi, W] = -\frac{g}{N}\partial_y\left(N\left(T_e + T_i\right)\right) + \sigma\sqrt{T_e + T_i}\left(1 - \mathrm{e}^{\Lambda-\phi/T_e}\right) + \nu\boldsymbol{\nabla}_\perp^2 W \tag{B.2}$$

$$\frac{3}{2}\partial_t(NT_e) + \frac{3}{2}[\phi, NT_e] = -\sigma\gamma_e NT_e\sqrt{T_e + T_i}\mathrm{e}^{\Lambda-\phi/T_e} + \chi_e\boldsymbol{\nabla}_\perp^2 NT_e \tag{B.3}$$

$$\frac{3}{2}\partial_t(NT_i) + \frac{3}{2}\left[\phi, NT_i\right] = -\sigma\gamma_e NT_i\sqrt{T_e + T_i} + \chi_i\boldsymbol{\nabla}_\perp^2 NT_i \tag{B.4}$$

With $W = \boldsymbol{\nabla}_\perp^2\phi + \boldsymbol{\nabla}\cdot\left(\frac{1}{N}\boldsymbol{\nabla}_\perp P_i\right)$ Note that in this derivation the collisional terms $\pm\frac{3m_e}{m_i}\tau_e^{-1}\left(P_e - P_i\right)$ are neglected in the following derivation as they have no impact on the results (in agreement with their low order of magnetude $\propto m_e/m_i$)

B.2 Linear Analysis

Each field f is split into a mean and a fluctuating part $f = \overline{f} + \widetilde{f}$, and an assumption of small amplitude of fluctuations, $\frac{\widetilde{f}}{\overline{f}} << 1$ is made

B.2.1 Steady State Solutions

In order to study the linear stability of the system, we supposed that a quasi steady-state is reached so we have $\partial_t\overline{N} = \partial_t\overline{\phi} = \partial_t\overline{W} = \partial_t\overline{T_e} = \partial_t\overline{T_i} = 0$. And the steady-state regime gives us the following set of equations. In the linear analysis we keep only the first order of development with respect to the

small value $\frac{\widetilde{f}}{\overline{f}}$

$$\begin{cases} 0 &= -\sigma\overline{N}\sqrt{\overline{T}} + D\boldsymbol{\nabla}_\perp^2\overline{N} \\ 0 &= \nu\boldsymbol{\nabla}_\perp^4\overline{\phi} + \nu T_i\boldsymbol{\nabla}_\perp^4\overline{\phi} \\ 0 &= -\sigma\gamma_e\overline{NT_e}\sqrt{\overline{T}} + \chi\boldsymbol{\nabla}_\perp^2\overline{NT_e} \\ 0 &= -\sigma\gamma_i\overline{NT_i}\sqrt{\overline{T}} + \chi\boldsymbol{\nabla}_\perp^2\overline{NT_i} \end{cases} \tag{B.5}$$

where $\overline{T} = \overline{T_e} + \overline{T_i}$

In the following will make the assumption that:

- all mean fields $\overline{N}$, $\overline{\phi}$, $\overline{T_e}$, $\overline{T_i}$, $\overline{W}$ are independent of y
- the mean potential follows the value of the floating potential $\overline{\phi} = \Lambda\overline{T_e}$ (so we have $\mathrm{e}^{\Lambda - \overline{\phi}/\overline{T_e}} = 1$)
- all mean field radial profiles are decaying exponential $\overline{X} \propto \exp\left\{\frac{-x}{\lambda_X}\right\}$ the e-folding length is noted λ_X

Note one can estimate the typical ratio between $\lambda_{T_{e/i}}$ and λ_N from the steady state equations, for example for electron the first and third equations of (B.5) writes:

$$\begin{cases} \sigma\overline{N}\sqrt{\overline{T}} &= D\boldsymbol{\nabla}_\perp^2\overline{N} \\ \sigma\gamma_e\overline{NT_e}\sqrt{\overline{T}} &= \chi\boldsymbol{\nabla}_\perp^2\overline{NT_e} \end{cases} \tag{B.6}$$

If one substitutes $\sigma\overline{N}\sqrt{\overline{T}}$ in the second equations, one obtains:

$$\gamma_e\overline{T_e}D\boldsymbol{\nabla}_\perp^2\overline{N} = \chi\boldsymbol{\nabla}_\perp^2\overline{NT_e} \tag{B.7}$$

Here one has $\chi = D$, and $N = N_0\exp(-x/\lambda_N)$ and $T_e = T_{e,0}\exp(-x/\lambda_{T_e})$. The previous equation rewrites:

$$\gamma_e\exp(-x/\lambda_{T_e})\frac{\exp(-x/\lambda_N)}{\lambda_N^2} = \frac{\exp(-x/\lambda_{T_e})\exp(-x/\lambda_N)}{\lambda_{P_e}^2} \text{ with } \lambda_{P_e} = \frac{\lambda_N\lambda_{T_e}}{\lambda_N + \lambda_{T_e}} \tag{B.8}$$

Which can be simplified in:

$$\sqrt{\gamma_e} = \frac{\lambda_N + \lambda_{T_e}}{\lambda_{T_e}} \tag{B.9}$$

Finally one finds $\lambda_{T_e} = \frac{\lambda_N}{\sqrt{\gamma_e}-1}$ the same can be done with T_i and gives: $\lambda_{T_i} = \frac{\lambda_N}{\sqrt{\gamma_i}-1}$.

B.2.2 Preliminary calculation

For two fields X and Y:

$$\begin{aligned}\left[\overline{X}+\widetilde{X},\overline{Y}+\widetilde{Y}\right] &= \cancel{\left[\overline{X},\overline{Y}\right]}+\left[\overline{X},\widetilde{Y}\right]+\left[\widetilde{X},\overline{Y}\right]+\cancel{\left[\widetilde{X},\widetilde{Y}\right]}\\ &= \partial_x\overline{X}\partial_y\widetilde{Y}-\cancel{\partial_y\overline{X}\partial_x\widetilde{Y}}+\cancel{\partial_x\widetilde{X}\partial_y\overline{Y}}-\partial_x\overline{Y}\partial_y\widetilde{X}\\ &= \partial_x\overline{X}\partial_y\widetilde{Y}-\partial_x\overline{Y}\partial_y\widetilde{X}\end{aligned}$$

$$\sqrt{\overline{T_e}+\overline{T_i}+\widetilde{T_e}+\widetilde{T_i}}=\sqrt{\overline{T_e}+\overline{T_i}}+\frac{1}{2}\frac{\widetilde{T_e}+\widetilde{T_i}}{\sqrt{\overline{T_e}+\overline{T_i}}}=\sqrt{\overline{T}}+\frac{1}{2}\frac{\widetilde{T_e}+\widetilde{T_i}}{\sqrt{\overline{T}}}$$

$$\mathrm{e}^{\Lambda-\frac{\overline{\phi}+\widetilde{\phi}}{\overline{T_e}+\widetilde{T_e}}}=1+\Lambda\frac{\widetilde{T_e}}{\overline{T_e}}-\Lambda\frac{\widetilde{\phi}}{\overline{\phi}}=1+\Lambda\frac{\widetilde{T_e}}{\overline{T_e}}-\frac{\widetilde{\phi}}{\overline{T_e}}$$

Let us also introduce $E=\ln N$ for simplification of the calculation and to overcome the dependence on $\overline{N}$. Using: $\ln\left(\overline{N}\left(1+\frac{\widetilde{N}}{\overline{N}}\right)\right)=\ln\overline{N}+\ln\left(1+\frac{\widetilde{N}}{\overline{N}}\right)\simeq\ln\overline{N}+\frac{\widetilde{N}}{\overline{N}}$, we obtain that at first order of development $\overline{E}=\ln\overline{N}$ and $\widetilde{E}=\frac{\widetilde{N}}{\overline{N}}$. It is evident that $\frac{\partial_x N}{N}=\partial_x E=-\frac{1}{\lambda_N}$. We also have $\partial_y\widetilde{E}=\partial_y\left(\frac{\widetilde{N}}{\overline{N}}\right)=\frac{\partial_y\widetilde{N}}{\overline{N}}=\partial_y\widetilde{E}$ as $\overline{N}$ is independant of y, the same way we have $\partial_t\widetilde{E}=\frac{\partial_t\widetilde{N}}{\overline{N}}$ Finally we have $\frac{\partial_x\widetilde{N}}{\overline{N}}=\partial_x\widetilde{E}+\widetilde{E}\partial_x$, and $\frac{\partial_x^2\widetilde{N}}{\overline{N}}=\partial_x^2\widetilde{E}+2\partial_x\overline{E}\partial_x\widetilde{E}+\partial_x^2\overline{E}\widetilde{E}$

B.2.3 Density equation

$$\partial_t(\overline{N}+\widetilde{N})+\left[\overline{\phi}+\widetilde{\phi},\overline{N}+\widetilde{N}\right]=-\sigma(\overline{N}+\widetilde{N})\sqrt{\overline{T}+\widetilde{T_i}+\widetilde{T_e}}\,\mathrm{e}^{\Lambda-\frac{\overline{\phi}+\widetilde{\phi}}{\overline{T_e}+\widetilde{T_e}}}+D\boldsymbol{\nabla}_\perp^2(\overline{N}+\widetilde{N})$$

$$\partial_t\widetilde{N}+\partial_x\overline{\phi}\partial_y\widetilde{N}-\partial_x\overline{N}\partial_y\widetilde{\phi}=-\sigma\overline{N}\sqrt{\overline{T}}-\sigma\overline{N}\sqrt{\overline{T}}\left(\Lambda\frac{\widetilde{T_e}}{\overline{T_e}}-\frac{\widetilde{\phi}}{\overline{T_e}}\right)-\sigma\overline{N}\frac{\widetilde{T_e}+\widetilde{T_i}}{2\sqrt{\overline{T}}}-\sigma\sqrt{\overline{T}}\widetilde{N}+D\boldsymbol{\nabla}_\perp^2\overline{N}+D\boldsymbol{\nabla}_\perp^2\widetilde{N}$$

in steady state and by dividing all term by N:

$$\partial_t\widetilde{E}+\partial_x\overline{\phi}\partial_y\widetilde{E}-\partial_x\overline{E}\partial_y\widetilde{\phi}=-\sigma\Lambda\sqrt{\overline{T}}\left(\frac{\widetilde{T_e}}{\overline{T_e}}-\frac{\widetilde{\phi}}{\overline{\phi}}\right)-\frac{1}{2}\sigma\overline{N}\frac{\widetilde{T_e}}{\sqrt{\overline{T}}}-\frac{1}{2}\sigma\frac{\widetilde{T_i}}{\sqrt{\overline{T}}}-\sigma\sqrt{\overline{T}}\widetilde{E}+D(\boldsymbol{\nabla}_\perp^2-\frac{2}{\lambda_N}+\frac{1}{\lambda_N^2})\widetilde{E}$$

Finally we obtain :

$$\left(\partial_t+\Lambda\partial_x\overline{T_e}\partial_y+\sigma\sqrt{\overline{T}}-D\boldsymbol{\nabla}_\perp^2\right)\widetilde{E}+\left(-\sigma\frac{\sqrt{\overline{T}}}{\overline{T_e}}-\partial_x\overline{E}\partial_y\right)\widetilde{\phi}+\sigma\left(\frac{\sqrt{\overline{T}}}{\overline{T_e}}\Lambda+\frac{1}{2\sqrt{\overline{T}}}\right)\widetilde{T_e}+\left(\frac{\sigma}{2\sqrt{\overline{T}}}\right)\widetilde{T_i}=0 \tag{B.10}$$

B.2.4 Vorticity equation

$$\partial_t\left(\overline{W}+\widetilde{W}\right)+\left[\overline{\phi}+\widetilde{\phi},\overline{W}+\widetilde{W}\right]=-\frac{g}{\overline{N}+\widetilde{N}}\partial_y\left(\left(\overline{N}+\widetilde{N}\right)\left(\overline{T}+\widetilde{T_e}+\widetilde{T_i}\right)\right)$$
$$+\sigma\sqrt{\overline{T}+\widetilde{T_e}+\widetilde{T_i}}\left(1-\mathrm{e}^{\Lambda-\frac{\overline{\phi}+\widetilde{\phi}}{\overline{T_e}+\widetilde{T_e}}}\right)+\nu\boldsymbol{\nabla}_\perp^2\left(\overline{W}+\widetilde{W}\right)$$

$$\partial_t\widetilde{W}+\partial_x\overline{\phi}\partial_y\widetilde{W}-\partial_x\overline{W}\partial_y\widetilde{\phi}=-\frac{g}{\overline{N}+\underbrace{\cancel{\widetilde{N}}}_{\text{2nd order}}}\partial_y\left(\overline{T}\widetilde{N}\right)-\frac{g}{\overline{N}+\cancel{\widetilde{N}}}\partial_y\left(\overline{N}\widetilde{T_e}\right)-\frac{g}{\overline{N}+\cancel{\widetilde{N}}}\partial_y\left(\overline{N}\widetilde{T_i}\right)$$
$$-\sigma\left(\sqrt{\overline{T}}+\underbrace{\frac{\widetilde{T_e}}{2\sqrt{\overline{T}}}+\frac{\cancel{\widetilde{T_i}}}{2\sqrt{\overline{T}}}}_{\text{2nd order}}\right)\left(\Lambda\frac{\widetilde{T_e}}{\overline{T_e}}-\frac{\widetilde{\phi}}{\overline{T_e}}\right)+\nu\boldsymbol{\nabla}_\perp^2\left(\overline{W}+\widetilde{W}\right)$$

In steady state we have $\nu\boldsymbol{\nabla}_\perp^2\overline{W}=0$:

$$\partial_t\widetilde{W}+\partial_x\overline{\phi}\partial_y\widetilde{W}-\partial_y\widetilde{\phi}\partial_x\overline{W}=-\frac{g\overline{T}}{\overline{N}}\partial_y\widetilde{N}-g\partial_y\widetilde{T_e}-g\partial_y\widetilde{T_i}+\sigma\sqrt{\overline{T}}\frac{\widetilde{\phi}}{\overline{T_e}}-\sigma\Lambda\sqrt{\overline{T}}\frac{\widetilde{T_e}}{\overline{T_e}}+\nu\boldsymbol{\nabla}_\perp^2\widetilde{W}$$

Finally we obtain :

$$\left(\frac{g\overline{T}}{N}\partial_y\right)\widetilde{E}+\left(-\partial_x\overline{W}\partial_y-\sigma\frac{\sqrt{\overline{T}}}{\overline{T_e}}\right)\widetilde{\phi}+\left(\partial_t+\Lambda\partial_x\overline{T_e}\partial_y-\nu\boldsymbol{\nabla}_\perp^2\right)\widetilde{W}+\left(g\partial_y+\sigma\Lambda\frac{\sqrt{\overline{T}}}{\overline{T_e}}\right)\widetilde{T_e}+\left(g\partial_y\right)\widetilde{T_i}=0 \tag{B.11}$$

B.2.5 Poisson equation

$$W=\boldsymbol{\nabla}_\perp^2\phi+\boldsymbol{\nabla}\cdot\left(\frac{1}{N}\boldsymbol{\nabla}_\perp P_i\right)$$
$$=\boldsymbol{\nabla}_\perp^2\phi+\boldsymbol{\nabla}_\perp^2T_i+\boldsymbol{\nabla}\cdot\left(T_i\boldsymbol{\nabla}_\perp\ln N\right))$$

$$=\boldsymbol{\nabla}_\perp^2\left(\overline{\phi}+\widetilde{\phi}\right)+\boldsymbol{\nabla}_\perp^2\left(\overline{T_i}+\widetilde{T_i}\right)+\boldsymbol{\nabla}\cdot\left(\left(\overline{T_i}+\widetilde{T_i}\right)\boldsymbol{\nabla}_\perp\left(\ln\left(\overline{N}+\widetilde{N}\right)\right)\right)$$
$$=\partial_x^2\overline{\phi}+\boldsymbol{\nabla}_\perp^2\widetilde{\phi}+\partial_x^2\overline{T_i}+\boldsymbol{\nabla}_\perp^2\widetilde{T_i}+\underbrace{\boldsymbol{\nabla}\cdot\left(\overline{T_i}\boldsymbol{\nabla}_\perp\ln\left(\overline{N}\left(1+\frac{\widetilde{N}}{\overline{N}}\right)\right)\right)}_{=A_1}+\underbrace{\boldsymbol{\nabla}\cdot\left(\widetilde{T_i}\boldsymbol{\nabla}_\perp\ln\left(\overline{N}\left(1+\frac{\widetilde{N}}{\overline{N}}\right)\right)\right)}_{=A_2}$$

$$\boldsymbol{\nabla}_\perp\ln\left(\overline{N}\left(1+\frac{\widetilde{N}}{\overline{N}}\right)\right)=\begin{pmatrix}\partial_x\overline{E}\\ \cancel{\partial_y\overline{E}}\end{pmatrix}+\begin{pmatrix}\partial_x\widetilde{E}\\ \partial_y\widetilde{E}\end{pmatrix}=\begin{pmatrix}\partial_x\overline{E}+\partial_x\widetilde{E}\\ \partial_y\widetilde{E}\end{pmatrix}$$

We can develop A_1 : Let us note that $\partial_x\overline{E}=\partial_x\ln\overline{N}$ is independent of x as $N\propto\exp(-X/\lambda_N)$.

$$
\begin{aligned}
A_1 &= \boldsymbol{\nabla} \cdot \begin{pmatrix} \overline{T_i}\left(\partial_x \overline{E} + \partial_x \widetilde{E}\right) \\ \\ \overline{T_i}\partial_y \widetilde{E} \end{pmatrix} \\
&= \partial_x\left(\overline{T_i}\partial_x \overline{E}\right) + \partial_x\left(\overline{T_i}\partial_x \widetilde{E}\right) + \partial_y\left(\overline{T_i}\partial_y \widetilde{E}\right) \\
&= \partial_x \overline{E}\partial_x \overline{T_i} + \partial_x \overline{T_i}\partial_x \widetilde{E} + \overline{T_i}\partial_x^2 \widetilde{E} + \overline{T_i}\partial_y^2 \widetilde{E} \\
&= \partial_x \overline{E}\partial_x \overline{T_i} + \partial_x \overline{T_i}\partial_x \widetilde{E} + \overline{T_i}\boldsymbol{\nabla}_\perp^2 \widetilde{E}
\end{aligned}
$$

A_2 is calculated the same way (with $\widetilde{T_i}$ instead of $\overline{T_i}$) and leads to:

$$A_2 = \partial_x \overline{E}\partial_x \widetilde{T_i}$$

Finally, the vorticity can be written:

$$
\begin{aligned}
W = &\underbrace{\partial_x^2 \overline{\phi} + \partial_x^2 \overline{T_i} + \partial_x \overline{T_i}\partial_x \overline{E}}_{=\overline{W}} \\
&+ \boldsymbol{\nabla}_\perp^2 \widetilde{\phi} + \boldsymbol{\nabla}_\perp^2 \widetilde{T_i} + \overline{T_i}\boldsymbol{\nabla}_\perp^2 \widetilde{E} + \partial_x \overline{T_i}\partial_x \widetilde{E} + \partial_x \overline{E}\partial_x \widetilde{T_i}
\end{aligned}
$$

As $\widetilde{W} = W - \overline{W}$, we have:

$$-\left(\partial_x \overline{T_i}\partial_x + \overline{T_i}\boldsymbol{\nabla}_\perp^2\right)\widetilde{N} - \boldsymbol{\nabla}_\perp^2 \widetilde{\phi} + \widetilde{W} - \left(\boldsymbol{\nabla}_\perp^2 + \partial_x \overline{E}\partial_x\right)\widetilde{T_i} = 0 \tag{B.12}$$

B.2.6 Energy equation

B.2.7 preliminary calculation

Let us first develop advection terms and diffusive terms which are identical for electronic and ionic energy conservation equations.
Advection:

$$
\begin{aligned}
\frac{3}{2}\left[\overline{\phi} + \widetilde{\phi}, \left(\overline{N} + \widetilde{N}\right)\left(\overline{T_\alpha} + \widetilde{T_\alpha}\right)\right] =& \frac{3}{2}\left(\left(\overline{N} + \cancel{\widetilde{N}}\right)\left[\overline{\phi} + \widetilde{\phi}, \overline{T_\alpha} + \widetilde{T_\alpha}\right] + \left(\overline{T_\alpha} + \cancel{\widetilde{T_\alpha}}\right)\left[\overline{\phi} + \widetilde{\phi}, \widetilde{N} + \overline{N}\right]\right) \\
=& \frac{3}{2}\left(\overline{N}\partial_x \overline{\phi}\partial_y \widetilde{T_\alpha} - \overline{N}\partial_x \overline{T_\alpha}\partial_y \widetilde{\phi} + \overline{T_\alpha}\partial_x \overline{\phi}\partial_y \widetilde{N} - \overline{T_\alpha}\partial_x \overline{N}\partial_y \widetilde{\phi}\right) \\
=& \frac{3}{2}\left(\overline{N}\partial_x \overline{\phi}\partial_y \widetilde{T_\alpha} - \left(\overline{N}\partial_x \overline{T_\alpha}\partial_y + \overline{T_\alpha}\partial_x \overline{N}\partial_y\right)\widetilde{\phi} + \overline{T_\alpha}\partial_x \overline{\phi}\partial_y \widetilde{N}\right)
\end{aligned} \tag{B.13}
$$

Diffusion:

$$
\begin{aligned}
\chi_\alpha \boldsymbol{\nabla}_\perp^2\left(\overline{N} + \widetilde{N}\right)\left(\overline{T_\alpha} + \widetilde{T_\alpha}\right) =& \chi_\alpha\left(\boldsymbol{\nabla}_\perp^2\left(\overline{NT_\alpha}\right) + \boldsymbol{\nabla}_\perp^2\left(\overline{N\widetilde{T_\alpha}}\right) + T_i\boldsymbol{\nabla}_\perp^2\left(\widetilde{N}\overline{T_\alpha}\right)\right) \\
=& \chi_\alpha \boldsymbol{\nabla}_\perp^2\left(\overline{NT_\alpha}\right) + \chi_\alpha\left(\partial_x^2 \overline{T_\alpha} + 2\partial_x \overline{T_\alpha}\partial_x + \overline{T_\alpha}\boldsymbol{\nabla}_\perp^2\right)\widetilde{N} \\
&+ \chi_\alpha\left(\partial_x^2 \overline{N} + 2\partial_x \overline{N}\partial_x + \overline{N}\boldsymbol{\nabla}_\perp^2\right)\widetilde{T_\alpha}
\end{aligned} \tag{B.14}
$$

B.2.8 electronic energy conservation

$$\frac{3}{2}\partial_t\left(\overline{N}+\widetilde{N}\right)\left(\overline{T_e}+\widetilde{T_e}\right)+\frac{3}{2}\left[\overline{\phi}+\widetilde{\phi},\left(\overline{N}+\widetilde{N}\right)\left(\overline{T_e}+\widetilde{T_e}\right)\right]=\underbrace{-\sigma\gamma_e\left(\overline{N}+\widetilde{N}\right)\left(\overline{T_e}+\widetilde{T_e}\right)\sqrt{\overline{T}+\widetilde{T_e}+\widetilde{T_i}}\,\mathrm{e}^{\Lambda-\frac{\overline{\phi}+\widetilde{\phi}}{\overline{T_e}+\widetilde{T_e}}}}_{=A}$$
$$+\chi\boldsymbol{\nabla}_\perp^2\left(\overline{N}+\widetilde{N}\right)\left(\overline{T_e}+\widetilde{T_e}\right)$$

Let us develop first A:

$$\begin{aligned}A=&-\sigma\gamma_e\left(\overline{N}+\widetilde{N}\right)\left(\overline{T_e}\sqrt{\overline{T}}+\sqrt{\overline{T}}\widetilde{T_e}+\frac{\overline{T_e}}{2\sqrt{\overline{T}}}\left(\widetilde{T_e}+\widetilde{T_i}\right)\right)\left(1+\Lambda\frac{\widetilde{T_e}}{\overline{T_e}}-\frac{\widetilde{\phi}}{\overline{T_e}}\right)\\=&-\sigma\gamma_e\overline{NT_e}\sqrt{\overline{T}}-\sigma\gamma_e\overline{N}\left(\left(\sqrt{\overline{T}}\left(\Lambda+1\right)+\frac{\overline{T_e}}{2\sqrt{\overline{T}}}\right)\widetilde{T_e}-\sqrt{\overline{T}}\widetilde{\phi}+\frac{\overline{T_e}}{2\sqrt{\overline{T}}}\widetilde{T_i}\right)-\sigma\gamma_e\overline{T_e}\sqrt{\overline{T}}\widetilde{N}\end{aligned}$$

Using (2.4), (2.5) and the development of A we obtain:

$$\begin{aligned}&\frac{3}{2}\left(\overline{N}\partial_t\widetilde{T_e}+\overline{T_e}\partial_t\widetilde{N}+\overline{N}\partial_x\overline{\phi}\partial_y\widetilde{T_e}-\left(\overline{N}\partial_x\overline{T_e}\partial_y+\overline{T_e}\partial_x\overline{N}\partial_y\right)\widetilde{\phi}+\overline{T_e}\partial_x\overline{\phi}\partial_y\widetilde{N}\right)\\&=-\sigma\gamma_e\overline{NT_e}\sqrt{\overline{T}}-\sigma\gamma_e\overline{T_e}\sqrt{\overline{T}}\widetilde{N}-\sigma\gamma_e\overline{N}\left(\sqrt{\overline{T}}\left(\Lambda+1\right)+\frac{\overline{T_e}}{2\sqrt{\overline{T}}}\right)\widetilde{T_e}+\sigma\gamma_e\overline{N}\sqrt{\overline{T}}\widetilde{\phi}-\sigma\gamma_e\overline{N}\frac{\overline{T_e}}{2\sqrt{\overline{T}}}\widetilde{T_i}\\&\quad+\chi_e\boldsymbol{\nabla}_\perp^2\left(\overline{NT_\alpha}\right)+\chi_e\left(\partial_x^2\overline{T_\alpha}+2\partial_x\overline{T_\alpha}\partial_x+\overline{T_\alpha}\boldsymbol{\nabla}_\perp^2\right)\widetilde{N}+\chi_e\left(\partial_x^2\overline{N}+2\partial_x\overline{N}\partial_x+\overline{N}\boldsymbol{\nabla}_\perp^2\right)\widetilde{T_\alpha}\end{aligned}$$

in steady state and by dividing all term by N:

$$\begin{aligned}&\frac{3}{2}\left(\partial_t\widetilde{T_e}+\overline{T_e}\partial_t\widetilde{E}+\partial_x\overline{\phi}\partial_y\widetilde{T_e}-\left(\partial_x\overline{T_e}\partial_y+\overline{T_e}\partial_x\overline{E}\partial_y\right)\widetilde{\phi}+\overline{T_e}\partial_x\overline{\phi}\partial_y\widetilde{E}\right)\\&=-\sigma\gamma_e\overline{T_e}\sqrt{\overline{T}}\widetilde{E}-\sigma\gamma_e\left(\sqrt{\overline{T}}\left(\Lambda+1\right)+\frac{\overline{T_e}}{2\sqrt{\overline{T}}}\right)\widetilde{T_e}+\sigma\gamma_e\sqrt{\overline{T}}\widetilde{\phi}-\sigma\gamma_e\frac{\overline{T_e}}{2\sqrt{\overline{T}}}\widetilde{T_i}\\&\quad+\chi_e\left(\partial_x^2\overline{T_e}+2\partial_x\overline{T_e}\partial_x+\overline{T_e}\left(\boldsymbol{\nabla}_\perp^2-\frac{2}{\lambda_N}+\frac{1}{\lambda_N^2}\right)\right)\widetilde{E}+\chi_e\left(\partial_x^2\overline{E}+2\partial_x\overline{E}\partial_x+\boldsymbol{\nabla}_\perp^2\right)\widetilde{T_e}\end{aligned}$$

$$\begin{aligned}&\left(\frac{3}{2}\overline{T_e}\partial_t+\frac{3}{2}\Lambda\overline{T_e}\partial_x\overline{T_e}\partial_y+\sigma\gamma_e\overline{T_e}\sqrt{\overline{T}}-\chi\left(\partial_x^2\overline{T_e}+2\partial_x\overline{T_e}\partial_x+\overline{T_e}\left(\boldsymbol{\nabla}_\perp^2-\frac{2}{\lambda_N}+\frac{1}{\lambda_N^2}\right)\right)\right)\widetilde{E}\\&\qquad+\left(-\sigma\gamma_e\sqrt{\overline{T}}-\frac{3}{2}\left(\partial_x\overline{T_e}+\overline{T_e}\partial_x\overline{E}\right)\partial_y\right)\widetilde{\phi}\\&+\left(\frac{3}{2}\partial_t+\frac{3}{2}\Lambda\partial_x\overline{T_e}\partial_y+\sigma\gamma_e\left((\Lambda+1)\sqrt{\overline{T}}+\frac{\overline{T_e}}{2\sqrt{\overline{T}}}\right)-\chi(\partial_x^2\overline{E}+2\partial_x\overline{E}\partial_x+\boldsymbol{\nabla}_\perp^2)\right)\widetilde{T_e}+\sigma\gamma_e\frac{\overline{T_e}}{2\sqrt{\overline{T}}}\widetilde{T_i}=0\end{aligned}\tag{B.15}$$

B.2.9 Ionic energy equation

$$\frac{3}{2}\partial_t\left(\overline{N}+\widetilde{N}\right)\left(\overline{T_i}+\widetilde{T_i}\right)+\frac{3}{2}\left[\overline{\phi}+\widetilde{\phi},\left(\overline{N}+\widetilde{N}\right)\left(\overline{T_i}+\widetilde{T_i}\right)\right]=\underbrace{-\sigma\gamma_i\left(\overline{N}+\widetilde{N}\right)\left(\overline{T_i}+\widetilde{T_i}\right)\sqrt{\overline{T}+\widetilde{T_e}+\widetilde{T_i}}}_{=B}$$
$$+\chi\boldsymbol{\nabla}_\perp^2\left(\overline{N}+\widetilde{N}\right)\left(\overline{T_i}+\widetilde{T_i}\right)$$

Let us first develop B:

$$\begin{aligned}B=&-\sigma\gamma_i\left(\overline{N}+\widetilde{N}\right)\left(\overline{T_i}\sqrt{\overline{T}}+\sqrt{\overline{T}}\widetilde{T_i}+\frac{\overline{T_i}}{2\sqrt{\overline{T}}}\left(\widetilde{T_e}+\widetilde{T_i}\right)\right)\\=&-\sigma\gamma_i\overline{NT_i}\sqrt{\overline{T}}-\sigma\gamma_i\overline{N}\left(\sqrt{\overline{T}}+\frac{\overline{T_i}}{2\sqrt{\overline{T}}}\right)\widetilde{T_i}+\sigma\gamma_i\overline{N}\frac{\overline{T_i}}{2\sqrt{\overline{T}}}\widetilde{T_e}+\sigma\gamma_i\overline{T_i}\sqrt{\overline{T}}\widetilde{N}\end{aligned}$$

Using (2.4), (2.5) and the development of B we obtain:

$$\begin{aligned}&\frac{3}{2}\left(\overline{N}\partial_t\widetilde{T_i}+\overline{T_i}\partial_t\widetilde{N}+\overline{N}\partial_x\overline{\phi}\partial_y\widetilde{T_i}-\left(\overline{N}\partial_x\overline{T_i}\partial_y+\overline{T_i}\partial_x\overline{N}\partial_y\right)\widetilde{\phi}+\overline{T_i}\partial_x\overline{\phi}\partial_y\widetilde{N}\right)\\&=-\sigma\gamma_i\overline{NT_i}\sqrt{\overline{T}}-\sigma\gamma_i\overline{N}\left(\sqrt{\overline{T}}+\frac{\overline{T_i}}{2\sqrt{\overline{T}}}\right)\widetilde{T_i}+\sigma\gamma_i\overline{N}\frac{\overline{T_i}}{2\sqrt{\overline{T}}}\widetilde{T_e}+\sigma\gamma_i\overline{T_i}\sqrt{\overline{T}}\widetilde{N}\\&\quad+\chi_e\boldsymbol{\nabla}_\perp^2\left(\overline{NT_\alpha}\right)+\chi_e\left(\partial_x^2\overline{T_\alpha}+2\partial_x\overline{T_\alpha}\partial_x+\overline{T_\alpha}\boldsymbol{\nabla}_\perp^2\right)\widetilde{N}+\chi_e\left(\partial_x^2\overline{N}+2\partial_x\overline{N}\partial_x+\overline{N}\boldsymbol{\nabla}_\perp^2\right)\widetilde{T_i}\end{aligned}$$

In steady state (B.5) and by dividing all terms by N:

$$\begin{aligned}&\frac{3}{2}\left(\partial_t\widetilde{T_i}+\overline{T_i}\partial_t\widetilde{E}+\partial_x\overline{\phi}\partial_y\widetilde{T_i}-\left(\partial_x\overline{T_i}\partial_y+\overline{T_i}\partial_x\overline{E}\partial_y\right)\widetilde{\phi}+\overline{T_i}\partial_x\overline{\phi}\partial_y\widetilde{N}\right)\\&=-\sigma\gamma_i\left(\sqrt{\overline{T}}+\frac{\overline{T_i}}{2\sqrt{\overline{T}}}\right)\widetilde{T_i}+\sigma\gamma_i\frac{\overline{T_i}}{2\sqrt{\overline{T}}}\widetilde{T_e}+\sigma\gamma_i\overline{T_i}\sqrt{\overline{T}}\widetilde{E}\\&\quad+\chi_i\left(\partial_x^2\overline{T_i}+2\partial_x\overline{T_i}\partial_x+\overline{T_i}\left(\boldsymbol{\nabla}_\perp^2-\frac{2}{\lambda_N}+\frac{1}{\lambda_N^2}\right)\right)\widetilde{E}+\chi_i\left(\partial_x^2\overline{E}+2\partial_x\overline{E}\partial_x+\boldsymbol{\nabla}_\perp^2\right)\widetilde{T_i}\end{aligned}$$

$$\begin{aligned}&\left(\frac{3}{2}\overline{T_i}\partial_t+\frac{3}{2}\Lambda\overline{T_i}\partial_x\overline{T_e}\partial_y+\sigma\gamma_i\overline{T_i}\sqrt{\overline{T}}-\chi\left(\partial_x^2\overline{T_i}+2\partial_x\overline{T_i}\partial_x+\overline{T_i}\left(\boldsymbol{\nabla}_\perp^2-\frac{2}{\lambda_N}+\frac{1}{\lambda_N^2}\right)\right)\right)\widetilde{E}+\left(-\frac{3}{2}\partial_x\left(\overline{NT_i}\right)\partial_y\right)\widetilde{\phi}\\&+\left(\sigma\gamma_i\frac{\overline{T_i}}{2\sqrt{\overline{T}}}\right)\widetilde{T_e}+\left(\frac{3}{2}\partial_t+\frac{3}{2}\Lambda\partial_x\overline{T_e}\partial_y+\sigma\gamma_i\left(\sqrt{\overline{T}}+\frac{\overline{T_i}}{2\sqrt{\overline{T}}}\right)-\chi(\partial_x^2\overline{E}+2\partial_x\overline{E}\partial_x+\boldsymbol{\nabla}_\perp^2)\right)\widetilde{T_i}=0\end{aligned}\tag{B.16}$$

B.3 Spectral Analysis

We assume to find a solution of the form :

$$\begin{cases} \widetilde{E} = \sum_{k_x,k_y} \widehat{E}_{k_x,k_y} \exp(ik_x x + ik_y y) \exp(\omega_k t) \\ \widetilde{\phi} = \sum_{k_x,k_y} \widehat{\phi}_{k_x,k_y} \exp(ik_x x + ik_y y) \exp(\omega_k t) \\ \widetilde{T_e} = \sum_{k_x,k_y} \widehat{T_e}_{k_x,k_y} \exp(ik_x x + ik_y y) \exp(\omega_k t) \\ \widetilde{T_i} = \sum_{k_x,k_y} \widehat{T_e}_{k_x,k_y} \exp(ik_x x + ik_y y) \exp(\omega_k t) \end{cases}$$

Where $\widehat{E}, \widehat{\phi}, \widehat{T_e}, \widehat{T_i}$ are the Fourier transforms of $\widetilde{E}, \widetilde{\phi}, \widetilde{T_e}, \widetilde{T_i}$ respectively
As all average profiles are decaying exponential, we have $\frac{\partial_x^\alpha \overline{X}}{\overline{X}} = (\frac{\partial_x \overline{X}}{\overline{X}})^\alpha = -\frac{1}{\lambda_X^\alpha}$.
The equation (B.10), (B.11), (B.15), and (B.16) can be written in Fourier space as :

$$\left(\omega_k - \Lambda \frac{\overline{T_e}}{\lambda_{T_e}} i k_y + \sigma\sqrt{\overline{T}} + D\left(k_\perp^2 + 2\frac{ik_x}{\lambda_N} - \frac{1}{\lambda_N^2}\right)\right)\widehat{E}_{k_x,k_y} + \left(-\sigma\frac{\sqrt{\overline{T}}}{\overline{T_e}} + \frac{ik_y}{\lambda_N}\right)\widehat{\phi}_{k_x,k_y} + \sigma\left(\frac{\sqrt{\overline{T}}}{\overline{T_e}}\Lambda + \frac{1}{2\sqrt{\overline{T}}}\right)\widehat{T_e}_{k_x,k_y} + \frac{\sigma}{2\sqrt{\overline{T}}}\widehat{T}_{ik_x,k_y} = 0 \quad \text{(B.17)}$$

$$\left(g\overline{T} i k_y\right)\widehat{E}_{k_x,k_y} + \left(-\partial_x\overline{W} i k_y - \sigma\frac{\sqrt{\overline{T}}}{\overline{T_e}}\right)\widehat{\phi}_{k_x,k_y} + \left(\omega_k - \Lambda\frac{\overline{T_e}}{\lambda_{T_e}} i k_y + \nu k_\perp^2\right)\widehat{W}_{k_x,k_y} + \left(g i k_y + \sigma\Lambda\frac{\sqrt{\overline{T}}}{\overline{T_e}}\right)\widehat{T_e}_{k_x,k_y} + \left(g i k_y\right)\widehat{T}_{ik_x,k_y} = 0 \quad \text{(B.18)}$$

$$\left(\frac{\overline{T_i}}{\lambda_{T_i}} i k_x + \overline{T_i} k_\perp^2\right)\widehat{E}_{k_x,k_y} + k_\perp^2\widehat{\phi}_{k_x,k_y} + \widehat{W}_{k_x,k_y} + \left(k_\perp^2 + \frac{ik_x}{\lambda_N}\right)\widehat{T}_{ik_x,k_y} = 0 \quad \text{(B.19)}$$

$$\left(\frac{3}{2}\overline{T_e}\omega_k - \frac{3}{2}\Lambda\frac{\overline{T_e}^2}{\lambda_{T_e}} i k_y + \sigma\gamma_e\overline{T_e}\sqrt{\overline{T}} - \chi_e\left(\frac{\overline{T_e}}{\lambda_{T_e}^2} - 2\frac{\overline{T_e}}{\lambda_{T_e}} i k_x - \overline{T_e}\left(k_\perp^2 + 2\frac{ik_x}{\lambda_N} - \frac{1}{\lambda_N^2}\right)\right)\right)\widehat{E}_{k_x,k_y} + \left(-\sigma\gamma_e\sqrt{\overline{T}} + \frac{3}{2}\left(\frac{\overline{T_e}}{\lambda_N} + \frac{\overline{T_e}}{\lambda_{T_e}}\right) i k_y\right)\widehat{\phi}_{k_x,k_y} + \left(\frac{3}{2}\omega_k - \frac{3}{2}\Lambda\frac{\overline{T_e}}{\lambda_{T_e}} i k_y + \sigma\gamma_e\left((\Lambda+1)\sqrt{\overline{T}} + \frac{\overline{T_e}}{2\sqrt{\overline{T}}}\right) - \chi_e\left(\frac{1}{\lambda_N^2} - 2\frac{ik_x}{\lambda_N} - k_\perp^2\right)\right)\widehat{T_e}_{k_x,k_y} + \sigma\gamma_e\frac{\overline{T_e}}{2\sqrt{\overline{T}}}\widehat{T}_{ik_x,k_y} = 0 \quad \text{(B.20)}$$

$$\left(\frac{3}{2}\overline{T_i}\omega_k - \frac{3}{2}\Lambda\frac{\overline{T_i T_e}}{\lambda_{T_e}}ik_y + \sigma\gamma_i\overline{T_i}\sqrt{\overline{T}} - \chi_i\left(\frac{\overline{T_i}}{\lambda_{T_i}^2} - 2\frac{\overline{T_i}}{\lambda_{T_i}}ik_x - \overline{T_i}\left(k_\perp^2 + 2\frac{ik_x}{\lambda_N} - \frac{1}{\lambda_N^2}\right)\right)\right)\widehat{E}_{k_x,k_y}$$
$$+\left(\frac{3}{2}\left(\frac{\overline{T_i}}{\lambda_N} + \frac{1}{\lambda_{T_i}}\right)ik_y\right)\widehat{\phi}_{k_x,k_y} + \sigma\gamma_i\frac{\overline{T_i}}{2\sqrt{\overline{T}}}\widehat{T_e}_{k_x,k_y}$$
$$+\left(\frac{3}{2}\omega_k - \frac{3}{2}\Lambda\frac{\overline{T_e}}{\lambda_{T_e}}ik_y + \sigma\gamma_i\left(\sqrt{\overline{T}} + \frac{\overline{T_i}}{2\sqrt{\overline{T}}}\right) - \chi_i\left(\frac{1}{\lambda_N^2} - 2\frac{ik_x}{\lambda_N} - k_\perp^2\right)\right)\widehat{T}_{ik_x,k_y} = 0 \quad \text{(B.21)}$$

Where $k_\perp^2 = k_x^2 + k_y^2$

This system of 4 equations with 4 unknowns has a non-zero solution if and only if its determinant is null, so we have a condition on ω_k for given values of $k_x, k_y, \Lambda, \sigma, D, \nu, \chi_e, \chi_i, \gamma_e, \gamma_i, g, \overline{T_e}, \overline{T_i}, \lambda_N, \lambda_{T_e}, \lambda T_i$:

$$
\begin{vmatrix}
\omega_k - \Lambda\frac{\overline{T_e}}{\lambda_{T_e}}ik_y + \sigma\sqrt{\overline{T}} & -\frac{\sigma\sqrt{\overline{T}}}{\overline{T_e}} + \frac{ik_y}{\lambda_N} & 0 & \sigma\left(\frac{\sqrt{\overline{T}}}{\overline{T_e}}\Lambda + \frac{1}{2\sqrt{\overline{T}}}\right) & \frac{\sigma}{2\sqrt{\overline{T}}} \\
+D\left(k_\perp^2 + 2\frac{ik_x}{\lambda_N} - \frac{1}{\lambda_N^2}\right) & & & & \\
g\overline{T}ik_y & -\partial_x\overline{W}ik_y - \sigma\frac{\sqrt{\overline{T}}}{\overline{T_e}} & \omega_k - \Lambda\frac{\overline{T_e}}{\lambda_{T_e}}ik_y + \nu k_\perp^2 & gik_y + \sigma\Lambda\frac{\sqrt{\overline{T}}}{\overline{T_e}} & gik_y \\
\frac{\overline{T_i}}{\lambda_{T_i}}ik_x + \overline{T_i}k_\perp^2 & k_\perp^2 & 1 & 0 & k_\perp^2 + \frac{ik_x}{\lambda_N} \\
\frac{3}{2}\overline{T_e}\omega_k - \frac{3}{2}\Lambda\frac{\overline{T_e}^2}{\lambda_{T_e}}ik_y & -\sigma\gamma_e\sqrt{\overline{T}} & 0 & \frac{3}{2}\omega_k - \frac{3}{2}\Lambda\frac{\overline{T_e}}{\lambda_{T_e}}ik_y & \sigma\gamma_e\frac{\overline{T_e}}{2\sqrt{\overline{T}}} \\
+\sigma\gamma_e\overline{T_e}\sqrt{\overline{T}} - \chi_e\Big(\frac{\overline{T_e}}{\lambda_{T_e}^2} - 2\frac{\overline{T_e}}{\lambda_{T_e}}ik_x & +\frac{3}{2}\left(\frac{\overline{T_e}}{\lambda_N} + \frac{\overline{T_e}}{\lambda_{T_e}}\right)ik_y & & +\sigma\gamma_e\left((\Lambda+1)\sqrt{\overline{T}} + \frac{\overline{T_e}}{2\sqrt{\overline{T}}}\right) & \\
-\overline{T_e}\left(k_\perp^2 + 2\frac{ik_x}{\lambda_N} - \frac{1}{\lambda_N^2}\right)\Big) & & & -\chi_e\left(\frac{1}{\lambda_N^2} - 2\frac{ik_x}{\lambda_N} - k_\perp^2\right) & \\
\frac{3}{2}\overline{T_i}\omega_k - \frac{3}{2}\Lambda\overline{T_i}\frac{\overline{T_e}}{\lambda_{T_e}}ik_y + \sigma\gamma_i\overline{T_i}\sqrt{\overline{T}} & \frac{3}{2}\left(\frac{\overline{T_i}}{\lambda_N} + \frac{\overline{T_i}}{\lambda_{T_i}}\right)ik_y & 0 & \sigma\gamma_i\frac{\overline{T_i}}{2\sqrt{\overline{T}}} & \frac{3}{2}\omega_k - \frac{3}{2}\Lambda\frac{\overline{T_e}}{\lambda_{T_e}}ik_y \\
-\chi_i\Big(\frac{\overline{T_i}}{\lambda_{T_i}^2} - 2\frac{\overline{T_i}}{\lambda_{T_i}}ik_x & & & & +\sigma\gamma_i\left(\sqrt{\overline{T}} + \frac{\overline{T_i}}{2\sqrt{\overline{T}}}\right) \\
-\overline{T_i}\left(k_\perp^2 + 2\frac{ik_x}{\lambda_N} - \frac{1}{\lambda_N^2}\right)\Big) & & & & -\chi_i(\frac{1}{\lambda_N^2} - 2\frac{ik_x}{\lambda_N} - k_\perp^2)
\end{vmatrix}
$$

$$
\begin{aligned}
\partial_x W =& \partial_x^3\overline{\phi} + \partial_x^3\overline{T_i} - \frac{\partial_x^2\overline{T_i}}{\lambda_N} \\
=& -\Lambda\frac{\overline{T_e}}{\lambda_{T_e}^3} - \frac{\overline{T_i}}{\lambda_{T_i}^3} - \frac{\overline{T_i}}{\lambda_{T_i}^2}\frac{1}{\lambda_N}
\end{aligned}
$$

Bibliography

[Arnoux 13] G Arnoux, T Farley, C Silva, S Devaux, M Firdaouss, D Frigione, RJ Goldston, J Gunn, J Horacek, S Jachmich*et al.* *Scrape-off layer properties of ITER-like limiter start-up plasmas in JET.* Nuclear Fusion, vol. 53, no. 7, page 073016, 2013.

[Berk 91] HL Berk, DD Ryutov & Yu A Tsidulko. *Temperature-gradient instability induced by conducting end walls.* Physics of Fluids B: Plasma Physics (1989-1993), vol. 3, no. 6, pages 1346–1354, 1991.

[Berk 93] H-L Berk, RH Cohen, DD Ryutov, Yu A Tsidulko & XQ Xu. *Electron temperature gradient induced instability in tokamak scrape-off layers.* Nuclear Fusion, vol. 33, no. 2, page 263, 1993.

[Bisai 13] N Bisai & PK Kaw. *Role of ion temperature on scrape-off layer plasma turbulence.* Physics of Plasmas, vol. 20, no. 4, page 042509, 2013.

[Braginskii 65] SI Braginskii. *Transport processes in a plasma.* Reviews of plasma physics, vol. 1, page 205, 1965.

[Bufferand 15] Hugo Bufferand, Guido Ciraolo, Yannick Marandet, Jérome Bucalossi, Ph Ghendrih, Jamie Gunn, N Mellet, Patrick Tamain, R Leybros, Nicolas Fedorczak*et al.* *Numerical modelling for divertor design of the WEST device with a focus on plasma–wall interactions.* Nuclear Fusion, vol. 55, no. 5, page 053025, 2015.

[Bufferand 17] H Bufferand, C Baudoin, J Bucalossi, G Ciraolo, J Denis, N Fedorczak, D Galassi, Ph Ghendrih, R Leybros, Y Marandet*et al.* *Implementation of drift velocities and currents in SOLEDGE2D-EIRENE.* Nuclear Materials and Energy, 2017.

[Burrell 97] KH Burrell. *Effects of E× B velocity shear and magnetic shear on turbulence and transport in magnetic confinement devices.* Physics of Plasmas, vol. 4, no. 5, pages 1499–1518, 1997.

[Carralero 14] D. Carralero, G. Birkenmeier, H.W. Müller, P. Manz, P. deMarne, S.H. Müller, F. Reimold, U. Stroth, M. Wischmeier, E. Wolfrum & The ASDEX Upgrade Team. *An experimental investigation of the high density transition of the scrape-off layer transport in ASDEX Upgrade.* Nuclear Fusion, vol. 54, no. 12, page 123005, 2014.

[Carreras 96] BA Carreras, C Hidalgo, E Sánchez, MA Pedrosa, R Balbin, I García-Cortés, B Van Milligen, DE Newman & VE Lynch. *Fluctuation-induced flux at the plasma edge in toroidal devices.* Physics of Plasmas, vol. 3, no. 7, pages 2664–2672, 1996.

[Cartier-Michaud 16] T Cartier-Michaud, Philippe Ghendrih, Yanick Sarazin, J Abiteboul, Hugo Bufferand, Guilhem Dif-Pradalier, Xavier Garbet, Virginie Grandgirard, Guillaume Latu, C Norscini*et al. Projection on Proper elements for code control: Verification, numerical convergence, and reduced models. Application to plasma turbulence simulations.* Physics of Plasmas, vol. 23, no. 2, page 020702, 2016.

[Chankin 97] AV Chankin. *Classical drifts in the tokamak SOL and divertor: models and experiment.* Journal of nuclear materials, vol. 241, pages 199–213, 1997.

[Chankin 06] AV Chankin, DP Coster, R Dux, Ch Fuchs, G Haas, A Herrmann, LD Horton, A Kallenbach, M Kaufmann, Ch Konz*et al. SOLPS modelling of ASDEX upgrade H-mode plasma.* Plasma physics and controlled fusion, vol. 48, no. 6, page 839, 2006.

[Chankin 13] AV Chankin & DP Coster. *The role of drifts in the plasma transport at the tokamak core–SOL interface.* Journal of Nuclear Materials, vol. 438, pages S463–S466, 2013.

[Chen 17] B Chen, XQ Xu, TY Xia, M Porkolab, E Edlund, B LaBombard, J Terry, JW Hughes, SF Mao, MY Ye*et al. Edge turbulence and divertor heat flux width simulations of Alcator C-Mod discharges using an electromagnetic two-fluid model.* Nuclear Fusion, vol. 57, no. 11, page 116025, 2017.

[Chodura 86] Chodura. Physics of plasma–wall interaction in controlled fusion. 1986.

[Cohen 94] Ronald H Cohen, Nathan Mattor & Xueqiao Xu. *Scrape-Off Layer Turbulence Theory.* Contributions to Plasma Physics, vol. 34, no. 2-3, pages 232–246, 1994.

[Colin 15a] C Colin. *Turbulent transport modelling in the edge plasma of tokamaks: Verification, Validation, Simulation and Synthetic Diagnostics.* PhD thesis, 2015.

[Colin 15b] Clothilde Colin, Patrick Tamain, Frederic Schwander, Eric Serre, Hugo Bufferand, Guido Ciraolo, Nicolas Fedorczak & Ph Ghendrih. *Impact of the plasma-wall contact position on edge turbulent transport and poloidal asymmetries in 3D global turbulence simulations.* Journal of Nuclear Materials, vol. 463, pages 654–658, 2015.

[Dejarnac 15] R. Dejarnac, P.C. Stangeby, R.J. Goldston, E. Gauthier, J. Horacek, M. Hron, M. Kocan, M. Komm, R. Panek, R.A. Pitts & P. Vondracek. *Understanding narrow {SOL} power flux component in {COMPASS} limiter plasmas by use of Langmuir probes.* Journal of Nuclear Materials, no. 0, pages –, 2015.

[D'Ippolito 11] DA D'Ippolito, JR Myra & SJ Zweben. *Convective transport by intermittent blob-filaments: Comparison of theory and experiment.* Physics of Plasmas, vol. 18, no. 6, page 060501, 2011.

[Dudson 08] BD Dudson, N Ben Ayed, A Kirk, HR Wilson, G Counsell, X Xu, M Umansky, PB Snyder, B Lloyd*et al. Experiments and simulation of edge turbulence and filaments in MAST.* Plasma Physics and Controlled Fusion, vol. 50, no. 12, page 124012, 2008.

[Eich 11] T Eich, B Sieglin, A Scarabosio, W Fundamenski, RJ Goldston, A Herrmann & ASDEX Upgrade Team. *Inter-ELM power decay length for JET and ASDEX upgrade: Measurement and comparison with heuristic drift-based model.* Physical review letters, vol. 107, no. 21, page 215001, 2011.

[Eich 13a] T Eich, B Sieglin, A Scarabosio, A Herrmann, A Kallenbach, GF Matthews, S Jachmich, S Brezinsek, M Rack, RJ Goldston*et al. Empiricial scaling of inter-ELM power widths in ASDEX Upgrade and JET.* Journal of Nuclear Materials, vol. 438, pages S72–S77, 2013.

[Eich 13b] Thomas Eich, AW Leonard, RA Pitts, W Fundamenski, RJ Goldston, TK Gray, A Herrmann, A Kirk, A Kallenbach, O Kardaun*et al. Scaling of the tokamak near the scrape-off layer H-mode power width and implications for ITER.* Nuclear Fusion, vol. 53, no. 9, page 093031, 2013.

[Faitsch 15] M Faitsch, B Sieglin, T Eich, HJ Sun & A Herrmann. *Change of the scrape-off layer power width with the toroidal B-field direction in ASDEX upgrade.* Plasma Physics and Controlled Fusion, vol. 57, no. 7, page 075005, 2015.

[Fedorczak 11] Nicolas Fedorczak, James Paul Gunn, Ph Ghendrih, G Ciraolo, H Bufferand, L Isoardi, P Tamain & P Monier-Garbet. *Experimental investigation on the poloidal extent of the turbulent radial flux in tokamak scrape-off layer.* Journal of Nuclear Materials, vol. 415, no. 1, pages S467–S470, 2011.

[Fedorczak 13] N Fedorczak, Ph Ghendrih, P Hennequin, GR Tynan, PH Diamond & P Manz. *Dynamics of tilted eddies in a transversal flow at the edge of tokamak plasmas and the consequences for L–H transition.* Plasma Physics and Controlled Fusion, vol. 55, no. 12, page 124024, 2013.

[Fedorczak 17] Nicolas Fedorczak, JP Gunn, N Nace, A Gallo, C Baudoin, H Bufferand, G Ciraolo, Th Eich, Ph Ghendrih & Patrick Tamain. *Width of turbulent SOL in circular plasmas: a theoretical model validated on experiments in Tore Supra tokamak.* Nuclear Materials and Energy, vol. 12, pages 838–843, 2017.

[Fundamenski 07] W Fundamenski, Odd Erik Garcia, Volker Naulin, RA Pitts, Anders Henry Nielsen, J Juul Rasmussen, J Horacek, JP Graves*et al. Dissipative processes in interchange driven scrape-off layer turbulence.* Nuclear fusion, vol. 47, no. 5, page 417, 2007.

[Fundamenski 11] W Fundamenski, T Eich, S Devaux, S Jachmich, M Jakubowski, H Thomsen, G Arnoux, F Militello, E Havlickova, D Moulton*et al.* *Multi-parameter scaling of divertor power load profiles in D, H and He plasmas on JET and implications for ITER.* Nuclear Fusion, vol. 51, no. 8, page 083028, 2011.

[Galassi 17] D. Galassi, P. Tamain, H. Bufferand, G. Ciraolo, Ph. Ghendrih, C. Baudoin, C. Colin, N. Fedorczak, N. Nace & E. Serre. *Drive of parallel flows by turbulence and large-scale $E \times B$ transverse transport in divertor geometry.* Nuclear Fusion, vol. 57, no. 3, page 036029, 2017.

[Gallo 16] A Gallo, N Fedorczak, R Maurizio, C Theiler, S Elmore, B Labit, H Reimerdes, F Nespoli, P Ghendrih, T Eich*et al.* *Effect of plasma geometry on divertor heat flux spreading: MONALISA simulations and experimental results from TCV.* Nuclear Materials and Energy, 2016.

[Ghendrih 11] Ph Ghendrih, K Bodi, H Bufferand, Guillaume Chiavassa, Guido Ciraolo, Nicolas Fedorczak, Livia Isoardi, A Paredes, Yanick Sarazin, Eric Serre*et al.* *Transition to supersonic flows in the edge plasma.* Plasma Physics and Controlled Fusion, vol. 53, no. 5, page 054019, 2011.

[Goldston 12] RJ Goldston. *Heuristic drift-based model of the power scrape-off width in low-gas-puff H-mode tokamaks.* Nuclear Fusion, vol. 52, no. 1, page 013009, 2012.

[Goldston 15] RJ Goldston. *Theoretical aspects and practical implications of the heuristic drift SOL model.* Journal of Nuclear Materials, 2015.

[Gulejová 07] B. Gulejová, R.A. Pitts, M. Wischmeier, R. Behn, D. Coster, J. Horacek & J. Marki. *SOLPS5 modelling of the type III ELMing H-mode on TCV.* Journal of Nuclear Materials, vol. 363, pages 1037–1043, 2007. Plasma-Surface Interactions-17.

[Gunn 07] JP Gunn, C Boucher, M Dionne, I Ďuran, V Fuchs, T Loarer, I Nanobashvili, R Pánek, J-Y Pascal, F Saint-Laurent*et al.* *Evidence for a poloidally localized enhancement of radial transport in the scrape-off layer of the Tore Supra tokamak.* Journal of Nuclear Materials, vol. 363, pages 484–490, 2007.

[Gunn 13] JP Gunn, R Dejarnac, P Devynck, N Fedorczak, V Fuchs, C Gil, M Kočan, M Komm, M Kubič, T Lunt*et al.* *Scrape-off layer power flux measurements in the Tore Supra tokamak.* vol. 438, pages S184–S188, 2013.

[Günter 05] S Günter, Q Yu, J Krüger & K Lackner. *Modelling of heat transport in magnetised plasmas using non-aligned coordinates.* Journal of Computational Physics, vol. 209, no. 1, pages 354–370, 2005.

[Halpern 17] F.D. Halpern & P. Ricci. *Velocity shear, turbulent saturation, and steep plasma gradients in the scrape-off layer of inner-wall limited tokamaks.* Nuclear Fusion, vol. 57, no. 3, page 034001, 2017.

[Hinton 71] FL Hinton & CW Horton Jr. *Amplitude limitation of a collisional drift wave instability.* The Physics of Fluids, vol. 14, no. 1, pages 116–123, 1971.

[Hinton 74] FL Hinton & RD Hazeltine. *Kinetic theory of plasma scrape-off in a divertor tokamak.* Physics of Fluids (1958-1988), vol. 17, no. 12, pages 2236–2240, 1974.

[Horacek 10] J Horacek, J Adamek, HW Müller, J Seidl, Anders Henry Nielsen, V Rohde, F Mehlmann, C Ionita, E Havlíčková*et al. Interpretation of fast measurements of plasma potential, temperature and density in SOL of ASDEX Upgrade.* Nuclear Fusion, vol. 50, no. 10, page 105001, 2010.

[Horacek 15] J Horacek, P Vondracek, R Panek, R Dejarnac, M Komm, RA Pitts, M Kocan, RJ Goldston, PC Stangeby, E Gauthier*et al. Narrow heat flux channels in the COMPASS limiter scrape-off layer.* Journal of Nuclear Materials, vol. 463, pages 385–388, 2015.

[Hornung 13] Grégoire Hornung, Frédéric Clairet, GL Falchetto, Roland Sabot, Hugo Arnichand & Laure Vermare. *Turbulence correlation properties measured with ultrafast sweeping reflectometry on tore supra.* Plasma Physics and Controlled Fusion, vol. 55, no. 12, page 125013, 2013.

[Horton 05] LD Horton, AV Chankin, YP Chen, GD Conway, DP Coster, T Eich, E Kaveeva, C Konz, B Kurzan, J Neuhauser*et al. Characterization of the H-mode edge barrier at ASDEX Upgrade.* Nuclear fusion, vol. 45, no. 8, page 856, 2005.

[Jovanović 08] D Jovanović, PK Shukla & F Pegoraro. *Effects of the parallel electron dynamics and finite ion temperature on the plasma blob propagation in the scrape-off layer.* Physics of Plasmas, vol. 15, no. 11, page 112305, 2008.

[Kallenbach 04] A Kallenbach, Y Andrew, M Beurskens, G Corrigan, T Eich, S Jachmich, M Kempenaars, A Korotkov, A Loarte, G Matthews*et al. EDGE2D modelling of edge profiles obtained in JET diagnostic optimized configuration.* Plasma physics and controlled fusion, vol. 46, no. 3, page 431, 2004.

[Kočan 11] M Kočan, JP Gunn, S Carpentier-Chouchana, A Herrmann, A Kirk, M Komm, HW Müller, J-Y Pascal, RA Pitts, V Rohde*et al. Measurements of ion energies in the tokamak plasma boundary.* Journal of Nuclear Materials, vol. 415, no. 1, pages S1133–S1138, 2011.

[Kočan 15] M Kočan, RA Pitts, G Arnoux, I Balboa, PC de Vries, R Dejarnac, I Furno, RJ Goldston, Y Gribov, J Horacek*et al. Impact of a narrow limiter SOL heat flux channel on the ITER first wall panel shaping.* Nuclear Fusion, vol. 55, no. 3, page 033019, 2015.

[Lawson 57] John D Lawson. *Some criteria for a power producing thermonuclear reactor.* Proceedings of the Physical Society. Section B, vol. 70, no. 1, page 6, 1957.

[Lipschultz 07] B Lipschultz, X Bonnin, G Counsell, A Kallenbach, A Kukushkin, K Krieger, A Leonard, A Loarte, R Neu, RA Pitts*et al. Plasma–surface interaction, scrape-off layer and divertor physics: implications for ITER.* Nuclear Fusion, vol. 47, no. 9, page 1189, 2007.

[Loarte 99] A Loarte, S Bosch, A Chankin, S Clement, A Herrmann, D Hill, K Itami, J Lingertat, B Lipschultz, K McCormick*et al. Multi-machine scaling of the divertor peak heat flux and width for L-mode and H-mode discharges.* Journal of nuclear materials, vol. 266, pages 587–592, 1999.

[Loarte 07] A Loarte, B Lipschultz, AS Kukushkin, GF Matthews, PC Stangeby, N Asakura, GF Counsell, G Federici, A Kallenbach, K Krieger*et al. Power and particle control.* Nuclear Fusion, vol. 47, no. 6, page S203, 2007.

[Loizu 14] J Loizu, P Ricci, FD Halpern, S Jolliet & A Mosetto. *Effect of the limiter position on the scrape-off layer width, radial electric field and intrinsic flows.* Nuclear Fusion, vol. 54, no. 8, page 083033, 2014.

[Madsen 11] Jens Madsen, Odd E Garcia, Jeppe Stærk Larsen, Volker Naulin, Anders H Nielsen & Jens Juul Rasmussen. *The influence of finite Larmor radius effects on the radial interchange motions of plasma filaments.* Physics of Plasmas, vol. 18, no. 11, page 112504, 2011.

[Makowski 12] MA Makowski, D Elder, Travis K Gray, Brian LaBombard, CJ Lasnier, AW Leonard, Rajesh Maingi, TH Osborne, PC Stangeby, JL Terry*et al. Analysis of a multi-machine database on divertor heat fluxesa).* Physics of Plasmas, vol. 19, no. 5, page 056122, 2012.

[Marandet 16] Y Marandet, N Nace, M Valentinuzzi, P Tamain, H Bufferand, G Ciraolo, P Genesio & N Mellet. *Assessment of the effects of scrape-off layer fluctuations on first wall sputtering with the TOKAM-2D turbulence code.* Plasma Physics and Controlled Fusion, vol. 58, no. 11, page 114001, 2016.

[Meier 16] ET Meier, RJ Goldston, EG Kaveeva, MA Makowski, S Mordijck, VA Rozhansky, I Yu Senichenkov & SP Voskoboynikov. *Analysis of drift effects on the tokamak power scrape-off width using SOLPS-ITER.* Plasma Physics and Controlled Fusion, vol. 58, no. 12, page 125012, 2016.

[Mosetto 13] Annamaria Mosetto, Federico D Halpern, Sébastien Jolliet, Joaquim Loizu & Paolo Ricci. *Turbulent regimes in the tokamak scrape-off layer.* Physics of Plasmas, vol. 20, no. 9, page 092308, 2013.

[Mosetto 15] Annamaria Mosetto, Federico D Halpern, Sébastien Jolliet, Joaquim Loizu & Paolo Ricci. *Finite ion temperature effects on scrape-off layer turbulence.* Physics of Plasmas, vol. 22, no. 1, page 012308, 2015.

[Myra 97] JR Myra, DA D'Ippolito & JP Goedbloed. *Generalized ballooning and sheath instabilities in the scrape-off layer of divertor tokamaks.* Physics of Plasmas, vol. 4, no. 5, pages 1330–1341, 1997.

[Myra 06] JR Myra, DA D'Ippolito, DP Stotler, SJ Zweben, BP LeBlanc, JE Menard, RJ Maqueda & J Boedo. *Blob birth and transport in the tokamak edge plasma: Analysis of imaging data.* Physics of plasmas, vol. 13, no. 9, page 092509, 2006.

[Naulin 08] Volker Naulin, T Windisch & O Grulke. *Three-dimensional global fluid simulations of cylindrical magnetized plasmas.* Physics of Plasmas, vol. 15, no. 1, page 012307, 2008.

[Olsen 16] Jeppe Olsen, Jens Madsen, Anders Henry Nielsen, Jens Juul Rasmussen & Volker Naulin. *Temperature dynamics and velocity scaling laws for interchange driven, warm ion plasma filaments.* Plasma Physics and Controlled Fusion, vol. 58, no. 4, page 044011, 2016.

[Pitcher 97] Charles Spencer Pitcher & PC Stangeby. *Experimental divertor physics.* Plasma Physics and Controlled Fusion, vol. 39, no. 6, page 779, 1997.

[Rasmussen 15] J Juul Rasmussen, Anders Henry Nielsen, Jens Madsen, Volker Naulin & GS Xu. *Numerical modeling of the transition from low to high confinement in magnetically confined plasma.* Plasma Physics and Controlled Fusion, vol. 58, no. 1, page 014031, 2015.

[Rasmussen 16] J Juul Rasmussen, A H Nielsen, J Madsen, V Naulin & G S Xu. *Numerical modeling of the transition from low to high confinement in magnetically confined plasma.* Plasma Physics and Controlled Fusion, vol. 58, no. 1, page 014031, 2016.

[Reiser 17] D Reiser & T Eich. *Drift-based scrape-off particle width in X-point geometry.* Nuclear Fusion, vol. 57, no. 4, page 046011, 2017.

[Ricci 09] Paolo Ricci & BN Rogers. *Transport scaling in interchange-driven toroidal plasmas.* Physics of Plasmas, vol. 16, no. 6, page 062303, 2009.

[Ricci 10] Paolo Ricci & BN Rogers. *Turbulence phase space in simple magnetized toroidal plasmas.* Physical review letters, vol. 104, no. 14, page 145001, 2010.

[Ricci 12] P Ricci, FD Halpern, S Jolliet, J Loizu, A Mosetto, A Fasoli, I Furno & C Theiler. *Simulation of plasma turbulence in scrape-off layer conditions: the GBS code, simulation results and code validation.* Plasma Physics and Controlled Fusion, vol. 54, no. 12, page 124047, 2012.

[Ricci 13] Paolo Ricci & BN Rogers. *Plasma turbulence in the scrape-off layer of tokamak devices.* Physics of Plasmas, vol. 20, no. 1, page 010702, 2013.

[Ryter 14] F Ryter, L Barrera Orte, B Kurzan, RM McDermott, G Tardini, E Viezzer, M Bernert, R Fischer*et al.* *Experimental evidence for the key role of the ion*

heat channel in the physics of the L–H transition. Nuclear Fusion, vol. 54, no. 8, page 083003, 2014.

[Ryutov 04] DD Ryutov & RH Cohen. *Instability driven by sheath boundary conditions and limited to divertor legs.* Contributions to Plasma Physics, vol. 44, no. 1-3, pages 168–175, 2004.

[Sarazin 98] Y Sarazin & Ph Ghendrih. *Intermittent particle transport in two-dimensional edge turbulence.* Physics of Plasmas, vol. 5, no. 12, pages 4214–4228, 1998.

[Sarazin 03] Y. Sarazin, Ph. Ghendrih, G. Attuel, C. Clément, X. Garbet, V. Grandgirard, M. Ottaviani, S. Benkadda, P. Beyer, N. Bian & C. Figarella. *Theoretical understanding of turbulent transport in the {SOL}.* Journal of Nuclear Materials, vol. 313 - 316, no. 0, pages 796–803, 2003. Plasma-Surface Interactions in Controlled Fusion Devices 15.

[Scarabosio 13] A Scarabosio, T Eich, A Herrmann, B Sieglin, JET-EFDA contributors*et al. Outer target heat fluxes and power decay length scaling in L-mode plasmas at JET and AUG.* Journal of Nuclear Materials, vol. 438, pages S426–S430, 2013.

[Scarabosio 15] A Scarabosio, T Eich, F Hoppe, I Paradela, B Sieglin, F Reimold, M Rack, M Groth, M Wischmeier, G Arnoux*et al. Scaling of the divertor power spreading (S-factor) in open and closed divertor operation in JET and ASDEX Upgrade.* Journal of Nuclear Materials, vol. 463, pages 49–54, 2015.

[Sieglin 16] B Sieglin, T Eich, M Faitsch, A Herrmann, D Nille, A Scarabosio & ASDEX Upgrade Team. *Density dependence of SOL power width in ASDEX upgrade L-Mode.* Nuclear Materials and Energy, 2016.

[Soukhanovskii 11] VA Soukhanovskii, J-W Ahn, RE Bell, DA Gates, S Gerhardt, R Kaita, E Kolemen, BP LeBlanc, R Maingi, M Makowski*et al. Taming the plasma–material interface with the'snowflake'divertor in NSTX.* Nuclear Fusion, vol. 51, no. 1, page 012001, 2011.

[Soukhanovskii 13] VA Soukhanovskii, RE Bell, Ahmed Diallo, S Gerhardt, S Kaye, E Kolemen, BP LeBlanc, A McLean, JE Menard, SF Paul*et al. Advanced divertor configurations with large flux expansion.* Journal of Nuclear Materials, vol. 438, pages S96–S101, 2013.

[Stangeby 00] Stangeby. The plasma boundary of magnetic fusion devices. 2000.

[Sun 15] H J Sun, E Wolfrum, T Eich, B Kurzan, S Potzel, U Stroth & the ASDEX Upgrade Team. *Study of near scrape-off layer (SOL) temperature and density gradient lengths with Thomson scattering.* Plasma Physics and Controlled Fusion, vol. 57, no. 12, page 125011, 2015.

[Tamain 14] Patrick Tamain, H Bufferand, Guido Ciraolo, Clothilde Colin, Ph Ghendrih, Frédéric Schwander & Eric Serre. *3D Properties of Edge Turbulent Transport*

in Full-Torus Simulations and their Impact on Poloidal Asymmetries. Contributions to Plasma Physics, vol. 54, no. 4-6, pages 555–559, 2014.

[Tamain 15] P Tamain, Ph Ghendrih, H Bufferand, G Ciraolo, C Colin, N Fedorczak, N Nace, F Schwander & E Serre. *Multi-scale self-organisation of edge plasma turbulent transport in 3D global simulations.* Plasma Physics and Controlled Fusion, vol. 57, no. 5, page 054014, 2015.

[Tamain 16] P Tamain, Hugo Bufferand, Guido Ciraolo, C Colin, D Galassi, Ph Ghendrih, Frédéric Schwander & Eric Serre. *The TOKAM3X code for edge turbulence fluid simulations of tokamak plasmas in versatile magnetic geometries.* Journal of Computational Physics, vol. 321, pages 606–623, 2016.

[Taylor 89] RJ Taylor, ML Brown, BD Fried, H Grote, JR Liberati, GJ Morales, P Pribyl, D Darrow & M Ono. *H-mode behavior induced by cross-field currents in a tokamak.* Physical review letters, vol. 63, no. 21, page 2365, 1989.

[Terry 00] PW Terry. *Suppression of turbulence and transport by sheared flow.* Reviews of Modern Physics, vol. 72, no. 1, page 109, 2000.

[Thornton 14] AJ Thornton, A Kirk, MAST Team*et al. Scaling of the scrape-off layer width during inter-ELM H modes on MAST as measured by infrared thermography.* Plasma Physics and Controlled Fusion, vol. 56, no. 5, page 055008, 2014.

[Valanju 10] PM Valanju, M Kotschenreuther & SM Mahajan. *Super X divertors for solving heat and neutron flux problems of fusion devices.* Fusion engineering and design, vol. 85, no. 1, pages 46–52, 2010.

[Wagner 82] F Wagner, G Becker, K Behringer, D Campbell, A Eberhagen, W Engelhardt, G Fussmann, O Gehre, J Gernhardt, G v Gierke*et al. Regime of improved confinement and high beta in neutral-beam-heated divertor discharges of the ASDEX tokamak.* Physical Review Letters, vol. 49, no. 19, page 1408, 1982.

[Wang 14] L Wang, HY Guo, GS Xu, SC Liu, KF Gan, HQ Wang, XZ Gong, Y Liang, XL Zou, JS Hu*et al. Scaling of divertor power footprint width in RF-heated type-III ELMy H-mode on the EAST superconducting tokamak.* Nuclear Fusion, vol. 54, no. 11, page 114002, 2014.

[Wenninger 14] RP Wenninger, M Bernert, T Eich, E Fable, G Federici, A Kallenbach, A Loarte, C Lowry, D McDonald, R Neu*et al. DEMO divertor limitations during and in between ELMs.* Nuclear Fusion, vol. 54, no. 11, page 114003, 2014.

[Weynants 92] R Retal Weynants, G Van Oost, G Bertschinger, J Boedo, P Brys, T Delvigne, KH Dippel, F Durodie, H Euringer, KH Finken*et al. Confinement and profile changes induced by the presence of positive or negative radial electric fields in the edge of the TEXTOR tokamak.* Nuclear Fusion, vol. 32, no. 5, page 837, 1992.

[Wischmeier 15] M Wischmeier*et al. High density operation for reactor-relevant power exhaust.* Journal of Nuclear Materials, vol. 463, pages 22–29, 2015.

[Zohm 13] H Zohm, C Angioni, E Fable, G Federici, G Gantenbein, T Hartmann, K Lackner, E Poli, L Porte, O Sauter*et al. On the physics guidelines for a tokamak DEMO.* Nuclear Fusion, vol. 53, no. 7, page 073019, 2013.

[Zweben 07] SJ Zweben, JA Boedo, O Grulke, C Hidalgo, B LaBombard, RJ Maqueda, P Scarin & JL Terry. *Edge turbulence measurements in toroidal fusion devices.* Plasma Physics and Controlled Fusion, vol. 49, no. 7, page S1, 2007.